Electronic Band Structure and Transport Studies of Oxide Materials

By

Arnaud Pastel Nono Tchiomo

Supervised by
Prof. Bryan P. Doyle, *University of Johannesburg*
Co-Supervised by
Dr Prosper Ngabonziza, *Max-Planck-Institute for Solid State Research, Stuttgart, Germany; University of Johannesburg*
and
Prof. Aletta R.E. Prinsloo, *University of Johannesburg*

A thesis
submitted in fulfillment of the requirements for the degree of
Doctor of Philosophy

Department of Physics, University of Johannesburg, South Africa

25 November 2020

Abstract

Oxides provide an almost unlimited source of materials with exotic properties including superconductivity and magnetism. The emergent field of oxide electronics comes as a replacement of the widely successful field of study that included research on transistor-like structures made from semiconductors, that were mainly silicon based. Research in the area of oxide electronics is mostly motivated by the fact that the limits of what can be done with the current generation of electronics have been approached. Barium tin oxide ($BaSnO_3$) is a transparent oxide material with a perfect cubic perovskite structure. It is an insulator in the bulk with a wide band gap. However, when lightly doped with La, $BaSnO_3$ becomes conducting while retaining its transparency. As a transparent conducting oxide (TCO) material, bulk single crystals of La-doped $BaSnO_3$ exhibit outstanding electrical and physical properties. Despite its wide band gap, bulk La-doped $BaSnO_3$ displays a very high room temperature electron mobility compared to that of conventional TCO materials. It is also stable, keeping its intrinsic and extrinsic properties under high thermal stresses in various gas environments. These characteristics make La-doped $BaSnO_3$ a suitable material for applications such as optical electrodes in solar cells, smart coatings, sensors, flat panels and liquid crystal displays as well as in optoelectronics.

In this thesis, experimental research devoted to producing epitaxial La-doped $BaSnO_3$ thin films of high electron mobility were conducted around optimizing the growth conditions and selecting the best single crystal substrate. The epitaxial thin films were prepared on perovskite oxide single crystal substrates, such as $SrTiO_3$ (001), $DyScO_3$ (110), $TbScO_3$ (110) and $GdScO_3$ (110), and non-perovskite substrates, such as MgO (001), using the pulsed laser deposition technique (PLD). Growth parameters including oxygen background pressure, substrate temperature during thin film deposition as well as film and buffer layer thicknesses were optimized. The optimization of each of these parameters exclusively focused on improving the electron mobility. The electronic transport properties of the grown films were investigated through Hall effect measurements, on samples structured in the van der Pauw geometry. Techniques including reflection high-energy electron diffraction (RHEED), low-energy electron diffraction (LEED) and atomic force microscopy (AFM) were used to investigate the surface characteristics of the films. X-ray diffraction (XRD) and transmission electron microscopy (TEM) were both utilized to analyze the structural and microstructural properties of these films, while X-ray photoemission spectroscopy (XPS) and angle-resolved photoemission spectroscopy (ARPES) were employed for the study of the near-surface composition and the electronic band structure.

In this present work, a new growth strategy has been developed and established to improve the electronic transport characteristics, not only in La-doped $BaSnO_3$ thin films, but also in other TCO systems. It is based on the enhancement of the electron mobility which follows substantial improvements in the structural characteristics of the thin films. In particular, the use of a buffer layer, $SrZrO_3$, which can be deposited at extremely high temperature to improve the crystallinity of the La-doped $BaSnO_3$ thin films provided a breakthrough. For $SrZrO_3$ grown at the optimal temperature of 1300 °C, an enhanced room temperature electron mobility of 140 $cm^2\ V^{-1}\ s^{-1}$ was achieved. This mobility value is about 30% higher than the value of 100 $cm^2\ V^{-1}\ s^{-1}$ reported in as-grown La-doped $BaSnO_3$ thin films using PLD, and is the highest to date for films prepared by PLD without resorting to any post-growth treatment. The enhanced electron mobility is related to other studied characteristics, including the low density of crystallographic defects. These transport and structure properties suggest that

the films have great potential for application. Additional research activities which led to the creation of a two dimensional electron system (2DES) at the surface of $SrTiO_3$ (100) are also addressed in this work. The possibility of tailoring the 2DES at the interface of $Al/SrTiO_3$ (100) heterostructure is also explored.

Declaration

I, the undersigned, hereby declare that the thesis submitted for the degree to the University of Johannesburg is my original work, and that any work done by others or by myself previously has been acknowledged and referenced accordingly. This research project has not been formerly submitted to another university for a degree.

Arnaud Pastel Nono Tchiomo, 25 November 2020

Contents

1. Alkaline Earth Stannates, the New Candidate Material for Transparent Conducting Oxide Technology

1.1 Introduction

Research efforts in understanding the properties of matter have led to the discovery of compounds that have revolutionized the world. Rapid progress in materials science has favored the evolution of new and competitive technologies, especially in electronics. Materials that make electronic devices more functional, cheap, strong, light and more sustainable have been developed throughout the years and have contributed to improving the living conditions of populations. For instance, the ability to control the properties of materials has resulted in the engineering of a new class of materials that are transparent and conduct electricity with unconventional functionalities. These materials are greatly used in the solar cell industry. They have also revolutionized screen displays with liquid crystal displays (LCD), organic light-emitting diodes (OLED) and transparent displays; and have made devices smarter with the technology of touch panels, virtual reality and transparent-flexible electronics. These materials are still the subject of great interest in the research community, and research activities continue towards the enhancement of the electronic properties of epitaxial oxide thin films; the understanding of their conductivity mechanisms, which requires establishing a proper correlation between the transport properties and the electronic band structure; and the efforts to reduce the density of structural defects in the thin oxide films and at the interface of oxide heterostructures. The presented work also aims to contribute to this active field.

1.2 Why is La-Doped $BaSnO_3$ Interesting?

La-doped barium tin oxide or barium stannate (La-doped $BaSnO_3$) is a transparent conducting oxide (TCO) material that has attracted much attention recently due to its room temperature high electron mobility (despite its wide band gap), and therefore for its potential in transparent oxide electronics [1, 2, 3, 4, 5]. TCOs exhibit high electrical conductivity while retaining their transparency. The most widely used TCO material in electronic devices is indium tin oxide. However, because of the scarcity and the high cost of the In metal, alkaline earth stannates, with general formula $ASnO_3$ (A=Ba, Sr and Ca), were found as a possible replacement due to their supreme physical and electronic properties [1, 2]. Among them, $BaSnO_3$ was found to have a simple crystallographic structure. It was also discovered that it could exhibit a high and stable conductivity at high temperatures after being lightly doped with La, making it a suitable material for applications such as optical electrodes in solar cells, smart coatings, sensors, flat panel and liquid crystal displays as well as optoelectronic devices [6, 7, 8, 9, 10, 11]. In fact, the present surge of interest in $BaSnO_3$ materials comes after Kim *et al.* [1] discovered in 2012 that at room temperature, a La-doped $BaSnO_3$ single crystal behaves like an n-type conductor with a high electron mobility of about 320 $cm^2\ V^{-1}s^{-1}$ at a doping concentration of $8 \times 10^{19}\ cm^{-3}$. In device designing, however, to realize superior electronic and optoelectronic performances, epitaxial thin films are preferred over bulk single crystals. This is because of the limited scope of applications implementing functional materials in the bulk form. This

limitation is associated with the large thickness (in the order of several millimeter) of the single crystals which is far greater than the diffusion length (in the order of several micrometer) of the free carriers, resulting in extreme charge accumulation [12]. Nevertheless, attempts to achieve high electron mobility in epitaxial La-doped $BaSnO_3$ thin films comparable to that in single crystals have always been limited by the presence of a large number of dislocations and defects originating either from the growth method/conditions and/or the large lattice mismatch between the substrate and the film grown on top [13, 14, 15, 16, 17]. These dislocations act as scattering cores and reduce the number of free electrons and also lower the electron mobility [16]. However, the implementation of La-doped $BaSnO_3$ as an active channel in electronic devices, such as thin-film transistors, requires the thin films to have an electron mobility above or comparable to that in conventional semiconductor materials.

Research to date has been conducted in a systematic fashion and dedicated to improving the electron mobility in La-doped $BaSnO_3$ thin films [14, 15, 16, 17, 18]. Firstly, research efforts are focused on optimizing the growth conditions [16, 19, 20]. Parameters such as oxygen partial pressure, laser fluence, substrate temperature during growth and film thickness are critical for the physical properties of the films. Also, to reduce relaxation at the film-substrate interface, a buffer layer of same or different material as the grown film is often used [17, 20, 21, 22, 23]. Furthermore, the methods by which the films are deposited play an important role [17, 18, 19, 24, 25, 26]. Three deposition techniques including sputtering, molecular beam epitaxy (MBE) and pulsed laser deposition (PLD) are commonly used. Secondly, efforts are directed towards choosing the best single crystal substrate in a bid to reduce the large lattice mismatch and temper the dislocations and defects [17, 18, 24, 25]. A lattice-matched material such as a $BaSnO_3$ single crystal substrate is ideal, but it is difficult to make and therefore not available on the market. Alternatively, compounds with the same structure (perovskite) are adopted and the density of dislocations at the interface varies with the substrate used [17, 18]. For example, films fabricated with $SrTiO_3$ substrates have more dislocations than those made on scandate substrates such as $DyScO_3$, $TbScO_3$, $PrScO_3$ and $SmScO_3$ [17, 18]. Thirdly, there is focus on the structural, microstructural, optical and electrical characterization as for epitaxial semiconductor films [13, 14, 15, 16, 17, 18, 23]. This characterization is effective in getting insight into the physical properties and elemental composition of the films, in perceiving their crystalline structure at the atomic level and to discern the type of defects or impurities [13, 17, 23]. These analyses are critical in determining whether the films are suitable for specific use in electronic devices. Nevertheless, the mechanisms that provide such a high room temperature mobility in La-doped $BaSnO_3$ are still poorly explained. A conduction mechanism can be said to be well understood if an appropriate correlation is made between transport properties and electronic structure [27]. To gain a fundamental knowledge of the electronic transport in this system, a full comprehension of the electronic band structure is needed.

A detailed analysis of the band structure can provide quantitative information on the Fermi velocity and scattering relaxation time, which are both strongly dependent on carrier concentration [4, 28]. For several years, the electronic band structure of La-doped $BaSnO_3$ had only been investigated through density functional theory (DFT) calculations [4, 28, 29] and indirectly through Fourier transform infrared (FTIR) spectroscopy [30]. The computational calculations provided important information and description of the electronic band structure. These calculations revealed the size and the nature of the band gap, the composition of both the conduction band minimum (CBM) and the valence band maximum (VBM), as well as their position in the first Brillouin zone [4, 28, 29]. They also specified the effects of donor

dopants and defects (intrinsic and extrinsic) on the electronic structure. From first principle calculations based on hybrid DFT, the high electron mobility originates from both the electron effective mass and the reduction in the phonon scattering rate [4, 30]. Experimental studies of the band structure to identify which bands contribute to the high electron mobility in this system are very challenging. Nonetheless, some progress was recently made for both $BaSnO_3$ and La-doped $BaSnO_3$ thin films, confirming the structure of the bands and the nature of the gap between CBM and VBM [27, 31, 32]. More experimental work is still needed to clarify and obtain a better understanding of the factors that limit conduction.

1.3 Intention of this Study

In this thesis, a new growth strategy developed as part of this study to improve the electronic transport properties in epitaxial La-doped $BaSnO_3$ thin films is demonstrated. In particular, the enhancement of the electron mobility which follows substantial development in the structural characteristics of the thin films is elaborated. Complementary knowledge and understanding of both the surface and electronic band structures of these films are also provided.

Epitaxial thin films of La-doped $BaSnO_3$ have been grown in a PLD chamber. Thorough analyses of their surface, structure and electrical properties have been carried out. The transport characteristics for PLD grown La-doped $BaSnO_3$ thin films have been optimized, and a correlation with the spectroscopic results have been drawn. This thesis is structured in chapters as described below.

Chapter 2 presents an overview of the current knowledge on the La-doped $BaSnO_3$ system. Details regarding La-doped $BaSnO_3$ as a TCO material and its fascinating properties are presented. The potential origins of the high electron mobility in the system are addressed and the efforts by different researchers to improve it are described. Finally, the current progress in investigating the electronic band structure is shown.

In chapter 3, the theory behind the experimental techniques used to grow and characterize the films is explained. The growth process, starting from the *ex situ* preparation of the substrates to the PLD growth of the films is described. The methods employed for surface, structural and electrical characterizations are detailed. These methods are: reflection high-energy-electron diffraction (RHEED), low-energy-electron diffraction (LEED), as well as atomic force microscopy (AFM) for the surface characterization; X-ray diffraction (XRD), transmission electron microscopy (TEM) and X-ray photoemission spectroscopy (XPS) for the structural characterization; and magnetoresistance in the Van der Pauw geometry for the electrical characterization. This chapter concludes with the presentation of angle-resolved photoemission spectroscopy (ARPES), which is the technique adopted to investigate the electronic band structure of the thin films.

Chapter 4 presents and discusses all the surface, structural and electronic transport results obtained from the growth and the characterization of the La-doped $BaSnO_3$ thin films. The chapter starts with the optimization of the growth parameters such as the oxygen background pressure, the substrates temperature, as well as the thicknesses of the active film and buffer layers. The growth was optimized to achieve optimal electron mobility in the La-doped $BaSnO_3$ thin films. Films directly grown on the substrates or using buffer layers of $BaSnO_3$ or $SrZrO_3$ exhibit improved high electron mobility. These transport results are the best to date for thin films of La-doped $BaSnO_3$ grown by PLD. The smoothness of the growth and the smoothness

of the film surfaces are discussed, followed by analyses of the crystalline quality and strain states of the films. Epitaxial thin films of smooth surfaces were fabricated. Secondary phases were not detected in the films, which suggests films of high crystallinity. The in-plane and out-of-plane lattice constants of the grown films were calculated. These values provide an indication about the density of defects in the films. Afterwards, a microstructural analysis of these defects was carried out. The grown films present defects such as stacking faults and threading dislocations originating from misfit dislocations, which affect the electronic characteristics. Misfit dislocations are generated from the large lattice mismatch between the as-deposited film and the substrates that are used for the growth. The strategy developed by us to reduce the density of these defects in the films and enhance their electronic transport properties is described.

In chapter 5, the chemical composition and elemental quantification of the films are described, followed by the electronic band structure analysis. Details are provided for the CBM and the valence band which corroborate the results from computational simulations and previous experimental work. At the end of this chapter, an attempt to correlate the electronic transport and the band structure results is made.

In chapter 6, the preliminary results of a project dedicated to investigating the properties of the interface of the Al/$SrTiO_3$ heterostructure are addressed. A background of knowledge that helps to understand the importance of such heterostructure is briefly presented.

The last chapter gives a summary of this study. It also includes a brief overview of the remaining challenges in the La-doped $BaSnO_3$ system together with the possible considerations for future investigations.

Bibliography

[1] H. J. Kim, U. Kim, H. M. Kim, T. H. Kim, H. S. Mun, B. G. Jeon, K. T. Hong, W. J. Lee, C. Ju, K. H. Kimy, and K. Char, Appl. Phys. Express **5**, 061102 (2012).

[2] Q. Z. Liu, H. F. Wang, F. Chen, and W. Wu, J. Appl. Phys. **103**, 093709 (2008).

[3] H. J. Kim, U. Kim, T. H. Kim, J. Kim, H. M. Kim, B. G. Jeon, W. J. Lee, H. S. Mun, K. T. Hong, J. Yu, K. Char, and K. H. Kim, Phys. Rev. B **86**, 165205 (2012).

[4] D. O. Scanlon, Phys. Rev. B **87**, 161201 (2013).

[5] H. F. Wang, Q. Z. Liu, F. Chen, G. Y. Gao, W. Wu, and X. H. Chen, Appl. Phys. **101**, 106105 (2007).

[6] J. Park, U. Kim, and K. Char, Appl. Phys. Lett. **108**, 092106 (2016).

[7] W.-J. Lee, H. J. Kim, J. Kang, D. H. Jang, T. H. Kim, J. H. Lee, and K. H. Kim, Annu. Rev. Mater. Res. **47**, 391 (2017).

[8] H. Ohta, K. Nomura, H. Hiramatsu, K. Ueda, T. Kamiya, M. Hirano, and H. Hosono, Solid State Electron. **47**, 2261 (2003).

[9] D. S. Ginley, and C. Bright, MRS Bull. **25**, 15 (2000).

[10] K. Nomura, H. Ohta, K. Ueda, T. Kamiya, M. Hirano, and H. Hosono, Science **300**, 1269 (2003).

[11] K. Ellmer, Nat. Photonics **6**, 809 (2012).

[12] X.-D. Wang, W.-G. Li, J.-F. Liao, and D.-B. Kuang, Sol. RRL **3**, 1800294 (2019).

[13] W. Y. Wang, Y. L. Tang, Y. L. Zhu, J. Suriyaprakash, Y. B. Xu, Y. Liu, B. Gao, S. W. Cheong, and X. L. Ma, Sci. Rep. **5**, 16097 (2015).

[14] A. V. Sanchela, M. Wei, H. Zensyo, B. Feng, J. Lee, G. Kim, H. Jeen, Y. Ikuhara, and H. Ohta, Appl. Phys. Lett. **112**, 232102 (2018).

[15] S. Yu, D. Yoon, and J. Son, Appl. Phys. Lett. **108**, 262101 (2016).

[16] H. Mun, U. Kim, H. Min Kim, C. Park, T. Hoon Kim, H. Joon Kim, K. Hoon Kim, and K. Char, Appl. Phys. Lett. **102**, 252105 (2013).

[17] H. Paik, Z. Chen, E. Lochocki, H. Ariel Seidner, A. Verma, N. Tanen, J. Park, M. Uchida, S. Shang, B. C. Zhou, M. Brützam, R. Uecker, Z. K. Liu, D. Jena, K. M. Shen, D. A. Muller, and D. G. Schlom, APL Mater. **5**, 116107 (2017).

[18] S. Raghavan, T. Schumann, H. Kim, J. Y. Zhang, T. A. Cain, and S. Stemmer, APL Mater. **4**, 016106 (2016).

[19] K. Ganguly, A. Prakash, B. Jalan, and C. Leighton, APL Mater. **5**, 056102 (2017).

[20] J. Shin, Y. M. Kim, Y. Kim, C. Park, and K. Char, Appl. Phys. Lett. **109**, 262102 (2016).

[21] C. Park, U. Kim, C. J. Ju, J. S. Park, Y. M. Kim, and K. Char, Appl. Phys. Lett. **105**, 203503 (2014).

[22] J. Shiogai, K. Nishihara, K. Sato, and A. Tsukazaki, AIP Adv. **6**, 065305 (2016).

[23] A. Prakash, P. Xu, A. Faghaninia, S. Shukla, J. W. Ager, C. S. Lo, and B. Jalan, Nat. Commun. **8**, 15167 (2017).

[24] P. V. Wadekar, J. Alaria, M. O'Sullivan, N. L. O. Flack, T. D. Manning, L. J. Phillips, K. Durose, O. Lozano, S. Lucas, J. B. Claridge, and M. J. Rosseinsky, Appl. Phys. Lett. **105**, 052104 (2014).

[25] W.-J. Lee, H. J. Kim, E. Sohn, T. H. Kim, J.-Y. Park, W. Park, H. Jeong, T. Lee, J. H. Kim, K.-Y. Choi, and K. H. Kim, Appl. Phys. Lett. **108**, 082105 (2016).

[26] D. Yoon, S. Yu, and J. Son, NPG Asia Mater. **10**, 363 (2018).

[27] E. B. Lochocki, H. Paik, M. Uchida, D. G. Schlom, and K. M. Shen, Appl. Phys. Lett. **112**, 181603 (2018).

[28] S. Sallis, D. O. Scanlon, S. C. Chae, N. F. Quackenbush, D. A. Fischer, J. C. Woicik, J.-H. Guo, S.-W. Cheong, and L. F. J. Piper, Appl. Phys. Lett. **103**, 042105 (2013).

[29] K. Krishnaswamy, B. Himmetoglu, Y. Kang, A. Janotti, and C. G. Van De Walle, Phys. Rev. B **95**, 205202 (2017).

[30] C. A. Niedermeier, S. Rhode, K. Ide, H. Hiramatsu, H. Hosono, T. Kamiya, and M. A. Moram, Phys. Rev. B **95**, 161202 (2017).

[31] B. S. Joo, Y. J. Chang, L. Moreschini, A. Bostwick, E. Rotenberg, and M. Han, Curr. Appl. Phys. **17**, 595 (2017).

[32] Z. Lebens-Higgins, D. O. Scanlon, H. Paik, S. Sallis, Y. Nie, M. Uchida, N. F. Quackenbush, M. J. Wahila, G. E. Sterbinsky, D. A. Arena, J. C. Woicik, D. G. Schlom, and L. F. Piper, Phys. Rev. Lett. **116**, 027602 (2016).

2. Recent Developments in Transparent Conducting Oxide La-Doped $BaSnO_3$ Systems

2.1 Introduction

In this chapter, the characteristic features of $BaSnO_3$ and La-doped $BaSnO_3$ materials that make them suitable for applications in various domains are firstly discussed. Then, the factors that are reported to contribute and also to limit the high electrical performance in oxide heterostructures based La-doped $BaSnO_3$ thin films are addressed. Afterwards, research efforts to circumvent those limitations and improve the electronic transport properties of La-doped $BaSnO_3$ thin films are presented. Finally, theoretical and experimental studies of the electronic structure of $BaSnO_3$ and La-doped $BaSnO_3$ systems are addressed.

2.1.1 Discovery, Advancement, and Applications of Transparent Conducting Oxides

In 1907, Bädeker [1] published that oxidized thin metal films of Cd prepared in a glow discharge chamber became transparent while retaining their electrical conductivity. These thin films were the first transparent conducting oxides (TCOs) ever reported [2]. Transparent and conductive behaviors are generally mutually exclusive. Good conductors such as metals are opaque to visible light. These have many closely-spaced energy levels available to electrons. So, a photon (light) has enough energy to excite one of these electrons to move to the next energy level and get absorbed in the process. In transparent materials (typically insulators), which have wide band gaps on the other hand, visible light passes through without getting absorbed or scattered. The ability of combining current flow and transparency in a material is of great technological importance, which has led to increasing efforts in developing and designing new TCO materials for specialized applications [2, 3, 4, 5]. For more than 5 decades, undoped and impurity-doped binary oxides such as CdO, ZnO, SnO_2 and In_2O_3 have prevailed as the primary *n*-type TCO materials. These oxides have degenerate semiconducting behavior with a conduction band shape that guarantees plasma absorption in the infrared [2, 3, 6]. They have an outstanding adhesion to most substrates and can be grown at room temperature (RT). Their processing or deposition conditions depend upon the targeted application. For instance, infrared reflectivity and high transparency are preferred over good conductivity and optimum optical transmissivity during the manufacturing of architectural glass used as radiation filters [2, 3, 5, 6, 7]. On the other hand, maximum optical transmission in the visible spectrum coupled with minimum electrical sheet resistance should be achieved in TCO materials dedicated for optoelectronic applications [2, 3, 6, 7].

The principal commercial TCOs including Sn-doped In_2O_3, F or Al-doped ZnO, and F-doped SnO_2 have been extensively employed in the three dominant markets for TCOs which are architectural glass applications for energy-efficient windows, flat-panel displays and photovoltaic modules. Due to the low-cost production and the low emissivity of SnO_2, F-doped SnO_2 has been most often employed for window coatings in functional glass. The transparency of coated windows can be electrically controlled (electrochromic windows) and used for heat or light

management in the housing, aeronautic and automotive domains, among others [2, 6, 8, 9]. For optoelectronic applications, there have been sweeping strides throughout the years in displays and photovoltaics, mostly based on Sn-doped In_2O_3 and Al-doped ZnO, respectively [6, 7, 8, 10, 11, 12, 13, 14, 15, 16]. There has been significant advancement in smart displays for the new technology of smart devices, larger flat-screen televisions of higher-definition, larger portable computers screens of higher-resolution, touch screens and plasma displays together with an important rise in the manufacturing of thin film photovoltaic cells.

In all the applications mentioned above, TCOs have the role of transparent conductive electrodes, simultaneously transmitting light and conducting electrical current. These electrodes are thin films deposited by various techniques including dc-magnetron sputtering of ceramic targets in a gas mixture of Ar and O_2 [17, 18, 19], and chemical evaporation onto hot glass by spraying [19, 20]. The thin films preparation (deposition, optimization and treatment procedures) leads to single crystalline films, which can often contain some crystallographic defects, such as dislocations, grain boundaries, stacking faults and point defects (mostly oxygen vacancies). These defects generate additional scattering processes, that, added to the intrinsic ionized impurity scattering, contribute to limiting the electron mobility in these TCO materials [2, 11]. The reported RT carrier mobilities for a maximum doping level in the order of 10^{21} cm^{-3} vary as follows: $\approx 20 - 100$ cm^2 V^{-1} s^{-1} for Sn-doped In_2O_3, $\approx 1 - 5$ cm^2 V^{-1} s^{-1} for Al-doped ZnO, and $\approx 15 - 50$ cm^2 V^{-1} s^{-1} for F-doped SnO_2 [21, 22]. A summary of the electron mobility as a function of the carrier concentration for these TCOs in single crystal and thin film forms is shown in Fig. 2.1, along with that of some semiconductors for

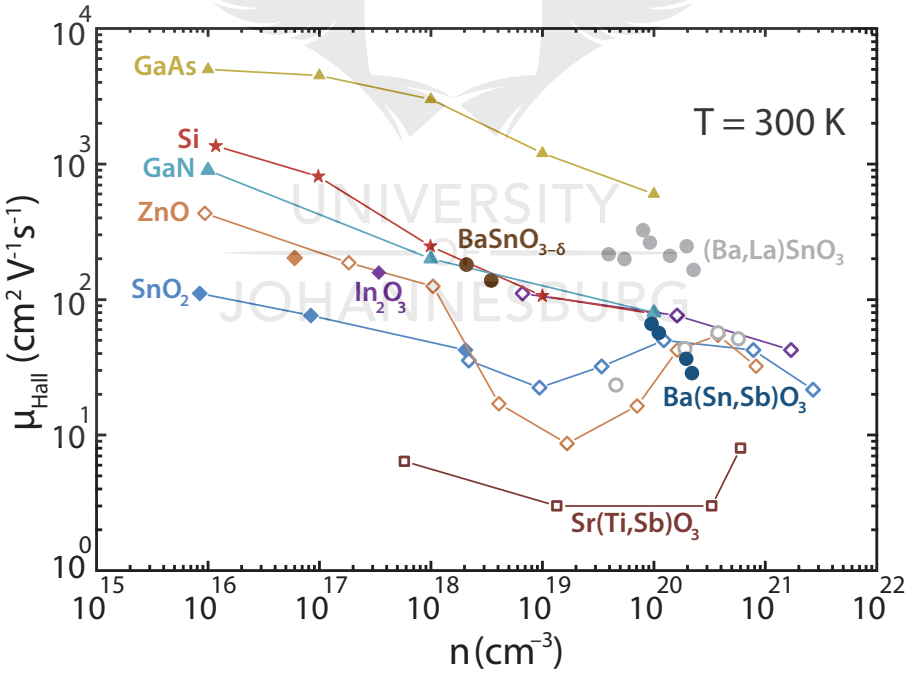

Figure 2.1: RT electron mobility as a function of the carrier density for some TCO and semiconductor single crystals and thin films. The open symbols represent the mobility values for thin films whereas the solid symbols represent those of single crystals. (Ba,La)SnO_3 and Ba(Sn,Sb)O_3 stand for $BaSnO_3$ single crystals doped with La and Sb respectively in the Ba and the Sn sites; and Sr(Ti,Sb)O_3 stands for $SrTiO_3$ thin film doped with Sb in the Ti site. The image was adapted from Ref. [22].

comparison.

Although film growth processes of binary TCO compounds are relatively simple due to their chemical composition, the cost and scarcity of In and the toxicity of Cd have triggered the search for new eco-friendly *n*-type TCO compounds. An example of such materials is the perovskite La-doped lead zirconate titanate of formula $La_xPb_{1-x}(Zr_yTi_{1-y})O_3$ also known as PLZT. PLZT has proved its potential as a solid-state device material for applications in infrared detectors [23], signal processing [24], photoconductor memory [25], as well as switching devices [26]. It has also been employed in various optical applications including display devices [27], image sensors and storage [28], photochromics and electrochromics [29].

2.1.2 Doped $BaSnO_3$

Ternary materials with the perovskite structure are key for the next generation of *n*-type TCO thin films for specialized applications [30]. Such compounds have significantly greater adjustable chemical composition compared to binary systems, leading to more control of the physical, optical, chemical and electrical properties [3, 6, 7, 30]. Very recently, a particular transparent perovskite oxide compound has been the subject of great interest, due to its physical and electrical characteristics. This is barium stannate ($BaSnO_3$), which can be effectively doped to form a degenerate *n*-type TCO, and exhibits high electrical conductivity, combined with the ability to withstand high temperatures while retaining its intrinsic optical and structural properties [31, 32]. This material has thus been extensively investigated for potential application in optoelectronic devices, as a replacement for Sn-doped In_2O_3, since the mobility in lightly La-doped $BaSnO_3$ single crystals was found to be about 3 times higher than that in Sn-doped In_2O_3 for similar doping levels [31]. $BaSnO_3$ had already attracted attention in the past [32, 33, 34, 35, 36, 37]. It has been employed as gas sensors, and used in various applications to strengthen and enhance the physical properties of other materials [33, 34]. In an invention made in 1943 related to the production of glass enamels, it was included in the composition of the enamel to achieve high resistance to alkalis [33]. From the mixture of perovskite ceramic substances such as $BaSnO_3$, barium titanate ($BaTiO_3$) and barium zirconate ($BaZrO_3$), materials with high dielectric constants were synthesized in 1948. Owing to their high dielectric constants, these materials were useful for applications in electro-mechanical devices, low frequency distribution and communication systems [34].

Beginning in the 1970s, the electrical properties of $BaSnO_3$ were investigated and the type of conductivity established. Prokopalo [35] found *n*-type conductivity originating from the occupancy of oxygen vacancies by dopant electrons, and observed a large increase in the conductivity at higher concentrations of the non-isovalent cation dopants. Shimizu *et al.* [32] found that the *n*-type semiconducting nature of $BaSnO_3$ was stable at a temperature $\approx$ 900 °C in an oxygen partial pressure below 10^2 Pa; making it a suitable oxygen sensor for the detection of the stoichiometric air to fuel ratio. To get more insight into the processes involved in the semiconductor gas sensing, Ostrick *et al.* [36] simultaneously performed *in situ* Hall and conductivity measurements on $BaSnO_3$ ceramics for temperatures ranging from 650 °C to 1050 °C. They found a thermal stability in the conductivity behavior over the entire temperature range. In the Hall measurements, a strong dependence of the carrier density and the mobility on the oxygen partial pressure at temperatures above and below 900 °C, respectively, were observed. In the same year (1997), they prepared thin films of $BaSnO_3$ by radio frequency sputtering [37]. The Hall results were similar to those of the ceramic materials and correlated with the cross-sensitivity of the films to the oxygen concentration in

the synthetic air over the entire temperature range.

In 2012, Kim *et al.* [31] prepared both single crystals and thin films of $BaSnO_3$ and La-doped $BaSnO_3$ (La introduced in the Ba site). They measured the variation of the resistance of the La-doped $BaSnO_3$ film with temperature by successively annealing the film in different gas environments such as argon, oxygen and air. They noticed a change of about 8% in the resistance values after annealing at 530 °C for 5 hours first in argon, and then in oxygen; and a variation of only 1.7% after transitioning from annealing in oxygen to annealing in air at the same temperature and for the same duration, indicating excellent stability of the oxygen atoms at high temperature. Furthermore, Bacur *et al.* [38] found that $BaSnO_3$ had a stable dielectric constant in a wide range of high frequencies (50 kHz – 500 kHz) and temperatures. These results suggest that La-doped $BaSnO_3$ systems have potential use in high power electronic and high frequency devices as well as thermally stable ceramic capacitors [31, 38]. Kim *et al.* also performed Hall measurements on La-doped $BaSnO_3$ single crystals and thin films and obtained a record electron mobility value in single crystals compared to similar transparent oxide materials. The high transparency combined with the high electron mobility in the thin films [31], points to the great potential of La-doped $BaSnO_3$ materials in transparent oxide electronics [39].

This chapter is dedicated to reported advances in enhancing the carrier mobility in electron-doped $BaSnO_3$, more precisely in La-doped $BaSnO_3$ thin films. The crystallographic structure (perovskite) of $BaSnO_3$ is first presented, followed by the possible origins of the high mobility from a simple one-band model observed in both La-doped $BaSnO_3$ single crystals and thin films. Several scattering mechanisms reported to limit this high mobility as with the most used TCOs are also covered. Finally, progress in fabricating La-doped $BaSnO_3$ epitaxial thin films of improved mobility are presented, along with the efforts to understand, at a more detailed band structure level, the origin of this high conductivity.

2.2 High Mobility and Scattering Mechanisms in Doped $BaSnO_3$

2.2.1 The Cubic Perovskite Structure of $BaSnO_3$

Perovskite is the name first given to the mineral $CaTiO_3$, discovered in 1859 in the Ural Mountains by the Prussian mineralogist Gustav Rose, and named to honor the Russian mineralogist Count Lev Aleksevich von Petrovski [40]. The name perovskite is commonly employed to refer to a large family of compounds with the general chemical formula ABX_3, where A and B are large and medium-sized cations, respectively, and X an anion [41, 42]. In the case of perovskite oxides, where $X = O$ (oxygen), the A site is mostly an alkali metal or an alkaline earth metal ion with the valence state between $1+$ and $3+$; whereas the B site is a transition metal or metal ion and its oxidation state is determined by electro-neutrality, considering that the three oxygens per unit cell contribute a factor of -6. More generally, the electro-neutrality in perovskite oxide compounds can be written as

$$q_A + q_B = -3q_O, \tag{2.1}$$

where q_A, q_B and q_O are the charges on A, B and O ions, respectively. Oxide materials with the perovskite structure are characterized by a variety of solid state properties such as superconductivity, ferroelectricity, piezoelectricity and magnetism [41, 42, 43, 44, 45, 46, 47, 48, 49, 50].

Transparent perovskite oxides are captivating since they form a broad class of structurally identical compounds including insulators, semiconductors and metals, whose electronic properties can be altered in a controllable fashion to produce novel functional properties [41, 42].

$BaSnO_3$ is an example of a perovskite oxide, which has a perfect cubic structure (space group $Pm\bar{3}m$), as shown in Fig. 2.2. Ba^{2+} and Sn^{4+} ions occupy the corners and the center of the cube, respectively, and O^{2-} ions occupy the center of each face, forming a regular three-dimensional octahedron (SnO_6) around Sn^{4+}, as illustrated in Fig. 2.2(a). The octahedra is not tilted or distorted as can be clearly seen in Fig. 2.2(b) representing a $3 \times 3 \times 3$ supercell of $BaSnO_3$. Furthermore, as shown in Fig. 2.2(c), the angle of the O^{2-}—Sn^{4+}—O^{2-} bonds is 180° and all the Sn^{4+}—O^{2-} bonds are of equal length. The coordination of Ba^{2+} is illustrated

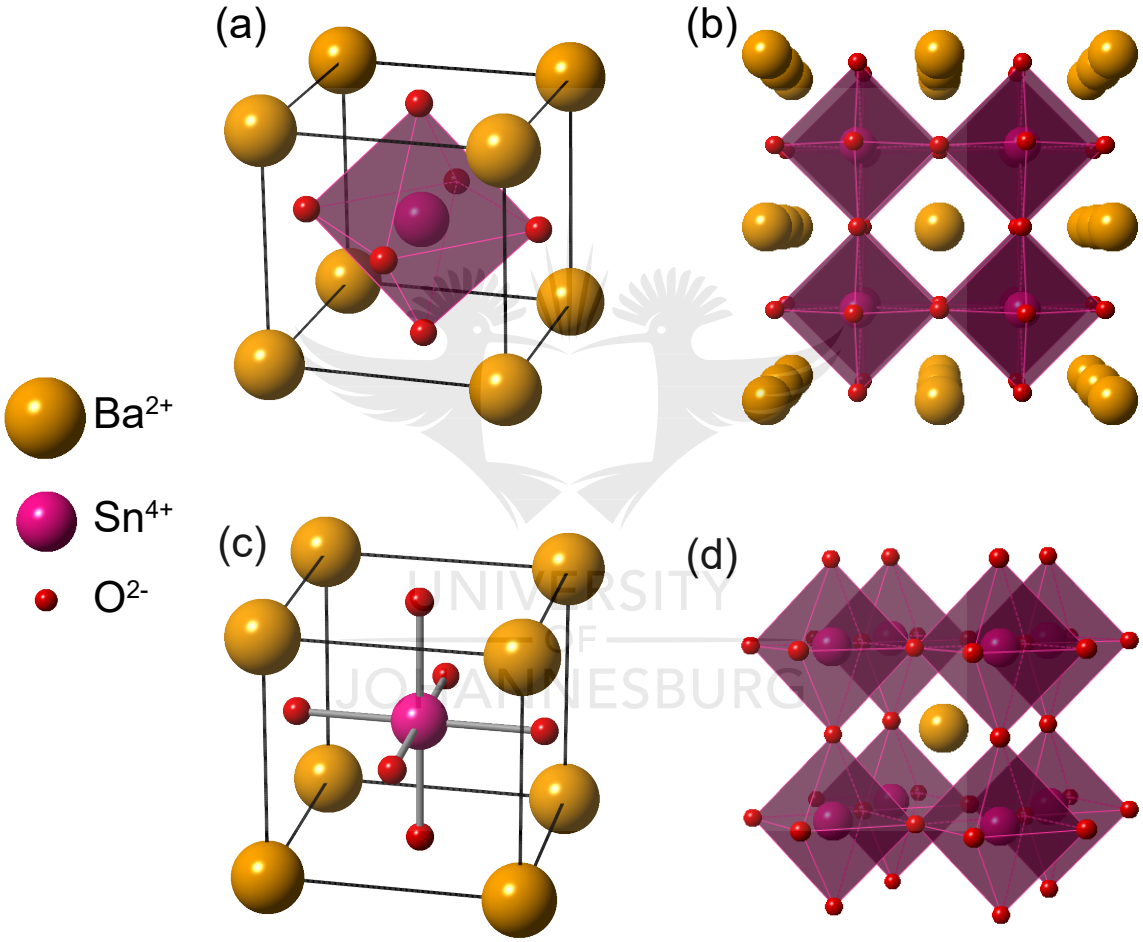

Figure 2.2: The perfect cubic structure of perovskite $BaSnO_3$. (a) A unit cell represented with Ba^{2+} and Sn^{4+} ions at the corners and center of the cube, respectively, and O^{2-} ions at the center of each face. Sn^{4+} is coordinated to 6 O^{2-} ions, as realized by the regular three dimensional SnO_6 octahedra of O^{2-}. (b) A $3 \times 3 \times 3$ supercell whereby all the SnO_6 octahedra are well aligned, not distorted or tilted. (c) The same unit cell as in (a) showing the Sn^{4+}—O^{2-} bonds which are of regular lengths, with an ideal 180° of O^{2-}—Sn^{4+}—O^{2-} bonding. (d) A unit cell represented with Sn^{4+} at the corners of the cube such that one O^{2-} ion is located in the middle of each of the 12 edges to form a network of corner-sharing octahedra with O^{2-} ions from the closest unit cells. Ba^{2+} then sits at the center of the cube, coordinated by the 12 O^{2-} ions. The unit cell is drawn from the centers of the 8 Sn atoms.

in Fig. 2.2(d), which shows a unit cell constituted of Sn^{4+} ions at the corners of the cube with a Ba^{2+} ion at the center and an O^{2-} ion located in the middle of each of the 12 edges. The Ba^{2+} ion is then surrounded by a framework of octahedra built with O^{2-} ions from the closest unit cells giving a coordination of 12. These descriptions confirm the perfect cubic structure of $BaSnO_3$ and could contribute to the origin of the high electron mobility of this system. Several values of the lattice parameter have been reported, varying from 4.108 Å [40] to 4.116 Å [31, 51, 52, 53]. The latter value has been largely reported for ceramic targets, single crystals and epitaxially grown thin films, which are summarized in Section 2.3 of this chapter.

2.2.2 Contributing Factors to the High Mobility in La-Doped $BaSnO_3$ Systems

$BaSnO_3$ is a material in which *n*-type doping can be achieved by substitution with donor electrons either on the Ba site or the Sn site. There are several reports on the electrical properties of $BaSnO_3$ doped with La (on the Ba site) and with Sb (on the Sn site) [22, 54, 55]. It is found that Sb doping results in less electron mobility in both single crystals and thin films. This is due to the significant amount of electrically inactive ionized Sb dopant that remains in the lattice as impurities and causes additional scattering. The effect of these residual impurities is important as the Sb ions lie in the SnO_6 octahedra, where the conduction mechanism is believed to occur through the 5s state of the Sn^{4+} ions and the 2p state of the O^{2-} ions. The maximum RT electron mobilities reported in Sb-doped $BaSnO_3$ single crystals and thin films are respectively 79.4 $cm^2\ V^{-1}\ s^{-1}$ and $< 10\ cm^2\ V^{-1}\ s^{-1}$, for carrier densities between 1×10^{20} and $4 \times 10^{20}\ cm^{-3}$ [55, 56]. On the other hand, a maximum RT mobility of 320 $cm^2\ V^{-1}\ s^{-1}$ was found in $BaSnO_3$ single crystals doped to $8 \times 10^{19}\ cm^{-3}$ with La [31]. The comparison of the RT mobility values of La-doped $BaSnO_3$ single crystals with those of the most popular semiconductors such as GaAs, GaN and Si, along with some other representative TCO single crystals and thin films is shown in Fig. 2.1. It is seen that at doping concentrations $\geq 10^{19}\ cm^{-3}$, the mobility is above that of In_2O_3. However, this value is lower than that of GaAs, and is the second-highest among TCOs after CdO [57] (not summarized in Fig. 2.1).

Heteroepitaxial growth of La-doped $BaSnO_3$ thin films has been intensively reported. Figure 2.3 summarizes the efforts in fabricating high mobility La-doped $BaSnO_3$ thin films (or oxide heterostructures based La-doped $BaSnO_3$ thin films) for a period of time up to early 2017. The films were made using sputtering, PLD and MBE on various substrates including $SrTiO_3$, $PrScO_3$ and MgO. Despite all the efforts in optimizing and improving the growth conditions in state-of-the-art facilities, the mobility in thin films has not reached that of single crystals, and has always been limited to values smaller than 200 $cm^2\ V^{-1}\ s^{-1}$.

A good practice in attempting to understand the mobility limiting factors is to start with the potential origins of the high electron mobility in $BaSnO_3$ system. The simple cubic perovskite structure of $BaSnO_3$ material with the perfect 180° angle of the O—Sn—O bonds in the corner-sharing SnO_6 octahedra network (see Fig. 2.2), together with a highly dispersive Sn 5s derived conduction band are key elements for its high electrical mobility [58]. In a simple one-band model, the electron mobility (μ) is inversely proportional to the electron effective mass (m^*), and directly proportional to the electron scattering relaxation time (τ). This is expressed by [59, 60, 61]

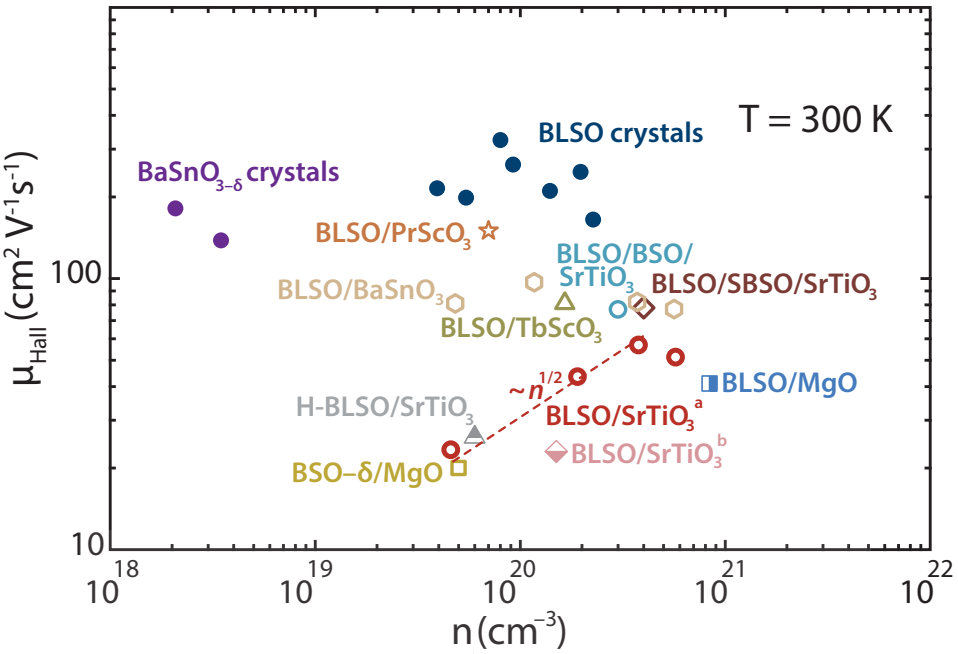

Figure 2.3: RT electron mobility as a function of the carrier density for several La-doped $BaSnO_3$ (BLSO) thin films deposited on different substrates by growth techniques such as PLD, MBE and sputtering. The open symbols represent the mobility value for thin films whereas the solid symbols represent that of single crystals. The image was adapted from Ref. [22].

$$\mu = \frac{q\tau}{m^*}, \tag{2.2}$$

where q is the elementary charge. This implies that high mobility is achieved for simultaneous low m^* and low scattering rate τ^{-1} (or simply high relaxation time between successive scattering which result in loss in momentum). Thus, a systematic quantitative analysis of the electron effective mass m^* and the average scattering rate τ^{-1} is crucial for understanding the electronic transport in $BaSnO_3$. The value of m^* is extracted from the plasma frequency (ω_p), which for $BaSnO_3$ is mostly obtained by reflectivity measurements on a Fourier transform infrared spectrometer. m^* and ω_p are related by [60, 61]

$$\omega_p^2 = \frac{nq^2}{\epsilon m^*}. \tag{2.3}$$

The carrier concentration, n, and the dielectric constant, ϵ, are determined by Hall effect and optical spectroscopy measurements on the specimen, respectively. Different values of m^* have been proposed from DFT calculations and optical properties measurements. From most calculations, the RT mobility originates from both the small m^* and the reduction in the scattering rate. The dielectric function, infrared spectra and optical absorption of $BaSnO_3$ have been simulated using DFT to estimate or predict the values of m^*. Some of the theoretical values reported are: $0.4m_0$ for both $BaSnO_3$ and 3.7% La-doped $BaSnO_3$ crystals [62]; $0.22m_0$ for a 3% La-doped $BaSnO_3$ crystal [63]; $0.2m_0$ [64], $0.22m_0$ [65] and anisotropic values along

different directions in the Brillouin zone varying between $0.028m_0$ and $0.09m_0$ [66, 67], and between $0.469m_0$ and $1.463m_0$ [68] for bulk $BaSnO_3$; where m_0 is the electron rest mass. The large difference in m^* values from $0.028m_0$ to $1.463m_0$ is associated with considerations in the implementation of the calculations. Figure 2.4 represents the experimental data of m^* at the conduction band minimum for La-doped $BaSnO_3$ thin films, extracted from the plasma frequency for free carrier absorption in the Drude model. It is seen that its value increases from $0.19m_0$ to $0.36m_0$ for doping levels of 1.6×10^{19} cm^{-3} and 7.6×10^{20} cm^{-3}, respectively [69]. The value of $0.27\pm0.05m_0$ at $n = 1.5\times10^{20}$ cm^{-3} was reported by the same research group for La-doped $BaSnO_3$ thin films co-doped with interstitial hydrogen [70]. Allen *et al.* [71] reported the value of $0.19\pm0.01m_0$ at the conduction band edge of La-doped $BaSnO_3$ thin films, doped to 1.6×10^{20} cm^{-3}. The following experimental values have also been reported for La-doped $BaSnO_3$ thin films: $0.42m_0$ at 2.81×10^{20} cm^{-3} [56]; $0.35\pm0.02m_0$ at 8.9×10^{19} cm^{-3} [72]; $0.40\pm0.01m_0$ at $n \geq 1.4\times10^{19}$ cm^{-3} [73] and $0.396m_0$ at 3.27×10^{20} cm^{-3} [74] by thermopower modulation measurements.

These reported values are comparable to those of extensively studied TCO materials such as ZnO: $0.28m_0$, In_2O_3: $0.35m_0$ and SnO_2: $0.23m_0$ [75], although they exhibit less RT mobility compared to La-doped $BaSnO_3$ single crystals. As a result, it is difficult to attribute the origin of the high electrical mobility in $BaSnO_3$ system to the small value of m^*. Additionally, as depicted in Fig. 2.4, m^* increases with the concentration of dopants, and continues to increase even when the highest electron mobility is achieved at the doping level of 8×10^{19} cm^{-3} [31]. The high mobility in $BaSnO_3$ could rather be due to reduced scattering properties. Therefore, quantitative analysis of the scattering rate and scattering mechanisms is required to clarify the dominant factor that imparts such high electrical properties. Several scattering mechanisms have been identified and modeled to account for their effect on the electronic transport properties.

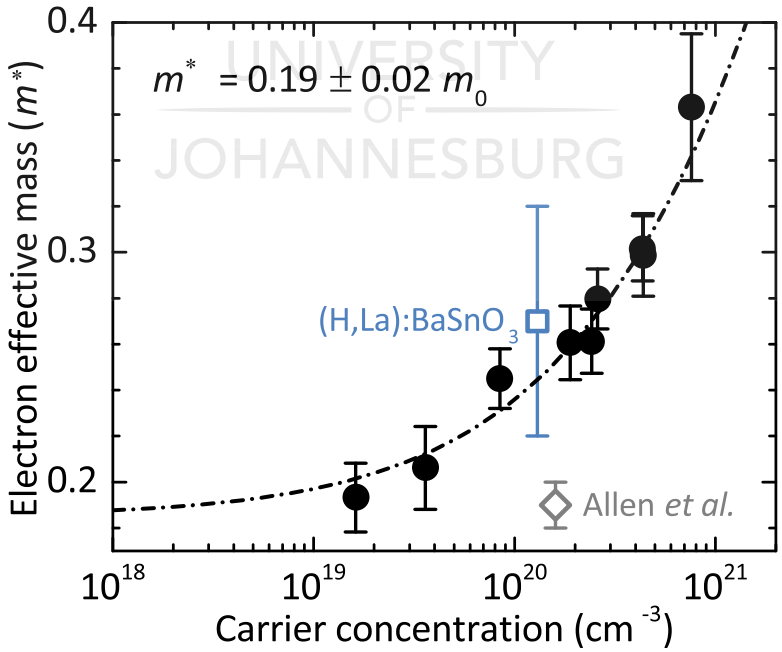

Figure 2.4: Electron effective mass (m^*) in La-doped $BaSnO_3$ thin films as a function of the La dopant concentration. The image was adapted from Ref. [69].

2.2.3 Mechanisms Limiting the Mobility in La-Doped $BaSnO_3$ Thin Films

Scattering mechanisms are known to contribute in limiting the electron mobility in epitaxially grown thin films [56, 70, 76, 77, 78, 79]. Their reducing effect is demonstrated for example in *n*-type Si-doped GaN films, where scattering by dislocations is the dominant mechanism in the low doping regime ($< 5 \times 10^{17}$ cm^{-3}), and ionized impurity scattering dominant in the high doping regime [80, 81, 82]. However, these two scattering mechanisms are not the only factors determining the electrical mobility in degenerate semiconductor systems. Lattice scattering such as phonon scattering, scattering at stacking faults and point defects should also be considered [80, 81]. These mechanisms have been extensively analyzed analytically, theoretically, and experimentally, to account for their contribution to the electronic transport properties of the thin films [60, 65, 69, 83, 84, 85, 86, 87].

a) Analytical modeling of the mobility limiting factors

In epitaxially grown thin films, the overall electron mobility, μ_{tot}, is governed by the above scattering mechanisms, and for degenerately doped semiconductors, it can be written using Matthiesen's rule as [60, 83, 84]

$$\frac{1}{\mu_{\text{tot}}} = \frac{1}{\mu_{\text{dis}}} + \frac{1}{\mu_{\text{Imp}}} + \frac{1}{\mu_{\text{latt}}}. \tag{2.4}$$

Here μ_{dis}, μ_{Imp}, and μ_{latt} represent the mobility contribution due to dislocation, impurity and lattice scattering, respectively. Each component in Equation (2.4) is discussed below. The component contributing to the total mobility due to scattering by dislocations (μ_{dis}) is expressed by [85]

$$\mu_{\text{dis}} = \frac{8qa^2(3n)^{\frac{2}{3}}}{\pi^{\frac{5}{3}} h N_{\text{dis}}} \Big(1 + \zeta(n)\Big)^{\frac{3}{2}}, \tag{2.5}$$

where

$$\zeta(n) = \frac{h^2 \epsilon (3\pi^2 n)^{\frac{1}{3}}}{2q^2 m^*}, \tag{2.6}$$

and h is the Planck constant, ϵ is the static dielectric constant, n is the carrier concentration, q and m^* are the electron charge and effective mass respectively, a is the lattice constant and N_{dis} is the density of dislocations, which is experimentally determined.

The component of the mobility associated with scattering at ionized impurities (μ_{IMP}) is calculated as [85]

$$\mu_{\text{IMP}} = \frac{3\epsilon^2 h^3 n}{q^3 m^{*2} N_{\text{IMP}} \left[\ln\Big(1 + \zeta(n)\Big) - \frac{\zeta(n)}{1+\zeta(n)}\right]}, \tag{2.7}$$

where N_{IMP} is the density of ionized impurities, which is assumed to be equal to the concentration of donor dopants (*n*-type).

As for the last term on the right hand side of Equation (2.4), the analytical model for the contribution of lattice scattering to the mobility is given for longitudinal optical (LO) phonon scattering [69, 88, 89] as

$$\mu_{latt} = \frac{q}{2\alpha\omega_l m^* \left(1+\frac{\alpha}{6}\right)^3} f(\alpha) \left[\exp\left(\frac{h\omega_l}{2\pi k_B T}\right) - 1\right], \tag{2.8}$$

where ω_l is the LO phonon frequency, k_B is the Boltzmann constant, α is the coupling constant for the electron-phonon interaction and $f(\alpha)$ is a slowly varying quantity of order 5/4 for $3 < \alpha < 6$ [88].

Equations (2.5) to (2.7) show the strong dependence of dislocation and impurity scattering on the net concentration of carriers, and therefore describe their contribution to the mobility with respect to the doping regime. Equations (2.4) to (2.8) were also reported to describe the mobility limiting mechanisms in *n*-type degenerate La-doped $BaSnO_3$ systems [55, 62, 69, 86]. The degenerate regime is reached in La-doped $BaSnO_3$ at doping concentrations exceeding 1×10^{19} cm^{-3} [62]. In such degenerate systems, the concentration of ionized impurity electrons is temperature independent, and therefore, dictate the low temperature transport properties [90, 91]. Thus, phonon scattering can be neglected at low temperature, but considered as a major electron mobility limiting mechanism at high temperature (Equation (2.8)), along with dislocation scattering and impurity scattering [62, 85, 86].

b) Theoretical and experimental considerations of the scattering mechanisms

The scattering mechanisms mentioned above have been abundantly simulated with DFT calculations for La-doped $BaSnO_3$ systems, and their contribution to the total electron mobility reported [65, 69, 86, 87]. For instance, Prakash *et al.* [86] have modeled the effect of scattering mechanisms such as, piezoelectric (PE), acoustic phonon deformation potential (AC), longitudinal polar optical phonon (LO), transverse optical phonon (TO), threading dislocations (DIS), and ionized impurities (IMP). The studies were conducted by analyzing the dependence of mobilities on temperature for as-grown La-doped $BaSnO_3$ samples, as well as calculated bulk $BaSnO_3$ (including the mobility contribution of the individual scattering mechanisms). These studies were performed considering different doping regimes, low (1.51×10^{19} cm^{-3}), intermediate (4.06×10^{20} cm^{-3}) and high (1.02×10^{21} cm^{-3}). The results of these investigations are shown in Fig. 2.5. Looking at the figure, it can be seen that LO scattering governs the mobility only in the intermediate regime (see Fig. 2.5(b)), only at temperatures above 200 K, and that its effect on the mobility is almost independent of the doping level. On the other hand, TO, PE, and AC scattering do not directly govern the mobility in any of the regimes (see Figs. 2.5(a) to 2.5(c)). However, TO and AC scattering show a noticeable dependency on the doping regime. This is seen as their associated mobility values decrease from low (Fig. 2.5(a)) to intermediate (Fig. 2.5(b)) regimes. This dependency starts to weaken at higher concentrations of La electrons (Fig. 2.5(c)) introduced into the $BaSnO_3$ lattice as indicated by the very small variation (or no change at all) in the mobility values.

It is also seen that the dominant mobility limiting factors are DIS and IMP, as these limit the mobility in the entire temperature range for low (Fig. 2.5(a)) and high (Fig. 2.5(c)) doping

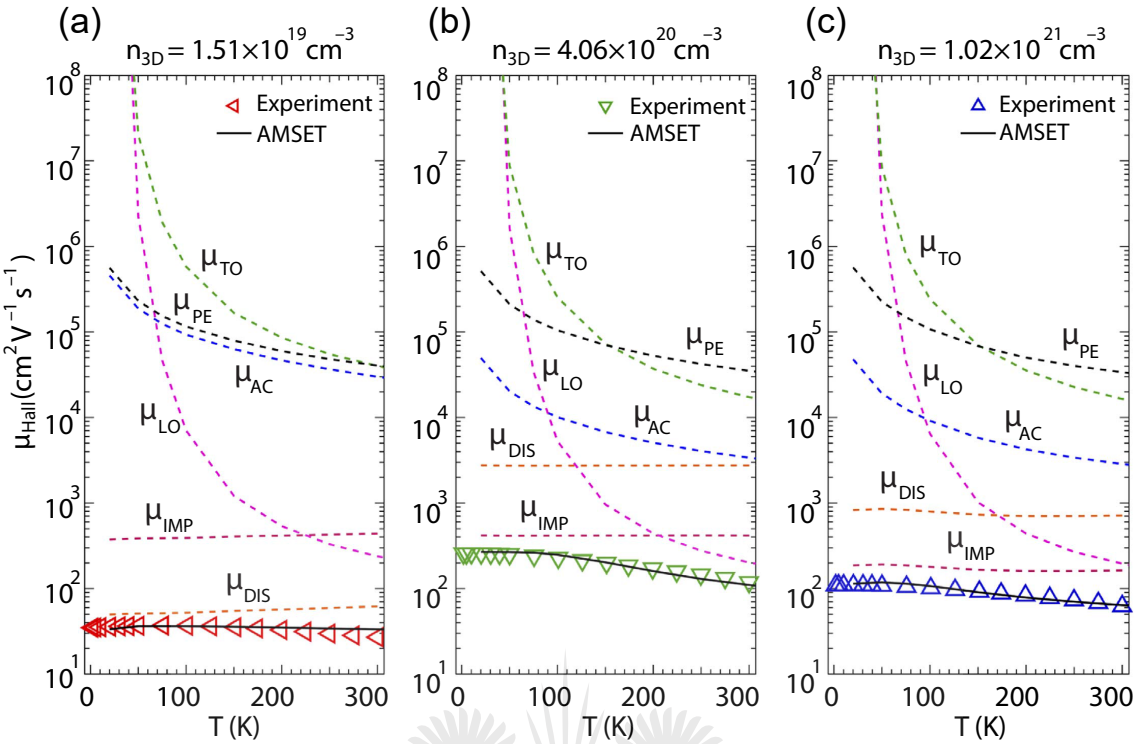

Figure 2.5: (a)-(c) Temperature dependence of electron mobility (μ) for La-doped $BaSnO_3$ samples at different La doping levels, with the calculated contribution of several scattering mechanisms (dashed lines) such as PE (μ_{PE}), DIS (μ_{DIS}), AC (μ_{AC}), LO (μ_{LO}), TO (μ_{TO}) and IMP (μ_{IMP}). The experimental data (symbols) are plotted alongside the calculated values (solid lines) obtained from DFT employing the AMSET[1]package. These images were adapted from Ref. [86].

regimes, respectively. IMP scattering also dominates at intermediate doping, but only below 200 K (Fig. 2.5(b)). Furthermore, the behavior of the mobility values for DIS scattering with respect to the carrier concentration is related to both the calculated scattering rate and dislocation density. A larger scattering rate was found for the low doping regime, and roughly the same lower value for the other two regimes. The calculated dislocation density values are 2.3×10^{12} cm^{-2}, 7.0×10^{11} cm^{-2} and 2.8×10^{12} cm^{-2}, from Fig. 2.5(a) (low regime) to 2.5(c) (high regime), respectively. Thus, the contribution of the DIS scattering to the mobility is expected to increase from low to intermediate regime, and then decrease at high doping. This can also be explained considering the value of the inverse screening length due to dislocation defects which is smaller at low doping regime, combined with the effect of dislocation density.

Experimentally, it has been largely reported that threading dislocations which originate from the structural film–substrate mismatch, are responsible for the relatively low mobility achieved in epitaxial thin films, compared to the high mobility value reported in single crystals [76, 77, 79, 92, 93, 94, 95]. One of the major obstacles in achieving high performance thin films is the availability of lattice matched substrates [77, 92, 93, 95]. In the growth of oxide heterostructures based La-doped $BaSnO_3$ thin film, the most difficult parameter to satisfactorily control and realize higher electron mobility is the choice of the substrate [76, 77, 79, 93, 95]. All

[1]The AMSET model is an efficient package for *ab initio* computations of the electronic transport properties in solid state materials. One of its features includes calculating the rate of scattering mechanisms using the material properties [96].

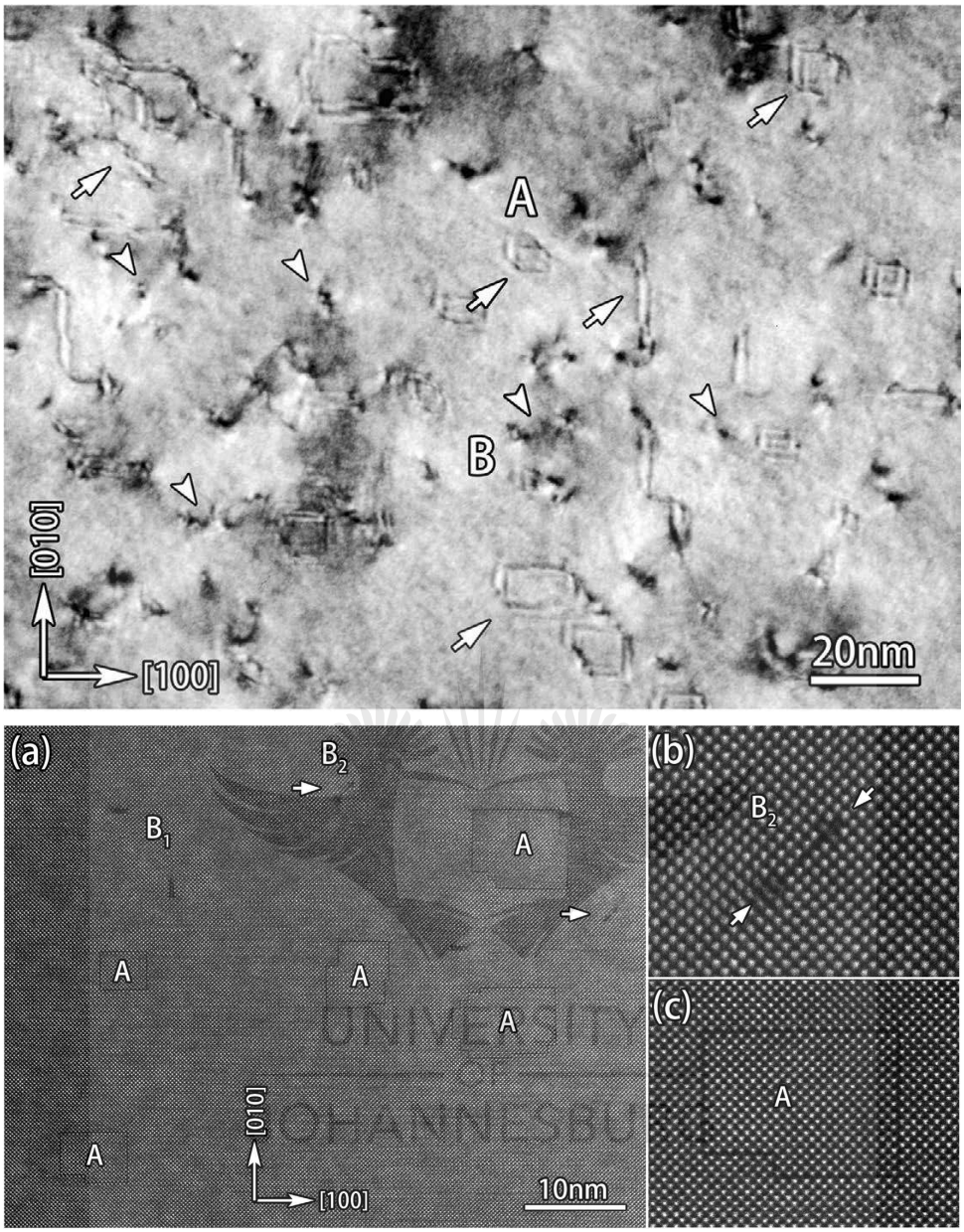

Figure 2.6: Plan-view STEM images of a 0.001% La-$BaSnO_3$/$LaScO_3$/$SrTiO_3$ film.
Upper panel: bright field image showing stacking faults indicated with long arrows (line contrasts A), and threading dislocations marked with short arrows (dark spots B).
Lower panel: low magnification high angle annular dark field (LM-HAADF) STEM images presenting (a) polygon-like shapes stacking faults denoted by A, and two types of threading dislocations (B_1 and B_2). The defects B_2 and A are atom resolved and shown in (b) and (c), respectively. The images were adapted from Ref. [78].

the films summarized in Section 2.3 and fabricated with state-of-the-art techniques, such as MBE and PLD suffered structural defects, and the best of them grown by MBE could not attain a mobility value of 200 $cm^2\ V^{-1}\ s^{-1}$ [76]. Indeed, microstructural characterization of the films using transmission electron microscopy (TEM) have revealed the presence of a remarkable number of planar defects such as stacking faults and line defects such as threading dislocations

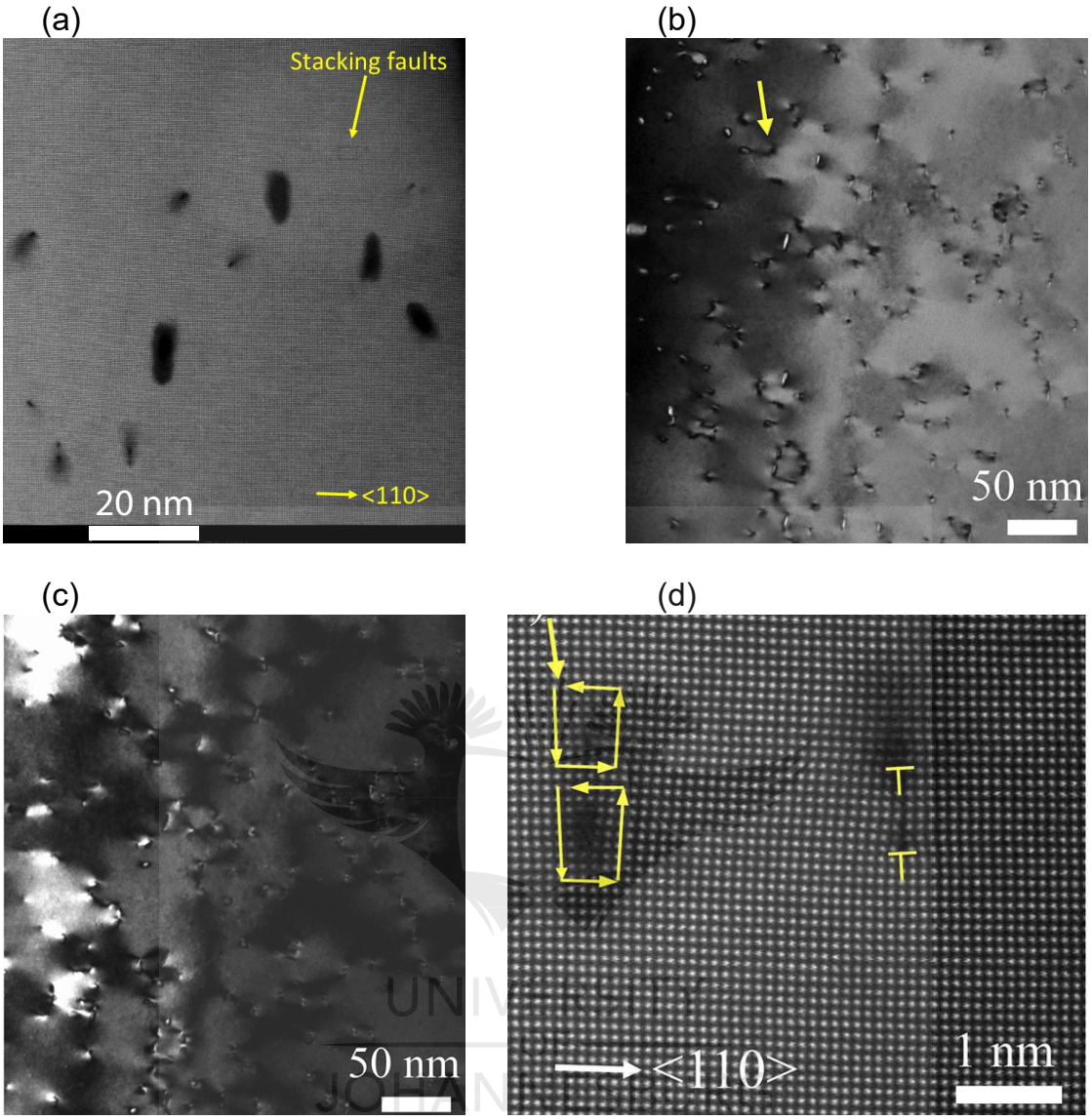

Figure 2.7: Plan-view STEM images of La-$BaSnO_3$/$BaSnO_3$/$DyScO_3$ film. (a) LM-HAADF STEM image presenting a single loop-shaped stacking fault, designated by a yellow arrow. Bright field (b) and dark field (c) STEM images showing threading dislocations, indicated with dark contrasts in (b), and bright contrasts in (c). The yellow arrow in (b) points to a TD. (d) High resolution HAADF STEM image displaying four edge type threading dislocations, and the Burgers circuit drawn around two of them. The yellow arrow points to the lack of closure of the Burgers circuit. The dislocation edges are represented by the dislocation symbols ⊥. The images were adapted from Ref. [76].

[76, 77, 78, 79, 92, 94, 95]. Experimentalists have largely reported these defects as primary factors limiting the electron mobility in La-doped $BaSnO_3$ thin films [76, 77, 79, 92, 93, 94, 95].

Threading dislocations originate from misfit dislocations (MDs), which are generated at the film-substrate interface when the strain due to the mismatch is released [76, 77, 79, 94, 95]. The percentage of mismatch between the film and the substrate varies with the substrate employed for film deposition. The reported values for the commonly used substrates are:

3.8%−3.9% with $TbScO_3$ (110) [97], 3.6% with $GdScO_3$ (110) [97], 4.2% with $DyScO_3$ (001) [76], 5.0%−5.5% with $SrTiO_3$ (001) [76, 77, 79, 92, 93, 94, 95, 97, 98, 99], 3.08% with $SmScO_3$ (110) [93], 2.18%−%2.3 with $PrScO_3$ (110) [76, 77] and 2.2% with MgO [94]. To reduce this large lattice mismatch, especially in films with $SrTiO_3$ (001) substrate, researchers resort to inserting an adhesion layer (buffer layer), generally of $BaSnO_3$, between the film and the substrate. Wang *et al.* [78] have reported that Ruddlesden-Popper faults, which are a particular type of stacking faults, are the prevailing structural defects in PLD grown La-doped $BaSnO_3$ thin films. Indeed, they performed plan-view STEM (scanning transmission electron microscopy) measurements and recorded a high density of shear defects, together with threading dislocations as represented in Fig. 2.6. In their $LaScO_3$ buffered films grown on $SrTiO_3$ (001) substrates, they found about 2×10^{11} cm^{-2} stacking faults. On the other hand, in the LM-HAADF STEM micrograph of a $BaSnO_3$ buffered film grown by MBE on $DyScO_3$ substrate shown in Fig. 2.7(a), Paik *et al.* [76] reported loop-shaped stacking faults, corresponding to a density of 3×10^9 cm^{-2}. This value is two orders of magnitude lower than that found in the PLD grown films. Furthermore, they calculated 1.2×10^{11} cm^{-2} threading dislocations from plan-view STEM measurements (Figs. 2.7(b) to 2.7(d)), and concluded that both defect types contribute to the mobility limit in La-doped $BaSnO_3$ films. The TD defects observed in their film are indicated in Figs. 2.7(b) and 2.7(c) by the dark (illustrated by the yellow arrow) and bright contrasts, respectively, as well as in Fig. 2.7(d) by the dislocation symbols ($\perp$) and the lack of closure of the Burgers circuit.

2.3 Progress of Mobility Enhancement in La-Doped $BaSnO_3$ Thin Films

Several ways to enhance the electronic transport properties in epitaxial La-doped $BaSnO_3$ thin films have been identified. Firstly, the use of lattice matched substrates [99]. Secondly, the insertion of an insulating buffer layer between the film and the substrate to reduce or eliminate the interfacial defects due to lattice mismatch [69, 76, 79, 86, 100]. And thirdly, resort to post-growth treatments such as annealing in vacuum or in gas environment [94, 98, 101]. High quality epitaxial thin films of improved electrical properties have been prepared throughout the years on different perovskite/non-perovskite oxide single crystal substrates, mostly using the PLD and the MBE techniques [69, 76, 79, 100, 102]. In the early years of epitaxial La-doped $BaSnO_3$ thin film growth, the most significant achievement in high mobility grown samples was made by a research group at the Seoul National University [31, 62, 92]. They prepared epitaxial thin films of $La_{0.01}Ba_{0.99}SnO_3$, $La_{0.04}Ba_{0.96}SnO_3$ and $La_{0.07}Ba_{0.93}SnO_3$ directly on $SrTiO_3$ (001) substrates using the PLD technique, and reported a RT electron mobility up to 70 cm^2 V^{-1} s^{-1} at a doping concentration of $\approx 6 \times 10^{20}$ cm^{-3} in the $La_{0.07}Ba_{0.93}SnO_3$ films. Another research group later employed the MBE technique to directly deposit the thin films on $SrTiO_3$ (001) substrates, and improved the RT mobility to a value as high as ≈ 124 cm^2 V^{-1} s^{-1} at the carrier density of $\approx 6.4 \times 10^{19}$ cm^{-3} [77]. Figure 2.8 illustrates the temperature dependence of the carrier densities (n and n_{3D}), the electron mobilities (μ), and the resistivities (ρ and R_s) of these films. As can be seen in the upper panels in Figs. 2.8(a) and 2.8(b) (yellow markers), the carrier densities are almost independent of the temperature. This behavior coupled with the metallic behavior of the resistivities shown in the lower panels in Figs. 2.8(a) and 2.8(b) suggest that all these films are in a degenerately doped semiconducting regime [62, 77]. As for the electron mobilities, it is seen that they increase with decreasing temperature. In Fig. 2.8(a) (middle panel), the mobility increases from 300 K down to 2 K

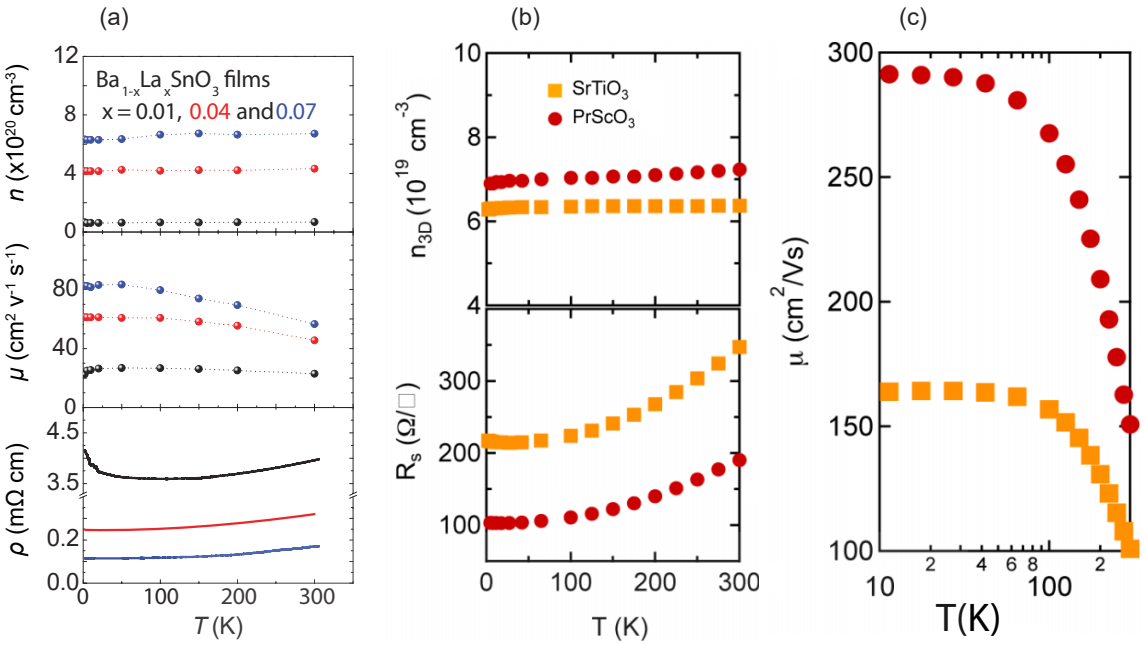

Figure 2.8: Temperature dependence of the carrier density (n and n_{3D}), the electron mobility (μ), and the resistivity (ρ and R_s) for La-doped $BaSnO_3$ thin films grown by (a) PLD on $SrTiO_3$ (001), and (b) and (c) MBE on $PrScO_3$ (110) and $SrTiO_3$ (001) substrates. The image in (a) was adapted from Ref. [62], and those in (b) and (c) were adapted from Ref. [77].

[62]; but in Fig. 2.8(c), it starts to saturate below 100 K [77]. Similar temperature dependent behavior of the carrier density, the mobility and the resistivity have been reported in MBE and PLD grown La-doped $BaSnO_3$ thin films [70, 76, 79, 86, 93, 100, 103].

All these studies pointed out the existence in the films of several scattering sources such as grain boundaries, threading dislocations and electrically inactive ionized impurities, which obstruct the movement of free carriers and therefore limit the electron mobility. This was extensively discussed in Section 2.2. To suppress the film/substrate mismatch, $BaSnO_3$ would be the suitable substrate. This has been reported once in literature by Lee *et al.* [99], who successfully grew epitaxial thin films of $La_xBa_{1-x}SnO_3$ ($x = 0.005 - 0.04$) by PLD directly on a $BaSnO_3$ single crystal substrate. They recorded a maximum RT mobility of 100 $cm^2\ V^{-1}\ s^{-1}$ at a doping level of 1.3×10^{20} cm^{-3}, though from the TEM measurements they could not detect any dislocations or grain boundaries in the film and at the interface. Another approach to improve the electron mobility in La-doped $BaSnO_3$ thin films is to use substrates with lattice parameters that are close to that of $BaSnO_3$ material, such as perovskite scandate substrates. Thus, an enhanced mobility up to 150 $cm^2\ V^{-1}\ s^{-1}$ with an associated carrier concentration of $\approx 7.1{\times}10^{19}$ cm^{-3} was recorded in epitaxial La-doped $BaSnO_3$ thin films prepared by MBE directly on $PrScO_3$ (110) substrates (see the red markers in Figs. 2.8(b) and 2.8(c)) [77]. The authors reported a lattice mismatch value of only -2.18% between the film and $PrScO_3$ (110), which is smaller compared to the value of -5.4% with $SrTiO_3$ (001) substrates, and therefore explains the difference in mobilities in films deposited on the respective substrates (see Fig. 2.8(c)).

These advanced results in epitaxial La-doped $BaSnO_3$ thin films growth triggered the importance of developing means and strategies that would lower the scattering mechanisms and

boost the electrical characteristics in this system. As mentioned above, one strategy that has been commonly employed is to grow an insulating layer between the film and the substrate. This additional layer, generally made from $BaSnO_3$ material acts as a buffer. Its primary role is to reduce the large lattice mismatch. Furthermore, growing thick buffer layers help to reduce the density of dislocations, as these tend to disappear in the middle of the growth [104, 105]. Thus, researchers optimized the thickness of the buffer layer and observed that higher electron mobility was reached in films containing adhesion layers of thicknesses varying from 50 to 330 nm [69, 76, 79, 86, 100, 102, 106].

A synopsis of the progress made in fabricating high mobility unbuffered and buffered epitaxial La-doped $BaSnO_3$ thin films is given in Table 2.1. As can be seen, a record RT mobility of 183 $cm^2\ V^{-1}\ s^{-1}$ at the carrier concentration of $1.2 \times 10^{20}\ cm^{-3}$ is realized for oxide MBE grown film on $DyScO_3$ (001) substrate with a 330 nm thick $BaSnO_3$ buffer layer [76]. This value is currently the highest reported RT mobility in La-doped $BaSnO_3$ based thin films considering all growth methods. The results in Table 2.1 show the significant improvement of the electron mobility with the use of both scandate substrates and buffer layer.

However, another approach has been very recently developed. It is the post-growth treatments of the films which contribute to annihilate extended defects induced by the disparity in the thermal expansion coefficients of the film and the substrate [94]. Indeed, several reports in literature suggest a considerable enhancement of the structural and electrical properties of epitaxial thin films after annealing of the grown films in vacuum and in different gas environments, such as hydrogen forming (H_2), argon (Ar), and nitrogen (N_2). Yu *et al.* [98] noted that the RT mobility of 3% La-doped films grown by PLD on $SrTiO_3$ (001) consistently doubled after a post-annealing treatment at high temperature (1000 °C) for 3h in N_2, as indicated in the temperature dependent electron mobility shown in Fig. 2.9(a). They reported an enhancement from 41 to 78 $cm^2\ V^{-1}\ s^{-1}$, while the carrier density remained unchanged at $\approx 4 \times 10^{20}\ cm^{-3}$. It should be noted that the fact that the concentration of carriers do not

Table 2.1: Synopsis of the growth of La-$BaSnO_3$ thin films with improved electron mobility.

Authors	Growth method	Substrate	Buffer layer	RT mobility ($cm^2\ V^{-1}\ s^{-1}$)	RT density (cm^{-3})
Sallis *et al.* [63]	PLD	$SrTiO_3$ (001)	—	48.5	2.2×10^{20}
Kim *et al.* [62]	PLD	$SrTiO_3$ (001)	—	70	$\approx 6\times10^{20}$
Prakash *et al.* [103]	MBE	$SrTiO_3$ (001)	—	105	2.5×10^{20}
Raghavan *et al.* [77]	MBE	$SrTiO_3$ (001)	—	≈ 124	$\approx 6\times10^{19}$
Lee *et al.* [99]	PLD	$BaSnO_3$ (001)	—	100	1.3×10^{20}
Lebens *et al.* [107]	MBE	$TbScO_3$ (110)	—	81	1.65×10^{20}
Raghavan *et al.* [77]	MBE	$PrScO_3$ (110)	—	150	$\approx 7\times10^{19}$
Park *et al.* [106]	PLD	$SrTiO_3$ (001)	$BaSnO_3$	66	1×10^{20}
Niedermeier *et al.* [69]	PLD	MgO	NiO	70	4.4×10^{20}
Shiogai *et al.* [79]	PLD	$SrTiO_3$ (001)	$BaSnO_3$	78	8.5×10^{19}
Shin *et al.* [102]	PLD	MgO	$BaSnO_3$	97.2	2.53×10^{20}
Prakash *et al.* [86]	MBE	$SrTiO_3$ (001)	$BaSnO_3$	120	3×10^{20}
Wang *et al.* [100]	MBE	Si (001)	$BaSnO_3$	128	1.4×10^{20}
Paik *et al.* [76]	MBE	$DyScO_3$ (001)	$BaSnO_3$	183	1.2×10^{20}

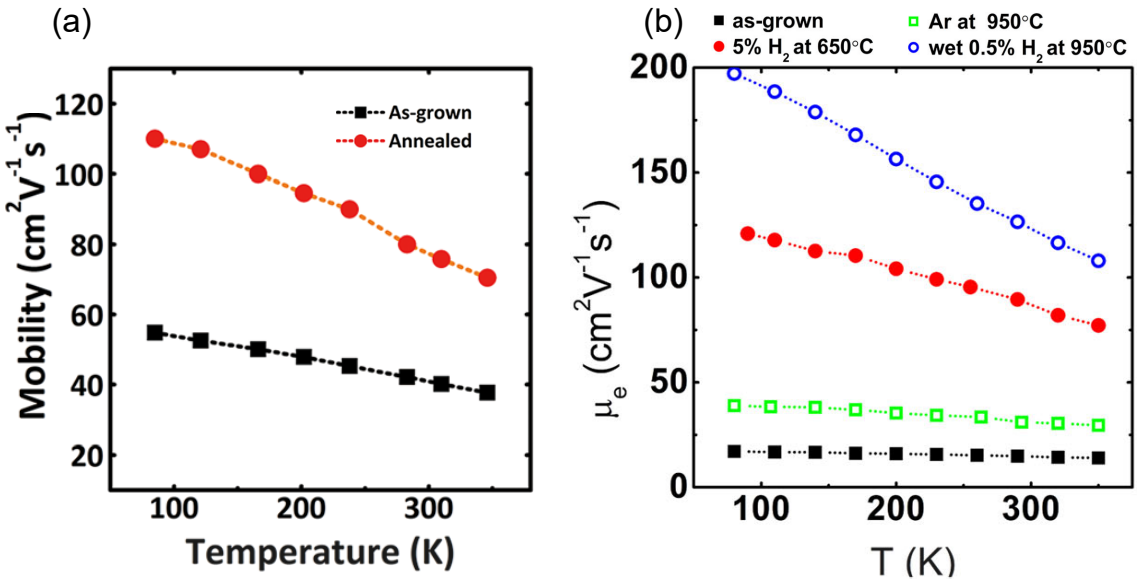

Figure 2.9: Temperature dependent electron mobility for La-doped $BaSnO_3$ films, comparing the electron mobility for these films before and after annealing in (a) N_2 gas at 1000 °C for 3h and (b) H_2 forming gas at 950 °C. The image in (a) was adapted from Ref. [98], and that in (b) was adapted from Ref. [94].

change after annealing point to the excellent thermal stability of the $BaSnO_3$ system. On the other hand, Cho *et al.* [101] reported that the mobility doubled after vacuum annealing of the films. They noted that vacuum annealing generates oxygen vacancies which lead to the reduction of the thermal stability of the films and result in an increase of the carrier density after the post-annealing process. They prepared epitaxial thin films of 0.1%, 0.55%, 1%, 2%, 5% and 7% La-doped on MgO (001) substrates by PLD and reported an enhancement of the mobility from ≈ 40 to ≈ 80 cm^2 V^{-1} s^{-1}; and the increase in the carrier density from $\approx 1.35 \times 10^{20}$ to $\approx 1.8 \times 10^{20}$ cm^{-3} after annealing in vacuum for 30 min at 750 °C. Moreover, after post-annealing treatment in H_2 forming gas at 950 °C, Yoon *et al.* [94] observed an enhancement of the electron mobility in 1% La-doped films prepared by PLD on $SrTiO_3$ (001), as indicated by the blue markers in the temperature dependent electron mobility presented in Fig. 2.9(b). They recorded an improvement of the RT mobility to a value as high as ≈ 122 cm^2 V^{-1} s^{-1} from the value before treatment of ≈ 15 cm^2 V^{-1} s^{-1}; and also an increase in the carrier concentration to $\approx 1.1 \times 10^{20}$ cm^{-3} from the initial value of $\approx 5.3 \times 10^{19}$ cm^{-3}. All the efforts to enhance the electron mobility reported above indicate that there is room for novel strategies that impede the scattering mechanisms and achieve mobilities in La-doped $BaSnO_3$ thin films comparable to that in single crystals.

2.4 Investigation of the Electronic Band Structure of $BaSnO_3$ Systems

Undoped $BaSnO_3$ is an insulator in bulk form [62]. In addition, the inherent defects are not shallow donors [65]. On the contrary, hydrogen impurities and donors such as F, La and Sb introduce conduction electrons into the conduction band [65]. This justifies the high conductivity observed experimentally in this material [62, 65]. However, to fully understand

the conduction mechanism in electron-doped $BaSnO_3$ system, a combined theoretical and experimental knowledge of its electronic band structure is required. The background to this will be discussed here.

2.4.1 Theoretical Approaches for $BaSnO_3$ Band Structure Analysis

The theoretical investigations have mostly been done using DFT calculations, either local density approximation (LDA) [62], generalized gradient approximation (GGA) [108], exchange-correlation functional augmented (PBE0) [65], or hybrid density functional theory (HSE06) [64, 68, 87, 109]. Both HSE06 and PBE0 calculations have been used to investigate the effect of intrinsic (oxygen vacancy, antisite and interstitial) and extrinsic (especially donor) defects on the $BaSnO_3$ band structure [65]. In literature, there are several reports on the nature (indirect or direct) and size of the band gap of $BaSnO_3$ crystals based on calculations, as summarized in Table 2.2. These calculations also give detailed descriptions of the constitution and position of both the conduction band minimum (CBM) and the valence band maximum (VBM) [62, 64, 65, 68, 87, 108, 109, 110, 111]. It has been reported that the CBM located at the Γ point of the Brillouin zone is composed of the Sn 5s orbitals, whereas the VBM located at the R point is mostly composed of the O 2p orbitals.

As for doped $BaSnO_3$ crystals, researchers reported on the Fermi level (E_F) shift upon electron filling of the conduction band. For instance, Kim *et al.* [62] employed LDA for the first time to compute the band structure of La-doped $BaSnO_3$ crystals. Figures 2.10(a) and 2.10(b) show their calculated band structure for undoped and La-doped $BaSnO_3$ crystals, respectively. They found that the E_F (which is located at 0 eV in the figures) in 3.7% La-doped $BaSnO_3$ crystals was moved upward to about 2 eV in the conduction band (compared to the Fermi position in undoped $BaSnO_3$), which they reported was composed of the Sn 5s states with a Sn-O antibonding nature (see Figs. 2.10(a) and 2.10(b)). Furthermore, they reported the formation of La 4f bands in the conduction band, 2 eV above E_F (see Fig. 2.10(b)). A similar composition of the conduction band has been reported by Li *et al.* [112], who also noted a E_F shift of 1.99 eV above the CBM in the band calculation of $La_{0.2}Ba_{0.8}SnO_3$. Their electronic band structure

Table 2.2: Theoretical prediction of the nature and size of the band gap in $BaSnO_3$ crystals.

Authors	Nature of the band gap	Size of the band gap (eV)
Kang *et al.* [113]	Direct	3.46
	Indirect	2.98
Sallis *et al.* [63] Singh *et al.* [114]	Indirect	3.22
Scanlon [65]	Indirect	3.20
		2.49
Liu *et al.* [64]	Direct	3.00
Li *et al.* [112]	Indirect	2.82
		2.66
Kim *et al.* [68]	Indirect	2.48
Krishnaswamy *et al.* [87, 109]	Direct	2.88
	Indirect	2.40

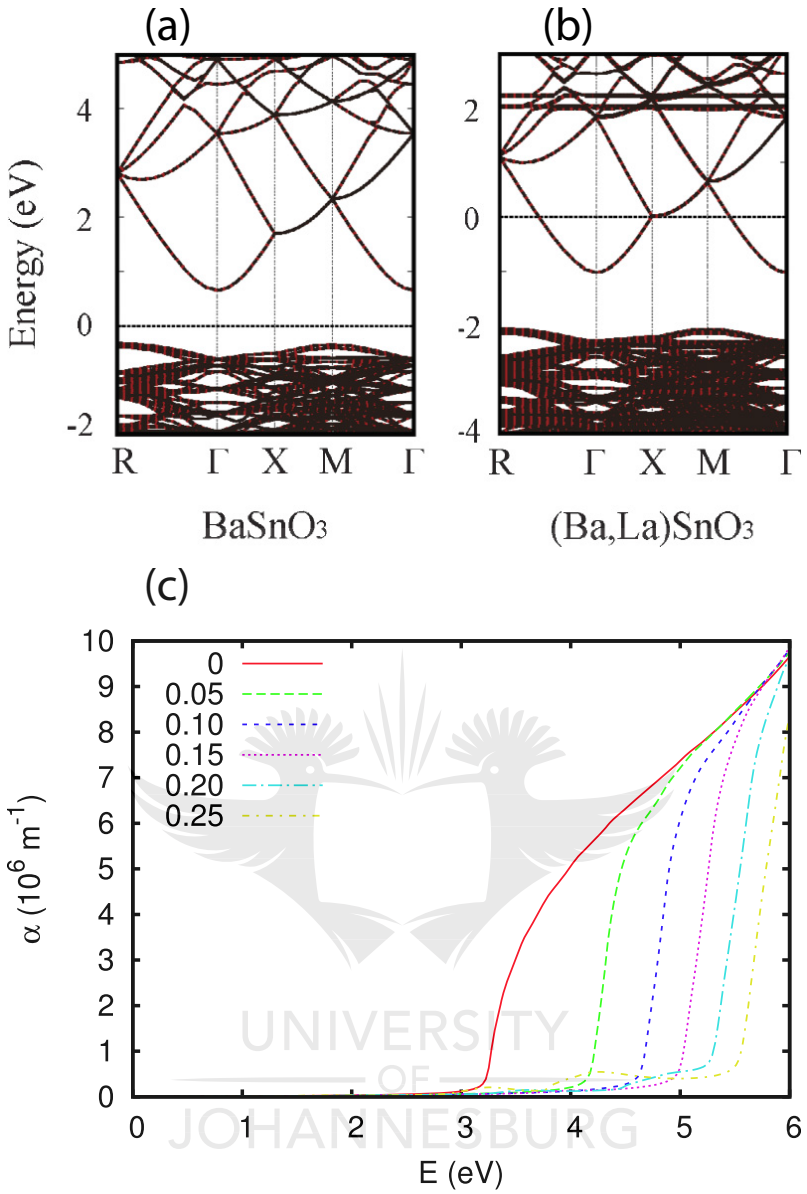

Figure 2.10: Electronic band structure calculation of (a) $BaSnO_3$ and (b) La-doped $BaSnO_3$ crystals. (c) Calculated absorption spectra for different La-doped $BaSnO_3$ crystals showing the evolution of the band gap with the La content. The images in (a) and (b) were adapted from Ref. [62], and that in (c) was taken from Ref. [112].

calculations were performed for $BaSnO_3$ crystals with several La doping concentrations using the general potential linearized augmented plane wave (LAPW) method, with the virtual crystal approximation to account for the doping. From their calculated absorption spectra, they observed an increase in the optical band gap with the doping percentage (the concentration of carriers introduced into the conduction band) as shown in Fig. 2.10(c). This behavior has been experimentally observed in La-doped $BaSnO_3$ thin films and single crystals [62, 69, 115]. Despite numerous theoretical reports on the electronic structure of undoped and doped $BaSnO_3$ crystals, experimental findings are needed to confirm the theoretical predictions and to provide more understanding of transport mechanisms at the band structure level.

2.4.2 Spectroscopic Measurements of the Band Structure of $BaSnO_3$

Several research groups have experimentally extracted the numerical value of the $BaSnO_3$ band gap. Kim *et al.* [62] recorded both indirect and direct optical band gap values of 2.95 eV and 3.10 eV respectively, from the UV-visible-near-infrared spectra of $BaSnO_3$ single crystals. Prokopalo *et al.* [116] found a value of 3.1 eV from investigating the photoconductivity on $BaSnO_3$ single crystals. The band gap value has also been determined from analysis of optical absorption data. Performing RT UV–visible diffuse reflectance spectroscopy measurements on $BaSnO_3$ single crystals, the values of 3.1 eV [58, 110] and 3.4 eV [111, 117] were reported. On the other hand, Chambers *et al.* [118] investigated the band alignment at the heterojunctions of hybrid MBE grown epitaxial $BaSnO_3$ thin films on $SrTiO_3$ (001) and $LaAlO_3$ (001) and found both direct and indirect band gaps from spectroscopic ellipsometry measurements of the insulating films. They reported indirect band gap values of 2.91 eV on $SrTiO_3$ and 2.95 eV on $LaAlO_3$; and direct band gap values of 3.57 eV on $SrTiO_3$ and 3.55 eV on $LaAlO_3$. Using the same characterization approach, Seo *et al.* [72] recorded the value of 3.3 eV for $BaSnO_3$ thin films grown on $SrTiO_3$ (001) by pulsed electron deposition.

Very recently, Joo *et al.* [119] used angle resolved photoemission spectroscopy (ARPES) to completely characterize the electronic band structure of insulating $BaSnO_3$ thin films epitaxially grown by PLD on Nb-doped $SrTiO_3$ (001) substrates. Their work yielded for the first time experimental evidence of the nature and size of the band gap by determining the position in momentum space and the energy of both the VBM and the CBM as presented in Fig. 2.11. In Fig. 2.11(a), the integrated density of states spectrum of the film collected *in situ* at 100 K with a photon energy of 123 eV yields: O 2p states at energy between -7 eV and -4 eV; the valence band leading edge situated at about -3.7 eV; the in-gap state (β) at -1.75 eV associated with localized in-gap states; and occupied states in the conduction band close to E_F originating from electron doping induced by native defects such as oxygen vacancies or antisite defects. In Fig. 2.11(b), the energy distribution curves (EDCs) at the high symmetry points extracted from ARPES scans show the momentum position of both the VBM and the CBM and demonstrate the precise nature of the band gap. The CBM is found to be at the Γ point and the VBM at the R point confirming the indirect nature of the band gap in $BaSnO_3$ material. Furthermore, the energetic position of the VBM is found at 3.88 eV and that of the CBM at -0.15 eV giving a value of ≈ 3.7 eV for the band gap.

A complete structural/electronic structure characterization of $BaSnO_3$ material includes knowledge of its chemical purity and elemental quantification, the oxidation state and chemical environment of its relevant atomic levels, and its surface atomic composition (stoichiometry). These details are provided by x-ray photoemission spectroscopy (XPS). From the XPS characterization of powder $BaSnO_3$, Larramona *et al.* [117] recorded that Ba 3d and Sn 3d multiplets are respectively in Ba^{2+} and Sn^{4+} states; and located at binding energies of Ba $3d_{\frac{5}{2}}$: 780.3 eV, Ba $3d_{\frac{3}{2}}$: 795.6 eV and Sn $3d_{\frac{5}{2}}$: 485.7 eV, Sn $3d_{\frac{3}{2}}$: 494.5 eV. In the O 1s signal, they detected two components at 529.7 eV and 531.7 eV that they respectively attributed to lattice O^{2-} ions and chemisorbed water. Furthermore, after a systematic elemental quantification, they calculated the atomic composition of the surface and found the ratios O/Sn (2.60) and Ba/Sn (0.77), which were lower than the expected stoichiometric values of 3 and 1 respectively. This led them to conclude that the surface of the material was SnO_2 enriched. As for epitaxial $BaSnO_3$ thin films grown by PLD on $SrTiO_3$ (001), Jaim *et al.* [120] identified only Sn^{4+} and Ba^{2+} valence states evidenced by the energies of their primary regions Sn $3d_{\frac{5}{2}}$: 486.6 eV, Sn

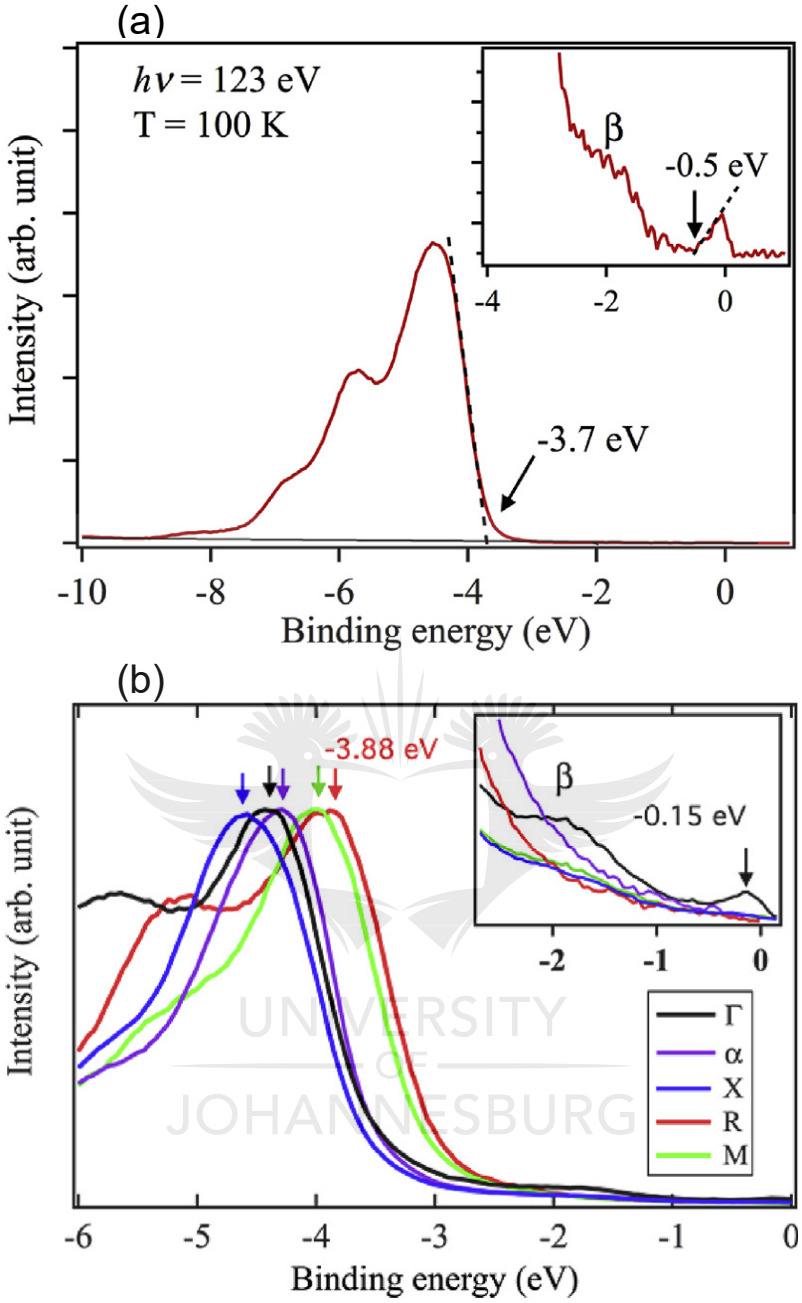

Figure 2.11: Valence band structure of $BaSnO_3$ thin film measured by ARPES. Angle-integrated ARPES spectra (a) and energy distribution curves (EDCs) obtained at various high symmetry points indicating the energy position of the VBM and CBM (b). The images were taken from Ref. [119].

$3d_{\frac{3}{2}}$: 495 eV; and Ba $3d_{\frac{5}{2}}$: 779.4 eV, Ba $3d_{\frac{3}{2}}$: 794.7 eV; and a peak at 780.7 eV associated with Ba hydroxylate upon air exposure. Moreover, in the O 1s region which is represented in Fig. 2.12(a), apart from the lattice oxygen at 529.3 eV (black curve), they recorded two additional peaks; one peak at 531.3 eV (dark blue curve) which they attributed to oxygen vacancies resulting from oxygen deficiency during growth, and the other at 533 eV (purple curve) associated with the loosely bound oxygen at the surface of the films. After annealing

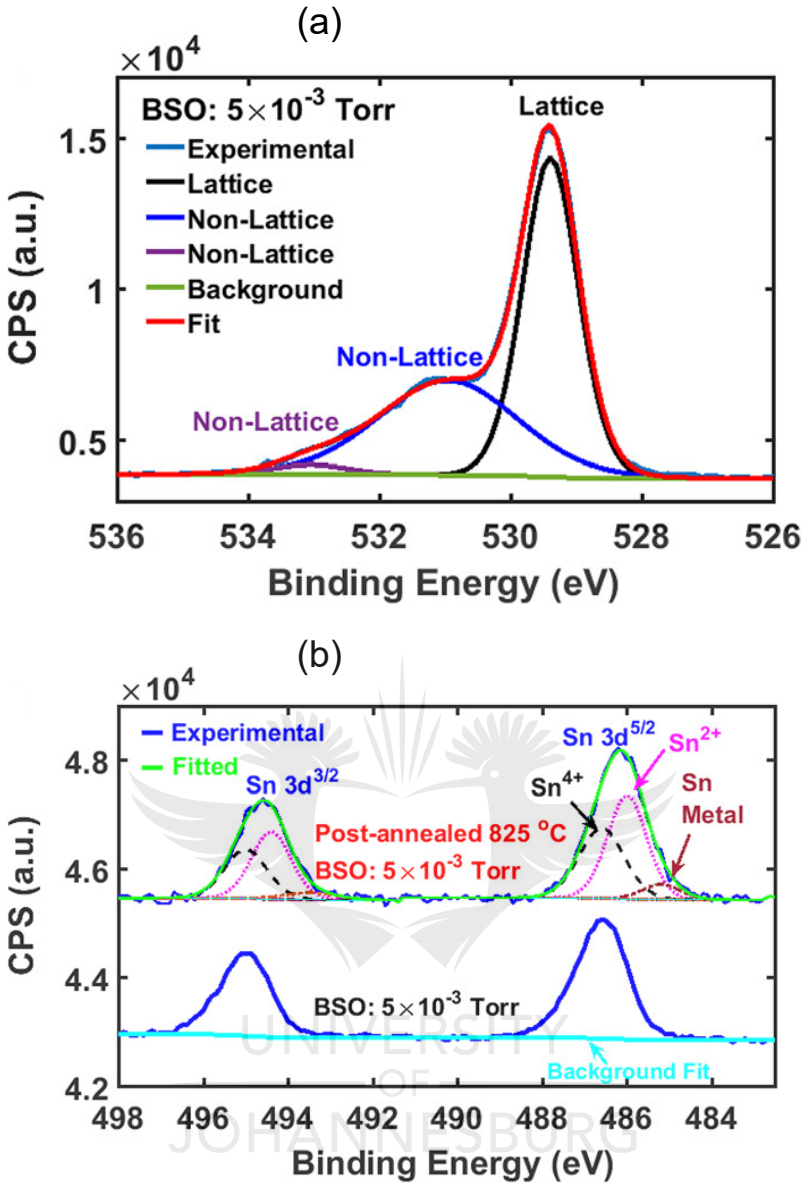

Figure 2.12: High resolution XPS spectra of $BaSnO_3$ thin film deposited in 5×10^{-3} Torr of oxygen partial pressure. (a) The O 1s region for the sample as-grown is shown. (b) The Sn 3d regions for the sample before and after annealing at 825 °C under 6.67 mbar of oxygen environment are presented. The images were adapted from Ref. [120].

of the films at 825 °C under high oxygen pressure (6.67 mbar), they detected a mixture of Sn^{4+} and Sn^{2+} states with a small amount of Sn metals (Fig. 2.12(b)) along with the shift of Ba $3d_{\frac{5}{2}}$ peak toward higher binding energy. This suggests that the chemical composition of the surface has been radically altered. On the contrary, Chambers *et al.* [118] reported a high degree of symmetry in the Sn $3d_{\frac{5}{2}}$ spectra when evaluating the valence band and the conduction band offsets in $BaSnO_3/SrTiO_3$ and $BaSnO_3/LaAlO_3$ heterostructures using *ex situ* high resolution XPS (the samples were made in a MBE system, exposed to air ambient before being transferred into the vacuum chamber for spectroscopic measurement). Moreover, they observed that the Ba 4d doublet was asymmetric and was fitted with an additional dou-

blet component located $\approx$ 1 eV at the higher binding energy side of the main Ba $4d_{\frac{5}{2}}$ peak. They assigned this extra component to oxidized or hydroxylated Ba surface component. This suggests that their sample surface was BaO terminated.

2.4.3 Spectroscopic Measurements of La-Doped $BaSnO_3$ Thin Films

As with $BaSnO_3$, the electronic band structure of La-doped $BaSnO_3$ thin films has been investigated through optical spectroscopic experiments such as reflection ellipsometry. There are several reports on the value of the optical band gap for La-doped $BaSnO_3$ thin films. Firstly, Liu *et al.* [115] reported an increase in the optical band gap from 3.49 eV to 4.0 eV with increasing La doping content ($La_xBa_{1-x}SnO_3$) from 0 to 0.2, as shown in Fig. 2.13(a). Later on, Seo *et al.* [72] reported an optical band gap value of 3.57 eV for 4% La-doped films, shifted by 0.18 eV toward higher photon energy (Fig. 2.13(b)) compared to undoped films. Finally, Niedermeier *et al.* [69] observed a direct relationship between the determined optical band gap and the carrier concentration. In fact, they noted a shift of the optical absorption edge from 3.7 eV to 4.4 eV when the density of the conduction electrons increases from 1.6×10^{19} cm^{-3} to 4.4×10^{20} cm^{-3} due to the conduction band filling effect, as presented in Fig. 2.13(c). They stated that their results point to a more pronounced nonparabolicity of the conduction band. The above findings confirm the theoretical prediction in Ref. [112] that the optical band gap increases when more carriers are introduced into the conduction band due to the E_F moving upward.

The first photoemission spectroscopic approaches to characterize the electronic structure of La-doped $BaSnO_3$ thin films were realized for PLD and MBE grown thin films employing *ex situ* XPS, x-ray emission-absorption spectroscopy (XES/XAS) and hard x-ray photoemission spectroscopy (HAXPES) [63, 107]. It was found that the La 3d core XPS signal of samples measured without surface preparation was very weak or undetectable [63]. On the other hand, HAXPES spectra showed increasing La 3d core peak intensities with increasing La doping percentage, followed with large increases of the asymmetry in the Sn $3d_{\frac{5}{2}}$ core levels and shifts to higher binding energies of the valence band leading edge (Fig. 2.14(b)) and core levels such as Ba $3d_{\frac{5}{2}}$, O 1s and Ba 5p [107]. It should be noted that La 3d core electrons could be detected in HAXPES because this spectroscopic technique is more bulk sensitive than XPS [63, 107]. The HAXPES spectrum of the valence band region in Fig. 2.14(a) shows occupied states in the conduction band (filled to 0.26 eV below E_F) and an energetic separation VBM$-E_F$ of about 3.48 eV [63]; whereas that in Fig. 2.14(b) shows the increase in the intensity of the filled band together with the shift to higher binding energies with the amount of La doping, pointing to an electrostatically driven band gap renormalization [107].

The orbital character of the states at the VBM and CBM was experimentally determined by the combination of O *K*-edge XES/XAS and HAXPES measurements and DFT O 2p partial density of states (PDOS) calculations and it was found that the VBM is mostly derived from O 2p orbitals and the CBM is derived from Sn 5s orbitals with a small contribution of O 2p character [63, 107]. On the contrary, as illustrated in Fig. 2.13(d), the EDCs extracted near the Γ point in raw ARPES spectra of several thin films with different La content (from 1% to 10%) show that the valence band shifts towards lower binding energies as the La doping level increases, indicating upwards band bending [97]. This also contradicts the calculations and the optical spectroscopic experiments shown in Figs. 2.13(a) to 2.13(c). However, in the case of photoemission spectroscopic measurements, this opposite trend suggests that the

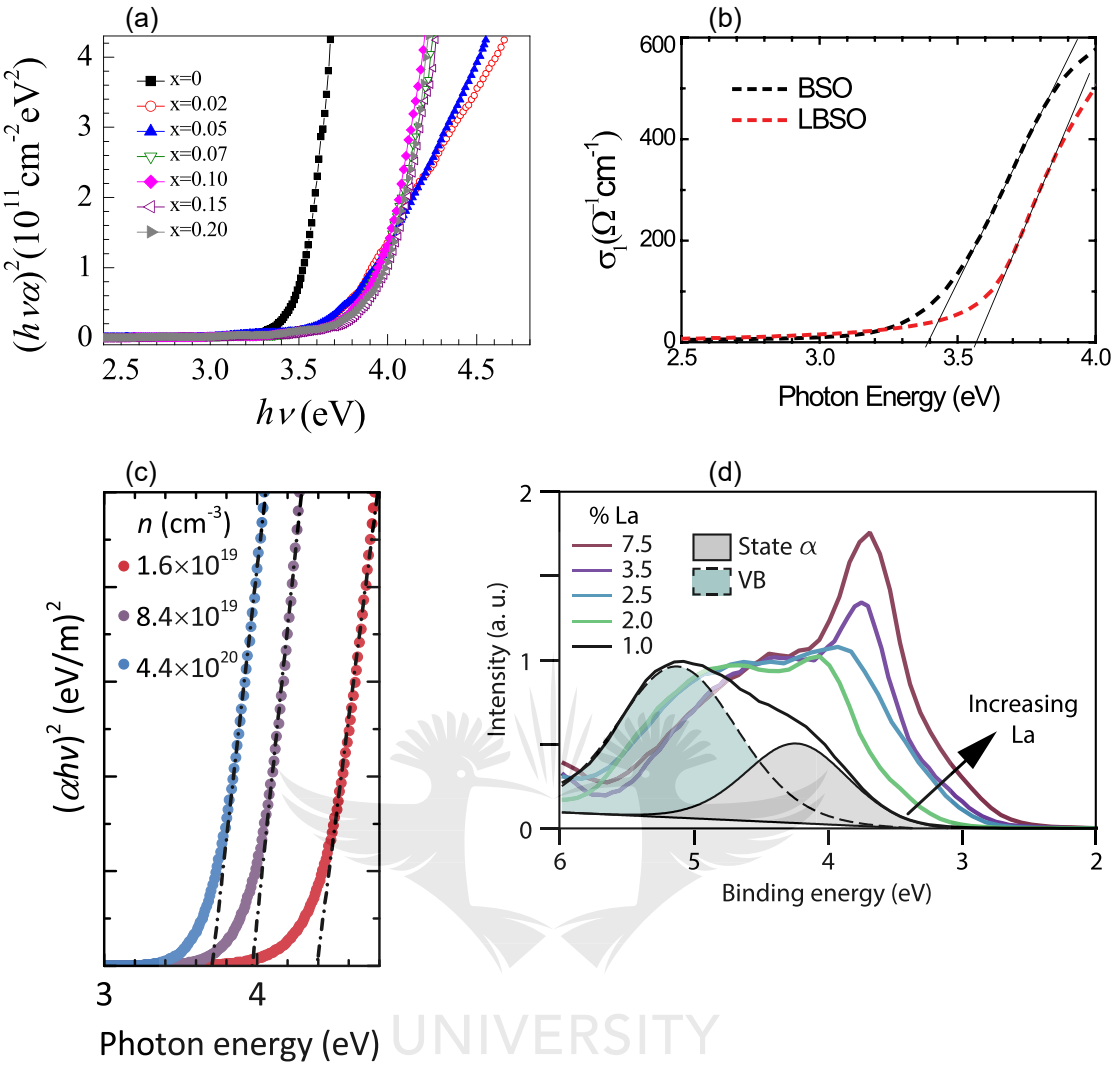

Figure 2.13: (a)-(c) Optical absorption spectra showing the increase in the optical band gap with the La doping content in doped $BaSnO_3$ thin films. (d) EDCs of La-doped $BaSnO_3$ samples measured near the symmetry point Γ with a He II source (photon energy of 40.8 eV). The image in (a) was adapted from Ref. [115], that in (b) was adapted from Ref. [72], that in (c) was taken from Ref. [69], and (d) was adapted from Ref. [97].

chemical potential of the surface (surface sensitive measurements-ARPES) and that of the bulk (bulk sensitive measurements-HAXPES) have an opposite evolution. This observation was indeed made early in 2018 when ARPES was first used to analyze the electronic band structure of MBE grown La-doped $BaSnO_3$ epitaxial thin films. Extremely dispersive bands are seen from ARPES scans of a $La_{0.035}Ba_{0.965}SnO_3$ sample acquired with helium I (He I, photon energy of 21.2 eV) over the binding energy range 4 eV to 10 eV (upper panel in Fig. 2.14(c)). Furthermore, the valence band leading edge is found at 3.5 eV and occupied states are seen in the conduction band below E_F, leading to an optical band gap value of 3.5 eV measured from the angle-integrated valence band shown in Fig. 2.14(c).

Additional features are observed in the valence band (α peak), in the band gap (β peak) and the CBM (metallic state, labeled MS) as shown in the lower panel in Fig. 2.14(c). The peaks

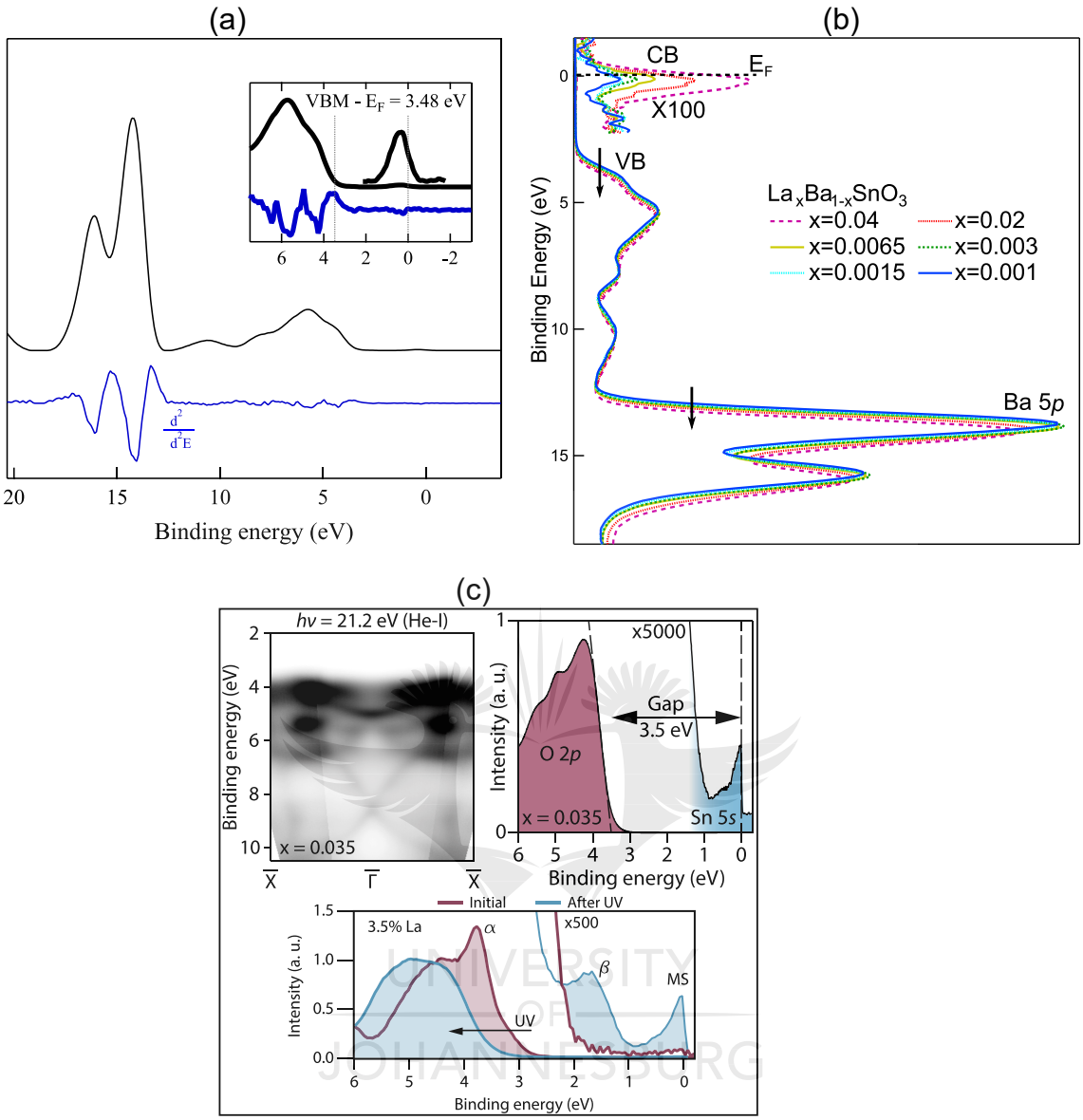

Figure 2.14: (a) and (b) are HAXPES spectra of the La-doped $BaSnO_3$ valence band regions presenting (a) occupied states in the conduction band below E_F and the estimated band gap value [63], (b) Ba 5p and valence band regions showing the increasing intensity and the shift of the filled conduction band states with the La doping content [107]. (c) Top: ARPES map of the band structure of $La_{0.035}Ba_{0.965}SnO_3$ sample and its corresponding angle-integrated photoemission spectra measured with He I. Bottom: EDCs of the same sample measured near Γ with He II (40.8 eV) [97]. MS stands for metallic state which is the CBM. The image in (a) was adapted from Ref. [63], that in (b) was adapted from Ref. [107], and that in (c) was taken from Ref. [97].

α and β are attributed to oxygen adsorption and oxygen vacancies, respectively. The intensity of the peak α is found to increase with the increased doping, whereas the peak β and the MS appear only after illumination of the sample with UV light for several hours accompanied with an impressive increase in the MS intensity (Fig. 2.14(c)). Remarkably, while the β peak is formed/depleted in La-doped $BaSnO_3$ thin film upon illumination/light suppression, it is seen

in the band gap of a $BaSnO_3$ thin film immediately after growth as indicated in Ref. [119]. This ability of controlling surface electron density by creating/annihilating defects may be a useful feature in the new generation of electronic devices based on La-doped $BaSnO_3$.

2.5 Conclusion

In summary, La-doped $BaSnO_3$ is a material that exhibits the properties of TCOs. More precisely, it combines high electronic transport and transparent characteristics. Owing to these properties, La-doped $BaSnO_3$ is a material of interest in the research community. Numerous achievements have been made in the optimization of the structural and electrical characteristics of thin films based La-doped $BaSnO_3$, and more can still be learnt from this material.

Bibliography

[1] K. Bädeker, Ann. Phys. (Leipzig) **22**, 749 (1907).

[2] B. G. Lewis, and D. C. Paine, MRS Bull. **25**, 22 (2000).

[3] T. Minami, MRS Bull. **25**, 38 (2000).

[4] T. J. Coutts, D. L. Young, and X. Li, MRS Bull. **25**, 58 (2000).

[5] A. J. Freeman, K. R. Poeppelmeier, T. O. Masson, R. P. H. Chang, and T. J. Marks, MRS Bull. **25**, 45 (2000).

[6] D. S. Ginley, C. Bright, and G. Editors, MRS Bull. **25**, 15 (2000).

[7] E. Fortunato, D. Ginley, H. Hosono, and D. C. Paine, MRS Bulletin **32**, 242 (2007).

[8] K. L. Chopra, S. Major, and D.K. Pandya, Thin Solid Films **102**, 1 (1983).

[9] C. G. Granqvist, A. Azens, A. Hjelm, L. Kullman, G. A. Niklasson, D. Ronnow, M. S. Mattsson, M. Veszelei, and G. Vaivars, Sol. Energy **63**, 199 (1998).

[10] D. R. Kammler, D. D. Edwards, B. J. Ingram, T. O. Mason, G. B. Palmer, A. Ambrosini, and K. R. Poeppelmeier, *Photovoltaics for the 21st Century*, edited by V.K. Kapur, R.D. McConnel, D. Carlson, G. P. Ceasar, and A. Rohatgi (Electrochemical Society: Proc. **99**, 68 (1999) Pennington, NJ).

[11] Y. Nakato, K.-I. Kai, and K. Kawabe, Sol. Energy Mater. Sol. Cells **37**, 323 (1995).

[12] M. Green, W. C. Smith and J. A. Weiner, Thin Solid Films **38**, 89 (1976).

[13] G. H. Heilmeier, Sci. Am. **222**, 100 (1970).

[14] L. A. Goodman, RCA Rev. **35**, 613 (1974).

[15] T. Muranoi and M. Furukoshi, Thin Solid Films **48**, 309 (1978).

[16] J. C. Manifacier, J. P. Fillard, and J. M. Bind, Thin Solid Films **77**, 67 (1981).

[17] L. Holland, and G. Siddall, Vacuum **3**, 375 (1953).

[18] C. W. Ow-Yang, H.-Y. Yeom, B. Yaglioglu, and D. C. Paine, Mater. Res. Soc. Symp. Proc. **905E**, 7 (2006).

[19] T. J. Coutts, D. L. Young, and X. Li, Mater. Res. Soc. Symp. Proc. **623**, 199 (2000).

[20] R. E. Aitchison, Austr. J. Appl. Phys. **5**, 10 (1954).

[21] K. Ellmer, Nat. Photonics **6**, 809 (2012).

[22] W.-J. Lee, H. J. Kim, J. Kang, D. H. Jang, T. H. Kim, J. H. Lee, and K. H. Kim, Annu. Rev. Mater. Res. **47**, 391 (2017).

[23] S. T. Liu, J. D. Heaps, and N. Tufte, Ferroelectrics **3**, 281 (1972).

[24] E. A. Kraut, T. C. Lim, and B. R. Tittmann, Ferroelectrics **3**, 247 (1972).

[25] R. B. Atkin, Ferroelectrics **3**, 213 (1972).

[26] J. R. Maldonado, and A. H. Meitzler, Ferroelectrics **3**, 169 (1972).

[27] M. H. Francombe, Ferroelectrics **3**, 199 (1972).

[28] P. A. Schlosser, and D. D. Glower, Ferroelectrics **3**, 257 (1972).

[29] Z. J. Kiss, Phys. Today **23**, 42 (1970).

[30] S. Ismail-Beigi, F. J. Walker, S.-W. Cheong, K. M. Rabe, and C. H. Ahn, APL Mater. **3**, 062510 (2015).

[31] H. J. Kim, U. Kim, H. M. Kim, T. H. Kim, H. S. Mun, B. G. Jeon, K. T. Hong, W. J. Lee, C. Ju, K. H. Kimy, and K. Char, Appl. Phys. Express **5**, 061102 (2012).

[32] Y. Shimizu, Y. Fukuyama, T. Narikiyo, H. Arai, and T. Seiyama, Chem. Lett. **14**, 377 (1985).

[33] C. J. Harbert and R. F. Morrison, United States Pat. Off. **2356317**, 1 (1944).

[34] E. Wainer, United States Pat. Off. **2452532**, 1 (1948).

[35] O. I. Prokopalo, Ferroelectrics **14**, 683 (1976).

[36] B. Ostrick, M. Fleischer, and H. Meixner, J. Am. Ceram. Soc. **80**, 2153 (1997).

[37] B. Ostrick, M. Fleischer, U. Lampe, and H. Meixner, Sensors Actuators, B Chem. **44**, 601 (1997).

[38] R. A. Bucur, A. I. Bucur, S. Novaconi, and I. Nicoara, J. Alloys Compd. **542**, 142 (2012).

[39] Q. Z. Liu, H. F. Wang, F. Chen, and W. Wu, J. Appl. Phys. **103**, 093709 (2008).

[40] H. D. Megaw, Proc. Phys. Soc. **58**, 133 (1946).

[41] T. Wolfram and S. Ellialtioglu, *Electronic and Optical Properties of d-Band Perovskites* (Cambridge University Press, Cambridge, 2006).

[42] R. J. D. Tilley, *Perovskites: Structure–Property Relationships* (John Wiley & Sons, Ltd, Chichester, 2016).

[43] C. H. Ahn, J.-M. Triscone, and J. Mannhart, Nature **424**, 1015 (2003).

[44] O. Auciello, J. F. Scott, and R. Ramesh, Phys. Today **51**, 22 (1998).

[45] K. Dörr, J. Phys. D: Appl. Phys. **39**, R125 (2006).

[46] Y. Tokura and Y. Tomioka, J. Magn. Magn. Mater. **200**, 1 (1999).

[47] T. Kimura, T. Goto, H. Shintani, K. Ishizaka, T. Arima, and Y. Tokura, Nature **426**, 55 (2003).

[48] J. G. Bednorz and K. A. Müller, Z. Phys. B: Condens. Matter **64**, 189 (1986).

[49] R. J. Cava, J. Am. Ceram. Soc. **83**, 5 (2000).

[50] C. H. Ahn, A. Bhattacharya, M. Di Ventra, J. N. Eckstein, C. D. Frisbie, M. E. Gershenson, A. M. Goldman, I. H. Inoue, J. Mannhart, A. J. Millis, A. F. Morpurgo, D. Natelson, and J.-M. Triscone, Rev. Mod. Phys. **78**, 1185 (2006).

[51] T. Maekawa, K. Kurosaki, and S. Yamanaka, J. Alloy Compd. **416**, 214 (2006).

[52] T. Huang, T. Nakamura, M. Itoh, Y. Inaguma, and O. Ishiyama, J. Mater. Sci. **30**, 1556 (1995).

[53] E. H. Mountstevens, J. P. Attfield, and S. A. T. Redfern, J. Phys.: Condens. Matter **15**, 8315 (2003).

[54] Q. Liu, J. Dai, Z. Liu, X. Zhang, G. Zhu, and G. Ding, J. Phys. D: Appl. Phys. **43**, 455401 (2010).

[55] H. J. Kim, J. Kim, T. H. Kim, W. J. Lee, B. G. Jeon, J. Y. Park, W. S. Choi, D. W. Jeong, S. H. Lee, J. Yu, T. W. Noh, and K. H. Kim, Phys. Rev. B **88**, 125204 (2013).

[56] U. Kim, C. Park, T. Ha, R. Kim, H. S. Mun, H. M. Kim, H. J. Kim, T. H. Kim, N. Kim, J. Yu, K. H. Kim, J. H. Kim, and K. Char, APL Mater. **2**, 056107 (2014).

[57] E. Sachet, C. T. Shelton, J. S. Harris, B. E. Gaddy, D. L. Irving, S. Curtarolo, B. F. Donovan, P. E. Hopkins, P. A. Sharma, A. L. Sharma, J. Ihlefeld, S. Franzen, and J. P. Maria, Nat. Mater. **14**, 414 (2015).

[58] H. Mizoguchi, H. W. Eng, and P. M. Woodward, Inorg. Chem. **43**, 1667 (2004).

[59] P. Drude, Ann. Phys. **306**, 566 (1900).

[60] F. J. Blatt, *Physics of Electronic Conduction in Solids* (McGraw-Hill, New York, 1968).

[61] R. H. Bube, *Electronic Properties of Crystalline Solids* (Academic, New York, 1974).

[62] H. J. Kim, U. Kim, T. H. Kim, J. Kim, H. M. Kim, B. G. Jeon, W. J. Lee, H. S. Mun, K. T. Hong, J. Yu, K. Char, and K. H. Kim, Phys. Rev. B **86**, 165205 (2012).

[63] S. Sallis, D. O. Scanlon, S. C. Chae, N. F. Quackenbush, D. A. Fischer, J. C. Woicik, J.-H. Guo, S.-W. Cheong, and L. F. J. Piper, Appl. Phys. Lett. **103**, 042105 (2013).

[64] H. R. Liu, J. H. Yang, H. J. Xiang, X. G. Gong, and S. H. Wei, Appl. Phys. Lett. **102**, 112109 (2013).

[65] D. O. Scanlon, Phys. Rev. B **87**, 161201 (2013).

[66] E. Moreira, J. M. Henriques, D. L. Azevedo, E. W. S. Caetano, V. N. Freire, U. L. Fulco, and E. L. Albuquerque, J. Appl. Phys. **112**, 043703 (2012).

[67] E. Moreira, J. M. Henriques, D. L. Azevedo, E. W. S. Caetano, V. N. Freire, and E. L. Albuquerque, J. Solid State Chem. **187**, 186 (2012).

[68] B. G. Kim, J. Y. Jo, and S. W. Cheong, J. Solid State Chem. **197**, 134 (2013).

[69] C. A. Niedermeier, S. Rhode, K. Ide, H. Hiramatsu, H. Hosono, T. Kamiya, and M. A. Moram, Phys. Rev. B **95**, 161202 (2017).

[70] C. A. Niedermeier, S. Rhode, S. Fearn, K. Ide, M. A. Moram, H. Hiramatsu, H. Hosono, and T. Kamiya, Appl. Phys. Lett. **108**, 172101 (2016).

[71] S. James Allen, S. Raghavan, T. Schumann, K. M. Law, and S. Stemmer, Appl. Phys. Lett. **108**, 252107 (2016).

[72] D. Seo, K. Yu, Y. Jun Chang, E. Sohn, K. Hoon Kim, and E. J. Choi, Appl. Phys. Lett. **104**, 022102 (2014).

[73] A. V. Sanchela, T. Onozato, B. Feng, Y. Ikuhara, and H. Ohta, Phys. Rev. Mater. **1**, 034603 (2017).

[74] B. C. Luo, X. S. Cao, K. X. Jin, and C. L. Chen, Curr. Appl. Phys. **16**, 20 (2016).

[75] K. Ellmer, J. Phys. D. Appl. Phys. **34**, 3097 (2001).

[76] H. Paik, Z. Chen, E. Lochocki, H. Ariel Seidner, A. Verma, N. Tanen, J. Park, M. Uchida, S. Shang, B. C. Zhou, M. Brützam, R. Uecker, Z. K. Liu, D. Jena, K. M. Shen, D. A. Muller, and D. G. Schlom, APL Mater. **5**, 116107 (2017).

[77] S. Raghavan, T. Schumann, H. Kim, J. Y. Zhang, T. A. Cain, and S. Stemmer, APL Mater. **4**, 016106 (2016).

[78] W. Y. Wang, Y. L. Tang, Y. L. Zhu, J. Suriyaprakash, Y. B. Xu, Y. Liu, B. Gao, S. W. Cheong, and X. L. Ma, Sci. Rep. **5**, 16097 (2015).

[79] J. Shiogai, K. Nishihara, K. Sato, and A. Tsukazaki, AIP Adv. **6**, 065305 (2016).

[80] N. G. Weimann, L. F. Eastman, D. Doppalapudi, H. M. Ng, and T. D. Moustakas, J. Appl. Phys. **83**, 3656 (1998).

[81] H. M. Ng, D. Doppalapudi, T. D. Moustakas, N. G. Weimann, and L. F. Eastman, Appl. Phys. Lett. **73**, 821 (1998).

[82] D. C. Look, and J. R. Sizelove, Phys. Rev. Lett. **82**, 1237 (1999).

[83] S. Kasap, and P. Capper, *Springer Handbook of Electronic and Photonic Materials* (Springer, Gewerbestraße, 2017).

[84] B. R. Nag, *Theory of Electrical Transport in Semiconductors* (Pergamon, Oxford, 1972).

[85] D. C. Look, C.E. Stutz, R.J. Molnar, K. Saarinen, and Z. Liliental-Weber, Solid State Commun. **117**, 571 (2001).

[86] A. Prakash, P. Xu, A. Faghaninia, S. Shukla, J. W. Ager, C. S. Lo, and B. Jalan, Nat. Commun. **8**, 15167 (2017).

[87] K. Krishnaswamy, B. Himmetoglu, Y. Kang, A. Janotti, and C. G. Van De Walle, Phys. Rev. B **95**, 205202 (2017).

[88] F. E. Low, and D. Pines, Phys. Rev. **98**, 414 (1955).

[89] H. Fröhlich, and N. F. Mott, Proc. R. Soc. London A **171**, 496 (1939).

[90] D. C. Look, and R. J. Molnar, Appl. Phys. Lett. **70**, 3377 (1997).

[91] D. C. Look, D. C. Reynolds, J. W. Hemsky, J. R. Sizelove, R. L. Jones, and R. J. Molnar, Phys. Rev. Lett. **79**, 2273 (1997).

[92] H. Mun, U. Kim, H. Min Kim, C. Park, T. Hoon Kim, H. Joon Kim, K. Hoon Kim, and K. Char, Appl. Phys. Lett. **102**, 252105 (2013).

[93] P. V. Wadekar, J. Alaria, M. O'Sullivan, N. L. O. Flack, T. D. Manning, L. J. Phillips, K. Durose, O. Lozano, S. Lucas, J. B. Claridge, and M. J. Rosseinsky, Appl. Phys. Lett. **105**, 052104 (2014).

[94] D. Yoon, S. Yu, and J. Son, NPG Asia Mater. **10**, 363 (2018).

[95] A. Prakash, J. Dewey, H. Yun, J. S. Jeong, K. A. Mkhoyan, and B. Jalan, J. Vac. Sci. Technol. A **33**, 060608 (2015).

[96] https://hackingmaterials.lbl.gov/amset/.

[97] E. B. Lochocki, H. Paik, M. Uchida, D. G. Schlom, and K. M. Shen, Appl. Phys. Lett. **112**, 181603 (2018).

[98] S. Yu, D. Yoon, and J. Son, Appl. Phys. Lett. **108**, 262101 (2016).

[99] W.-J. Lee, H. J. Kim, E. Sohn, T. H. Kim, J.-Y. Park, W. Park, H. Jeong, T. Lee, J. H. Kim, K.-Y. Choi, and K. H. Kim, Appl. Phys. Lett. **108**, 082105 (2016).

[100] Z. Wang, H. Paik, Z. Chen, D. A. Muller, and D. G. Schlom, APL Mater. **7**, 022520 (2019).

[101] H. J. Cho, T. Onozato, M. Wei, A. Sanchela, and H. Ohta, APL Mater. **7**, 022507 (2019).

[102] J. Shin, Y. M. Kim, Y. Kim, C. Park, and K. Char, Appl. Phys. Lett. **109**, 262102 (2016).

[103] A. Prakash, P. Xu, X. Wu, G. Haugstad, X. Wang, and B. Jalan, J. Mater. Chem. C **5**, 5730 (2017).

[104] J. Jasinski and Z. Liliental-Weber, J. Electron. Mater. **31**, 429 (2002).

[105] S. K. Vasheghani Farahani, T. D. Veal, A. M. Sanchez, O. Bierwagen, M. E. White, S. Gorfman, P. A. Thomas, J. S. Speck, and C. F. McConville, Phys. Rev. B **86**, 245315 (2012).

[106] C. Park, U. Kim, C. J. Ju, J. S. Park, Y. M. Kim, and K. Char, Appl. Phys. Lett. **105**, 203503 (2014).

[107] Z. Lebens-Higgins, D. O. Scanlon, H. Paik, S. Sallis, Y. Nie, M. Uchida, N. F. Quackenbush, M. J. Wahila, G. E. Sterbinsky, D. A. Arena, J. C. Woicik, D. G. Schlom, and L. F. Piper, Phys. Rev. Lett. **116**, 027602 (2016).

[108] A. Slassi, Mater. Sci. Semicond. Process. **32**, 100 (2015).

[109] K. Krishnaswamy, L. Bjaalie, B. Himmetoglu, A. Janotti, L. Gordon, and C. G. Van de Walle, Appl. Phys. Lett. **108**, 083501 (2016).

[110] W. Zhang, J. Tang, and J. Ye, . Mater. Res. **22**, 1859 (2007).

[111] R. Claessen, M. G. Smith, J. B. Goodenough, and J. W. Allen, Phys. Rev. B **47**, 1788 (1993).

[112] Y. Li, L. Zhang, Y. Ma, and D. J. Singh, APL Mater. **3**, 011102 (2015).

[113] Y. Kang, H. Peelaers, K. Krishnaswamy, and C. G. Van DeWalle, Appl. Phys. Lett. **112**, 062106 (2018).

[114] D. J. Singh, Q. Xu, and K. P. Ong, Appl. Phys. Lett. **104**, 011910 (2014).

[115] Q. Liu, J. Liu, B. Li, H. Li, G. Zhu, K. Dai, Z. Liu, P. Zhang, and J. Dai, Appl. Phys. Lett. **101**, 241901 (2012).

[116] O. I. Prokopalo, E. G. Fesenko, M. A. Malitskaya, Y. M. Popov, and V. G. Smotrakov, Ferroelectrics **18**, 99 (1978).

[117] G. Larramona, C. Guticrrez, I. Pereira, M. R. Nunes, and F. M. A. Costa, J. Chem. Soc. Faraday Trans. 1 **85**, 907 (1989).

[118] S. A. Chambers, T. C. Kaspar, A. Prakash, G. Haugstad, and B. Jalan, Appl. Phys. Lett. **108**, 152104 (2016).

[119] B. S. Joo, Y. J. Chang, L. Moreschini, A. Bostwick, E. Rotenberg, and M. Han, Curr. Appl. Phys. **17**, 595 (2017).

[120] H. M. Jaim, S. Lee, X. Zhang, and I. Takeuchi, Appl. Phys. Lett. **111**, 172102 (2017).

3. Experimental Methods

3.1 Introduction

The fabrication of thin films is motivated by the scientific expectations and the targeted applications. These applications are strongly related to the growth techniques employed, which also have their advantages and drawbacks. For example, for the industrial production of devices such as Si-based integrated circuits where μ-sized dimensions are needed with high throughput, the growth method known as chemical vapor deposition (CVD) is preferred [1]. However, the rapid progress in nanoscale device engineering and the growing need for atomically controlled layer growth techniques have triggered the development of more versatile epitaxial growth methods. These techniques which include molecular beam epitaxy (MBE) and pulsed laser deposition (PLD), have the ability to produce multilayer structures, which are determinant for applications in electronic and optoelectronic devices. As an example, both techniques are heavily employed in the growth of epitaxial thin film semiconductors that display the high crystal purity and crystallographic perfection essential for quantum well devices [2]. This is made possible thanks to their capabilities of precise thickness and atomic layer growth control, which permit the production of high-quality film layers and complex structures exhibiting unprecedented functional properties.

PLD has particularly been recognized as a valuable nonthermal growth method. It offers the possibility to operate far from chemical equilibrium and choose more suitable growth conditions not readily accessible by thermal deposition techniques such as MBE [2, 3]. Additionally, as will be also discussed in the next chapter, it has been reported that epitaxial thin films prepared by PLD can exhibit smoother surfaces than those made using thermal techniques [4, 5, 6]. Furthermore, laser-based technology and in particular PLD has proved to be a powerful tool in the generation of combinatorial thin films and coatings, suited for applications in areas such as material processing, medicine (synthesis of biomaterials) and optical communication [7, 8].

This chapter is organized around two sections. In the first section, we present the PLD growth technique. The preliminary steps, i.e. the preparation steps which are fundamental for thin film deposition using the PLD method are reported. In the second section, we describe the theory and working principle of the various characterization methods. These techniques are grouped in categories of techniques such as diffraction, microscopy, magnetotransport and spectroscopy.

3.2 Pulsed Laser Deposition

The success in fabricating epitaxial thin films exhibiting high structural and electronic properties lies in the quality of the interface between the epitaxial layer and the host material. Therefore, before proceeding to film deposition, there is the requirement of having a clean and well prepared substrate. In this section, all the preliminary steps leading to the growth are addressed. These steps include the preparation of both the substrates and the targets. In addition, the PLD growth method is also described.

3.2.1 Substrate Preparation

To prepare heterostructures based on La-doped $BaSnO_3$ thin films, oxide single crystal substrates such as the perovskites $SrTiO_3$ (001), $DyScO_3$ (110), $TbScO_3$ (110) and $GdScO_3$ (110), and the non-perovskite MgO (001) were used. All these substrates were polished on the growth side and were $5 \times 5 \times 1$ mm^3 in size. The substrate preparation procedure consisted of two cleaning steps: an *ex situ* preparation, and an *in situ* preparation conducted inside the growth chamber directly before film deposition.

a) *Ex Situ* Preparation Steps

The *ex situ* preparation was intended to remove eventual chemicals such as greases and particles from the surfaces of the substrates was carried out in a flowbox in the chemistry lab. The cleaning sequence is detailed below:

- Firstly, the substrates were placed on a clean working surface and wetted with isopropanol. Using lens paper, also wetted with isopropanol, the surfaces of the substrates were gently polished. Both the substrate and the lens paper were frequently wetted with isopropanol during the process.
- Secondly, the substrates (deposited on a support carrying up to 5 substrates a the time) were inserted into a beaker filled with acetone, and cleaned in an ultrasound bath for 10 min at room temperature.
- Thirdly, the substrates were taken out, inserted in another beaker filled with isopropanol and cleaned in an ultrasound bath for 10 min. When transferring the substrates from one beaker to another, these were rinsed with isopropanol.
- Fourthly, the substrates were inserted into a beaker containing ultra pure water and cleaned in ultrasound for 10 min. When transferring the substrates, these were rinsed with water. For the MgO (001) substrates, this step was not performed. This is because it was realized that for optimal *ex situ* surface preparation, MgO substrates should not be cleaned in water.
- Finally, the substrates were blew dry using nitrogen and put in sample boxes and transported to the growth lab.

b) *In Situ* Termination

The *in situ* preparation consisted of a thermal treatment in the growth chamber. The whole process was conducted in an oxygen gas atmosphere maintained at the films deposition pressure. The *ex situ* cleaned substrates were loaded into a glove box connected to the PLD chamber, and mounted onto sample holders. Then, these were loaded into the load lock and transferred into the growth chamber. On the sample stage, the substrate was *in situ* terminated by annealing at a temperature of 1300 °C using a CO_2 laser that homogeneously heats the substrate from its back side. The termination process followed the phases labeled I to III in the temperature profile shown in Fig. 3.1(a). In I, the substrate is heated to the temperature of 650 °C at a rate of 2 K s^{-1}. Then, at a rate of 1 K s^{-1}, it is heated to the maximum termination temperature (1300 °C). This is illustrated as II in the heating curve (temperature profile). The thermal preparation was optimized for an annealing time of 200 s at 1300 °C (indicated by III in Fig. 3.1(a)). This surface treatment has proved to be reliable and effective in producing well-ordered surface structures, which constitute a good template for the growth

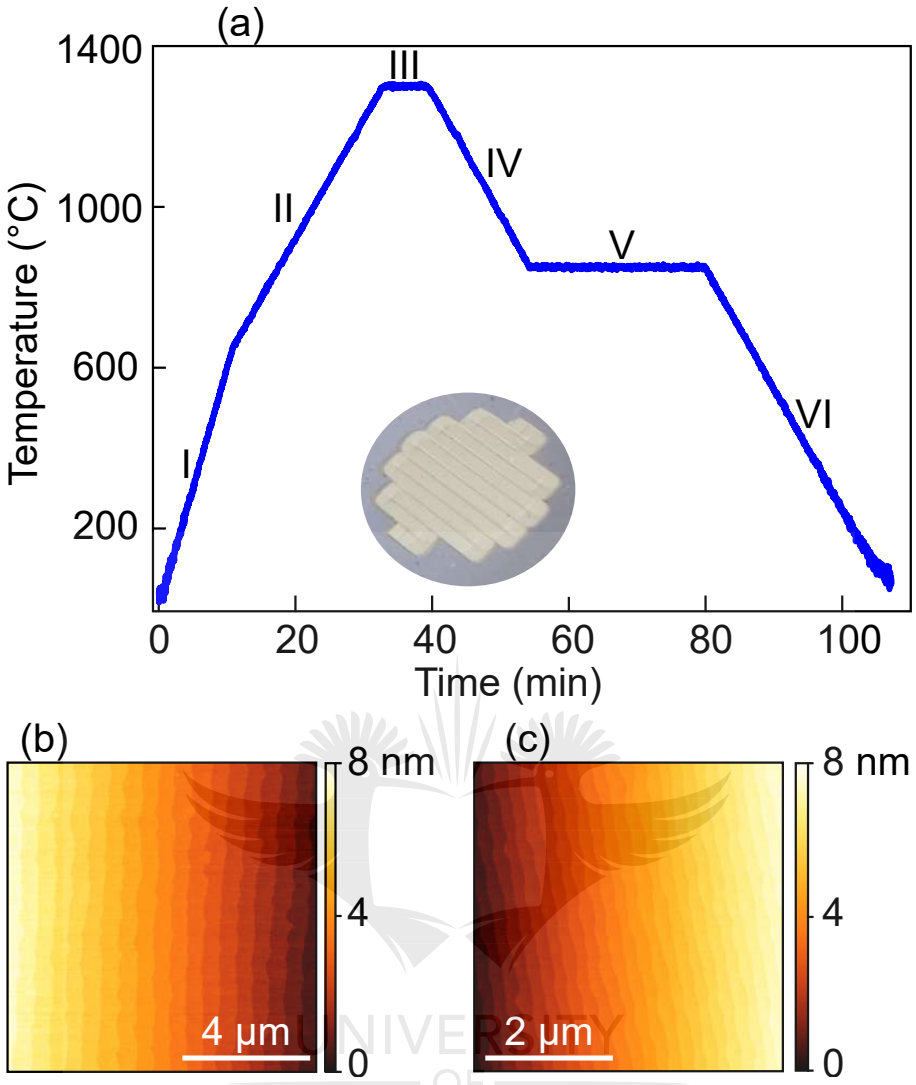

Figure 3.1: (a) Temperature profile indicating the different phases of the growth: substrate termination (I to III), cool down to the deposition temperature (IV), film deposition (V), and sample cool down to room temperature (VI). The inset in (a) is an image of the surface of a target taken with a cellphone camera. It shows the pattern left by the ablation laser. Surface morphologies of $TbScO_3$ (110) substrates terminated (b) *in situ* using the CO_2 heating laser and (c) *ex situ* by HF etching and annealing in a tube furnace. These images were taken with as atomic force microscope.

of epitaxial thin films [9, 10].

Figure 3.1(b) depicts a representative *in situ* terminated $TbScO_3$ (110) surface, where clear step and terrace structures can be seen. These structures are comparable to the morphology obtained with the standard preparation method which consists of etching in hydrofluoric acid solution (HF) and annealing in a tube furnace [11, 12, 13, 14]. For illustration, we have shown in Fig. 3.1(c) the surface structure of a $TbScO_3$ (110) substrate etched in HF, and annealed at 1000 °C in oxygen atmosphere for 2h in a tube furnace. As can be observed, both surfaces exhibit near identical morphology. However, the termination with the CO_2 laser has the advantage that it is done *in situ*. This favors the deposition on an already ordered and cleaned surface, whereas an additional treatment is required in the case of substrates

terminated *ex situ* in a tube furnace. Additionally, the etching process involves toxic HF solution, and therefore requires strict safety protocol. It is also time consuming as it consists of several steps. It should be mentioned that all the samples fabricated in the framework of this thesis were grown on substrates cleaned and terminated *in situ* following the procedures described above.

3.2.2 Thin Film Deposition

The PLD technique is based on the irradiation of a starting material known as target (which can be of complex composition) with short and intense laser pulses. A high energy flux (from the photons) is instantaneously transferred to the material, resulting in the removal (or ablation) of high kinetic energy species in the form of a plasma plume which are deposited on a substrate. This energetic effect sustains the epitaxial growth [4]. It also opens up the possibility of flat surface growth since the ejected species are capable of travelling several millimeters through the background gas pressure and nucleate on the substrate. In fact, depending on the application, a PLD system can be operated in any gas atmosphere to pressures up to 0.2 mbar [8]. Additionally, the PLD technique offers the advantages of stoichiometric growth of epitaxial films, and the deposition of superlattice structures.

In PLD growth, targets of desired materials are employed. For this study, all the targets used were purchased. Their surfaces are routinely cleaned before deposition. Targets of doped $La_xBa_{1-x}SnO_3$, and undoped $BaSnO_3$, $BaZrO_3$ and $SrZrO_3$ materials were used in this work. The doping percentage x in the doped targets was $x = 0.5\%$, 1%, 2%, 4% and 6%. These correspond to doping levels of 6.80×10^{19} cm^{-3}, 1.36×10^{20} cm^{-3}, 2.72×10^{20} cm^{-3}, 5.44×10^{20} cm^{-3} and 8.16×10^{20} cm^{-3}, respectively. These targets were cleaned in a glove box (also connected to the PLD system) following a rigorous procedure. The target cleaning process consisted of: i) polishing its surface using P800 sandpaper; ii) rinsing in isopropanol with an ultrasonic cleaner for 5 min at room temperature; and iii) drying on a hotplate for 30 min at 80 °C. Once transferred into the PLD chamber, the targets were preablated before being employed for the growth. This was done to ensure that their surfaces are free from any particles or foreign species. The preablation also guarantees that the ablation is brought to a steady state. An ablation pattern on a target can be seen in the inset in Fig. 3.1(a). Although the chamber is equipped with a shutter that opens and closes between the substrate and the target, we chose to keep all the substrates out of the deposition chamber during the preablation processes. When the preablation was completed, we transferred the substrate into the growth chamber.

Upon installing the substrate onto the sample stage, the chamber was prepared for deposition. Preparing the chamber firstly consisted of adjusting the oxygen background pressure to the desired value. This was done by letting a controlled flow of oxygen into the chamber. Film deposition in an oxygen environment ensures compensation of oxygen vacancies created in the oxide substrates due to exposure to high temperatures. Secondly, the setting the reflection high energy electron diffraction (RHEED) system was switched on and the electron beam adjusted onto the substrate surface to define specific diffraction conditions. The adjustment was achieved in two steps: 1- modification of the sample stage height to optimize the angle of incidence of the beam; and 2- rotation of the sample stage around the normal direction of the surface to optimize the azimuthal angle of beam incidence with respect to the crystallographic orientation of the substrate. RHEED is a very important tool in epitaxial thin film growth. It is employed for real time monitoring of the film surface growth dynamics and to determine the

layer deposition rate and film thickness. Hence, in this work, both qualitative and quantitative analyses of the RHEED data were carried out.

After setting the chamber, the heating laser was used for sample termination (see I–III in Fig. 3.1(a)). Since most of the samples fabricated in the framework of this thesis were grown at temperatures below the termination temperature of 1300 °C, the substrate was cooled to the deposition temperature at a rate of 1 K s^{-1}. Phase IV in the heating curve (Fig. 3.1(a)) illustrates the cooling to the deposition temperature, in this case of 850 °C. Once the substrate reached the growth temperature, we opened the attenuator of the ablation laser whose parameters (energy density and repetition rate) were set beforehand, and proceeded to the deposition (see phase V). After the growth, the sample was cooled down to room temperature at a rate of 1 K s^{-1} in an oxygen environment (see phase VI).

Figure 3.2 shows the schematics of the oxide heterostructures (samples) fabricated for this study. As illustrated in Fig. 3.2(a), the samples were fabricated by directly depositing the film layer on the substrate. However, since the properties of the film are greatly improved in samples prepared with an adhesion layer as described in Section 2.3, a buffer layer made of an insulation material was thus inserted between the film layer and the substrate as depicted in Fig. 3.2(b). A representation of the PLD system used to prepare these samples is shown in Fig. 3.3. It is a system equipped with an $x - y - z$ motion controlled targets table, with the distance target-substrate of 56 mm. It also comprises a KrF excimer ablation laser system with a pulse width of 25 ns and a wavelength of 248 nm; a CO_2 laser heating system that can produce a beam with a maximum power of 1.1 kW and 9.27 μm wavelength; and a RHEED system equipped with two-stage differential pumping and capable of operating at a maximum pressure of 1 mbar.

All the growth parameters (including the optimized parameters) such as laser density and frequency, oxygen background pressure, substrate temperature, and active film and buffer layer thickness are given in Tables A.1 and A.2 in the appendix section. The preparation of

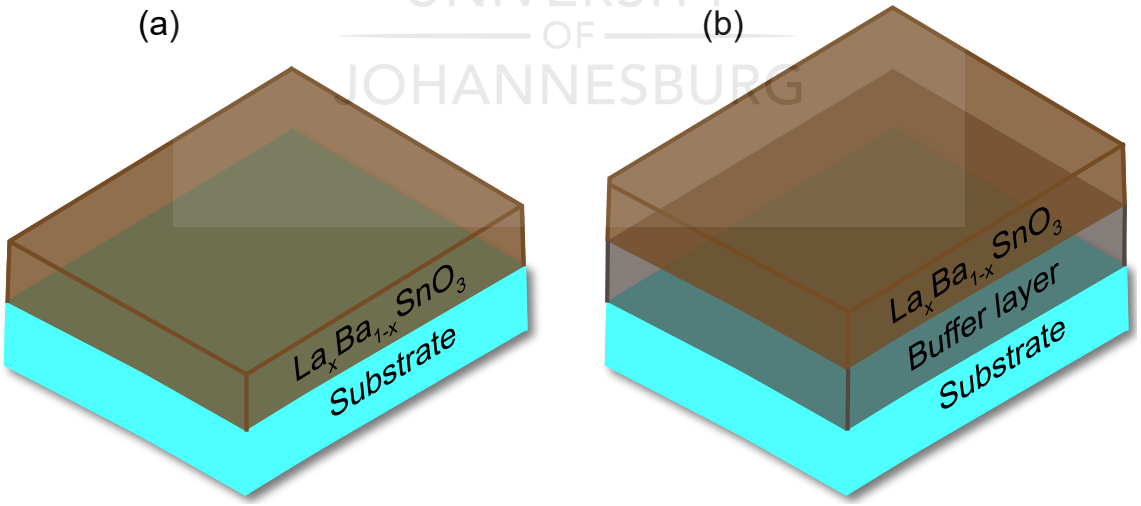

Figure 3.2: Schematics of the oxide heterostructures or samples grown as part of this thesis. (a) The active layer $La_xBa_{1-x}SnO_3$ is directly deposited on the substrate. (b) An insulting buffer layer is inserted between the active film layer and the substrate. This buffer layer is made of either $BaSnO_3$ or $BaZrO_3$ or $SrZrO_3$ material.

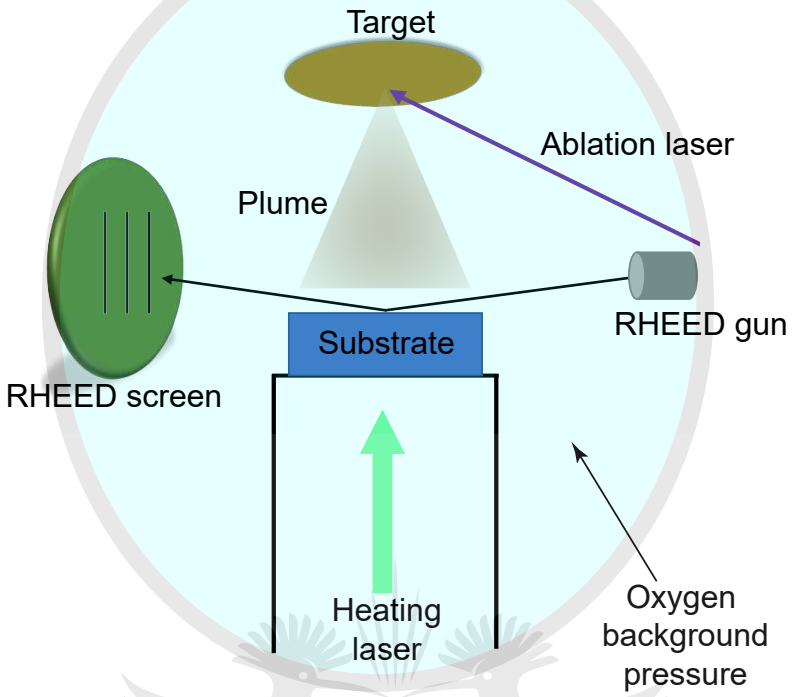

Figure 3.3: Schematic of the PLD system used to grow the samples presented in this thesis. Intense laser pulses are directed on a target. The plasma plume of material ablated from the target is deposited on the substrate which is kept at a high temperature by CO_2 laser heating. Simultaneously, the RHEED gun shoots electrons onto the substrate surface and the diffracted beam is collected on the fluorescent screen. The deposition of the film is conducted in a controlled oxygen background pressure.

the substrates, the deposition of the films and the electronic transport investigations were conducted in the Department of Solid State Quantum Electronics at the Max-Planck Institute for Solid State Research in Stuttgart, Germany.

3.3 Characterization Tools

This section is dedicated to the theory and experimental concepts of the different methods employed in characterizing the epitaxially grown films. Several characterization techniques were adopted: 1- the diffraction techniques which included RHEED, X-ray diffraction (XRD) and low energy electron diffraction (LEED); 2- microscopy techniques such as atomic force microscopy (AFM) and transmission electron microscopy (TEM); 3- magnetotransport; and 4- the spectroscopic techniques including X-ray photoemission spectroscopy (XPS) and angle resolved photoemission spectroscopy (ARPES).

3.3.1 Diffraction Techniques

The electronic performances of thin films are highly correlated to their structural purity or crystallinity. The analysis techniques based on diffraction are very powerful for understanding the crystalline structure of materials. Since the growth process is essentially determinant for

realizing high quality thin films with outstanding electrical properties, we first evaluated the growth quality of the films *in situ* during deposition using RHEED. This method helps to monitor the surface properties of the films in real time during growth. Then, *ex situ* diffraction techniques such as XRD to investigate the films crystalline structure; and LEED to analyze the surface structure and geometry of films that were cleaned in ultra-high vacuum (UHV) were employed. All these characterization tools are based on the diffraction of an incident beam by the specimen under study, when it is bombarded with electrons (in the case of LEED and RHEED) or with photons (in the case of XRD) [15, 16, 17]. The impinging beam has a specific characteristic described by the wave-particle duality, which is the de Broglie wavelength expressed as

$$\lambda = \frac{h}{p} = \frac{h}{\sqrt{2mq\mathrm{V}}} \tag{3.1}$$

and

$$\lambda = \frac{hc}{\mathrm{E_p}} = \frac{c}{\nu}. \tag{3.2}$$

Here, λ, p, m, q and V are the wavelength, the momentum, the mass, the charge and the acceleration voltage of the incident electron; h the Planck constant, $\mathrm{E_p}$ the kinetic energy of the photon, c the speed of light, and ν the photon frequency corresponding to the X-ray radiation used. Equations (3.1) and (3.2) ensure that the beam of electrons and photons have energy values which correspond to wavelengths that are comparable to atomic dimensions, such that the beams can experience diffraction from crystal lattice [1].

a) Low Energy Electron Diffraction

The LEED experimental set-up is illustrated in Fig. 3.4(a). As can be seen, the electron beam is accelerated from the electron gun towards the surface of the sample. It diffracts from the topmost surface atomic layers, and is elastically scattered onto the fluorescent screen. LEED is a surface sensitive measurement which maps the reciprocal lattice of the crystal surface [18]. The diffraction is defined by the Laue condition which is given by [15, 18]

$$\vec{\mathbf{K}}_\mathrm{f} - \vec{\mathbf{K}}_\mathrm{i} = \vec{\mathbf{G}}, \tag{3.3}$$

where $\vec{\mathbf{K}}_\mathrm{i}$ and $\vec{\mathbf{K}}_\mathrm{f}$ are, respectively, the wave vectors of the incident and scattered electron beams, and $\vec{\mathbf{G}}$ the surface reciprocal lattice vector. Equation (3.3) means that every diffraction beam on the fluorescent screen corresponds to the reciprocal vector. The energy-filtering grids placed in front of the screen suppress the lower energy electrons (inelastic secondary electrons). Only the elastically backscattered electrons with the appropriate energy form the diffraction pattern on the fluorescent screen (see Fig. 3.4(a)). Since LEED operates in the low energy regime, the mean free path of the electrons is small. The mean free path determines the distance an electron can travel in the crystal without being inelastically scattered. This means that only two to three atomic layers are involved in the elastic scattering process. Thus, LEED experiment imposes a two dimensional (2D) surface reciprocal lattice. This explains why, for

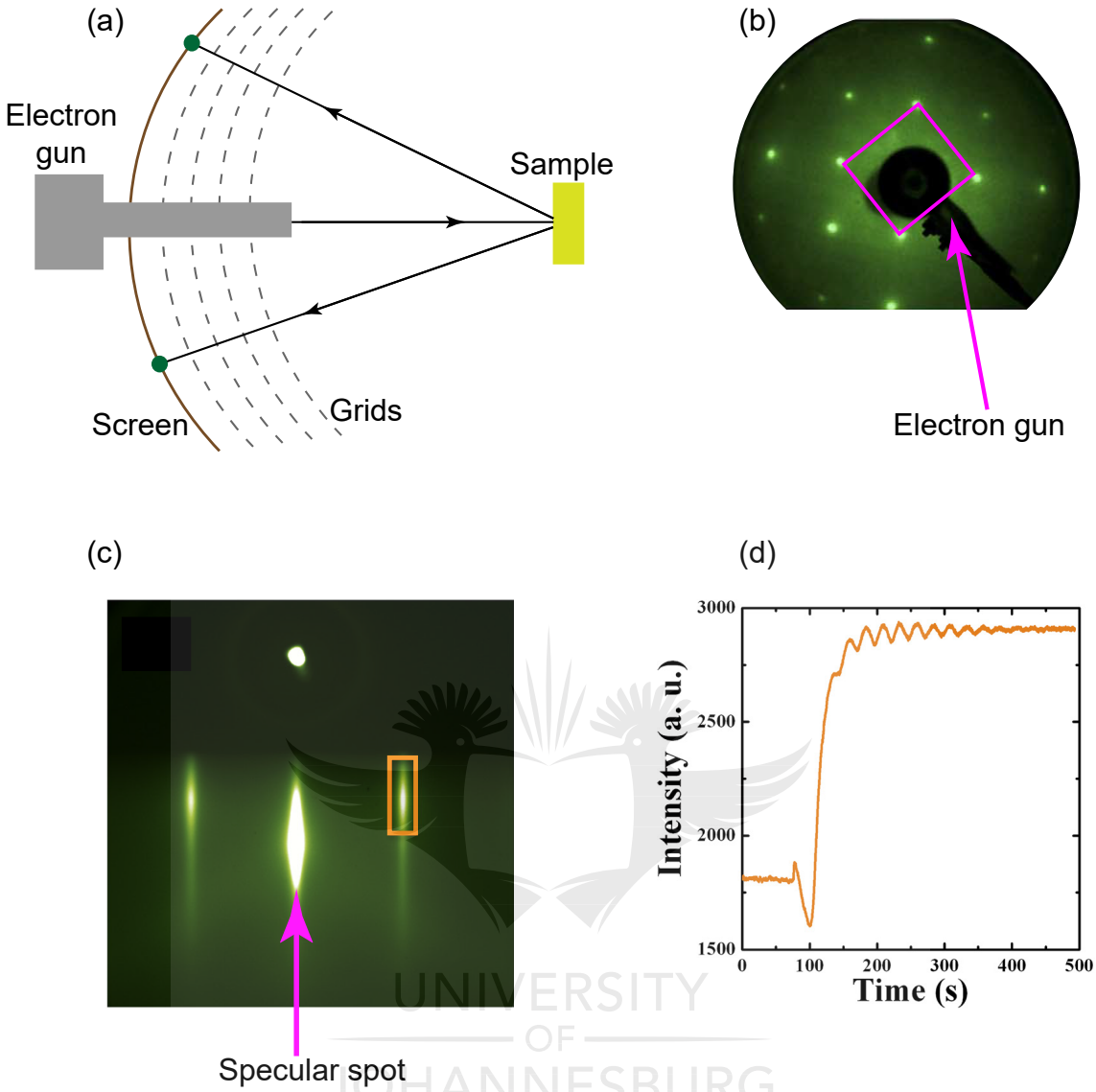

Figure 3.4: (a) Schematics of the LEED experiment. The electron beam arrives perpendicularly to the sample plane. The electrons are back-scattered and form a diffraction pattern on the fluorescent screen. The grids suppress electrons of lower energies. (b) LEED diffraction patterns forming a 1×1 surface structure at the surface of a $SrTiO_3$ (100) single crystal substrate. The patterns (bright spots) form square lattices (magenta square), typical of cubic structures. The arrow points at the back of the electron gun. (c) RHEED diffraction patterns viewed along the [110] azimuth of a La-$BaSnO_3$ thin film. The magenta arrow indicates the specular spot. The orange rectangle represents the area from which the RHEED intensity oscillations shown in (d) were recorded. The image in (b) was adapted from Ref. [19]; those in (c) and (d) were adapted from Ref. [20].

an elastic diffraction pattern to occur, only $\vec{K}_i^{\parallel}$ and $\vec{K}_f^{\parallel}$ should apply in Equation (3.3), such that the change $\vec{K}_f^{\parallel} - \vec{K}_i^{\parallel}$ is equal to the 2D surface reciprocal lattice $\vec{G}_{\parallel}$ [21, 22]. Therefore, the Laue condition in Equation (3.3) does not apply in the direction perpendicular to the crystal surface.

The specimens used in LEED experiments should have single crystalline structures with clean

and well-ordered surfaces. LEED then helps to accurately determine their surface orientation and symmetry. A 1×1 surface structure can be seen in Fig. 3.4(b), representing the LEED image of the surface of a $SrTiO_3$ (100) single crystal substrate, annealed in vacuum (pressure $< 10^{-9}$ mbar) at the temperature of 700 °C for 20 minutes [19]. The LEED diffraction patterns are the bright and sharp spots that are formed on the fluorescent screen. They illustrate square lattices in the reciprocal space, demonstrating the cubic crystallographic structure of $SrTiO_3$ in real space. One of the square lattices is shown by a magenta square (see Fig. 3.4(b)). The magenta arrow in the image points at the back of the electron gun, which is properly illustrated in profile view in Fig. 3.4(a).

In this study, the LEED experiment was used as a surface tool for two purposes. First, to check the cleanliness of the surfaces when cleaning the samples for spectroscopic measurements. Second, to identify the orientation of the surfaces which is essential for ARPES experiments. The LEED optics used in this work were mounted on an UHV chamber (See Section 3.3.4), and could produce electrons accelerated with voltage up to 500 V. The image of the diffracted spots were recorded with the help of a carefully aligned cellphone camera.

b) Reflection High Energy Electron Diffraction

The theory of RHEED is similar to that of LEED and expressed by Equation (3.3) [23]. The set-up of a RHEED experiment is shown in Fig. 3.3. The electrons emitted from the gun arrive at the sample surface at a very glancing incidence. They are elastically forward-scattered to form the diffraction patterns on the florescent screen. The RHEED system used in this study is a STAIB TorrRHEED. During operation, the electrons were accelerated at the voltage of 30 kV and the diffraction patterns on the screen were recorded with a CCD camera.

The angle at which the electrons hit the specimen surface is crucial for the diffraction pattern. Since the energy of the incident electrons is high, their penetration depth should be kept small to extract structural information only from the topmost surface layers. Hence, suitable calibration to keep the incidence angle as small as possible (1 to 8°) is required for the optimization of the RHEED pattern. This also ensures that the perpendicular component of the electron wave vector is small. Contrary to LEED, both the parallel and perpendicular components of the wave vectors in Equation (3.3) are considered in the Laue condition for a RHEED pattern, which results in a set of diffracted beams on either side of the specular reflected beam [15], as shown in Fig. 3.4(c). Figure 3.4(c) illustrates the RHEED diffraction patterns of the growth of a 60 nm thick La-doped $BaSnO_3$ thin film, deposited on $DyScO_3$ (001) substrate with a 330 nm $BaSnO_3$ buffer layer, using the MBE technique [20].

The investigation of the surface quality of the films during growth is associated with the analysis of the RHEED intensity oscillations. These oscillations depict the dynamics of the growth of the surface, and inform on the deposition mode. For example, the RHEED intensity oscillations as a function of time portraying the surface growth dynamics of the deposition of the $BaSnO_3$ buffer layer are shown in Fig. 3.4(d). These RHEED intensity oscillations that were recorded from the area marked by the orange rectangle in Fig. 3.4(c) illustrate growth following a 2D layer-by-layer mode which transits to a step-flow growth mode [20]. The layer-by-layer growth is indicated by clear and regular oscillations observed after the opening of the shutter at about 80 s (see Fig. 3.4(d)). The step-flow growth is recognized by the decay in the amplitude of these oscillations as observed from about 300 s into the growth until the end of the deposition. Such transient behavior was also reported in PLD grown $SrRuO_3$ thin films prepared on $SrTiO_3$ (001) substrates [24, 25, 26]. For instance, it was observed that after only two oscillations, the

overall RHEED intensity reached a steady state which persisted until the end of the growth, indicating a growth mode transition from layer-by-layer to step-flow [24]. Further valuable information that can be obtained from the analysis of the RHEED intensity oscillations is the thickness of the epitaxial layer. From the number of oscillations, the thickness of the film can be estimated, since one oscillation corresponds to the deposition of one unit cell of material [20, 27, 28].

c) X-ray Diffraction

Compared to LEED and RHEED, XRD is rather a bulk sensitive measurement which provides details on the arrangement of atomic planes and layers in the crystal [29]. As depicted in Fig. 3.5(a), the technique consists of directing a source of photons at the surface of a crystal at a certain angle ω. The incident photons are elastically scattered by parallel planes of atoms spaced by d_{hkl}, and diffracted only for constructive interference satisfying Bragg's law [30]

$$n\lambda = 2d_{hkl}\ \sin\theta; \tag{3.4}$$

where λ is the wavelength of the incident photons defined in Equation (3.2), n an integer representing the diffraction order, θ the diffracted angle such that 2θ is the angle between the incident and the scattered beams, and hkl the Miller indices used to label the different lattice planes. The diffracted beams are collected by a detector, which, as shown in Fig. 3.5(b), produces a pattern as an $x-y$ plot of the intensity of the diffracted beam versus the scattering angle (2θ). In such a pattern, each diffracted intensity maximum (or peak) corresponds to diffraction from a particular crystal lattice plane and is located at a specific angle (or position) 2θ governed by Equation (3.4). In other words, for a fixed value of λ (which is the case in most lab-based XRD experimental set-ups), a family of parallel planes generates a diffraction intensity peak only at a particular angle 2θ. Thus, the crystal plane spacings associated with the (hkl) planes are deduced from these respective positions. From the values of the plane spacing d_{hkl}, the hkl indices are also determined in order to completely characterize the (hkl) planes. For example, for a sample with a cubic crystallographic structure of lattice parameter a, this can be achieved using the formula [31, 32, 33]

$$d_{hkl} = \frac{a}{\sqrt{h^2 + k^2 + l^2}}. \tag{3.5}$$

XRD is indeed a powerful method for the structural characterization of materials. In epitaxial thin film growth, XRD provides a wealth of information regarding the crystallinity of the grown films. For instance, from the analysis of the diffraction peaks (or diffraction patterns) in the XRD pattern, knowledge about the crystalline purity, as well as the degree of crystallinity and smoothness of the grown films can be obtained. Figure 3.5(b) illustrates an example of a XRD diffraction pattern of a 25 nm thick La-doped $BaSnO_3$ thin film prepared on a $TbScO_3$ (110) substrate by MBE [28]. As can be seen in the figure, the diffracted peaks of the film only form the (00l) family of planes. These planes are indicated in the figure by (001), (002), (003) and (004), and they suggest an epitaxial growth (pure phase growth) of the La-doped $BaSnO_3$ thin film, which also has a single crystalline structure [20, 27, 28, 34, 35, 36]. The reflections of the $TbScO_3$ (110) substrate, also forming a family of peaks marked by the $*$ symbols, can also be seen.

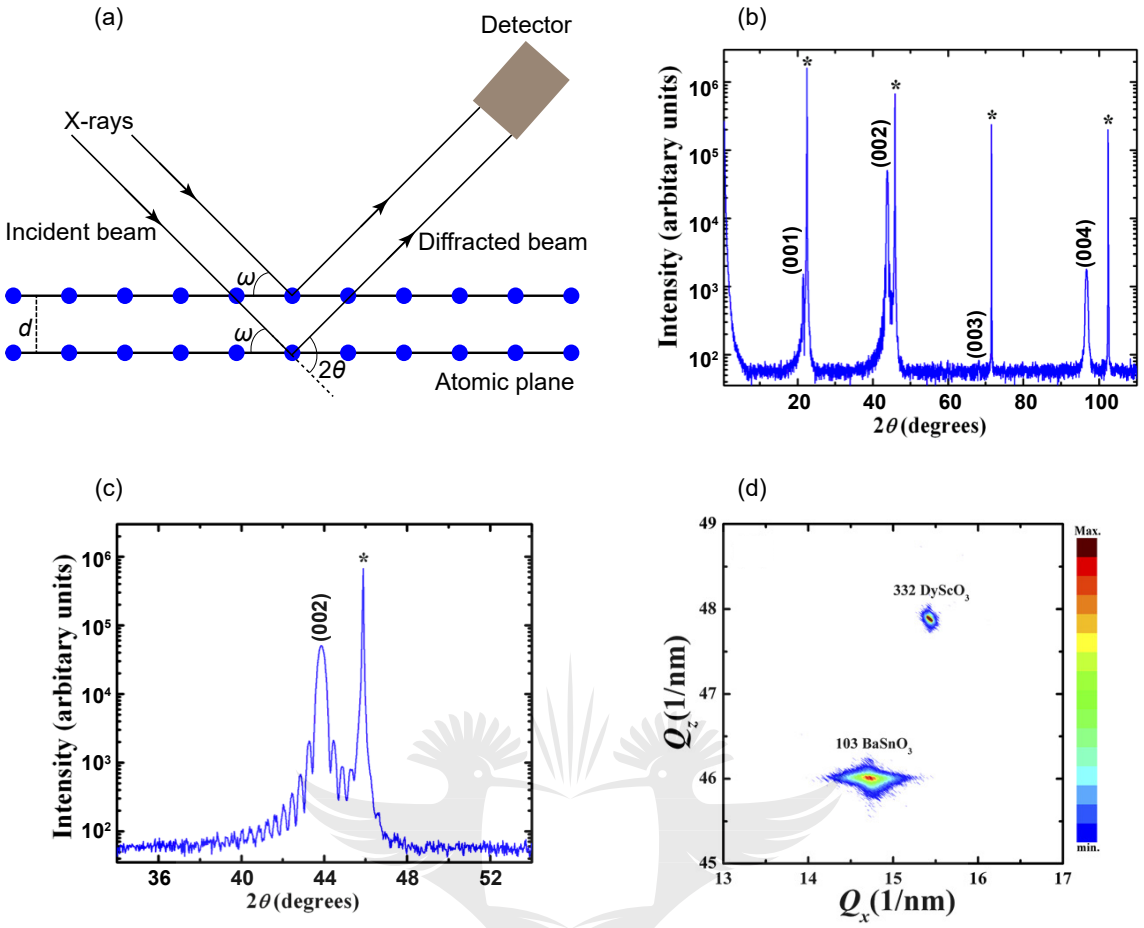

Figure 3.5: (a) Schematics of the XRD experiment. A parallel beam of photons is directed at the sample surface at an incident angle of ω. The photons interfere with parallel atom planes in the crystal. They are then scattered and diffracted by 2θ. The diffracted beam is collected by a detector and analyzed. (b) XRD pattern in the 2θ scan of a La-$BaSnO_3$ thin film prepared by MBE on $TbScO_3$ (110) substrate. The substrate planes are indicated by the $*$ symbols. (c) Close-up view of the pattern in (b) around the (002) film peak and a substrate peak, showing the Laue thickness fringes. (d) Reciprocal space map around the asymmetric (103) plane of a La-$BaSnO_3$ thin film and (332) reflection of the pseudocubic $DyScO_3$ (110) substrate, in a MBE grown film. The images in (b) and (c) were adapted from Ref. [28], and that in (d) was adapted from Ref. [20].

An enlargement around the (002) plane of the La-doped $BaSnO_3$ film and a reflection plane of the $TbScO_3$ (110) substrate is presented in Fig. 3.5(c). This enlargement helps to clearly observe the Laue thickness interference fringes that are formed around the (002) diffraction peak of the film. The presence of clear thickness fringes indicates the smoothness and the high structural quality of the La-doped $BaSnO_3$ thin film [20, 28, 35]. These interference fringes also help in determining the thickness of the film using X-ray reflectivity measurements. Additionally, based on information such as plane spacing and indexing provided by this (002) film peak, the value of the out-of-plane (c) lattice parameter of the epitaxial layer is calculated using Equation (3.5) [20, 27, 28, 34, 35, 36]. The value of c helps in detecting and quantifying crystal lattice defects such as misfits, strains, distortions and dislocations. The calculated c value compared to the lattice parameter value (a_t) of the bulk material in the case of a cubic lattice, informs on the strain status of the epitaxial thin film with respect to the growth

direction (the direction perpendicular to the surface of the substrate) [20, 27, 28].

The strain state of epitaxial thin films is further assessed through reciprocal space mappings, which are based on asymmetric Bragg geometries. Reciprocal space map measurements are sensitive to lattice parameters both perpendicular and parallel to the growth direction. Hence, these measurements provide the opportunity to extract both the in-plane (a) and out-of-plane (c) lattice parameters of the films, and also to qualitatively and quantitatively characterize their structural defects [20, 27, 28].

Heteroepitaxial growth of thin films are growth situations whereby materials of different types (also having different lattice parameters) are brought together to form structures called heterostructures (structures made of different types of materials). In such growth, the starting material (or target used to produce the thin films) generally has a larger lattice constant (a_{t}) compared to that of the substrate (a_{s}) on which the thin films are to be deposited. Thus, during the deposition of the epitaxial thin layers, two situations usually occur: First, the grown film can completely (partially) relax due to the large lattice mismatch between the as-grown film and the substrate [20, 27, 28, 34, 36]. This is seen when after deposition, the extracted in-plane a and out-of-plane c lattice constants of the film are equal (almost equal) to those of the initial material/target, a_{t}, indicating no distortion in the film lattice. Second, the deposited film can build an epitaxial strained relationship with the substrate, indicating a coherent growth or pseudomorphic growth of the thin film [37, 38, 39, 40, 41]. In this case, the in-plane lattice parameter of the grown film is equal or close to that of the substrate, $a = a_{\mathrm{s}}$, suggesting a compressive strain in the plane direction since the initial material had a larger lattice parameter ($a_{\mathrm{t}} > a_{\mathrm{s}}$). This compression is followed by a tetragonal distortion in the out-of-plane direction. The compression ratio or simply the strain in the film with respect to the plane direction denoted ε_x can be evaluated as [42]

$$\varepsilon_x = \frac{a - a_{\mathrm{t}}}{a_{\mathrm{t}}}. \tag{3.6}$$

ε_x in Equation (3.6) is expressed in percentage and indicates how much the in-plane lattice constant of the grown film deviates from the bulk lattice parameter value.

An example of a reciprocal space mapping is depicted in Fig. 3.5(d). It is the reciprocal space map around the asymmetric (103) reflection of a La-doped $BaSnO_3$ film peak and the (332) reflection of the pseudocubic $DyScO_3$ substrate peak [20]. The in-plane and out-of-plane lattice constants of both the La-doped $BaSnO_3$ thin film and the $DyScO_3$ (001) substrate can be extracted from the positions of the reciprocal vectors Q_x and Q_z, respectively. For the case portrayed in Fig. 3.5(d), the lattice parameters of the La-doped $BaSnO_3$ thin film are calculated as

$$a = \frac{1 \times 2\pi}{Q_x}, \tag{3.7}$$

and

$$c = \frac{3 \times 2\pi}{Q_z}. \tag{3.8}$$

Furthermore, the size of the grains in the film can be determined from the diffraction spot of the film in the reciprocal space map [43]. Hence, the lateral grain size, D, of the La-doped $BaSnO_3$ film in Fig. 3.5(d) can be extracted from the (103) reflection spot along the Q_x axis. The fitting of the contour profile of the (103) reflection with a peak function helps to extract the integral width (FWHM) [43] and then determine the lateral grain size since both the FWHM and D are inversely proportional to each other [44, 45].

It is important to emphasize that for the present study, the XRD data were acquired by the XRD service in the Department of Physical Chemistry of Solids at the Max-Planck Institute for Solid State Research in Stuttgart. The XRD measurements were carried on a two circle Panalytical X'Pert Pro diffractometer equipped with a Cu $K_{\alpha 1}$ X-Ray source producing photons of wavelength $\lambda = 1.542$ Å.

3.3.2 Microscopy Techniques

To image both the surface and the atomic structure of our samples with high magnification, we employed atomic force microscopy and transmission electron microscopy.

a) Atomic Force Microscopy

The surface quality of the grown films was carefully examined with AFM, directly after the samples were unloaded from the deposition chamber. The measurements were done using a Cypher Scanning Probe Microscope installed on a vibration-free table in the AFM laboratory at the Max Planck Institute for Solid State Research in Stuttgart.

As illustrated in Fig. 3.6, the AFM technique consists of scanning across the surface of the sample with a sharp tip (probe) located at the end of a cantilever arm [16, 46, 47]. The sample is placed on an $x - y - z$ motion controlled scanning stage. As the probe comes into contact with the surface (or gets close enough to the surface), a laser focused on the back of the cantilever measures the deflection caused by the force between the atoms from which the tip is made of and those of the sample surface. That force is qualitatively attractive or repulsive depending on the probe-sample distance. Quantitatively, this force can be represented by Hooke's law. The cantilever that bends acts as a spring of a certain stiffness, and the force is then proportional to its displacement with respect to its equilibrium position when it is not in interaction with the sample. As the tip sweeps across the surface, the change in the cantilever position (for measurements done in contact mode) or the change in its resonance frequency or amplitude (for measurements done in non-contact mode) is recorded to map the contours of the surface. In both modes, the tip-sample distance is regulated in such a way that a feedback loop maintains a constant force between the tip and the sample [46].

The signal resulting from the change in the cantilever position or amplitude, which is needed to preserve a constant tip-sample distance (force), represents the surface topography [16, 46, 47, 48, 49]. The surface profile parameter that is of most interest in surface topography characterization is the amplitude or height profile, which provides details about the roughness of the surface [48, 49, 50]. The most common amplitude parameters are the average roughness (R_a) and the root mean square (RMS) roughness (R_q). R_a is defined as the arithmetical average of the deviation of all the height profile points from the mean plane, whereas R_q constitutes the average of the measured height deviations taken from the mean plane. The latter serves as the standard deviation of height profile values. Thus, it is more sensitive to large deviations from the mean plane which is assumed to be at zero [48, 49, 50, 51].

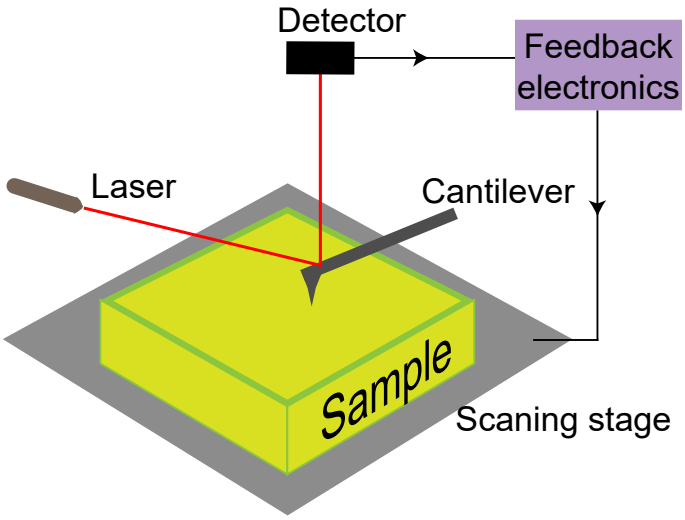

Figure 3.6: Schematics of the AFM experimental set-up. A laser focused on the back of a cantilever assists in measuring its deflection as the sample surface is scanned. The feedback electronics ensures a constant distance between the cantilever tip and the sample. The changes in the cantilever position are recorded to map the surface topography.

This parameter is the most considered in surface topography characterization. The maximum roughness peak height (R_p) which gives the height of the highest peak in the profile above the mean plane can also be taken into account in the analysis.

The surface morphology of a grown sample is also indicative of the growth mechanism as with RHEED intensity oscillations [24, 25, 26]. In addition to layer-by-layer and step-flow growth modes, a topographic AFM image can also tell if a growth follows step-bunching formation which is characterized by large terrace structures cross-faceting between neighboring step edges, or if it proceeds with the formation of 2D or 3D islands [25, 26]. Figure 3.7(a) shows a typical AFM image of a PLD fabricated $BaSnO_3$ (130 nm)/(Sr,Ba)SnO_3 (10 nm)/$SrTiO_3$ heterostructure [52]. It shows that, in the scanned area of 1×1 μm^2, the surface morphology of this sample is composed of step and terrace structures. The height profile (shown at the bottom of the AFM image), recorded along the white solid line across the AFM image, indicates that a step is 0.4 nm in height. As this value is consistent with the unit cell of the substrate, it is suggested that the sample growth proceeds mainly by a 2D step-flow mechanism [24, 25, 26]. In general, the terrace widths of the films are the same as those of the substrates in 2D step-flow growth mode [26]. To the contrary, the surface morphology in Fig. 3.7(b) which also shows step and terrace structures rather indicates a 2D layer-by-layer growth mode [24]. This is seen by the presence of 2D islands of different heights on the terraces. The heights of two islands given in the height profile are measured as indicated by the red and green markers along the solid black line across the AFM image. Figure 3.7(b) portrays the surface morphology at an early stage (about 30 s into the deposition) of the growth of a $SrRuO_3$ thin film on $SrTiO_3$ (001). As addressed in the RHEED section in Section 3.3.1, this growth progresses and transits to step-flow mode, marked by a film surface morphology that is quasi-identical to that of the $SrTiO_3$ (001) substrate (see Fig. 3.7(d)) [24]. The diverse growth mode observed in the $SrRuO_3$/$SrTiO_3$ heterostructure can also be found in heteroepitaxial growth of other complex materials [26].

The surface roughness of the epitaxially grown films usually presents a dependence on the thickness of the epitaxial layer. For instance, the variation of the RMS roughness with the thickness t of the $BaSnO_3$ buffer layer in a 0.5% La-$BaSnO_3$ (80 nm)/$BaSnO_3$ (80 nm)/$BaSnO_3$ (t)/(Sr,Ba)SnO_3 (10 nm)/$SrTiO_3$ heterostructure is illustrated in Fig. 3.7(c). It can be ob-

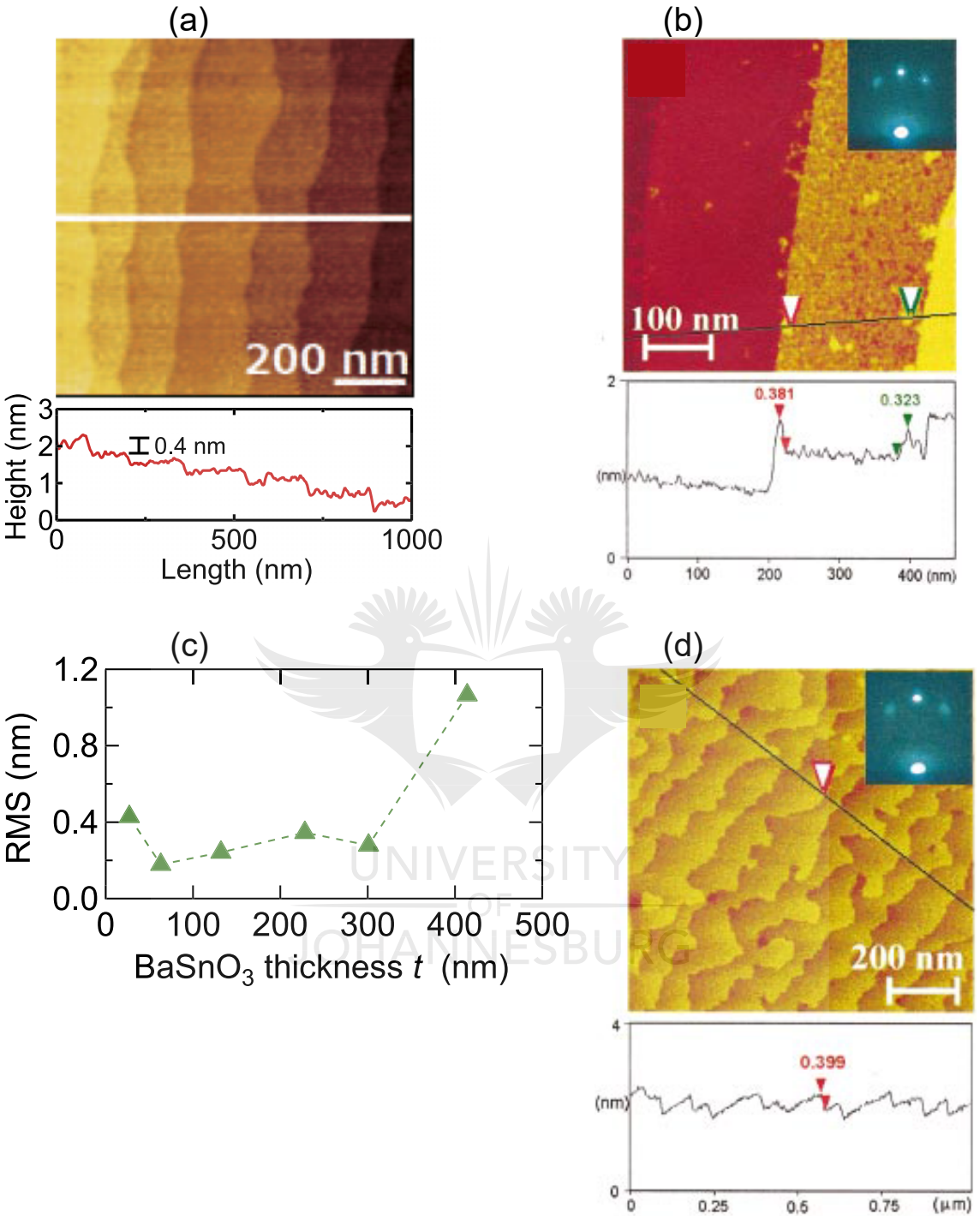

Figure 3.7: Typical AFM images of (a) $BaSnO_3$ (130 nm)/(Sr,Ba)SnO_3 (10 nm)/$SrTiO_3$, and (b) and (d) $SrRuO_3$/$SrTiO_3$ heterostructures. The surface height profiles shown at the bottom of the images are extracted from the solid lines (white and black) drawn on the AFM images. The surfaces present step and terrace structures. The insets in (b) and (d) represent the RHEED patterns associated with the AFM images. (c) RMS roughness as a function of the thickness t of the $BaSnO_3$ buffer layer in 0.5% La-$BaSnO_3$ (80 nm)/$BaSnO_3$ (80 nm)/$BaSnO_3$ (t)/(Sr,Ba)SnO_3 (10 nm)/$SrTiO_3$ heterostructure. The images in (a) and (c) were adapted from Ref. [52], and those in (b) and (d) were adapted from Ref. [24].

served in the figure that for good surface morphology, it is preferable to have $t < 300$ nm, since the RMS roughness drastically increases when the buffer layer t is greater than 300 nm [52].

b) Transmission Electron Microscopy

This technique is based on the transmission of a parallel beam of high energy electrons through a specimen which produces a magnified image of its internal structure [16]. The principle of the measurement method is illustrated in Fig. 3.8. The electrons beam emitted from the gun is accelerated perpendicularly towards the specimen by a high electric voltage generally 100 or 200 kV. Hence, these electrons have a wavelength described by Equation (3.1) that is much smaller than the typical spacing of atoms in a crystal, and therefore allows a high resolution imaging of the atomic arrangement [15]. The beam is concentrated and focused onto a precise area of the sample by a set of electromagnetic lenses (coils). As the specimen has been methodically prepared to be thin enough so that it is transparent to electrons, the beam is transmitted through and captures an image of the scanned region. This image (or transmitted beam) is then magnified by another lens, the projector lens, and made visible when it hits a fluorescent screen placed at the base of the system. In addition to the directly transmitted beam, the elastically and inelastically scattered electrons that arise from the interaction between the incident beam and the atoms of the sample can be recorded and analyzed.

TEM is an effective technique for the microstructural characterization of materials as depicted in Section 2.2.3. This measurement method provides information on the material structure, composition, bonding, strain and even lattice defects with an atomic resolution [53, 54, 55]. For instance, a high-resolution TEM (HRTEM) measurement helps to image the atomic structure of a sample. It consist of forming an image contrast that accounts for both the amplitude and phase of the diffracted beam. High-angle and medium-angle elastically scattered electrons can be collected using an annular dark field (ADF) detector to form Z-contrast imaging. This measurement is strongly sensitive to the atomic number Z of the elements, and thus to the

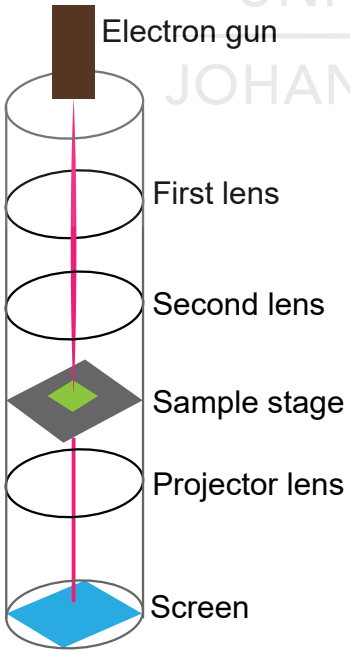

Figure 3.8: Schematics of the TEM experimental set-up. A beam of accelerated electrons is perpendicularly focused onto the sample by a set of coils. The electrons that are directly transmitted through the sample, as well as those that are elastically and inelastically scattered, are magnified by the projector lens and recorded on a fluorescent screen.

composition of the specimen or more precisely to the variations in impurity concentration. On the other hand, the analysis of the energy distribution of the electrons that have passed thorough the sample and suffered inelastic scattering can tell about the specimen chemistry, atomic electronic structure, valence state and thickness [56, 57]. This measurement technique is called electron energy-loss spectroscopy (EELS). A spectrometer mounted at the base of the TEM system records the inelastically scattered electrons and produces the spectrum of electron energy-loss. Furthermore, defects such as misfits and dislocations can be imaged at the atomic level by performing weak-beam dark field (WB-DF) or weak-beam bright field (WB-BF) TEM measurements. These measurements consist of forming diffraction images where the important detail contrasts transferred by weakly excited beams are provided in either bright field or dark field mode.

The TEM data presented in this thesis were acquired using state-of-the-art aberration-corrected TEM systems in the Stuttgart Center for Electron Microscopy (StEM), at the Max-Planck Institute for Solid State Research.

3.3.3 Magnetotransport Measurements

To investigate the electronic transport properties of the grown samples, their electrical characteristics such as the resistivity (ρ), the carrier density (n), and the electron mobility (μ) were studied. These parameters can be extracted from the Hall effect measurement, which is one of the most frequently employed electrical characterization technique of semiconductors [1, 58, 59, 60, 61]. The physical principle of the Hall effect consists of perpendicularly applying a magnetic field ($\mathbf{B}$) to a specimen across which a current is flowing. The presence of the transverse magnetic field generates a force known as the Lorentz force that deflects the moving electrons at right angles from the direction of the current. As a result, a voltage drop commonly called the Hall voltage (V_H) is induced perpendicularly to the current flow. The slope of $V_H(\mathbf{B})$ determines the Hall coefficient (R_H) from which n and then μ are extracted [61]. In the framework of this study, the Hall effect experiments were performed using a Quantum Design Physical Properties Measurement System (PPMS). To do so, we proceeded as follows: firstly, the samples were structured in the Van der Pauw geometry using Au contacts as can be seen in Fig. 3.9. Then, the conventional four-point probe method was applied on the Au contacts to measure the temperature dependence of the longitudinal (R_{xx}) and transversal or Hall (R_{xy}) resistances. Finally, the measured resistances were used to compute the transport characteristics (ρ, n and μ).

The sample structuring was performed following the photolithography process in a clean room. This process consisted of covering the entire surface of the samples with a negative photoresist (spin coating). Then the covered samples were heated on a hot plate and exposed to ultraviolet (UV) radiation. For UV irradiation, the samples were transferred into a mask aligner, where a mask with the desired structure was installed. The samples were slowly agitated in a solution of water and developer to remove the photoresist from the regions non-exposed to the UV radiation. After this process, thin metallic layers of Ti (5 nm) and Au (30 nm) were respectively evaporated on the patterned samples. The lift-off process that followed revealed the Au contacts on the sample as shown in Fig. 3.9 (corner and middle features at the surface). This process consisted of dissolving the photoresist, and thus the metallic layers on top, using a particular solution followed by ultrasonic bath in acetone and isopropanol. The structured samples were then connected to the sample holder pins using Al-wires bonded to the Au contacts (see Fig. 3.9), and introduced into the PPMS for measurement. An excitation current

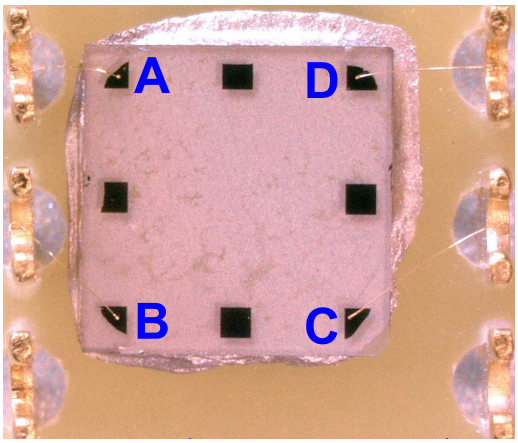

Figure 3.9: Sample structured in the Van der Pauw geometry, using metal contacts made of Au. The Au contacts are connected to the sample holder pins using Al-wires bonding. The electric connections at the corners of the sample labeled A, B, C and D were used for the measurement. The middle Au contacts were not used.

of 1 μA was injected into the sample during the measurements. R_{xx} and R_{xy} were each measured through two channels to obtain a more precise value of the resistances. For instance, to acquire R_{xx}, R_{xx1} and R_{xx2} were measured. For R_{xx1}, the current $I_{A\to B}$ was sent between the points A and B (vertical), and the voltage drop $V_{C\to D}$ between C and D was measured; and for R_{xx2}, the current was provided horizontally such that $I_{A\to D}$ was injected to measure $V_{C\to B}$. Similarly, to obtain R_{xy}, we measured R_{xy1} ($I_{A\to C}$; $V_{B\to D}$) and R_{xy2} ($I_{D\to B}$; $V_{A\to C}$). The longitudinal resistances (R_{xx1} and R_{xx2}) were measured as a function of the temperature (T). The values of the resistance were determined (by the PPMS) as the sample was cooled down from 300 K to 2 K at a rate of 2 K min^{-1}. As for the measurements of the Hall resistances (R_{xy1} and R_{xy2}), the magnetic field **B** was turned on. The values of the resistance were recorded as a function of **B** at a specific (fixed) temperature T. At a given T value, **B** was swept from 0 to 2 T, then from 2 T to -2 T and finally from -2 T to 0 at a rate of 0.067 T min^{-1}. In the end, the resistance values were such that $R_{xx} = \frac{R_{xx1}+R_{xx2}}{2}$ and $R_{xy} = \frac{R_{xy1}+R_{xy2}}{2}$. Hence, the resistivity was calculated as

$$\rho = \frac{\pi}{\ln 2} R_{xx} \times t, \tag{3.9}$$

where t is the thickness of the film layer. The Hall coefficient R_H, extracted from the slope of R_{xy} as $R_{H_T} = \text{slope}_{R_{xy}} \times t$ was used to compute the carrier density and mobility respectively as

$$n_T = \frac{1}{qR_{H_T}} \tag{3.10}$$

and

$$\mu_T = \frac{R_{H_T}}{\rho}. \tag{3.11}$$

The subscript T in Equations (3.10) and (3.11) indicates that R_{H_T}, n_T and μ_T are obtained at a constant temperature T. It is noteworthy that n and μ were calculated in the units of cm^{-3} and cm^2 V^{-1} s^{-1}, respectively.

3.3.4 Spectroscopic Techniques

The surface atomic composition, the chemical state of the elements, and the electronic band structure (valence band structure) of the grown films were investigated using two spectroscopic techniques, XPS and ARPES. These techniques are based on the photoelectric effect (excitation of electrons with photons), and were performed in a UHV system [62, 63, 64]. As depicted in Fig. 3.10, photons from a monochromatic light source emitted with the energy $h\nu$, impinge on the surface of a sample, interact with the electrons from the sample and transfer their energy. The photoexcited electrons gain a certain kinetic energy, overcome the sample surface potential barrier and are ejected to the vacuum (Fig. 3.10(a)). An electron analyzer collects the photoemitted electrons. These electrons should reach the analyzer without colliding with particles from the surrounding, as this would result in scattering processes and subsequent alteration of their kinetic energy [63]. Thus, UHV (pressure ranging from 10^{-9} to 10^{-12} mbar) conditions are required in the photoemission process. The photoexcitation process can be mathematically written as [63, 65]

$$h\nu = \mathrm{E_{kin}} + \mathrm{E_b} + \phi_\mathrm{a}. \tag{3.12}$$

Equation (3.12) describes the energy conservation law. It means that an electron is removed from the sample and measured by the electron analyzer only if the excitation photon has an energy equal to the sum of its kinetic ($\mathrm{E_{kin}}$) and binding ($\mathrm{E_b}$) energies and the work function (ϕ_s) of the sample (see Fig. 3.10(a)). The $\mathrm{E_{kin}}$ of the photoelectrons is determined by the analyzer, and with the help of Equation (3.12), the value of $\mathrm{E_b}$ is found. In practice, sample and analyzer are in electrical contact via ground connections so that their Fermi levels are at the same energy level. This ensures, after some mathematical considerations, that the work function of the analyzer (ϕ_a) is considered in Equation (3.12) instead of ϕ_s, which would

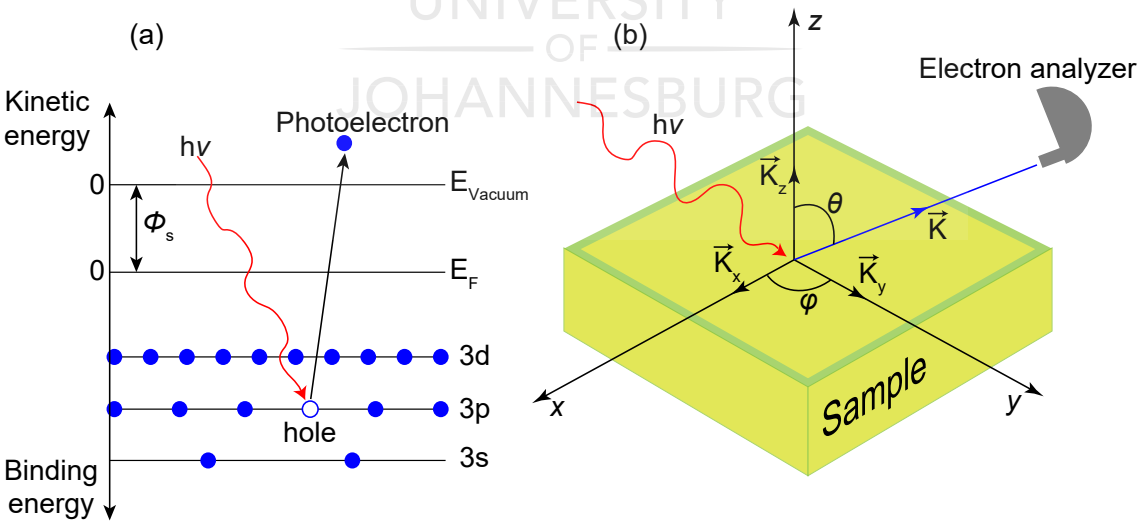

Figure 3.10: Schematics of the spectroscopic experiments. (a) Energetic diagram of the photoexcitation process involving the energy levels within the sample. (b) Photoexcitation process viewed from the sample surface. This geometry is consistent with an ARPES experiment where the emission angle, θ, as well as the sample rotation angle, φ, are considered in the photoemission.

require extra measurements and recalibration of the analyzer for each specimen loaded into the system.

The photoemission process is physically discussed within the three-step and one-step models. In the three-step model approach, the process is divided into three steps consisting of [66, 67, 68, 69]: 1- the photoexcitation of a bulk electron leading to the creation of a photoelectron; 2- the travel of the photoelectron to the surface of the crystal; and 3- emission of the photoelectron into vacuum after transmission through the surface potential barrier. To each of these steps, a probability of occurrence is associated. The total photoemission intensity which is a function of the E_{kin} of the photoelectron and the energy $h\nu$ of the photon would then be proportional to the product of these probabilities. This model treats a single electron in the system transitioning from its initial to its final eigenstates upon excitation, and does not account for the interaction between the electron leaving the material and those left behind. Although phenomenological, this model has been successful in describing the photoemission process for several decades. However, with quantum mechanical considerations, the photoemission process should not be expressed as separate and independent events, but rather as a one-step process [65, 70]. This approach is more realistic as it takes into account correlation effects due to interactions in the many-body system. The photoemission process is then fully described by the transition probability for an excitation between N-electron eigenstates (initial state) and one of the probable ionized $(N-1)$-electron eigenstates (final state). Here, the transition probability is defined with the consideration that for an electron to be emitted in vacuum, both the energy and momentum of the incident photon and the system of N-electron are conserved, and there is a finite overlap between initial and final state amplitudes. The photoemission process, especially within the one-step approach, is a complex physical phenomenon. The complete mathematical description of the theory behind it requires more complex quantum mechanical tools, and is described fully in Refs [66, 67, 68, 69, 70] if the reader should need this.

a) X-ray Photoemission Spectroscopy

In photoexcitation processes using X-rays, the impinging photon has enough energy to excite both the inner shell electrons (core electrons) and the outermost shell electrons (valence electrons) [63, 71]. The data delivered to the user are comprehensively governed by Equation (3.12). The analyzer collects the photoemitted electrons and measures their kinetic energies. Based on Equation (3.12), the acquisition software converts these energies into binding energies since the photon energy $h\nu$ and the work function ϕ_a are known. Thus, the XPS spectrum which is an $x-y$ plot of the intensities of the photoelectrons versus their kinetic or binding energies can be obtained. A typical XPS spectrum is composed of features such as the main core level peak(s) corresponding to the signature of a particular element (or particular elements depending on the range of electron energy scanned) in the specimen, the Auger peak(s) (not always), the background and the satellite peak(s) (not always).

The core level peak appears at a particular energy and is associated with the actual elemental (chemical) composition of the sample. However, to extract information such as atomic ratio, chemical environment and chemical bonds from a raw core electron spectrum, a systematic peak analysis much be carried out. Firstly, the background noise that may contribute to distorting the core peak at its extreme bottoms and introduce asymmetry must be subtracted from the main signal. There are several types of background subtraction that are commonly applied to an XPS spectrum during data analysis [63, 71]. For the analysis of the XPS data obtained as part of this thesis, the Shirley background subtraction method was used to account

for the effect of inelastic scattering of photoelectrons [100, 101]. Secondly, an appropriate fit function should be applied to the peak line shape, in order to identify all the components that contribute to the photoemission peak signal. There are also several peak line shape fitting functions that are usually employed in data analysis [71]. The Voigt function [102] was used to fit the spectra. The Voigt function is the convolution of the Gaussian and the Lorentzian distributions. It simultaneously takes into account the instrumental resolution and the lifetime broadening due to the filling of the core hole caused by the photoemission process by a secondary electron.

In XPS measurements, both the photoemitted and Auger electrons can be collected. For example, in the situation illustrated at the energy level in Fig. 3.10(a), an electron from the 3p orbital of the M shell is photoexcited and emitted from the atom leaving a hole (core hole) at this energy level. The system (in this case an atom) is then in an excited state (Koopmans' state [72]). To return to the ground state, an electron from the 3d orbital or a higher shell descents into the hole. The falling electron gives its energy (which is equivalent to the energetic separation between the two levels) to another electron which also leaves the atom. This process is the Auger effect, and the electrons that are ejected through such transitions are referred to as Auger electrons [63, 71, 73, 74].

The background represents the noise due to secondary electrons. These are electrons that have lost part of their energy in the photoemission process as a result of scattering processes (electron-electron and electron-phonon interactions) [63, 71, 74]. Indeed, XPS is a very surface sensitive method, as the depth below the surface from which the electrons can freely escape (without suffering inelastic scattering) is small ($\leq$ 10 nm) [71]. This is because the inelastic mean free path of the electron (photoelectron) at these energies is very small (0.4 nm on average [71]). Thus, the electrons in the photoemission spectrum containing valuable information about the specimen originate from the topmost surface layers.

A satellite structure originates from the photoionization of a core electron, and does not always appear in an XPS spectrum. However, when it occurs, it is seen as a peak a few eV to the higher binding energy side of the expected core level [75, 76, 77, 78]. The ionization of a core electron induces a perturbation in the energy levels of the atom, and is accompanied by several electronic effects [63, 76, 77, 78, 79]. For instance, following the formation of a core hole (positively charged), the valence electrons (outermost shell) often relax to compensate for the sudden change in the effective charge due to the loss of a shielding electron [73]. The core electron leaving the atom can interact with these relaxing electrons and lose some kinetic energy in the process [71, 73]. The system is then forced into an excited state, hence the formation of features at higher binding energies called shake-up satellites [71, 73, 80, 81]. This interaction could also result in the excitation and ejection of the valence electrons from the system to the continuum giving rise to shake-off satellites [71, 73, 80, 81].

Another category of satellites that arise from the photoionization of core electrons are plasmon satellites, which are associated with the collective excitations of the valence band electrons [82, 83]. There are two types of plasmon excitations, namely intrinsic and extrinsic plasmons. As mentioned before, the excitation of a core electron is accompanied by the sudden creation of a core hole. Intrinsic plasmons synchronously arise with the creation of the core hole, whereas extrinsic plasmon excitations are due to inelastic scattering events associated with the propagation of the photoelectron through the atom [82, 84]. The Coulomb potential of the core hole in the ionized atom creates a localized trap state that is screened by the conduction

electrons [85, 86, 87]. This results in a situation whereby two possible final states are accessible. If the localized state remains empty, the final state is referred to as unscreened. On the other hand, if the localized state is filled by transfer of an electron from the conduction band, the final state is referred to as screened [88, 89]. Such satellite structures have been extensively reported in core XPS spectra of transparent conducting oxides (TCOs) [83, 88, 89, 90, 91, 92, 93, 94], assuming that the unrelaxed Koopmans' state resulting from the removal of a core electron is not an eigenstate of the ionized atom, and should rather be projected onto screened and unscreened final eigenstates [83]. Furthermore, the plasmon energies in TCOs are mostly around 0.7 eV, comparable with intrinsic core electron line widths [89, 92]. Thus, a plasmon satellite structure is expected to overlap the core electron feature, resulting in a spectrum with an asymmetric line shape [88, 89, 92]. In the model developed to describe these satellites, it was found that the screened final state is the lower binding energy component with a dominant Gaussian character (narrower), and the unscreened state is a broader component at higher binding energy whose Lorentzian line width is determined by the scattering rate of the conduction electrons [83, 88, 89, 95].

Early in the application of photoemission techniques to simple metallic systems, it was found that plasmon satellites can significantly contribute to the structure of the core levels in XPS spectra [96]. Hence, the early research efforts in this area were oriented toward unraveling the relative contributions of extrinsic and intrinsic structure and toward rationalizing the pattern of multiple plasmon excitations [96]. A weak coupling model was developed several decades ago by Langreth suggesting that the intensity of the intrinsic plasmon satellite, I, should increase as the density of the conduction electrons (n) decreases according to the expression $I \propto n^{-1/3}$ [86, 97].

All the spectroscopic features described above are illustrated in the photoemission spectra shown in Fig. 3.11. Figure 3.11(a) represents an XPS spectrum acquired in the binding energy range from 760 eV to 818 eV on a cobalt film sublimated under high vacuum on a silicon wafer and exposed to an oxygen environment [98]. It is a scan around the Co 2p core level excited with a Mg K_α source producing photons with the energy of 1253.6 eV. Looking at the figure, it can be observed that in the energy range scanned, the expected main core peaks, Co $2p_{\frac{3}{2}}$ and Co $2p_{\frac{1}{2}}$, are present. Note that Co 2p is split into Co $2p_{\frac{3}{2}}$ and Co $2p_{\frac{1}{2}}$ due to the spin orbit coupling of the 2p orbital. The background feature is indicated by the black arrows in the figure. This background is fitted together with the peaks in the Co 2p spectrum. The Auger signals corresponding to electrons transitioning from V to K shells of the O 1s core level (shown in the inset) are also seen in the spectrum. Two satellite features associated with the excitation of the 2p orbital are also formed as labeled in the figure. These are shake-up satellites [71, 82].

Plasmon satellite structures are visible in the hard X-ray photoemission spectroscopy (HAXPES) spectra of In $3d_{\frac{5}{2}}$ core levels shown in Figs. 3.11(b) and 3.11(c). These are spectra measured at the photon energy of 8000 eV on amorphous In_2O_3–ZnO thin films deposited by dc magnetron sputtering on quartz glass substrates [92]. The sample in Fig. 3.11(b) labeled **S1** exhibits an electron density of 4.76×10^{20} cm^{-3}, whereas the sample in Fig. 3.11(c) labeled **S2** has a lower electron concentration of 0.80×10^{20} cm^{-3} [92]. The plasmon satellites are the peaks with the Lorentzian line shape (red dashed curves) at higher binding energies in the photoemission spectra. These satellites originate from the strong asymmetry in the In 3d core lines. This asymmetry is due to the interaction between the core holes and the conduction

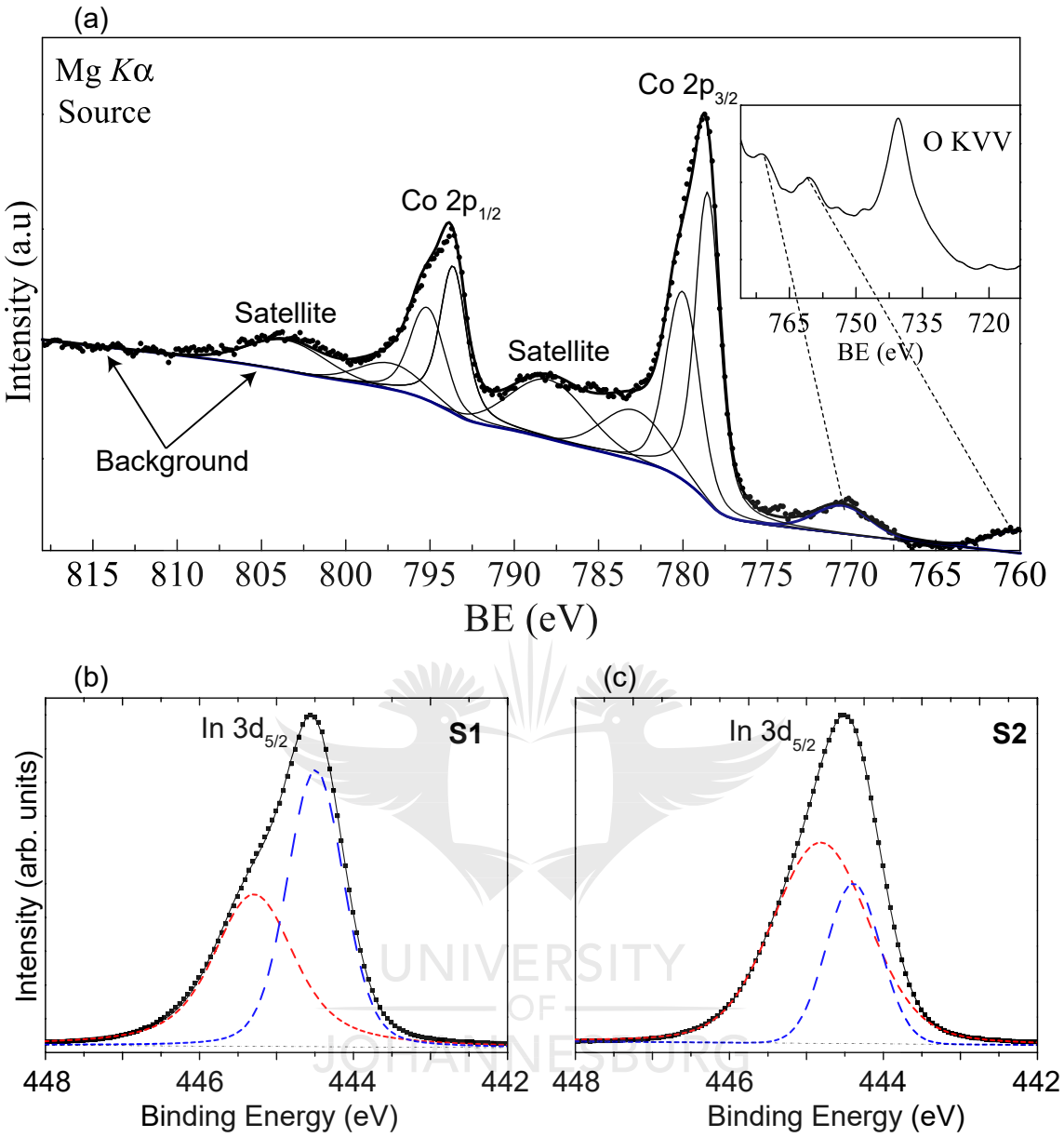

Figure 3.11: (a) XPS spectrum of Co 2p region measured with a Mg K_α source producing photons of 1253.6 eV. BE stands for binding energy. The inset shows the Auger electrons of O 1s. (b) HAXPES spectra around the In $3d_{\frac{5}{2}}$ core level measured with a photon energy of 8000 eV. The blue and red dashed curves are the screened and unscreened components, respectively, associated with the photoionization of In 3d core electrons. The image in (a) was adapted from Ref. [98], and those in (b) and (c) were adapted from Ref. [92].

electrons. Thus, as mentioned above, this gives rise to the broader satellite components on the high binding energy sides associated with unscreened final states [92]. The blue dashed narrower curves located at low binding energies are the main peaks corresponding to screened final states [92]. Moreover, it can be observed from the figures that the relative intensity of the screened state (blue dashed curve) decreases with decreasing carrier density (from **S1** to **S2**). Concomitantly, the relative intensity of the unscreened state (red dashed curve) increases

when the number of conduction electron decreases (also from **S1** to **S2**), in accord with the Langreth model. This would suggest that in the limit of zero carrier concentration, only the unscreened state will be present [88], and the peak will exhibit a perfectly symmetric line shape as observed in the XPS spectra of Sn 3d core levels of insulting materials [83, 89, 99].

b) Angle Resolved Photoemission Spectroscopy

As for the ARPES technique, in addition to Equation (3.12), the geometry of the experiment i.e. emission angle (θ) of the photoelectrons and sample rotation angle (φ) about the polar axis (z-axis) should be taken into consideration (see Fig. 3.10(b)). This allows the momentum of the electrons in vacuum to be measured. In an ARPES experiment, the excitation source (UV light) is used to excite the valence electrons. The experiment is thus dedicated to mapping the electronic band structure of the specimen, since the density of states of the electrons in the sample is given by the valence band region. To map the electronic band structure of a crystal using ARPES, the dispersion relation between the binding energy and the momentum $\vec{k}$ of the electron propagating inside the solid should be measured. This can be achieved using the E_{kin} measured for the photoelectrons together with their momentum $|\vec{K}| = \frac{\sqrt{2mE_{kin}}}{\hbar}$ in vacuum; where $\hbar$ is the reduced Planck constant. As can be observed in Fig. 3.10(b), the momentum (or wave vector) $\vec{K}$ has three components $\vec{K}_x$, $\vec{K}_y$ and $\vec{K}_z$, such that [65, 70]

$$|\vec{K}| = \begin{cases} K_x &= \frac{\sqrt{2mE_{kin}}}{\hbar} \sin\theta\cos\varphi \\ K_y &= \frac{\sqrt{2mE_{kin}}}{\hbar} \sin\theta\sin\varphi \\ K_z &= \frac{\sqrt{2mE_{kin}}}{\hbar} \cos\theta; \end{cases} \tag{3.13}$$

and its components parallel and perpendicular to the specimen surface are given by $\vec{K}_{\parallel} = \vec{K}_x + \vec{K}_y$ and $\vec{K}_{\perp} = \vec{K}_z$ respectively. The parallel component of the momentum is conserved due to the translational symmetry in the plane across the surface [65]. This is translated as the parallel component $\vec{k}_{\parallel}$ of the electrons momentum inside the sample is equal to that of the photoelectrons in vacuum, $\vec{k}_{\parallel} = \vec{K}_{\parallel}$, and given by [65, 70]

$$|\vec{k}_{\parallel}| = |\vec{K}_{\parallel}| = \frac{\sqrt{2mE_{kin}}}{\hbar} \sin\theta. \tag{3.14}$$

Equation (3.14) is the dispersion relation used in ARPES experiment to map the electronic band structure of solids [65]. A typical ARPES spectrum consists of a 2D snapshot of the energy (E_b) versus momentum. Note that E_b can be incorporated into the dispersion relation using the energy conservation law given in Equation (3.12). To analyze the ARPES data, momentum scans at constant energy values representing momentum distribution curves (MDC) and energy scans at constant momentum values defining energy distribution curves (EDCs) are employed. They help in extracting information about the electronic band structure such as the energy and momentum positions of both the VBM and the CBM, and the size and nature of the band gap.

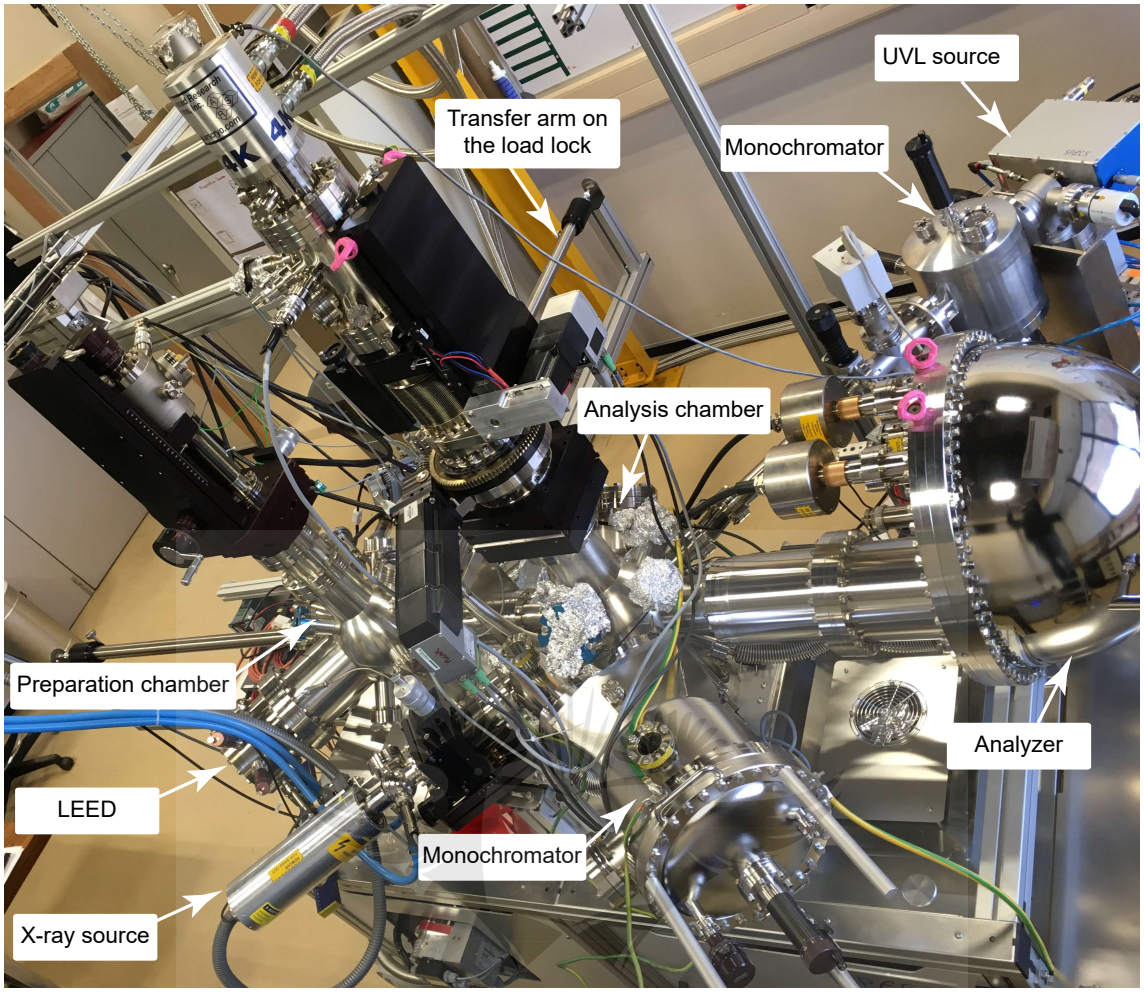

Figure 3.12: Photograph of the spectroscopic chamber available at the University of Johannesburg. The system is equipped with two chambers, the preparation chamber and the analysis chamber, an hemispherical electron energy analyzer, a LEED optics, two photon sources with monochromators for XPS and ARPES measurements, and a load lock through which the samples are loaded into the system. Two transfer arms help to move the samples from the load lock to the preparation chamber, and from the preparation chamber to analysis chamber. The base pressures in the load lock, the preparation and the analysis chambers are $\approx 1\times10^{-8}$ mbar, $\approx 7\times10^{-11}$ mbar and $\approx 3\times10^{-10}$ mbar, respectively. The vacuum is maintained with the help of several turbo pumps and an ion pump in the analysis chamber.

The XPS and ARPES data presented in this work were acquired in the *Electronic Structure Studies Research Group* at the University of Johannesburg (UJ). The samples were grown at the Max-Planck Institute for Solid State Research in Stuttgart, Germany, and transported "in air" to our facility at UJ where the spectroscopic measurements were conducted. XPS and ARPES are surface sensitive techniques probing only the very top surface layers. To efficiently quantify the fraction of each element in the films, access all the states in the valence band and determine the electronic band structure, the samples had to be systematically cleaned in vacuum to remove any surface contamination. The cleaning procedure consisted of annealing in oxygen environment at the temperature of about 700 °C, then performing LEED measurements, and finally running XPS acquisitions of the C 1s region. These are done to verify the surface quality. C 1s was the only foreign element at the surface of the films studied. The annealing

was done for an average time of 2 hours using an e-beam heater. A high voltage of 1 kV was applied to the filament to accelerate the electrons. The emitted electrons directly hit the back side the molybdenum sample holder on which the sample was clamped. The maximum power on the sample holder was 3.5 W. The temperature was indicated by a pyrometer set at an emissivity of 0.1. The surface treatment was conducted in the preparation chamber where the vacuum pressure was $\approx 7\times10^{-6}$ mbar (with oxygen flow), and included several cycles of annealing. The XPS and ARPES measurements were performed in the UHV analysis chamber where the base pressure was $\approx 3\times10^{-10}$ mbar.

Figure 3.12 shows the spectroscopic equipment available at UJ. It comprises two photon sources, the X-ray source and the UV light (UVL) source. The X-ray system is equipped with both Al and Ag anodes, and a monochromator; it can produce photons of 1486.71 eV (Al K_α) and 2984.31 eV (Ag L_α). The UVL system also comprises a monochromator and can deliver photons of 21.2 eV (He I) and 40.8 eV (He II). The analyzer is a PHOIBOS 150 hemispherical electron energy analyzer operating at constant pass energy, and equipped with a microchannel plate detector and a CCD camera.

3.4 Concluding Comments

This chapter covered the technical section of this thesis. It provides an overview of the experimental techniques that were used to grow and analyze the properties of La-doped $BaSnO_3$ thin films. It was decided not to cover in too much depth the concepts related to the theory and the instrumentation of the measurement techniques employed in this study. These techniques are properly referenced in the text, should the reader be interested to go more in-depth. However, we presented in detail the key elements that will help the reader to understand the results shown in this work.

Bibliography

[1] S. Kasap, and P. Capper, *Springer Handbook of Electronic and Photonic Materials* (Springer, Gewerbestraße, 2017).

[2] P. R. Willmott, and J. R. Huber, Rev. Mod. Phys. **72**, 315 (2000).

[3] D. B. Chrisey, and G. K. Hubler, *Pulsed Laser Deposition of Thin Films* (John Wiley, New York, 1994).

[4] B. Shin, and M. J. Aziz, Phys. Rev. B **76**, 085431 (2007).

[5] B. Shin, J. P. Leonard, J. W. McCamy, and M. J. Aziz, Appl. Phys. Lett. **87**, 181916 (2005).

[6] P. Ohresser, J. Shen, J. Barthel, M. Zheng, C. V. Mohan, M. Klaua, and J. Kirschner, Phys. Rev. B **59**, 3696 (1999).

[7] H. Koinuma, and I. Takeuchi, Nat. Mater. **3**, 429 (2004).

[8] P. M. Ossi, *Advances in the Application of Lasers in Materials Science* (Springer, Gewerbestraße, 2018).

[9] M. Jäger, A. Teker, J. Mannhart, and W. Braun, Appl. Phys. Lett. **112**, 111601 (2018).

[10] W. Braun, M. Jäger, G. Laskin, P. Ngabonziza, W. Voesch, P. Wittlich, and J. Mannhart, APL Mater. **8**, 071112 (2020).

[11] W.-J. Lee, H. Lee, K.-T. Ko, J. Kang, H. J. Kim, T. Lee, J.-H. Park, and K. H. Kim, Appl. Phys. Lett. **111**, 231604 (2017).

[12] M. Kawasaki, K. Takahashi, T. Maeda, R. Tsuchiya, M. Shinohara, O. Ishiyama, T. Yonezawa, M. Yoshimoto, and H. Koinuma, Science 266, **1540** (1994).

[13] G. Koster, B. L. Kropman, G. J. Rijnders, D. H. Blank, and H. Rogalla, Appl. Phys. Lett. **73**, 2920 (1998).

[14] G. Koster, B. L. Kropman, G. J. Rijnders, D. H. Blank, and H. Rogalla, Mater. Sci. Eng. B **56**, 209 (1998).

[15] A. Patané, and N. Balkan, *Semiconductor Research* (Springer, New York, 2012).

[16] N. V. Richardson, and S. Holloway, *Handbook of Surface Science: Physical Structure. Ed. by W. N. Unertl* (Elsevier, North Holland, 1996).

[17] M. Razeghi, *Fundamentals of Solid State Engineering* (Springer, Gewerbestraße , 2006).

[18] M. A. Van Hove, and S. Y. Tong, *Surface Crystallography by LEED: Theory, Computation and Structural Results* (Springer, Berlin, 2012).

[19] C. Chen, J. Avila, E. Frantzeskakis, A. Levy, and M. C. Asensio, Nat. Commun. **6**, 8585 (2015).

[20] H. Paik, Z. Chen, E. Lochocki, H. Ariel Seidner, A. Verma, N. Tanen, J. Park, M. Uchida, S. Shang, B. C. Zhou, M. Brützam, R. Uecker, Z. K. Liu, D. Jena, K. M. Shen, D. A. Muller, and D. G. Schlom, APL Mater. **5**, 116107 (2017).

[21] H. Lüth, *Solid Surfaces, Interfaces and Thin Films* (Springer, New York, 2015).

[22] M. A. Van Hove, W. H. Weinberg, and C. M. Chan, *Low-Energy Electron Diffraction: Experiment, Theory and Surface Structure Determination* (Springer, Berlin, 2012).

[23] P. K. Larsen, and P. J. Dobson, *Reflection High-Energy Electron Diffraction and Reflection Electron Imaging of Surfaces* (Springer, Boston, 2012).

[24] J. Choi, C. B. Eom, G. Rijnders, H. Rogalla, and D. H. A. Blank, Appl. Phys. Lett. **79**, 1447 (2001).

[25] F. Sánchez, M. V. García-Cuenca, C. Ferrater, M. Varela, G. Herranz, B. Martínez, and J. Fontcuberta, Appl. Phys. Lett. **83**, 902 (2003).

[26] W. Hong, H. N. Lee, M. Yoon, H. M. Christen, D. H. Lowndes, Z. Suo, and Z. Zhang, Phys. Rev. Lett. **95**, 095501 (2005).

[27] A. Prakash, J. Dewey, H. Yun, J. S. Jeong, K. A. Mkhoyan, and B. Jalan, J. Vac. Sci. Technol. A **33**, 060608 (2015).

[28] Z. Lebens-Higgins, D. O. Scanlon, H. Paik, S. Sallis, Y. Nie, M. Uchida, N. F. Quackenbush, M. J. Wahila, G. E. Sterbinsky, D. A. Arena, J. C. Woicik, D. G. Schlom, and L. F. Piper, Phys. Rev. Lett. **116**, 027602 (2016).

[29] M. Lee, *X-ray Diffraction for Materials Research: From Fundamentals to Applications* (CRC Press, Waretown, 2016).

[30] W. H. Bragg, and W. L. Bragg, Proc. R. Soc. Lond. A **88**, 428 (1913).

[31] C. Suryanarayana, and M. G. Norton, *X-ray Diffraction: A Practical Approach* (Plenum Press, New York and London, 1998).

[32] W. L. Bragg, *The Crystalline State: Volume I* (The Macmillan Company, New York, 1934).

[33] Y. Waseda, E. Matsubara, and K. Shinoda, *X-ray Diffraction Crystallography: Introduction, Examples and Solved Problems* (Springer, Berlin, 2011).

[34] A. Prakash, P. Xu, A. Faghaninia, S. Shukla, J. W. Ager, C. S. Lo, and B. Jalan, Nat. Commun. **8**, 15167 (2017).

[35] J. Shiogai, K. Nishihara, K. Sato, and A. Tsukazaki, AIP Adv. **6**, 065305 (2016).

[36] S. Raghavan, T. Schumann, H. Kim, J. Y. Zhang, T. A. Cain, and S. Stemmer, APL Mater. **4**, 016106 (2016).

[37] P. R. Berger, K. Chang, P. Bhattacharya, J. Singh, and K. K. Bajaj, Appl. Phys. Lett. **53**, 684 (1988).

[38] D. A. King, and D. P. Woodruff, *Growth and Properties of Ultrathin Epitaxial Layers* (Elsevier, North Holland, 1997).

[39] M. Kneiß, P. Storm, A. Hassa, D. Splith, H. von Wenckstern, M. Lorenz, and M. Grundmann, APL Mater. **8**, 051112 (2020).

[40] J. P. Bosco, G. M. Kimball, N. S. Lewis, and H. A. Atwater, J. Cryst. Growth **363**, 205 (2013).

[41] M. Huijben , G. Koster , D. H. A. Blank, and G. Rijnders, Phase Transit. **81**, 703 (2008).

[42] P. Kidd, *XRD of gallium nitride and related compounds: strain, composition and layer thickness*, (Panalytical: Almelo, Netherlands, 2009).

[43] H. J. Cho, T. Onozato, M. Wei, A. Sanchela, and H. Ohta, APL Mater. **7**, 022507 (2019).

[44] J. I. Langford, and A. J. C. Wilson, J. Appl. Cryst. **11**, 102 (1978).

[45] P. Scherrer, Nachr. Ges. Wiss. Göttingen **26**, 98 (1918).

[46] B. Voigtländer, *Atomic Force Microscopy* (Springer, Gewerbestraße, 2019).

[47] G. Binnig, and C. F. Quate, Phys. Rev. Lett. **56**, 930 (1986).

[48] A. Méndez-Vilas, and J. Díaz, *Modern Research and Educational Topics in Microscopy* (Formatex Research Center, Badajoz, 2007).

[49] E. S. Gadelmawla, M. M. Koura, T. M. A. Maksoud, M. Elewa, and H. H. Soliman, J. Mater. Process. Technol. **123**, 133 (2002).

[50] B. Bhushan, *Modern Tribology Handbook, Two Volume Set* (CRC Press, Boca Raton, 2000).

[51] A. Maksumov, R. Vidu, A. Palazoglu, and P. Stroeve, J. Colloid Interface Sci. **272**, 365 (2004).

[52] J. Shiogai, K. Nishihara, K. Sato, and A. Tsukazaki, AIP Adv. **6**, 065305 (2016).

[53] D. B. Williams, and C. B. Carter, *Transmission Electron Microscopy: A Textbook for Materials Science* (Springer, New York, 2009).

[54] Z. Luo, *A Practical Guide to Transmission Electron Microscopy: Fundamentals* (Momentum Press, New York, 2016).

[55] G. H. Michler, *Electron Microscopy of Polymers* (Springer, Berlin, 2008).

[56] R. F. Egerton, Rep. Prog. Phys. **72**, 016502 (2009).

[57] H. Ibach, and D. L. Mills, *Electron Energy Loss Spectroscopy and Surface Vibrations* (Academic Press, New York, 1982).

[58] J. W. Orton, and P. Blood, *The Electrical Characterization of Semiconductors: Measurement of Minority Carrier Properties, Volume 1* (Academic Press, New York, 1990).

[59] P. Blood, and J. W. Orton, *The Electrical Characterization of Semiconductors: Majority Carriers and Electron States, Volume 2* (Academic Press, New York, 1992).

[60] D. K. Schroder, *Semiconductor Material and Device Characterization* (John Wiley & Sons, Inc., Hoboken, 2006).

[61] E. N. Kaufmann, *Characterization of Materials* (John Wiley & Sons, Inc., Hoboken, 2012).

[62] P. Van der Heide, *X-ray Photoelectron Spectroscopy. An Introduction to Principles and Practices* (John Wiley & Sons, Hoboken, 2012).

[63] S. Hofmann, *Auger-and X-ray Photoelectron Spectroscopy in Materials Science: A User-Oriented Guide* (Springer Science & Business Media, Heidelberg, 2012).

[64] V.I. Nefedov, *X-Ray Photoelectron Spectroscopy of Solid Surfaces* (CRC Press, Waretown, 1988).

[65] A. Damascelli, Phys. Scr. **T109**, 61 (2004).

[66] P. J. Feibelman, and D. E. Eastman, Phys. Rev. B **10**, 4932 (1974).

[67] H. Y. Fan, Phys. Rev. **68**, 43 (1945).

[68] C. N. Berglund, and W. E. Spicer, Phys. Rev. **136**, A1030 (1964).

[69] S. K. Sharma, D. S. Verma, L. U. Khan, S. Kumar, and S. B. Khan, *Handbook of Materials Characterization* (Springer, Cham, 2018).

[70] A. Damascelli, Z. Hussain, and Z.-X. Shen, Rev. Mod. Phys. **75**, 473 (2003).

[71] J. A. C. Santana, *Quantitative Core Level Photoelectron Spectroscopy* (Morgan & Claypool Publishers, San Rafael, USA, 2016).

[72] T. Koopmans, Physica **1**, 104 (1934).

[73] P. Persson, S. Lunell, A. Szöke, B. Ziaja, and J. Hajdu, Protein Sci. **10**, 2480 (2001).

[74] J. W. Niemantsverdriet, *Spectroscopy in Catalysis: An Introduction* (John Wiley & Sons, Verlag, 2007).

[75] C. G. Allen, and P. M. Tucker, Chem. Phys. Lett. **43**, 254 (1976).

[76] G. K. Wertheim, and A. Rosencwaig, Phys. Rev. Lett. **26**, 1179 (1971).

[77] M. O. Krause, T. A. Carlson, and K. D. Dismukes, Phys. Rev. **170**, 37 (1968).

[78] T. Novakov, Phys. Rev. B **3**, 2693 (1971).

[79] K. Siegbahn, C. Nordling, G. Johansson, J. Hedman, P. F. Heden, K. Hamrin, U. Gelius, T. Bergmark, L. O. Werme, R. Manne, and Y. Baer, *ESCA applied to free molecules* (North Holland, Amsterdam, 1969).

[80] G. B. Armen,T. Åberg, Kh. R. Karim, J. C. Levin, B. Crasemann, G. S. Brown, M. H. Chen, and G. E. Ice, Phys. Rev. Lett. **54**, 182 (1985).

[81] S. Svensson, B. Eriksson, N. Martensson, G. Wendin, and U. Gelius, J. Elec. Spec. Rel. Phenom. **47**, 327 (1988).

[82] https://fdocuments.in/document/x-ray-photoelectron-spectroscopy-xps-2-scudierodocuments571-xps-lecture2003pdfx-ray.html.

[83] R. G. Egdell, J. Rebane, T. J. Walker, and D. S. L. Law, Phys. Rev. B **59**, 1792 (1999).

[84] J.-J. Chang, and D. C. Langreth, Phys. Rev. B **8**, 4638 (1973).

[85] M. Campagna, G. K. Wertheim, H. R. Shanks, F. Zumsteg, and E. Banks, Phys. Rev. Lett. **34**, 738 (1975).

[86] J. N. Chazalviel, M. Campagna, and G. K. Wertheim, Phys. Rev. B **16**, 697 (1977).

[87] G. K. Wertheim, Chem. Phys. Lett. **65**, 377 (1979).

[88] C. Körber, V. Krishnakumar, A. Klein, G. Panaccione, P. Torelli, A. Walsh, J. L. F. Da Silva, S.-H. Wei, R. G. Egdell, and D. J. Payne, Phys. Rev. B **81**, 165207 (2010).

[89] R. G. Egdell, T. J. Walker, and G. Beamson, J. Electron Spectrosc. Relat. Phenom. **128**, 59 (2003).

[90] V. Christou, M. Etchells, O. Renault, P. J. Dobson, O. V. Salata, G. Beamson, and R. G. Egdell, J. Appl. Phys. **88**, 5180 (2000).

[91] R. G. Egdell, W. R. Flavell, and P. Taverner, J. Solid State Chem. **51**, 345 (1984).

[92] J. Jia, N. Oka, and Y. Shigesato, J. Appl. Phys. **113**, 163702 (2013).

[93] P. A. Cox, R. G. Egdell, C. Harding, A. F. Orchard, W. R. Patterson, and P. J. Tavener, Solid State Commun. **44**, 837 (1982).

[94] J. J. Mudd, T.-L. Lee, V. Muñoz-Sanjosé, J. Zúñiga-Pérez, D. Hesp, J. M. Kahk, D. J. Payne, R. G. Egdell, and C. F. McConville, Phys. Rev. B **89**, 035203 (2014).

[95] A. Kotani, and Y. Toyazawa, J. Phys. Soc. Jpn. **37**, 912 (1974).

[96] L. Ley, and M. Cardona, *Photoemission in Solids II* (Springer, Berlin, 1979).

[97] D. C. Langreth, Nobel Symp. **24**, 210 (1973).

[98] D. Cabrera-German, G. Gomez-Sosa, and A. Herrera-Gomez, Surf. Interface Anal. **48**, 252 (2016).

[99] S. A. Chambers, T. C. Kaspar, A. Prakash, G. Haugstad, and B. Jalan, Appl. Phys. Lett. **108**, 152104 (2016).

[100] J. Végh, J. Electron Spectrosc. Relat. Phenom. **151**, 159 (2006).

[101] D. A. Shirley, Phys. Rev. **55**, 4709 (1972).

[102] M. Schmid, H.-P. Steinrück, and J. M. Gottfried, Surf. Interface Anal. **46**, 505 (2014).

4. Surface, Structure and Transport Properties of La-Doped $BaSnO_3$ Thin Films

4.1 Introduction

Carrier density and carrier mobility are the fundamental electronic parameters of semiconductor materials [1, 2, 3]. Knowledge of their physical values is crucial in modeling and manufacturing modern electronic components and circuits [2]. These values are also a function of the surface and structure properties of the thin film semiconductors from which the electronic components are made [1, 3]. In this chapter, we report on the strong correlation between the electrical transport, the surface, and the structural characteristics of the epitaxial La-doped $BaSnO_3$ thin films grown by the PLD technique.

The purpose of this study was to grow epitaxial thin films of La-doped $BaSnO_3$ exhibiting outstanding electronic transport characteristics. To this end, numerous oxide heterostructures (samples) containing various La doping levels varying from 0.5% to 6% were studied. The samples were grown on different single crystal substrates, without and with an insulating buffer layer. The buffer layers were made from $BaSnO_3$, $BaZrO_3$ and $SrZrO_3$. The electronic mobility was optimized for the films directly deposited on $SrTiO_3$ (001), $DyScO_3$ (110) and $TbScO_3$(110) substrates, and for those prepared with $BaSnO_3$ and $SrZrO_3$ buffer layers, using the targets of 2%, 4% and 6% La doping. Insulating behavior was recorded in the films grown with a $BaZrO_3$ buffer layer, in those deposited on $GdScO_3$ (110), $MgAlO_4$ (001) and MgO (001) substrates, and in those fabricated with targets doped at 0.5% and 1% La. Thus, for consistency in structuring the chapter, it was decided to show the surface growth dynamics of some of these samples in the appendix section (see Appendix A.1).

This chapter is composed of four main sections which address the surface and electronic properties of the grown samples, and their structural and microstructural characteristics. The first section is built around the optimization of the room temperature (RT) high electron mobility in epitaxial La-doped $BaSnO_3$ thin films. In this section, the optimizations of both the oxygen deposition pressure and the substrate temperature are firstly addressed. Then, the thickness of the film and buffer layer are optimized with samples grown using the optimal oxygen pressure and substrate temperature. Following each optimization step, surface and transport properties are systematically presented.

In the second section of this chapter, a comparative analysis of the optimized high electron mobility for unbuffered and $BaSnO_3$ buffered films with respect to the La doping content and the substrates is firstly carried out. Then, the surface properties of the sample grown with a $SrZrO_3$ buffer layer (which enhances the electron mobility) on the optimized substrate using the optimized La doping percentage are presented. The transport characteristics of this sample are further compared with those of the films prepared on the other substrates with the optimized target. The structural and microstructural characteristics of these samples are addressed in the third and fourth sections, respectively, while drawing a correlation with their electronic transport properties.

4.2 Electron Mobility Optimization in La-Doped $BaSnO_3$ Thin Films

In this section, the surface quality of the La-doped $BaSnO_3$ thin films and their electronic transport data including the electron mobility, μ, the carrier concentration, n, and the resistivity, ρ, are investigated. The surfaces were firstly analyzed *in situ* during the deposition of the films using RHEED as described in Section 3.2.2, and secondly, *ex situ* using AFM as depicted in Section 3.3.2. The electronic transport properties were assessed through Hall effect measurements as portrayed in Section 3.3.3. Here, we investigate the properties of the films prepared directly on $SrTiO_3$ (001), $DyScO_3$ (110) and $TbScO_3$ (110) substrates, and those of the samples fabricated with an insulating buffer layer of $BaSnO_3$. The transport data were optimized through optimization of the oxygen background pressure, the substrate temperature, and the thicknesses of both the active film and the buffer layer.

4.2.1 Optimization of the Growth Pressure and Substrate Temperature

To achieve optimized electronic mobility in epitaxial La-doped $BaSnO_3$ thin films, the growth pressure and the substrate temperature were first optimized, using a target with 4% La doping content. Eight films grown on $SrTiO_3$ (001) substrates were prepared for these purposes. $SrTiO_3$ was chosen as the substrate for these analyses because of its intrinsic properties, which are recognized to play a critical role in oxide heterostructure growth [4, 5, 6, 7, 8]. For oxygen pressure optimization, the substrates were held at the temperature of 850 °C, while the background pressure was increased following the sequence 1.33×10^{-3}, 1.33×10^{-2} and 1.33×10^{-1} mbar. The optimization of the temperature of the substrates was conducted after evaluating the transport properties of these three films. Five samples were then grown at the optimized pressure, while varying the growth temperatures between 750 °C and 950 °C. The growth parameters of all these samples, including, the thickness of the film and buffer layers, and the energy density and repetition rate of the ablating laser, are provided in Table A.2 of the appendix section. Their surface characteristics are shown in Fig. 4.1, where the RHEED images are given on the upper panels, and the AFM images are represented on the lower ones with color scales in the z direction (height). The RHEED and AFM images for the samples used to optimize the deposition pressure are presented in Figs. 4.1(a) for the sample grown at 1.33×10^{-3} mbar, and 4.1(b) for the sample grown at 1.33×10^{-1} mbar. Those for the films employed in optimizing the deposition temperature are shown in Figs. 4.1(c) and 4.1(d) for the unbuffered and buffered samples grown at 750 °C, respectively, Fig. 4.1(e) for the buffered sample grown at 850 °C, and Fig. 4.1(f) for the buffered sample grown at 950 °C. It should be noted that the AFM images of the sample grown at 1.33×10^{-2} mbar and the unbuffered sample grown at 950 °C were not taken[1]. Therefore, the RHEED images of these samples are shown in Appendix A.2, for consistency in the figure layout.

As can be seen in the RHEED images of the unbuffered films (Figs. 4.1(a) to 4.1(c) and the images in Appendix A.2), broad and elongated diffraction patterns (streaks) are observed in Fig. 4.1(a), suggesting flat surface containing small domains [3]. In Figs. 4.1(b) and 4.1(c) on the other hand, the patterns are very sharp, implying that the surfaces are flat and smooth with

[1] This was because of the availability of the person responsible for sample wire bonding. At the time these samples were grown, the AFM laboratory was fully booked and there was an urgent need to know their electronic transport characteristics. Thus, the samples were directly bonded for measurement according to the availability of the person doing the bonding.

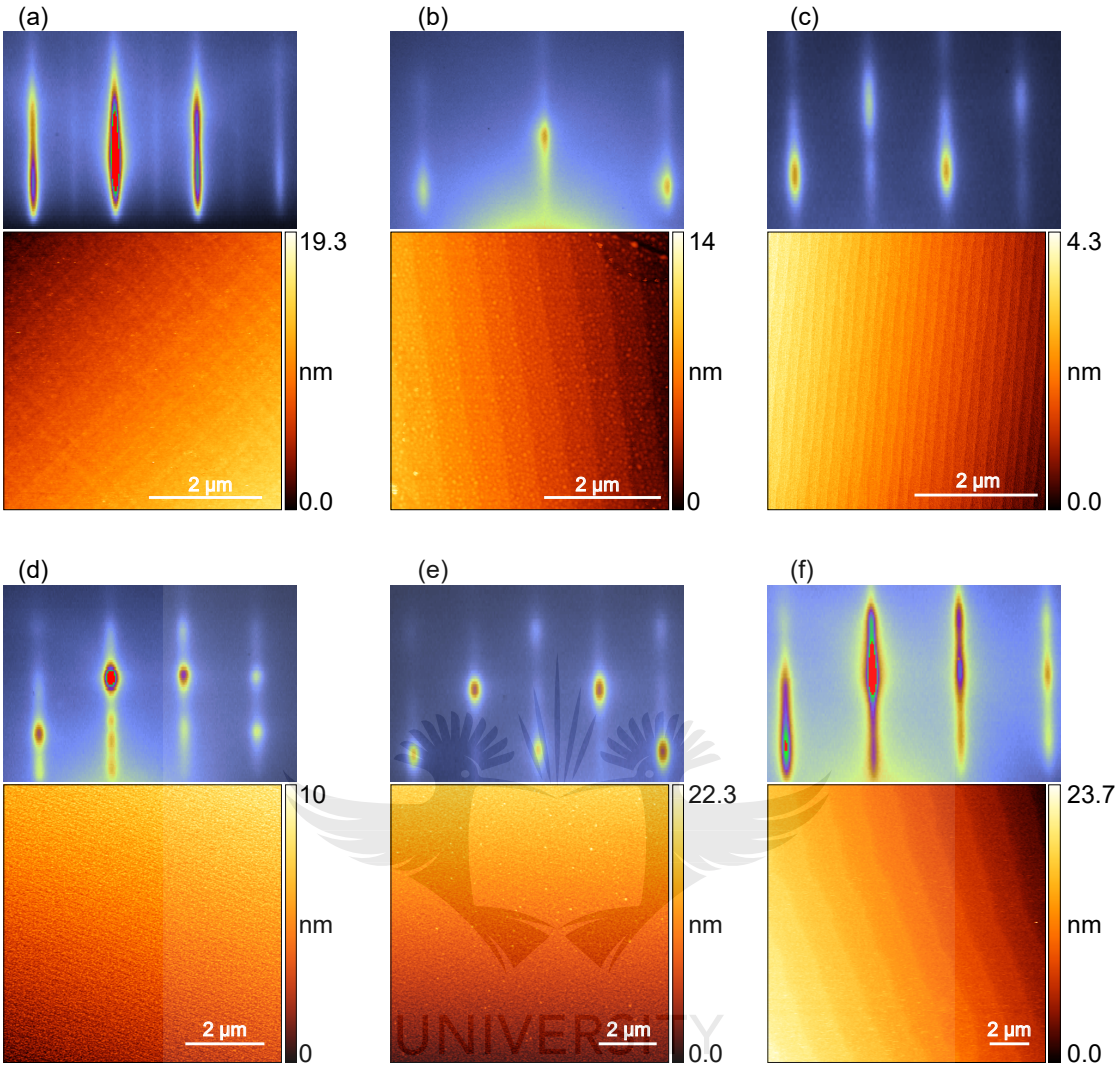

Figure 4.1: RHEED (upper panels) and AFM (lower panels) images for 4% La-$BaSnO_3$ samples prepared on $SrTiO_3$ (001), used for the optimization of the pressure and the temperature of the substrates. The samples in (a) and (b) are for pressure optimization, deposited at 850 °C, where (a) was grown at 1.33×10^{-3} mbar and (b) at 1.33×10^{-1} mbar. The RHEED image of the sample deposited at 1.33×10^{-2} mbar is shown in Appendix A.2. The samples in (c)-(f) are for substrate temperature optimization, grown at the optimized pressure of 1.33×10^{-1} mbar. (c) and (d) are unbuffered and $BaSnO_3$ buffered samples, respectively, grown at 750 °C, (e) is a $BaSnO_3$ buffered film grown at 850 °C, and (f) is a $BaSnO_3$ buffered sample grown at 950 °C. The RHEED image of the unbuffered sample grown at 950 °C is presented in Appendix A.2.

a perfect single crystalline structure [3, 9]. Comparing these five samples, it can be seen that 1.33×10^{-1} mbar of oxygen background pressure is suitable for single crystalline surface growth of La-doped $BaSnO_3$ thin films. As for the buffered films presented in Figs. 4.1(d) to 4.1(f) (all grown at 1.33×10^{-1} mbar), very sharp diffraction spots are formed for the samples prepared at the temperatures of 750 °C (Fig. 4.1(d)) and 850 °C (Fig. 4.1(e)), indicating atomically flat surfaces with an excellent single crystalline structure [3, 9], although the intensity of the spots are modulated along the reciprocal rods in Fig. 4.1(d). When the deposition temperature increases to 950 °C, the diffraction patterns elongate as indicated in Fig. 4.1(f). These are

streaky diffraction patterns [9], which are identical to those in Fig. 4.1(a). Similar streaky patterns were observed in the RHEED images of La-doped $BaSnO_3$ thin films grown by MBE on $SrTiO_3$ (001) and $DyScO_3$ (001) substrates, where smooth surfaces and cube-on-cube epitaxial growth were reported [10, 11, 12, 13]. Thus, the streaky patterns in Figs. 4.1(a) and 4.1(b) also indicate smooth surfaces.

The surface roughness parameters extracted from the surface topography (AFM images) of the samples discussed above are summarized in Table 4.1. It is noteworthy that the error bars for the surface roughness values presented in this study are of the order of $\pm 10^{-3}$ nm. Looking at the table, it can be seen that the root mean square (RMS) roughness values, R_q, of the surfaces depicted in Fig. 4.1, are very small and vary between 0.039 nm and 0.089 nm. These values indicate that the films have smooth and atomically flat surfaces [10, 11, 14, 15], in agreement with the RHEED observations. These values are one order of magnitude smaller, compared to the reported 0.12 to 0.5 nm in La-doped $BaSnO_3$ thin films prepared on $SrTiO_3$ (001) [10, 11, 16, 17, 18], 0.24 to 0.27 nm in La-doped $BaSnO_3$ thin films grown on $BaSnO_3$ (001) [14], and 0.16 to 0.44 nm in PLD grown indium tin oxide thin films [19, 20, 21]. The maximum roughness peak height, R_p, on the other hand, varies from 0.110 nm to 0.400 nm, and is smaller than the variation 0.8 to 0.9 nm that was previously reported [14].

Furthermore, clear, large, straight and uniform step and terrace structures can be seen in the AFM image in Fig. 4.1(b). From the height profile of this surface measured along a line across the terraces, it is found that each step is 6 Å in height, a value which represents more than 1 unit cell of the $SrTiO_3$ (001) substrate (lattice constant of 3.905 Å [22]). Additionally, the surface morphology of this sample also shows many 2D islands randomly distributed on the terraces. Based on the RHEED and AFM data, and the descriptions provided in Section 3.3.2, it can be assumed that this sample was grown in a 2D layer-by-layer mode. Likewise, small, uniform and straight step and terrace structures are visible in Fig. 4.1(c), and barely distinguishable ones in Fig. 4.1(d). The step edges in Fig. 4.1(c) are 3.6 Å in height, almost corresponding to the edge of a unit cell. Consistently with the RHEED patterns and the observations in Ref. [9], it can be concluded that this sample also grows in a layer-by-layer mode, same as for the samples with AFM images shown in Figs. 4.1(d) and 4.1(e). As for the surface morphology in Fig. 4.1(f), it can be seen that the step edges are not straight, but the terraces are clear and wide. The steps are 8 Å in height, about twice a unit cell. Similar surface microstructures with step heights of several unit cells were also reported in $BaSnO_3$ (001) [23] and $SrTiO_3$ (110)

Table 4.1: Surface roughness parameters extracted from the height profiles of the 4% La-$BaSnO_3$ samples prepared on $SrTiO_3$ (001) and shown in Fig. 4.1. The values in the table are given with a precision of the order of $\pm 10^{-3}$ nm.

Samples from Fig. 4.1	Scan area (μm^2)	Average roughness R_a (nm)	Root mean square roughness R_q (nm)	Maximum roughness peak height R_p (nm)	Step height (Å)
(a)	5×5	0.031	0.039	0.114	—
(b)	4.8×4.8	0.043	0.053	0.140	6
(c)	5×5	0.077	0.089	0.230	3.6
(d)	7.2×7.2	0.045	0.062	0.400	—
(e)	10×10	0.055	0.068	0.186	—
(f)	15×15	0.034	0.043	0.110	8

[24] substrates, annealed at 1250 °C in oxygen flow and 1100 °C air, respectively. In particular, this morphology, which suggests step edge faceting, is associated with relatively large in-plane and out-of-plane miscut angles of the substrates [23, 24, 25]. It is noteworthy that the surface morphology in Fig. 4.1(a) is different from others, especially from that in Fig. 4.1(e) where the step and terrace structures are not formed. This morphology is probably associated with the oxygen background pressure during thin film deposition [17]. In fact, this sample was grown in 10^{-3} mbar of oxygen pressure, whereas the others were prepared in 10^{-1} mbar.

Now, the electrical transport characteristics of these samples as a function of the oxygen background pressure are discussed. The RT μ, n and ρ of the samples used to optimize the growth pressure are presented in Fig. 4.2. As can be seen, the carrier mobility increases from 6.6 ± 0.2 to 17.7 ± 0.4 cm^2 V^{-1} s^{-1} when the oxygen pressure increases from 1.33×10^{-3} to 1.33×10^{-1} mbar. Concomitant with this increase in mobility, the carrier density reaches a value as low as $(5.39 \pm 0.06) \times 10^{19}$ cm^{-3}. As for the resistivity, its value abruptly decreases from 11.1 ± 0.1 to 1.928 ± 0.007 mΩ cm and increases again to 6.53 ± 0.08 mΩ cm at

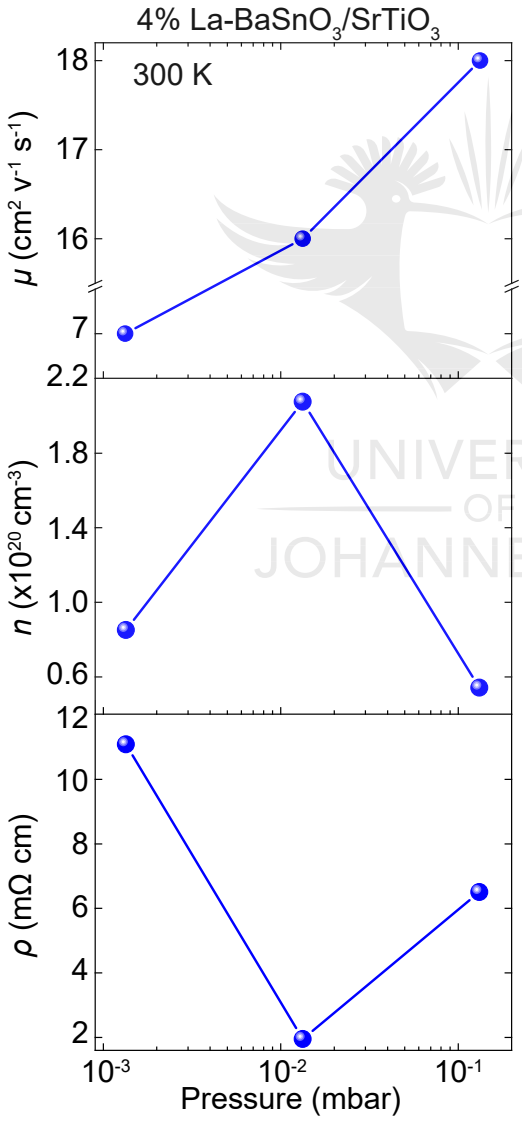

Figure 4.2: Optimization of the pressure for high mobility growth of epitaxial La-doped $BaSnO_3$ thin films. The RT mobility (μ), carrier density (n) and resistivity (ρ) are presented as a function of the oxygen deposition pressure for three 4% epitaxial La-doped $BaSnO_3$ samples directly prepared on $SrTiO_3$ (001) substrates.

higher growth pressure. These relatively high values of the resistivity are consistent with the relatively low mobility achieved in the respective samples, and are similar to those reported in La-doped $BaSnO_3$ thin films prepared by PLD on MgO (001) and $SrTiO_3$ (001) substrates at comparable carrier concentration [26, 27]. Based on the above observations, it can be concluded that 1.33×10^{-1} mbar is the optimal oxygen deposition pressure for the realization of the best electrical properties in the epitaxial La-doped $BaSnO_3$ thin films.

As for the optimal temperature of the substrates during thin films growth, it was observed that the unbuffered films grown at 750 °C had a RT mobility of 17.0 ± 0.4 cm^2 V^{-1} s^{-1} at a carrier density of $(6.38 \pm 0.08) \times 10^{19}$ cm^{-3} and resistivity of 5.77 ± 0.07 mΩ cm, similar to the electronic properties of the unbuffered film grown at 850 °C at the optimized pressure, as presented above in Fig. 4.2. It is noteworthy that both films are of the same thickness, and their surface characteristics (see Figs. 4.1(b) and 4.1(c) and Table 4.1) are also comparable. However, in the buffered films, the RT mobility for the film deposited at 750 °C reached a value as low as 3.26 ± 0.02 cm^2 V^{-1} s^{-1}, compared to 18.4 ± 0.1 cm^2 V^{-1} s^{-1} realized in the buffered film grown at 850 °C with the same film and buffer layer thicknesses. Similarly, the RT mobility value for the buffered films prepared at 950 °C was very low. A value of 1.48 ± 0.01 cm^2 V^{-1} s^{-1} was recorded. It should be mentioned that all of the unbuffered films fabricated at 950 °C were insulating. These results led to the use of 1.33×10^{-1} mbar and 850 °C as the optimal parameter values for the deposition pressure and temperature.

At a certain stage during the optimization process, all the samples fabricated on $SrTiO_3$ (001) substrates with 4% La-doped targets were insulating. This phenomenon, which could not be explained, repeatedly occurred even when using several different targets of 4% La doping content to prepare the thin films on all the substrates. Since the goal of this study was to optimize the electron mobility in the epitaxial La-doped $BaSnO_3$ thin films, it was then decided to switch to using 2% and 6% La-doped targets for further optimization of the growth parameters, such as, the thicknesses of the film and buffer layers. The film growth on perovskite scandate substrates, such as $DyScO_3$ (110) and $TbScO_3$ (110), was also explored, and it was realized that in comparison with $SrTiO_3$ (001) substrates, the films deposited on these substrates achieved improved mobility values, consistent with the reports summarized in Table 2.1.

4.2.2 Optimization of the Thickness of the Active and Buffer Layers

These optimizations were conducted using a target of $BaSnO_3$ doped at 6% with La, a target of undoped $BaSnO_3$ (insulating) for buffer layer deposition, and $TbScO_3$ (110) substrates. All the films and buffer layers were grown at the optimized temperature and pressure described in Section 4.2.1. The film thickness (t) was first optimized by directly depositing the films on the substrates, then the optimal film thickness value was used and the thickness (t') of the buffer layer (inserted between the film and the substrate) was optimized. As was discussed in Section 2.3, the use of a buffer layer in thin film growth helps to reduce the interfacial defects (between the active film layer and the substrate), and improves the electron mobility.

For the optimization of the thickness of the films, three samples were grown with the thicknesses $t = 25$, 50 and 100 nm. Their surface properties are shown in Figs. 4.3(a) to 4.3(c), respectively. As evidenced by the diffraction spots in the RHEED images (Fig. 4.3), these films have flat and single crystalline surfaces [3, 9]. The flatness of these surfaces is also confirmed by the very small values of the RMS roughness, summarized in Table 4.2, which also indicate

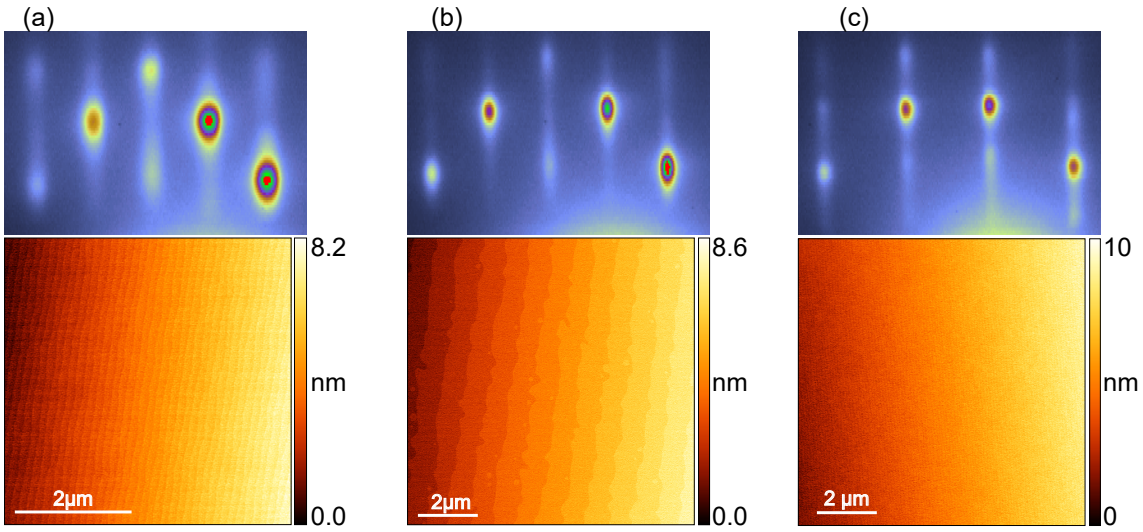

Figure 4.3: RHEED (upper panels) and AFM (lower panels) images for 6% La-$BaSnO_3$ (t)/$TbScO_3$ samples, used to optimize the thickness of the films. The films are (a) 25 nm, (b) 50 nm and (c) 100 nm thick, grown at the optimized pressure and temperature.

their smoothness. Moreover, as portrayed by the AFM images (Fig. 4.3), the surface topographies of these samples present step and terrace structures. The structures in Fig. 4.3(a) are small and uniform, but the step edges are not straight. The line profile reveals that each step is 3.3 Å in height. Larger structures are formed in Fig. 4.3(b), with faceted step edges, and are 3.7 Å in height. It is to be noted that these faceted structures are similar to those reported at the surfaces of $SrTiO_3$ (110) single crystal substrates annealed at high temperatures in air [24]. The structures in Fig. 4.3(c) are closely spaced but appear to be straight. Again, based on the above observations (RHEED and AFM) and the descriptions given in Section 3.3.2, it can be concluded that all the three samples were grown in a 2D layer-by-layer mode.

The RT electronic transport data of these samples plotted against their thicknesses are shown in Fig. 4.4. The highest RT mobility value, 76 ± 2 cm^2 V^{-1} s^{-1}, was achieved in the 25 nm thick film at a carrier density of $(3.71 \pm 0.05) \times 10^{20}$ cm^{-3}, with a corresponding resistivity value of 0.222 ± 0.003 mΩ cm. Increasing the film thickness to 50 nm resulted in a decrease of the RT mobility value to 66 ± 1 cm^2 V^{-1} s^{-1}. With further increase of the film thickness to 100 nm, the mobility value decreased to 52.2 ± 0.6 cm^2 V^{-1} s^{-1}, with a very slight increment in the carrier density and resistivity values to $(4.59 \pm 0.03) \times 10^{20}$ cm^{-3} and 0.261 ± 0.001 mΩ cm,

Table 4.2: Surface roughness parameters obtained from the height profiles of the AFM images of 6% La-$BaSnO_3$ (t)/$TbScO_3$ samples shown in Fig. 4.3. The values in the table are given with a precision of the order of $\pm 10^{-3}$ nm.

Sample thicknesses (Fig. 4.3)	Scan area (μm^2)	Average roughness R_a (nm)	Root mean square roughness R_q (nm)	Maximum roughness peak height R_p (nm)	Step height (Å)
(a): 25 nm	5×5	0.079	0.090	0.203	3.3
(b): 50 nm	10×10	0.028	0.036	0.112	3.7
(c): 100 nm	10×10	0.037	0.045	0.100	—

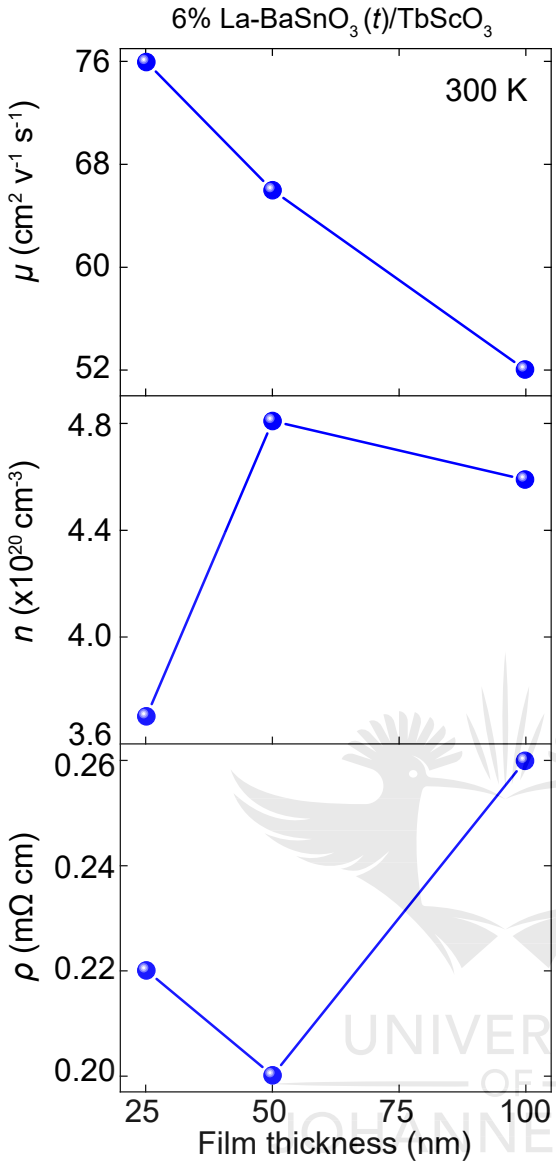

Figure 4.4: Optimization of the thickness of the films for high mobility growth of epitaxial La-doped $BaSnO_3$ thin films. The RT mobility (μ), carrier density (n) and resistivity (ρ) are plotted as functions of the La-doped $BaSnO_3$ film thicknesses, in 6% La-doped $BaSnO_3$ unbuffered samples prepared on $TbScO_3$ (110) substrates.

respectively. Therefore, 25 nm is the optimal La-doped $BaSnO_3$ film thickness that gives the best electronic characteristics.

However, it has been largely demonstrated that the electron mobility is considerably enhanced in buffered La-doped $BaSnO_3$ thin films [10, 13, 18, 26, 28, 29, 30]. Thus, to improve the RT mobility in the films, a $BaSnO_3$ buffer layer was introduced between the 25 nm thick film and the substrate. Buffer layers of various thicknesses (t') were grown, and a significant improvement of the RT mobility was achieved in the sample with the optimal buffer layer thickness of 100 nm. Five samples were prepared by varying the thickness of the buffer layer t' from 50 nm to 200 nm, as shown in Fig. 4.5. Looking at the figure, only the RHEED diffraction spots of the films fabricated with buffer layers of thicknesses 120 nm (Fig. 4.5(c)) and 150 nm (Fig. 4.5(d)) are very sharp, indicative of single crystalline surfaces [3, 9]. The surfaces of the other films seem to contain small out-of-phase domains [3], as their RHEED diffraction spots are relatively elongated. The AFM images (Fig. 4.5) show that the morphologies of all these

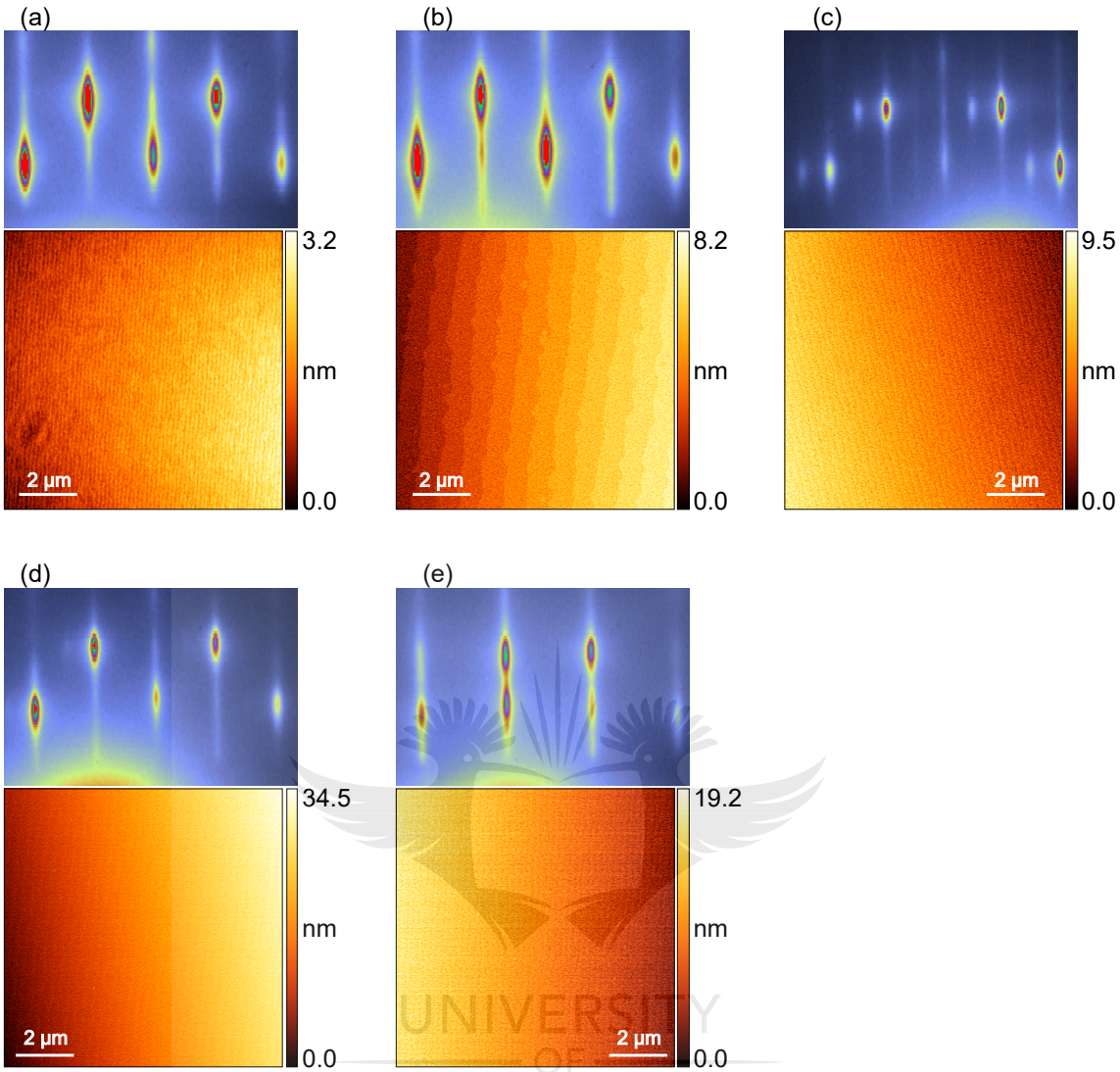

Figure 4.5: RHEED (upper panels) and AFM (lower panels) images for 6% La-$BaSnO_3$ (25 nm)/$BaSnO_3$ (t')/$TbScO_3$ samples, employed in the optimization of the thickness of the buffer layer, t'. The values of t' were varied as (a) 50 nm, (b) 100 nm, (c) 120 nm, (d) 150 nm and (e) 200 nm.

surfaces are composed of step and terrace structures, which are very small, apart from that of the film with a 100 nm thick buffer layer (Fig. 4.5(b)). For this sample, the step edges are not straight, but are faceted and are 4.7 Å in height [24]. Again, the RHEED and AFM results and the descriptions in Section 3.3.2 imply that these samples are grown following a layer-by-layer mode. The surface profile parameters of the five samples are given in Table 4.3, where it can be seen that they have flat and smooth surfaces. A clear dependence of the RMS roughness on the buffer layer thickness can be observed. This is plotted in Fig. 4.6(a). It is seen that, starting from the unbuffered sample ($t' = 0$), the roughness of the surfaces decreases with increasing buffer layer thickness, down to the smoothest value at 100 nm thickness. Above 100 nm, the RMS roughness drastically increases, indicating that the buffer layer enhances the surface properties of the films, up to a critical thickness. The change in the RMS roughness

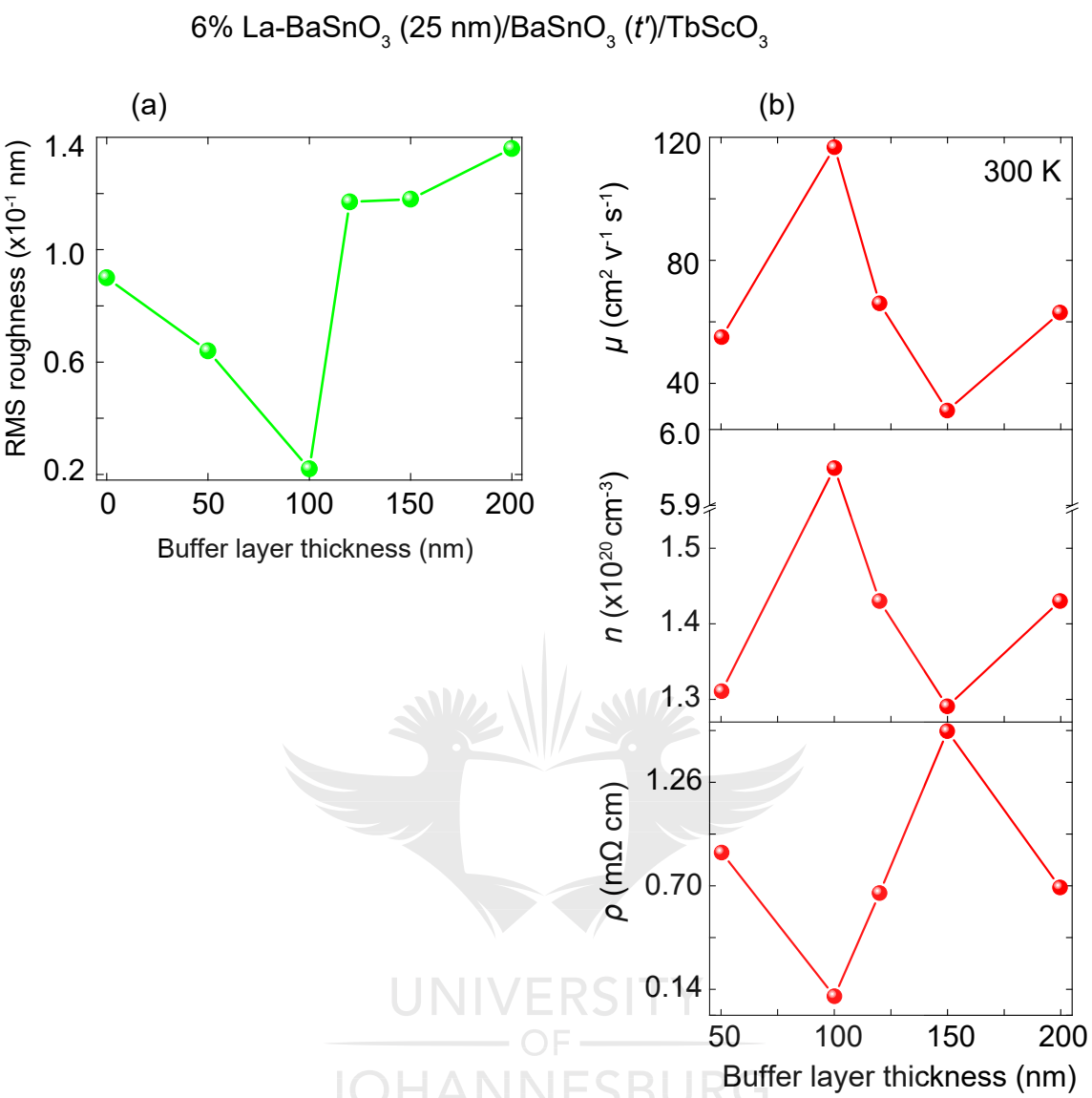

Figure 4.6: Variations of (a) the RMS roughness and (b) the RT mobility (μ), carrier density (n) and resistivity (ρ) of La-doped $BaSnO_3$ thin films as a function of the thickness (t') of the $BaSnO_3$ buffer layer. The films are grown on $TbScO_3$ (110) substrates. The thicknesses of the La-doped $BaSnO_3$ films are fixed to 25 nm, while t' is varied from 50 to 200 nm. Note that the variation in (a) starts from $t' = 0$ (unbuffered film). This is to show the importance of the buffer layer in smoothing the film surfaces.

is shown starting from $t' = 0$ to illustrate how the buffer layer contributes to improving the surface quality of the films grown on $TbScO_3$ (110) substrates.

Figure 4.6(b) illustrates the variation of the RT transport characteristics of these films with respect to the thickness of the buffer layer. As observed in the figure, the mobility value increases from 55 ± 2 cm^2 V^{-1} s^{-1} when the buffer layer thickness is 50 nm to 117 ± 3 cm^2 V^{-1} s^{-1} when the buffer layer thickness reaches 100 nm. Above 100 nm, the RT mobility considerably decreases and its value oscillates between 66 ± 2 cm^2 V^{-1} s^{-1} (120 nm), 31.3 ± 0.8 cm^2 V^{-1} s^{-1} (150 nm) and 63 ± 2 cm^2 V^{-1} s^{-1} (200 nm). The same trend is observed for the carrier den-

Table 4.3: Surface roughness parameters for La-$BaSnO_3$ (25 nm)/$BaSnO_3$ (t')/$TbScO_3$ samples. These parameters were extracted from the height profiles of the AFM images in Fig. 4.5. The values in the table are given with a precision of the order of $\pm 10^{-3}$ nm.

Buffer layer thickness Fig. 4.5	Scan area (μm^2)	Average roughness R_a (nm)	Root mean square roughness R_q (nm)	Maximum roughness peak height R_p (nm)	Step height (Å)
(a): 50 nm	10×10	0.055	0.064	0.138	—
(b): 100 nm	10×10	0.036	0.046	0.138	4.7
(c): 120 nm	10×10	0.099	0.117	0.330	—
(d): 150 nm	10×10	0.101	0.118	0.278	—
(e): 200 nm	10×10	0.113	0.136	0.383	—

sity with a value of $(5.95 \pm 0.08) \times 10^{20}$ cm^{-3} associated with the highest RT mobility. The RMS roughness values of the corresponding samples increase with buffer layer thicknesses as demonstrated in Fig. 4.6(a). Similar increases in surface roughness with respect to buffer layer thicknesses were also reported in PLD and MBE grown La-doped $BaSnO_3$ thin films on $SrTiO_3$ (001) and MgO (001) substrates [10, 18, 26, 28]. Thus, in the present case, the decrease in the carrier mobility and carrier density values at thicknesses above 100 nm can also then be attributed to the effect of the surface roughness. As expected, an opposite behavior to that of the mobility and carrier concentration is observed for the resistivity. More precisely, its value decreases from 0.219 ± 0.003 mΩ cm at the buffer layer thickness of 50 nm to a value as low as 0.089 ± 0.001 mΩ cm at 100 nm thick buffer layer. This value increases further for buffer layers with thicknesses above 100 nm to a value up to 1.54 ± 0.02 mΩ cm before decreasing again in the film with $t' = 200$ nm.

The above analysis leads to the conclusion that 100 nm is the optimal buffer layer thickness value enabling the full electronic capability of the epitaxial La-doped $BaSnO_3$ thin films. To confirm this result, the analysis was repeated on $DyScO_3$ (110) substrates. Four samples containing buffer layers of thicknesses $t'' = 50$, 100, 200 and 300 nm were prepared as presented in Fig. 4.7, respectively. As illustrated by the RHEED diffraction patterns in the figure and the surface properties summarized in Table 4.4, these samples also have flat, smooth and single crystalline surfaces [3, 9]. The topographic AFM images show a structure in Fig. 4.7(a) that is composed of 2D islands randomly distributed on the surface with very little variation in heights, and very small (fine) step and terrace structures in Figs. 4.7(b) to 4.7(d). These surface re-

Table 4.4: Surface roughness parameters from height profiles of 6% La-$BaSnO_3$ (25 nm)/$BaSnO_3$ (t'')/$DyScO_3$ samples shown in Fig. 4.7. The values in the table are given with a precision of the order of $\pm 10^{-3}$ nm.

Buffer layer thickness Fig. 4.7	Scan area (μm^2)	Average roughness R_a (nm)	Root mean square roughness R_q (nm)	Maximum roughness peak height R_p (nm)	Step height (Å)
(a): 50 nm	10×10	0.193	0.253	0.751	—
(b): 100 nm	10×10	0.048	0.061	0.195	—
(c): 200 nm	10×10	0.042	0.052	0.133	—
(d): 300 nm	10×10	0.074	0.096	0.417	—

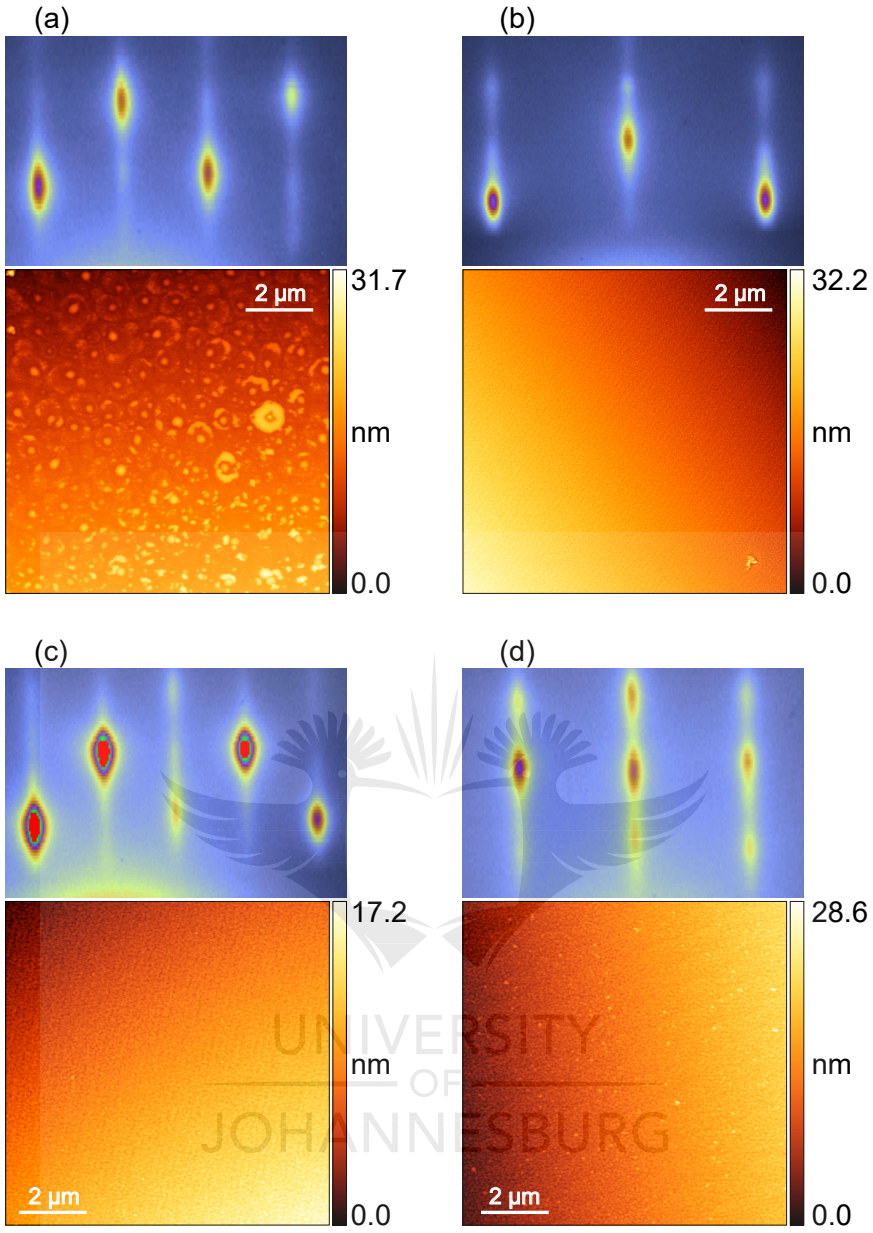

Figure 4.7: RHEED (upper panels) and AFM (lower panels) images for 6% La-$BaSnO_3$ (25 nm)/$BaSnO_3$ (t'')/$DyScO_3$ samples, used in the optimization of the thickness t'' of the buffer layers. t'' was varied as (a) 50 nm, (b) 100 nm, (c) 200 nm and (d) 300 nm.

sults and, again, the descriptions in Section 3.3.2, suggest that the film growth proceeded in a layer-by-layer mode.

Figure 4.8(a) shows the RMS roughness variation of the surface with t''. At first glance, it can be observed that the buffer layer tends to have an effect on the surface roughness that is opposite to that reported in buffered films prepared on $TbScO_3$ (110) substrates (see Fig.4.6(a)). It can be clearly observed in Fig. 4.8(a) that the smoother film is the one without buffer layer, $t'' = 0$, and that adding a layer between the film and the $DyScO_3$ (110) substrate results in rougher surfaces. As for the electronic transport characteristics, it can be seen in

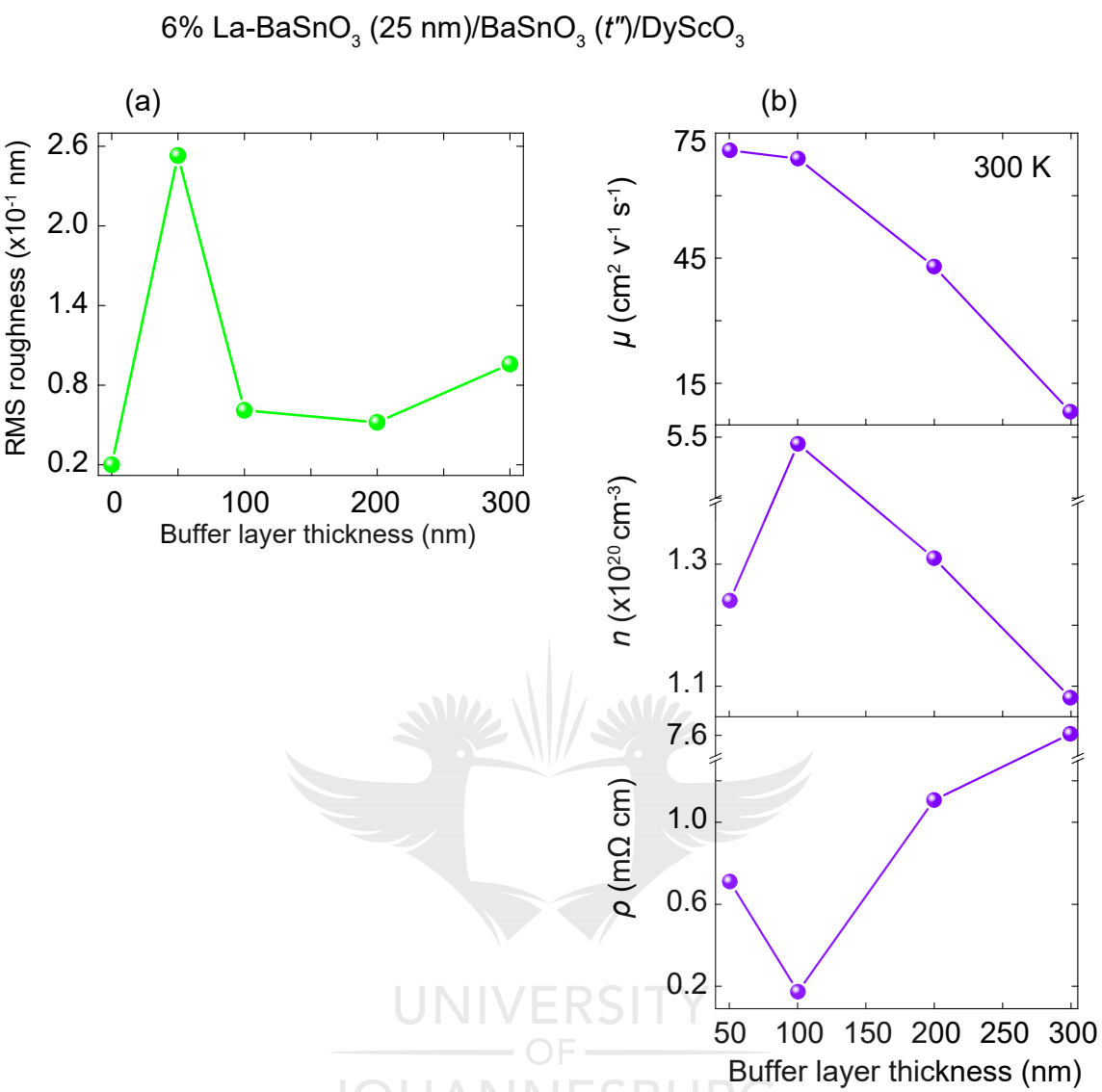

Figure 4.8: Changes in (a) the RMS roughness and (b) the RT mobility (μ), carrier concentration (n) and resistivity (ρ) of La-$BaSnO_3$ films with respect to the thickness (t'') of $BaSnO_3$ buffer layers. The experiment to determine the optimal buffer layer thickness was repeated with 25 nm thick films prepared on $DyScO_3$ (110), varying t'' from 50 nm to 300 nm.

Fig.4.8(b) that the RT mobility drastically decreases above $t'' = 100$ nm, similar to that observed in the case of buffered films deposited on $TbScO_3$ (110) substrates (see Fig. 4.6(b)). It can also be seen that the RT mobility values of the 50 and 100 nm thick buffered films are quite identical, 71 ± 2 cm^2 V^{-1} s^{-1} and 69 ± 2 cm^2 V^{-1} s^{-1}, respectively. Furthermore, a carrier density of $(5.49 \pm 0.07) \times 10^{20}$ cm^{-3} is associated with the RT mobility at 100 nm, which is comparable to that obtained above with $TbScO_3$ (110) substrate at the same buffer layer thickness. These results coupled with the lowest resistivity value of 0.165 ± 0.002 mΩ cm (see Fig. 4.8(b)) suggest that the best electrical properties are achieved in the film with a 100 nm buffer layer.

In the light of all the optimizations carried out above, it can be concluded that 25 nm is

the optimal film thickness value for both unbuffered and buffered films, while a 100 nm thick $BaSnO_3$ buffer layer is optimal for enhanced electron mobility in buffered epitaxial La-doped $BaSnO_3$ thin films.

The variation of the transport characteristics of the buffered films (grown with the optimized buffer layer) with respect to the thickness of the active layer was also studied. This was systematically conducted by varying the thicknesses of the active film layer from 25 nm to 1000 nm (1 μm) on 100 nm $BaSnO_3$ buffered samples prepared on $TbScO_3$ (110). It is noteworthy that in this study, $TbScO_3$ (110) is so far the substrate on which the optimal electronic transport properties are achieved. Figure 4.9 presents the surface properties of the samples employed for this analysis, and Table 4.5 summarizes their surface profile parameters.

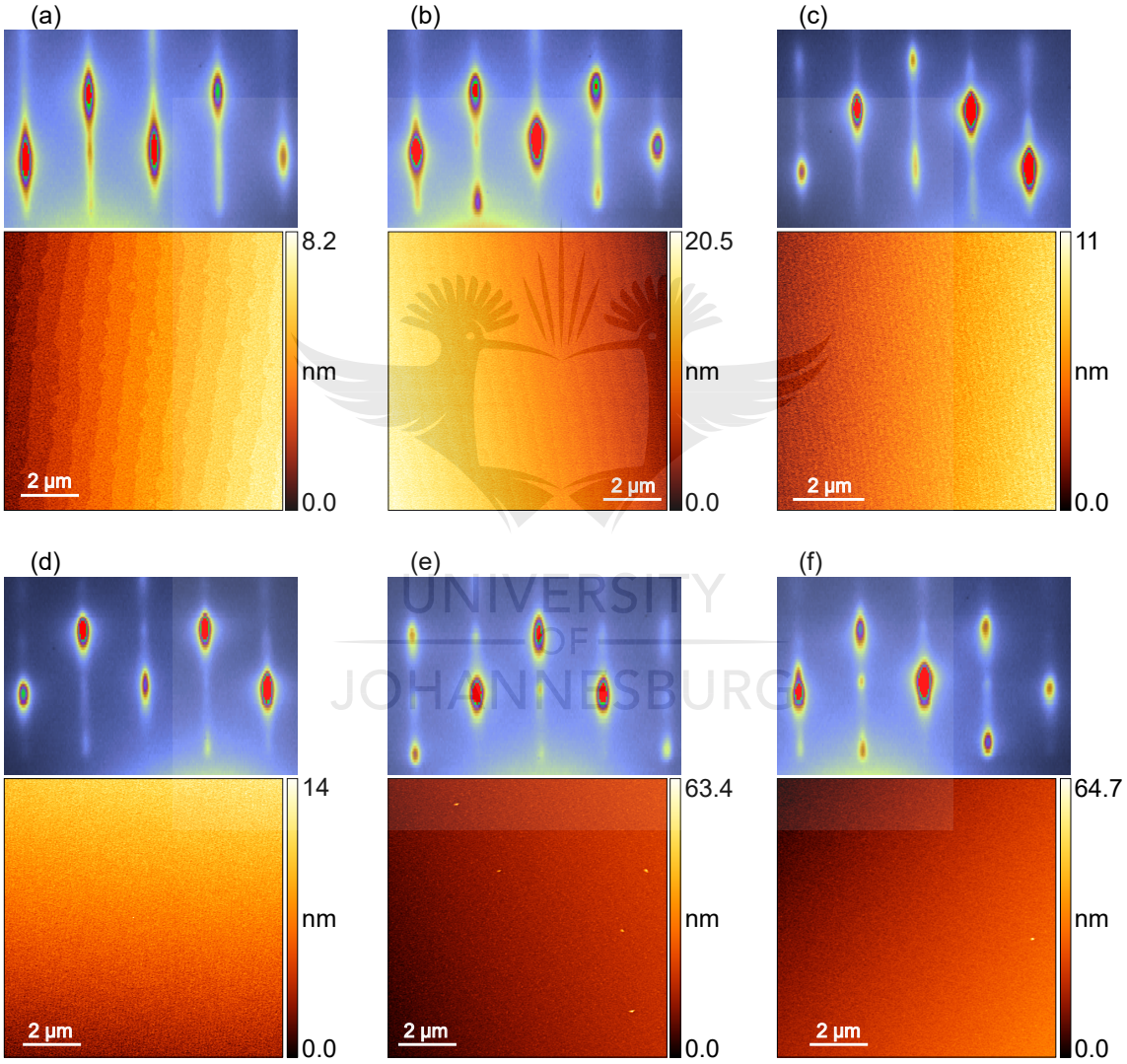

Figure 4.9: RHEED (upper panels) and AFM (lower panels) images for 6% La-$BaSnO_3$ (t)/$BaSnO_3$ (100 nm)/$TbScO_3$ samples, employed in the optimization of the thickness t of the films layer in buffered samples. The values of t were varied from 25 to 1000 nm, as (a) 25 nm, (b) 50 nm, (c) 100 nm, (d) 200 nm, (e) 500 nm and (f) 700 nm. The AFM image of the 1000 nm thick film was not measured. The RHEED image of this sample is presented in Appendix A.3.

Table 4.5: Surface roughness parameters for La-$BaSnO_3$ (t)/$BaSnO_3$ (100 nm)/$TbScO_3$ samples. These parameters were extracted from the height profiles of the AFM images in Fig. 4.9. The values in the table are given with a precision of the order of $\pm 10^{-3}$ nm.

Sample thickness Fig. 4.9	Scan area (μm^2)	Average roughness R_a (nm)	Root mean square roughness R_q (nm)	Maximum roughness peak height R_p (nm)	Step height (Å)
(a): 25 nm	10×10	0.036	0.046	0.138	4.7
(b): 50 nm	10×10	0.049	0.062	0.278	5.6
(c): 100 nm	8×8	0.057	0.070	0.205	—
(d): 200 nm	10×10	0.045	0.058	0.286	—
(e): 500 nm	10×10	0.102	0.115	0.449	—
(f): 700 nm	10×10	0.095	0.126	0.754	—

For the reader's convenience, the RHEED and AFM images of the 25 nm thick film that were previously shown in Fig. 4.5(b) are repeated here as Fig. 4.9(a). Judging by the size of the RHEED diffraction spots (Fig. 4.9) and the values of the surface roughness parameters (Table 4.5), it can be concluded that these films have flat, smooth and single crystalline surfaces [3, 9]. Also, it can be observed that the surface morphology of the 50 nm thick film (Fig. 4.9(b)) presents weakly perceivable step and terrace structures in which the step edges are not straight. The line profile on the terraces reveals that each step is 5.6 Å in height. Again, it can be assumed, based on the RHEED and AFM results and the descriptions in Section 3.3.2, that these films grow following a layer-by-layer mode.

The change in the RMS roughness with respect to the film's thickness was also investigated as portrayed in Fig. 4.10(a). A clear increase in the surface roughness of films with thicknesses above 25 nm can be observed. However, one can see that even at a film thickness of 700 nm, the RMS roughness is still as low as 0.126 nm. It should be mentioned that the surface topography of the 1000 nm thick film was not measured. This is because after the deposition, a very low resistance value indicating a complete metallic behavior was recorded using a multimeter. It was then decided not to proceed with further surface characterization of this sample. Figure 4.10(b) shows the RT transport data of the samples employed to optimize the thickness of the active film layer in 100 nm $BaSnO_3$ buffered samples prepared on $TbScO_3$ (110). As can be seen, the highest RT mobility recorded in the 25 nm film (see the Fig. 4.6(b)) drastically decreases to 73 ± 2 cm^2 V^{-1} s^{-1} when the film thickness increases to 50 nm. Above 50 nm, the mobility further deceases and oscillates between 29 ± 2 and 52 ± 1 cm^2 V^{-1} s^{-1}. These decreases in the carrier mobility of the films could be associated with the increasing surface roughness of the corresponding samples as shown in Fig. 4.10(a). The thicker film (1 μm) shows the lowest mobility at an extremely high carrier concentration of $(2.1 \pm 0.1) \times 10^{22}$ cm^{-3}, resulting in a very low resistivity value of $(10.3 \pm 0.3) \times 10^{-3}$ mΩ cm which suggests that this sample is completely metallic. The carrier density value in the 1 μm thick film is one order of magnitude higher than the upper range of the carrier concentration in highly degenerate indium tin oxide thin films [21, 31].

In general, a consistent trend was observed between the carrier density and the resistivity in all the films presented in Figs. 4.1 to 4.10. It can be seen that the resistivity decreased when the carrier density increased, and also that it increased when the density of carriers decreased. This is typical for degenerate semiconductors, as they behave like metals which are characterized

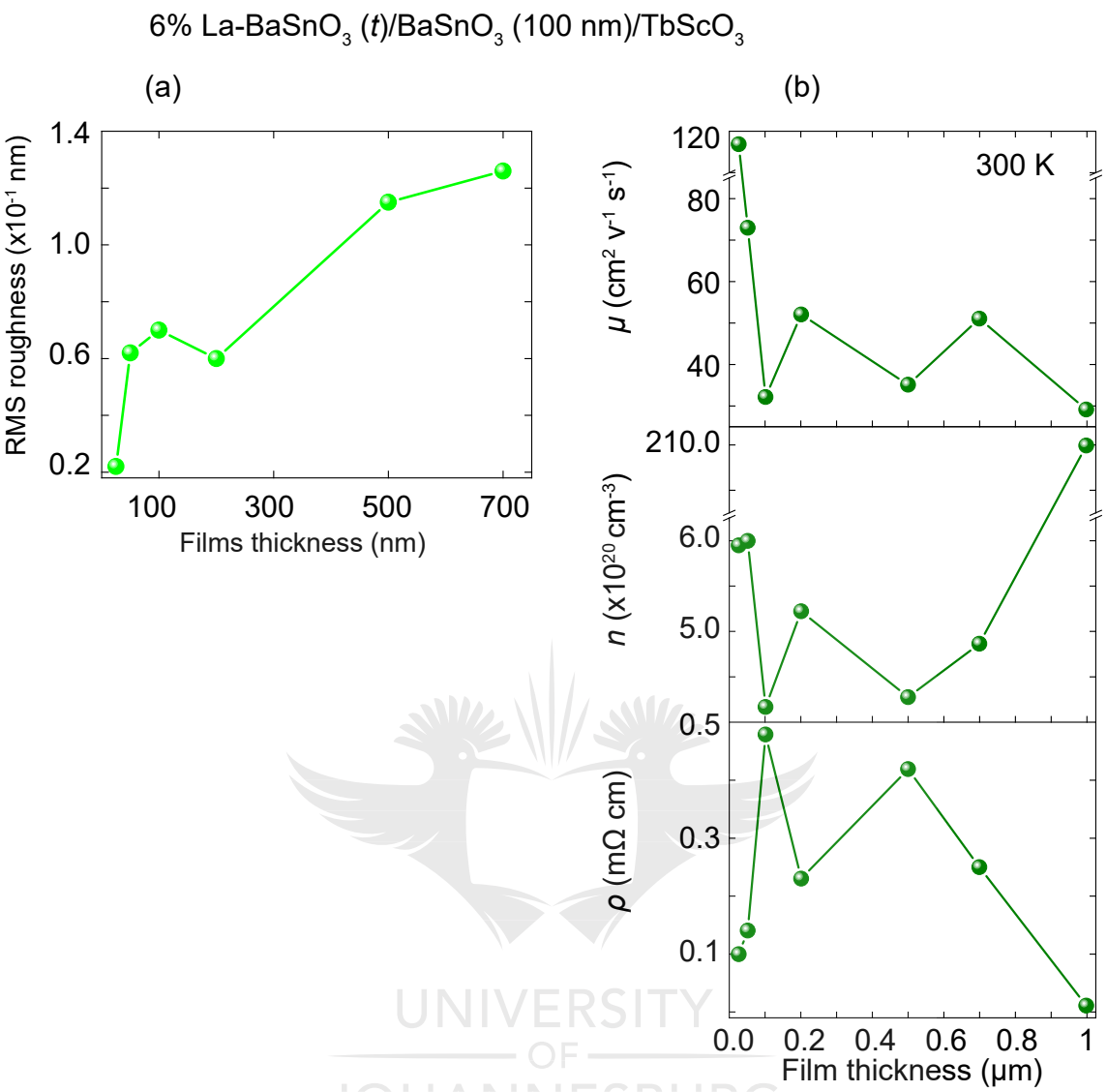

Figure 4.10: Variations of (a) the RMS roughness and (b) the RT mobility (μ), carrier density (n) and resistivity (ρ) of optimized 100 nm thick $BaSnO_3$ buffered samples with respect to the thickness t of the La-$BaSnO_3$ film layer. The films are grown on $TbScO_3$ (110) substrates. t is varied from 25 nm to 1000 nm.

by a large concentration of carriers and are therefore less resistive. Such behavior was also reported in epitaxial thin films of indium oxide and Sn-doped indium oxide grown by MBE on yttria-stabilized zirconia (YSZ) single crystal substrates [32].

4.2.3 Synopsis of the High Electron Mobility in Optimized Samples

In this section, a synopsis of the high electron mobilities achieved in the La-doped $BaSnO_3$ samples prepared as part of this thesis is given. This summary contains the samples discussed in Section 4.2.2, grown on $TbScO_3$ (110) and $DyScO_3$ (110), as well as the samples fabricated on $SrTiO_3$ (001), using the optimized parameters described in Sections 4.2.1 and 4.2.2. These samples were made with targets containing 2% and 6% La doping levels. The surface

characteristics of some of these samples were presented in Figs. 4.3(a), 4.5(b) and 4.7(a), and for additional samples, these are given in Appendix A.4. Comparisons of the RT electronic transport properties of unbuffered and $BaSnO_3$ buffered films with respect to the substrates on one hand, and with respect to the La doping percentage on the other hand are carried out. The comparative data are summarized in Table 4.6. The results shown in the table indicate that the highest RT mobilities are achieved in 6% La-doped unbuffered and buffered films. In the unbuffered samples, the highest RT mobility is realized in the film grown on $SrTiO_3$ (001) with a value reaching as high as 91 ± 2 cm^2 V^{-1} s^{-1} at a carrier density of $(4.05 \pm 0.05) \times 10^{20}$ cm^{-3}. In the 2% doped film deposited on $SrTiO_3$ (001) on the other hand, the RT mobility is limited to 64 ± 2 cm^2 V^{-1} s^{-1} at $(1.21 \pm 0.02) \times 10^{20}$ cm^{-3}. At comparable carrier densities, the best value obtained in the present study is higher than those previously reported in La-doped $BaSnO_3$ thin films directly deposited on $SrTiO_3$ (001) using the PLD technique [17, 33, 34, 35]. However, this value is lower than the values of 105 cm^2 V^{-1} s^{-1} [36] and $\approx$ 124 cm^2 V^{-1} s^{-1} [12] reported in MBE grown epitaxial La-doped $BaSnO_3$ thin films on $SrTiO_3$ (001), with carrier concentrations of 2.5×10^{20} cm^{-3} and $\approx 6 \times 10^{19}$ cm^{-3}, respectively.

For the unbuffered films fabricated on $DyScO_3$ (110), the mobility value is rather higher in the 2% doping than in the 6%, and reaches 69 ± 2 cm^2 V^{-1} s^{-1} at $(0.84 \pm 0.01) \times 10^{20}$ cm^{-3}. In those prepared on $TbScO_3$ (110) substrates on the other hand, the mobility values at 2% and 6% doping are very close. Their values peak at 75 ± 2 and 76 ± 2 cm^2 V^{-1} s^{-1}, respectively, but with more than twice as much carriers in the 6% La-doped film ($(3.71 \pm 0.05) \times 10^{20}$ cm^{-3} versus $(1.35 \pm 0.02) \times 10^{20}$ cm^{-3}). The above mobility values are higher than the value of 10.11 cm^2 V^{-1} s^{-1} reported in La-doped $BaSnO_3$ thin film prepared by PLD on $SmScO_3$ (110) substrate at a similar carrier density [35]. However, these values are smaller than 81 cm^2 V^{-1} s^{-1} at 1.65×10^{20} cm^{-3} [37] and 150 cm^2 V^{-1} s^{-1} at $\approx 7 \times 10^{19}$ cm^{-3} [12] recorded in MBE grown films on $TbScO_3$ (110) and $PrScO_3$ (110), respectively.

In the buffered films, the highest electron mobility is obtained in the film prepared on $TbScO_3$ (110), and reaches a maximum value of 117 ± 3 cm^2 V^{-1} s^{-1} at 6% doping, which is more than three times the mobility at 2% doping. In comparison, this high mobility value is close to the enhanced value of 122 cm^2 V^{-1} s^{-1} reported after post growth annealing at 950 °C in H_2 forming gas of a PLD grown epitaxial La-doped $BaSnO_3$ thin films on $SrTiO_3$ substrate [38]. This value is higher than the ones previously reported in $BaSnO_3$ buffered La-doped $BaSnO_3$

Table 4.6: Room temperature electrical characteristics (μ, ρ and n) of the optimized high mobility films prepared on $SrTiO_3$ (001) (STO), $DyScO_3$ (110) (DSO) and $TbScO_3$ (110) (TSO) substrates. The values of μ, ρ and n in the table are in the units of cm^2 V^{-1} s^{-1}, mΩ cm and cm^{-3}, respectively.

		Unbuffered films			$BaSnO_3$ buffered films		
		μ	n ($\times 10^{20}$)	ρ	μ	n ($\times 10^{20}$)	ρ
2%	STO	64 ± 2	1.21 ± 0.02	0.81 ± 0.01	38.5 ± 0.3	1.49 ± 0.01	1.09 ± 0.01
	DSO	69 ± 2	0.84 ± 0.01	1.08 ± 0.01	—	—	—
	TSO	75 ± 2	1.35 ± 0.02	0.62 ± 0.01	36 ± 1	1.53 ± 0.01	1.14 ± 0.07
6%	STO	91 ± 2	4.05 ± 0.05	0.169 ± 0.002	24 ± 1	0.96 ± 0.02	2.75 ± 0.03
	DSO	29 ± 1	2.55 ± 0.03	0.83 ± 0.01	71 ± 2	1.24 ± 0.02	0.71 ± 0.01
	TSO	76 ± 2	3.71 ± 0.05	0.222 ± 0.003	117 ± 3	5.95 ± 0.08	0.089 ± 0.001

thin films grown on $SrTiO_3$ (001) [18, 28] and MgO [26] by PLD. It is however smaller than the highest value of 183 $cm^2\ V^{-1}\ s^{-1}$ reported to date in epitaxial thin films of La-doped $BaSnO_3$, which was obtained in a $BaSnO_3$ buffered film grown by MBE on $DyScO_3$ (110) [13]. As for the buffered films prepared on $DyScO_3$ (110) substrates, it should be mentioned that the data for 2% La doping are not available as this sample was not grown. Nonetheless, a mobility value up to 71 ± 2 $cm^2\ V^{-1}\ s^{-1}$ is achieved in the buffered 6% La-doped film. Contrary to the unbuffered film, the mobility in the buffered film fabricated on $SrTiO_3$ (001) is the lowest at 6% doping level. It attains a value of 24 ± 1 $cm^2\ V^{-1}\ s^{-1}$ at $(0.96 \pm 0.02) \times 10^{20}$ cm^{-3}. This value is quite close to 38.5 ± 0.3 $cm^2\ V^{-1}\ s^{-1}$ recorded in the 2% doped buffered film at a carrier density of $(1.49 \pm 0.01) \times 10^{20}$ cm^{-3}.

In summary, the best transport properties are obtained in the epitaxial 6% La-doped $BaSnO_3$ thin film prepared on $TbScO_3$ (110) and containing a $BaSnO_3$ buffer layer. In literature, there are numerous reports of both electronic and structural properties enhancement in epitaxial thin films containing adhesion layer(s). For example, in GaN epitaxial layers grown on sapphire with AlN [39, 40, 41] and GaN [42, 43] buffer layers, and in $BaSnO_3$ buffered La-doped $BaSnO_3$ thin films deposited on $TbScO_3$ (110) [44] and $SrTiO_3$ (001) [28] substrates. The primary role of the additional buffer layer is to minimize the misfit dislocations originating from the large lattice mismatch between the film and the substrate, which generally results in the creation of threading dislocations that reduce the carrier mobility [28, 39, 40, 41, 42, 43, 44]. It is therefore unexpected that the electron mobility values decrease after the insertion of the undoped $BaSnO_3$ adhesion layer in the films. These decreases are more pronounced in the 2% La-doped buffered films. With the 6% doping, the mobility reduction is only observed in the buffered film grown on $SrTiO_3$ (001) (see Table 4.6).

4.3 Further Electron Mobility Enhancement

From the optimizations carried out above, it was concluded that the best electronic characteristics were realized in epitaxial 6% La-doped $BaSnO_3$ thin films of 25 nm thick, grown with a 100 nm $BaSnO_3$ buffer layer on $TbScO_3$ (110) substrates. Since the carrier mobility in this system is limited by the large concentration of structural defects such as threading dislocations as will be addressed in full in Section 4.4.3, the possibility of reducing these defects and enhancing the electronic mobility was explored. It was opted to insert another material, in particular $SrZrO_3$[2], between the La-doped $BaSnO_3$ thin film and the $TbScO_3$ (110) substrate. $SrZrO_3$ was chosen for two reasons: Firstly, because of its lattice parameter value, 4.109 Å [45, 46], which is close to the bulk lattice parameter values of $BaSnO_3$ (4.116 Å [47]) and $TbScO_3$ (3.960 Å [48]). Secondly, because of its low vapor pressure, which like in $TbScO_3$, allows for high temperature growth. It was hypothesized that this would lead to a lower defect density. Thus, $SrZrO_3$ epitaxial layers were grown at temperatures ranging from 850 °C to 1600 °C to find the optimal temperature value for the best structural, microstructural and electronic properties of the buffered films. It is noteworthy that the highest temperature growth, 1600 °C, is well below the melting temperature ≈ 2100 °C of $TbScO_3$ [48].

Knowing that the La-doped $BaSnO_3$ thin films were grown at 850 °C (optimized growth

[2] The surface, structure and transport data of this sample, together with those of the best samples prepared on $TbScO_3$ (110), without and with a $BaSnO_3$ buffer layer, were compiled into a paper entitled: *High-temperature-grown buffer layer boosts electron mobility in epitaxial La-doped $BaSnO_3$/$SrZrO_3$ heterostructures*, A. P. Nono Tchiomo *et al.*, APL Mater. 7, 041119 (2019).

temperature, see Section 4.2.1), after the deposition of the $SrZrO_3$ buffer layer at temperatures above 850 °C, the sample was immediately cooled down to the film growth temperature at the rate of 2 K/s and the oxygen pressure was adjusted. The optimal RT electron mobility was obtained in the films with $SrZrO_3$ buffer layers grown at 1300 °C in 1.36×10^{-2} mbar of oxygen. Immediately after the deposition of the buffer layer, the substrate temperature was reduced to 850 °C and the oxygen pressure increased to $\approx 1 \times 10^{-1}$ mbar (optimized growth pressure) for the deposition of the active layer. The surface growth dynamics and morphology of this sample are presented in Fig. 4.11. Figure 4.11(a) displays the surface growth of the $SrZrO_3$ thin film layer on $TbScO_3$ (110) at 1300 °C. The surface structure of the subsequent deposition of a 6% La-doped $BaSnO_3$ thin film on the $SrZrO_3$ layer grown on $TbScO_3$ (110) is shown in Fig. 4.11(b). Again, as can be seen from the diffraction spots and the surface roughness parameters given in Table 4.7, these samples have flat, smooth and single crystalline surfaces [3, 9].

The growth dynamics of these two films are illustrated in Figs. 4.11(c) and 4.11(d), respectively. These are typical RHEED intensity oscillations as a function of time [11, 13, 37], and were extracted from the areas marked with rectangles in Figs. 4.11(a) and 4.11(b). The RHEED intensity oscillations for the growth of the $SrZrO_3$ film layer shows clear oscillations throughout the deposition time, as depicted by the purple curve in Fig. 4.11(c). As for the deposition of the active film layer, the intensity of the oscillations drops after the deposition of several monolayers (at about 100 s into the growth cycle), but rapidly stabilizes and remains constant until the end of the growth (brown curve in Fig. 4.11(d)). This drop in intensity is associated with a relaxation in the film layer after reaching a certain critical thickness. These observations imply that both the film and the buffer layer are smoothly grown in a layer-by-layer mode, yielding epitaxial growth [11, 13, 37].

To evaluate the exact thickness of the film and the buffer layer, transformations of the RHEED intensity oscillations raw data were performed using the algorithm and the procedures for the analysis of RHEED data proposed by Braun [49, 50]. The results of this analysis are also shown in Figs. 4.11(c) and 4.11(d). The cyan curves represent the component of the RHEED intensity oscillations extracted from the raw data to obtain signals that are in phase with the progression of the construction of the surface during the deposition [49]. This is achieved by smoothing the purple and brown signals. The smoothing process consists of removing the 4 Hz and the 1 Hz modulation that is attributed to the pulse repetition rate associated with the deposition of the buffer and active layers, respectively. These signals (cyan curves) are then transformed following the steps described in Ref. [50] to obtain the shape of the light green and light blue curves shown in Figs. 4.11(c) and 4.11(d), respectively. Fitting of these signals with a sine function (black curves in Figs. 4.11(c) and 4.11(d)) permits reliable characterization of

Table 4.7: Surface roughness parameters of the $SrZrO_3$ (100 nm)/$TbScO_3$ and 6% La-$BaSnO_3$ (25 nm)/$SrZrO_3$ (100 nm)/$TbScO_3$ samples shown in Fig. 4.11. The values in the table are given with a precision of the order of $\pm 10^{-3}$ nm.

Samples from Fig. 4.11	Scan area (μm^2)	Average roughness R_a (nm)	Root mean square roughness R_q (nm)	Maximum roughness peak height R_p (nm)	Step height (Å)
(a)	10×10	0.112	0.139	0.407	—
(b)	1.1×1.1	0.024	0.031	0.064	—

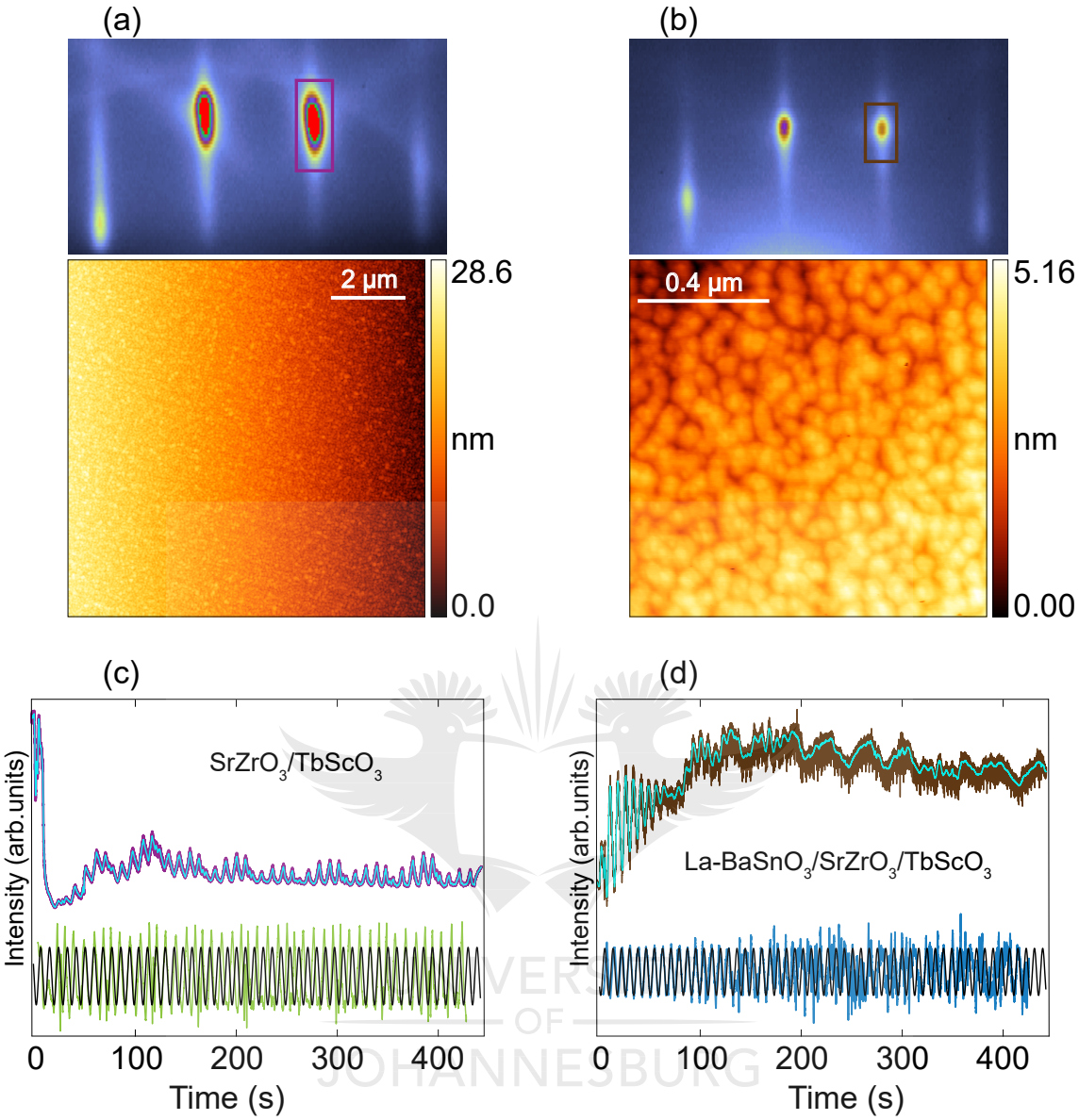

Figure 4.11: Surface properties for the growth of a 6% La-$BaSnO_3$ (25 nm)/$SrZrO_3$ (100 nm)/$TbScO_3$ sample. (a) and (c) represent the RHEED and AFM images, and the RHEED intensity oscillations for the growth of the $SrZrO_3$ (100 nm)/$TbScO_3$ thin film at 1300 °C. (b) and (d) show the RHEED and AFM data for the subsequent deposition of a 6% La-$BaSnO_3$ thin film on the $SrZrO_3$ layer. The rectangles in the RHEED images represent the regions over which the integrated intensity oscillations (purple and brown curves) as a function of time that are shown in (c) and (d), respectively, were recorded. These two signals were smoothed by respectively removing the 4 Hz and the 1 Hz modulation due to the pulse repetition rate, yielding the cyan curves. The cyan curves were transformed to obtained the light green and blue curves in (c) and (d), respectively (see text for further information). A sine function fit (black curves) to these latter was applied to obtained 48.7 oscillations in (c) and 55.1 oscillations in (d).

the oscillations. Thus, a total of 48.7 oscillations which are 9.24 s apart were computed from Fig. 4.11(c), and 55.1 oscillations with a period of 9.07 s were obtained from Fig. 4.11(d). In the absence of step-flow growth contributions, these would be equivalent to 48.7 monolayers of $SrZrO_3$ and 55.1 monolayers of La-doped $BaSnO_3$, respectively [51].

The temperature dependence of the resistivity (ρ), the carrier density (n), and mobility (μ) of this $SrZrO_3$ buffered sample (brown curves) are shown in Figs. 4.12 and 4.13, along with those of 6% La-doped $BaSnO_3$ unbuffered and $BaSnO_3$ buffered samples grown on $SrTiO_3$ (001) (red curves), $DyScO_3$ (110) (green curves), and $TbScO_3$ (110) (blue curves) substrates. The sphere symbols represent the data for the unbuffered samples, whereas the diamond symbols represent those of the buffered samples. These transport parameters were measured and calculated as described in Section 3.3.3, in the temperature range from 300 K to 2 K.

Figure 4.12 represents the temperature dependence of ρ at zero magnetic field. As can be seen in the figure, the resistivity of each of these films presents a positive temperature coefficient, consistent with previous studies on epitaxial La-doped $BaSnO_3$ thin films [10, 13, 17, 18, 34, 35, 47, 52]. As also discussed in Section 2.3, this positive temperature coefficient indicates a metallic behavior in all the films over almost the entire temperature range. However, a weak upturn can be perceived in the low temperature regions (below 50 K) of the samples with the highest resistivity values in Fig. 4.12(a) and 4.12(b). Notably, an upturn is seen in the temperature dependent resistivity of the buffered film grown on $SrTiO_3$ (001) (red diamonds), and in that of the unbuffered film grown on $DyScO_3$ (110) (green spheres). Similarly, an increase in the resistivity was observed in the low temperature region of the temperature dependent resistivity at $\approx$ 100 K in 7% La-$BaSnO_3$ thin films grown by PLD on $SrTiO_3$ (001) and $SmScO_3$ (110) substrates [35]; at 30 K in 7% La-$BaSnO_3$ thin films grown by PLD on $SrTiO_3$ (001) substrates [53]; at 32 K in 7% La-$BaSnO_3$ thin films grown by PLD on MgO (001) substrates [54]; at 100 K in $BaSnO_3$ thin films deposited on MgO (001) substrates by high pressure oxygen sputtering [16]; and at 80 K and 30 K in 7% Sb-$BaSnO_3$ and Gd-$BaSnO_3$ thin films grown by PLD on $SrTiO_3$ (001) [55] and MgO (001) [56] substrates, respectively. This low temperature characteristic, which can be attributed to weakly localized transport (electrons), suggests a low temperature metal-to-semiconductor transition [10, 53, 54, 55, 56, 57, 58], as was also reported in PLD grown Sb, La and Nb-doped $SrTiO_3$ thin films [59, 60, 61] and Sb-doped $BaSnO_3$ thin films [62]. The very small variation of the resistivity of all the films (Fig. 4.12) in the temperature range studied should also be noted. Compared to conventional activated semiconductors where the resistivity exponentially increases with decreasing temperature, this variation suggests almost constant resistivity values in the films when the temperature is decreased from 300 K to 2 K.

Figure 4.13(a) shows the temperature dependence of the carrier density, n, of the films. Considering this figure, two regions can be identified: A region at high temperature, between 300 K and 50 K, where the carrier densities are almost independent of the temperature; and a region at low temperature, below 50 K, where the concentration of the free carriers starts to decrease. These behaviors are comparable to previous reports [10, 12, 13, 17, 18, 34, 35, 38, 52, 58]. The temperature independent carrier density, together with the metallic behavior of the resistivity shown in Fig. 4.12, indicate that the transport properties in all the films are governed by electrons (n-type doping), and that these films are in a degenerately doped semiconducting regime, as was also addressed in Section 2.3. The degenerate doped regime is more pronounced in the films deposited on $SrTiO_3$ (001) (red curves), where the concentrations of the negatively charged free carriers show metallic behavior down to 2 K [10, 12, 13, 18, 34, 52]. In the films deposited on $DyScO_3$ (110) (green curves) and $TbScO_3$ (110) (blue and brown curves) on the other hand, the exponential character of n in the semiconducting regime begins to dominate below 50 K, and n starts to decrease following the freeze-out of the ionized dopant (La^{3+}) [35, 58].

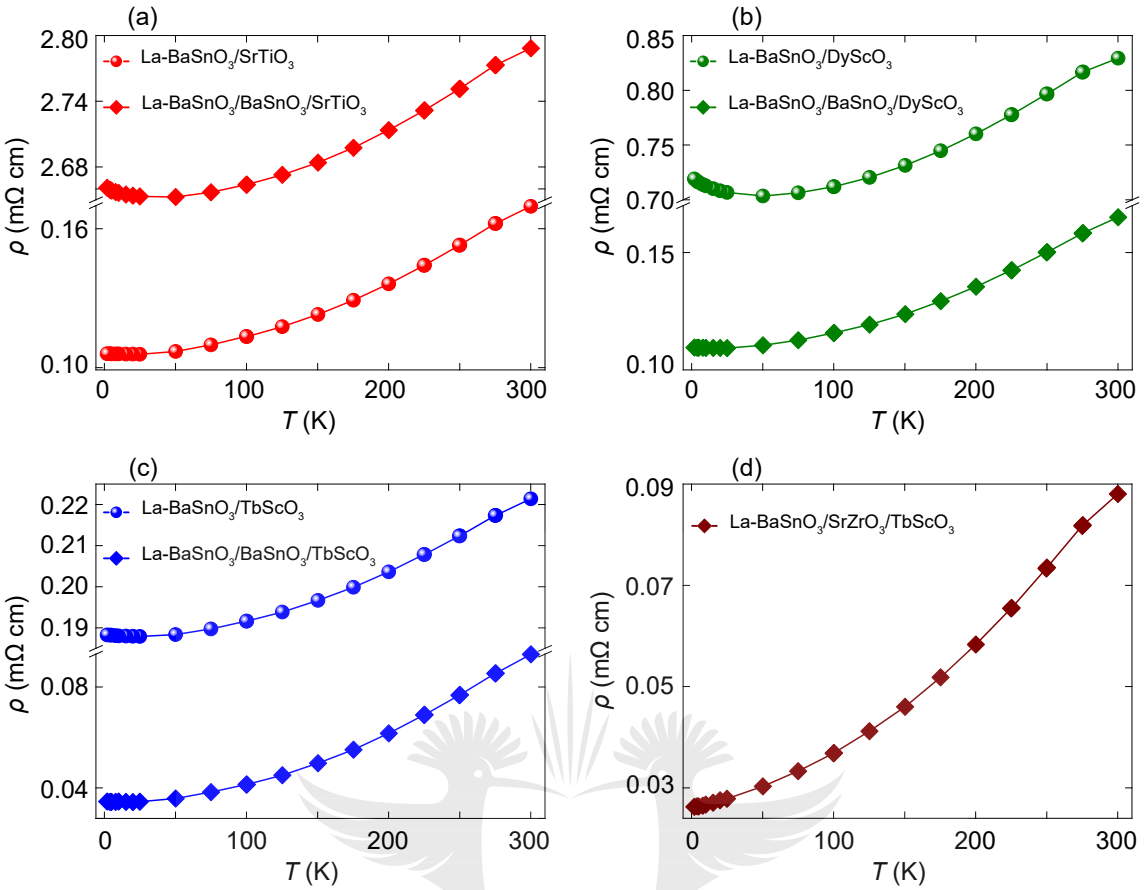

Figure 4.12: Temperature dependence of the resistivity (ρ) of 6% La-$BaSnO_3$ thin films (25 nm thick) grown at 850 °C on (a) $SrTiO_3$ (001) (red curves), (b) $DyScO_3$ (110) (green curves), and (c) and (d) $TbScO_3$ (110) (blue and brown curves) substrates, without (sphere symbols) and with (diamond symbols) 100 nm thick $BaSnO_3$ (grown at 850 °C) and $SrZrO_3$ (grown at 1300 °C) buffer layers. The film with $SrZrO_3$ is illustrated by the brown curves.

Table 4.8 gives the activation rate of the ionized La^{3+} dopant in each of these films. As stated in Section 3.2.2, doping a $BaSnO_3$ target with 6% La corresponds to introducing $\approx 8 \times 10^{20}$ cm^{-3} free carriers into the $BaSnO_3$ lattice. This doping level is represented by the orange solid line shown in the temperature dependent carrier density in Fig. 4.13(a), and indicates a 100% activation rate, i.e., when the target carrier density is equal to the measured carrier density. The values in Table 4.8 are obtained considering the RT carrier density values of the films, which were also summarized in Table 4.6 for the 6% La-doped unbuffered and

Table 4.8: Activation rate of the La dopant in the unbuffered and buffered films in Fig. 4.13 prepared on $SrTiO_3$ (001), $DyScO_3$ (110) and $TbScO_3$ (110) substrates.

	Unbuffered films	$BaSnO_3$ buffered films	$SrZrO_3$ buffered films
$SrTiO_3$	49.6%	46.8%	—
$DyScO_3$	31.4%	67.3%	—
$TbScO_3$	45.5%	72.9%	63.9%

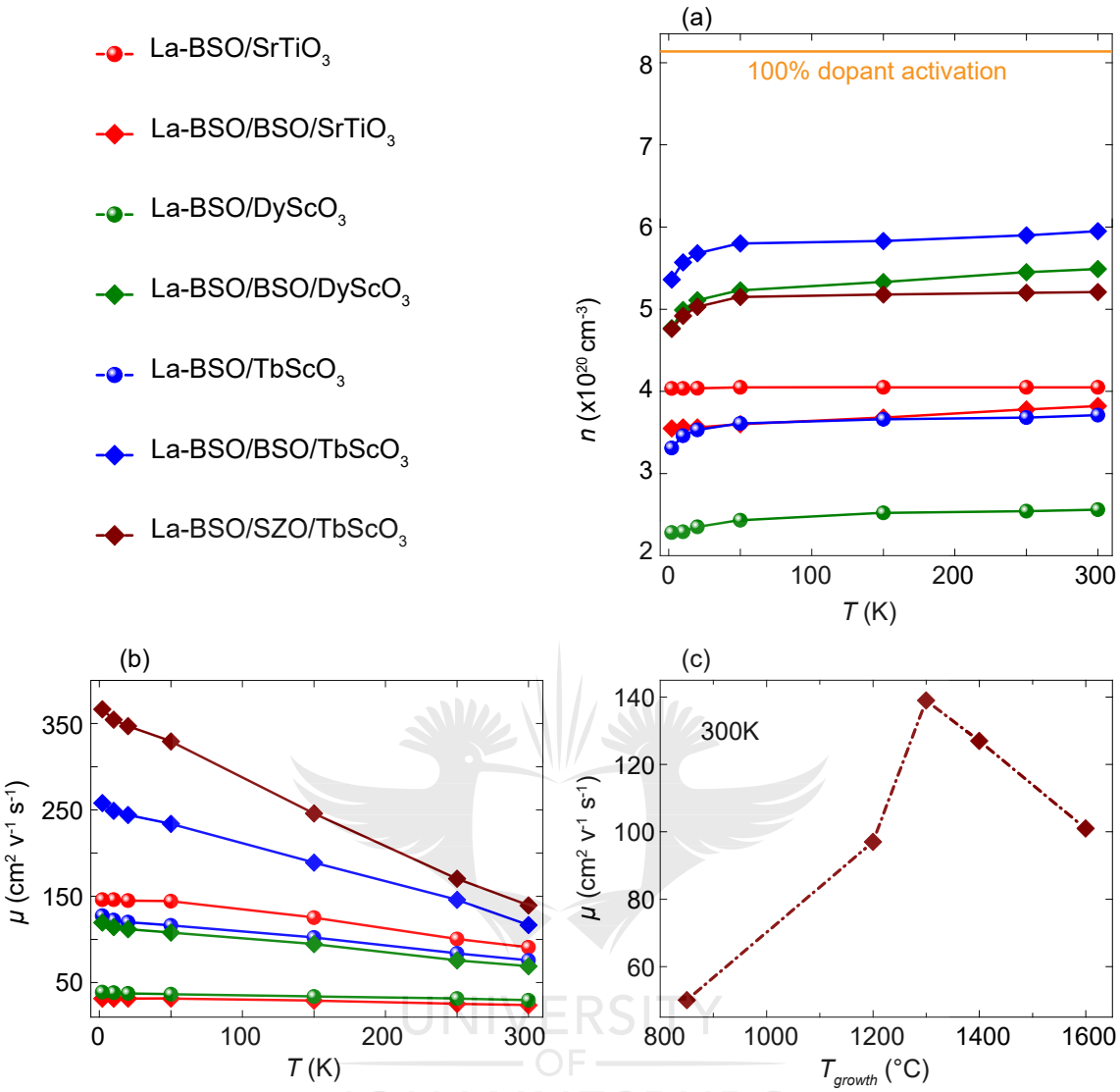

Figure 4.13: (a) and (b) Temperature dependence of the carrier concentration (n) and the mobility (μ) of 6% La-$BaSnO_3$ thin films (25 nm thick) grown at 850 °C on $SrTiO_3$ (001) (red curves), $DyScO_3$ (110) (green curves) and $TbScO_3$ (110) (blue and brown curves) substrates, without (sphere symbols) and with 100 nm thick $BaSnO_3$ (grown at 850 °C) and $SrZrO_3$ (grown at 1300 °C) buffer layers (diamond symbols). The film with $SrZrO_3$ is illustrated by the brown curves. (c) Mobility of 6% La-$BaSnO_3$ (25 nm)/$SrZrO_3$ (100 nm)/$TbScO_3$ films as a function of the growth temperature of $SrZrO_3$.

$BaSnO_3$ buffered films. As can be seen both from Table 4.8 and Fig. 4.13(a), the La dopant is not fully activated in any of the films, as the activation rates are below 100% in Table 4.8 and the n values are below the orange line in Fig. 4.13(a). This is due to charge-trapping near or at defect cores such as grain boundaries or dislocations, as strongly suggested in previous reports on La-doped $BaSnO_3$ thin films [26, 34, 35, 37]. The lowest activation rate in the unbuffered film grown on $DyScO_3$ (110) (green spheres) seems to suggest that the trapping mechanism is enhanced in that film [34]. Further discussions associating the carrier concentration to the density of defects in the films will follow in Section 4.5.

The dependence of the electron mobility μ on the temperature is presented in Fig. 4.13(b).

From the figure, it can be clearly observed that μ increases for all the films with decreasing temperature down to the lowest measured temperature (2 K). The low temperature increases of the electron mobility in the films are in agreement with previous reports on La-doped $BaSnO_3$ thin films [18, 34, 52]. This behavior is typical for semiconductor systems, and suggests a considerable reduction of lattice scattering at low temperature, particularly phonon, as expected in degenerate systems [18, 63, 64, 65, 66, 67]. The reduction of phonon scattering at low temperature in degenerate semiconductors was also addressed in Section 2.2.3. However, it is important to point out that mobility saturation in La-doped $BaSnO_3$ thin films below 50 K is also reported in literature [10, 12, 13, 35].

Moreover, considering Fig. 4.13(b), it can be observed that the RT mobility increases in samples prepared on $TbScO_3$ (110) (blue curves) from 76 ± 2 cm^2 V^{-1} s^{-1} in the unbuffered film (blue spheres) to 117 ± 3 cm^2 V^{-1} s^{-1} in the $BaSnO_3$ buffered sample (blue diamonds), indicating an improvement of the RT mobility. The enhancement of the mobility upon the insertion of the $BaSnO_3$ buffer layer can also be appreciated in the films fabricated on $DyScO_3$ (110) substrates (green curves). However, these improvements are still limited, most probably by the high density of threading dislocations [28, 41, 42, 43, 44] present in those films, as will be demonstrated in Section 4.5.

To reduce the concentration of threading dislocations, the $BaSnO_3$ buffer layer was replaced with $SrZrO_3$ buffer layers grown at very high temperatures. As discussed at the very beginning of this section, $SrZrO_3$ material was selected because of its comparable lattice parameter and its low vapor pressure. Several La-$BaSnO_3$/$SrZrO_3$ heterostructures were prepared by changing the growth temperatures of the $SrZrO_3$ layer while keeping the other growth parameters such as the oxygen background pressure, the laser fluence and laser repetition rate unchanged. In this way, the growth temperature of $SrZrO_3$ was optimized to achieve the highest RT carrier mobility in the films. It was observed that at temperatures above 1300 °C, the RT mobilities of the films started to decrease, as shown in Fig. 4.13(c) which represents the mobility in $SrZrO_3$ buffered films as a function of the growth temperature of $SrZrO_3$ buffer layer. This decrease was attributed to the volatility of Sr and Zr constituents which induce non-stoichiometry in the $SrZrO_3$ epitaxial layers [68]. The non-stoichiometry enhances the density of defects, such as shear and point defects [13], resulting in the reduction of the electron mobility in the films with $SrZrO_3$ grown above 1300 °C. Thus, 1300 °C was considered as the optimal growth temperature for the $SrZrO_3$. Let us recall that the sample illustrated by the brown curves in Fig. 4.13 was fabricated with a $SrZrO_3$ buffer layer grown at 1300 °C. For this sample, mobilities of 140 ± 4 cm^2 V^{-1} s^{-1} at RT and 367 ± 11 cm^2 V^{-1} s^{-1} at 2 K were achieved (Fig. 4.13(b)). The carrier density and resistivity associated with this high mobility are $(5.21 \pm 0.08) \times 10^{20}$ cm^{-3} and 0.086 ± 0.001 mΩ cm, respectively. This mobility is $\approx$ 30% higher than the value of 100 cm^2 V^{-1} s^{-1} previously reported in La-doped $BaSnO_3$ thin films grown by PLD on the lattice matched $BaSnO_3$ substrate [14], and 15% higher than the reported enhanced mobility value of 122 cm^2 V^{-1} s^{-1} after post annealing of the films at 950 °C in H_2 forming gas [38]. Therefore, it can be seen that the mobility recorded in the present study for the $SrZrO_3$ buffered film is the highest to date for PLD grown La-doped $BaSnO_3$ thin films without resorting to any post-growth treatment.

4.4 Structural Properties

After addressing the surface and electronic transport characteristics of the optimized samples, a systematic description of their structure is needed. XRD measurements were utilized, as described in Section 3.3.1, to probe the lattice structure of the films and assess their crystalline quality, their thickness and both their in-plane and out-of-plane lattice parameters. The values of the lattice constants provide knowledge on the strain states of the films, which gives an indication of the density of defects present in the films [10, 13, 17]. For clarity, only the XRD data of the optimized 6% La-doped $BaSnO_3$ samples, whose electrical properties were given in Fig. 4.13, will be discussed.

4.4.1 Phase Growth of La-Doped $BaSnO_3$ Thin Films

Typical $2\theta - \omega$ scans for the 6% La-$BaSnO_3$ thin films prepared on $SrTiO_3$ (001) (red curves), $DyScO_3$ (110) (green curves) and $TbScO_3$ (110) (blue curves) substrates, without and with $BaSnO_3$ buffer layers are presented in Fig. 4.14. A preferential orientation of the diffracted planes can be seen for these films. Only intense peaks from the (00l) family of the La-$BaSnO_3$ film planes (illustrated by $\star$ symbols) are observed, without any secondary phases or randomly oriented grains. These characteristics indicate pure phase growth of all the films on the substrates. The (00l) family planes of the cubic $SrTiO_3$ (001) and (hh0) family planes of both the pseudo-cubic $DyScO_3$ (110) and $TbScO_3$ (110) substrates are also visible (all indicated by $-$ symbols). These observations suggest an epitaxial growth of La-doped $BaSnO_3$ thin films on $SrTiO_3$ (001), $DyScO_3$ (110) and $TbScO_3$ (110) substrates, although ϕ scans were not performed to confirm the crystallinity. Nevertheless, results of the $2\theta - \omega$ scans obtained in this present study are in agreement with the results reported in literature, where the ϕ scans were also not shown [10, 11, 12, 14, 17, 18, 35]. It should be noted that in the limit of the laser parameters (energy density, frequency) that were used during these experiments, the above results are independent of the La doping percentage, the substrates deposition temperature, the oxygen background pressure and the thicknesses of both active and buffer layers. In other words, in the framework of our experiments, no matter what these parameters were, the films were always single crystalline and epitaxially grown on all the substrates.

Similarly, high crystallinity is observed in the highest mobility sample (25 nm thick 6% La-doped $BaSnO_3$ thin film) prepared on $TbScO_3$ (110) with a 100 nm $SrZrO_3$ buffer layer (grown at 1300 °C) as shown in Fig. 4.15. The epitaxial growth of $SrZrO_3$ is presented in Fig. 4.15(a), where one can only see the (00l) planes from its cubic structure. Perovskite $SrZrO_3$ is known to undergo a phase transition from orthorhombic to cubic at $\approx$ 1130 °C [69, 70, 71]. The (00l) diffraction patterns of the active La-$BaSnO_3$ film layer subsequently deposited on $SrZrO_3$ can be clearly observed in Fig. 4.15(b). It is important to highlight that the (003) diffraction plane only appears (weakly) in the buffered films such as seen around $2\theta = 65°$ in Fig. 4.14 for the La-$BaSnO_3$ films in samples (b), (d) and (f), and in Fig. 4.15 for both La-$BaSnO_3$ film and $SrZrO_3$ buffer layer. This diffraction plane is hardly observable in thin films, and its appearance here only demonstrates the excellent crystal quality of La-doped $BaSnO_3$ and $SrZrO_3$ films [17].

4.4.2 Crystalline Quality of the La-Doped $BaSnO_3$ Thin Films

Close up views of $2\theta - \omega$ scans around the (002) planes for the samples in Figs. 4.14 and 4.15(b) are displayed in Fig. 4.16. The (002) reflections of the films directly deposited on

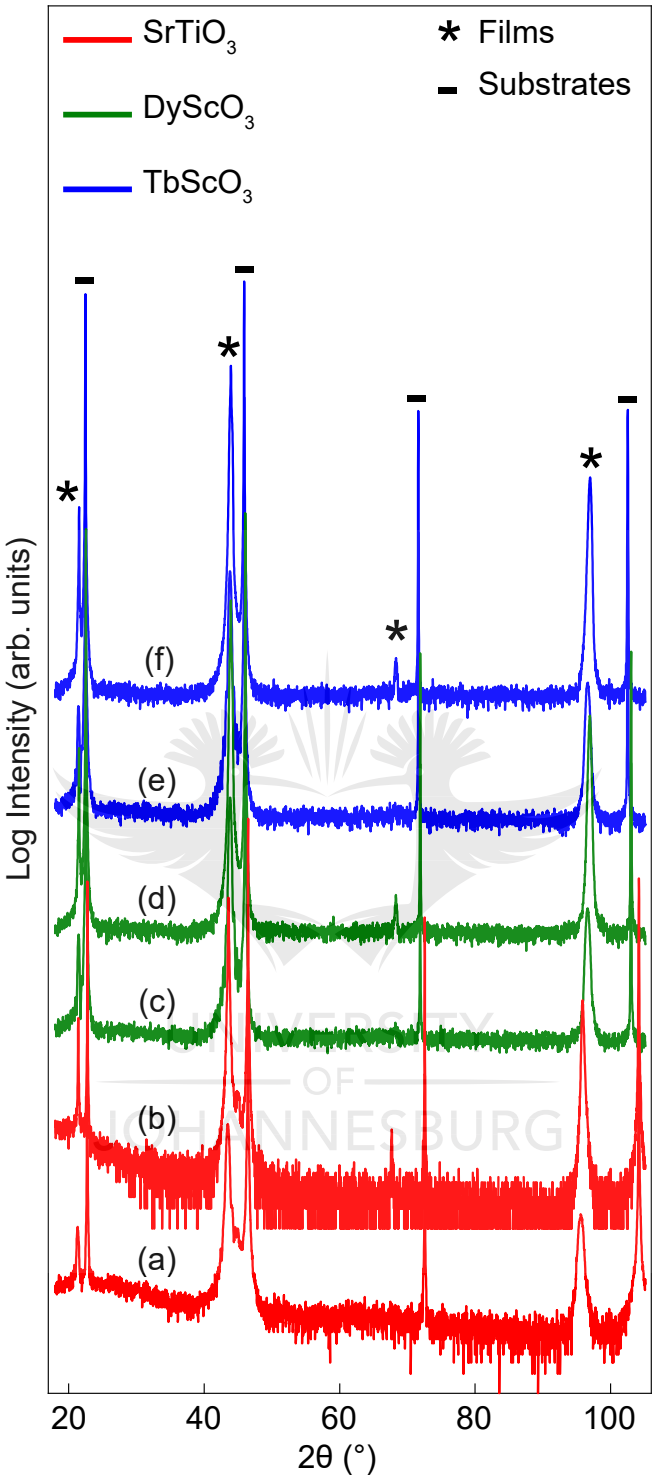

Figure 4.14: X-ray diffraction patterns in $2\theta - \omega$ scans for epitaxial 6% La-doped $BaSnO_3$ (25 nm) thin films grown on $SrTiO_3$ (001) (red curves), $DyScO_3$ (110) (green curves) and $TbScO_3$ (110) (blue curves) substrates, without and with 100 nm $BaSnO_3$ buffer layers. The films labeled (a), (c) and (e) are unbuffered; those labeled (b), (d) and (f) are buffered. Only the $(00l)$ family planes of La-$BaSnO_3$ films, $(00l)$ family peaks of $SrTiO_3$ and $(hh0)$ family peaks of both $DyScO_3$ and $TbScO_3$ are present, indicating pure phase growth in the cubic perovskite structure, and single crystalline films. The film planes are represented by $\star$ symbols, whereas the substrate planes are indicated by $-$ symbols.

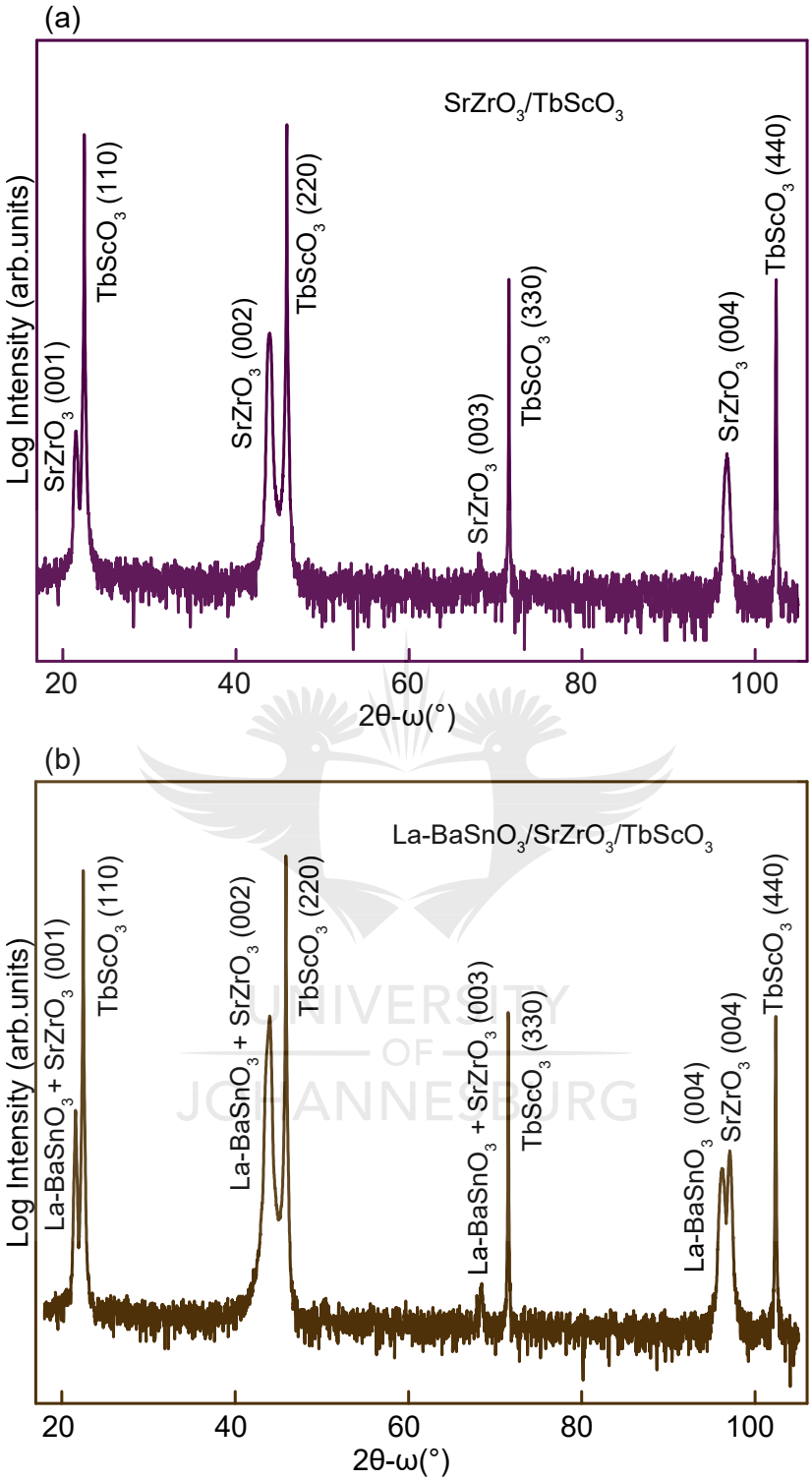

Figure 4.15: X-ray diffraction patterns in $2\theta - \omega$ scans for the best mobility sample, 6% La-doped $BaSnO_3$ thin film grown on $TbScO_3$ (110) with a $SrZrO_3$ buffer layer. (a) Growth of $SrZrO_3$ (100 nm)/$TbScO_3$ at 1300 °C. (b) Subsequent growth of 6% La-$BaSnO_3$ (25 nm)/$SrZrO_3$ (100 nm)/$TbScO_3$ thin film at 850 °C. Only the (00l) family peaks of both La-$BaSnO_3$ and $SrZrO_3$ film layers, and the (hh0) family of planes of $TbScO_3$ substrates are present, indicating pure phase growth and single crystalline films.

the substrates are presented in Fig. 4.16(a), and those of the films grown with $BaSnO_3$ and $SrZrO_3$ buffer layers are shown in Fig.4.16(b). The enlargement around the (002) peaks aids in emphasizing the high crystalline quality of our epitaxial thin films and the smoothness of their surfaces. These are evidenced by the presence of clear Pendellesung fringes in all the samples as can be seen in Figs. 4.16(a) and 4.16(b) [10, 11, 12, 19, 35]. This result is in agreement with the conclusions drawn from RHEED and AFM analyses. These fringes were used to determine the thickness of the films as described in Section 3.3.1. The fringes are more pronounced in unbuffered films (thinner, 25 nm active layer) as seen in Fig. 4.16(a), compared to buffered films (thicker, 25 nm active layer plus 100 nm buffer layer) where they are smeared together as observed in Fig. 4.16(b).

Additionally, the out-of-plane lattice parameter (c) in the direction perpendicular to the films surface can be extracted from the position of the (002) planes as described in Section 3.3.1. The (002) peaks for the films fabricated on $SrTiO_3$ (001) are shifted to lower angles (see the red curves in Figs. 4.16(a) and 4.16(b)). This results in larger d-spacings, and therefore also in expanded c values compared to those for the films grown on $DyScO_3$ (110) (green curve) and $TbScO_3$ (110) (blue and brown curves), for which the (002) film planes are at the same position. These shifts are attributed to residual strain in the films. The calculated c values for the films in Figs. 4.16(a) and 4.16(b) are summarized in Table 4.9. These values are consistent with previous reports on epitaxial La-doped $BaSnO_3$ thin films growth [10, 14, 17, 18, 35]. As can be seen from the table, the films deposited on $SrTiO_3$ (001), especially the unbuffered film with $c = 4.167 \pm 0.002$ Å, are largely expanded in the c direction. On the contrary, the c values for the films deposited on $DyScO_3$ (110) and $TbScO_3$ (110) (unbuffered and buffered) are nearly equal to the bulk lattice constant value of about 4.126 Å for polycrystalline 6% La-doped $BaSnO_3$ material [52, 72]. In general, a buffer layer introduced between the film layer and the substrate considerably reduces the c expansion, due to strain relaxation. It should be pointed out that the unbuffered film prepared on $TbScO_3$ (110) has a c value equal to that of the bulk, which decreases upon insertion of the $BaSnO_3$ buffer layer. The decrease in the c value is more pronounced for the film prepared with the $SrZrO_3$ buffer layer to the point where c becomes lower than the bulk value. However, this is unexpected considering that $SrZrO_3$ buffer layer inserted at high temperature compressively strained the film in the direction parallel to the surface. This will be addressed in more details in Section 4.4.3.

Figure 4.16(c) represents the two components fit (after background subtraction) of the La-$BaSnO_3$ (002) plane for the film grown on $DyScO_3$ (110) with a $BaSnO_3$ buffer layer (see Fig. 4.16(b)). It illustrates the decomposition of the (002) diffraction peaks of the $BaSnO_3$ buffered films in two peaks of distinctive shapes. From the figure, it is clear that the (002) peaks for the $BaSnO_3$ buffered films (Fig. 4.16(b)) are composed of two components located

Table 4.9: Out-of-plane (c) lattice constants calculated based on information from the (002) planes of the epitaxial 6% La-doped $BaSnO_3$ thin films in Fig. 4.16, prepared on $SrTiO_3$ (001), $DyScO_3$ (110) and $TbScO_3$ (110) substrates, without and with $BaSnO_3$ and $SrZrO_3$ buffer layers.

La-$BaSnO_3$ (4.126 Å)		$SrTiO_3$ (001) (Å)	$DyScO_3$ (110) (Å)	$TbScO_3$ (110) (Å)
Unbuffered films	c	4.167 ± 0.002	4.130 ± 0.002	4.126 ± 0.002
$BaSnO_3$ buffered films	c	4.135 ± 0.002	4.124 ± 0.002	4.120 ± 0.002
$SrZrO_3$ buffered film	c	—	—	4.113 ± 0.002

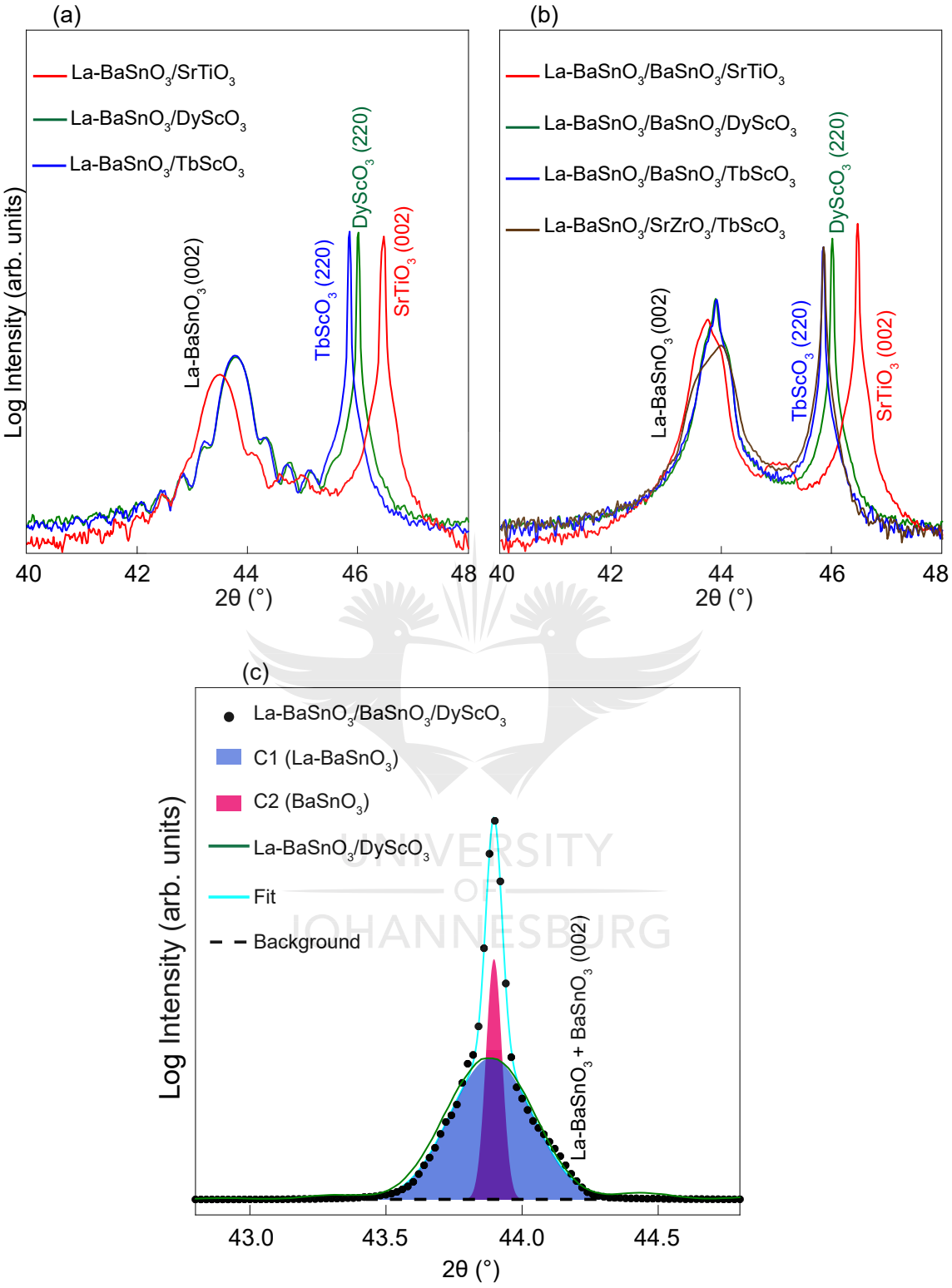

Figure 4.16: Close up views of $2\theta - \omega$ scans around the (002) planes of the samples in Figs. 4.14 and 4.15(b). (a) (002) diffraction planes of the films directly grown on the substrates. (b) (002) reflections of the films prepared with $BaSnO_3$ and $SrZrO_3$ buffer layers. (c) Two components fit of the La-$BaSnO_3$ (002) peak for the buffered film in (b) grown on $DyScO_3$ (110).

at the same position (diffraction angle), hence their particular shape (compared to the shape of the unbuffered films in Fig. 4.16(a)). There is a contribution from the La-doped $BaSnO_3$ active layer, labeled C1 (La-$BaSnO_3$), and a contribution from the $BaSnO_3$ buffer layer, labeled C2 ($BaSnO_3$). The La-$BaSnO_3$ (002) peak for the unbuffered film grown on $DyScO_3$ (110) (Fig. 4.16(a)) is plotted alongside the decomposed peaks to confirm the contribution of the La-doped $BaSnO_3$ film layer, as it matches well with C1 (La-$BaSnO_3$) component (see the green curve in Fig. 4.16(c)). On the contrary, the shape of the (002) peak for the $SrZrO_3$ buffered film in Fig. 4.16(b) (brown curve) indicates a slight offset in the relative positions of the La-$BaSnO_3$ film peak and the $SrZrO_3$ buffer layer peak. This offset is also well manifested in reciprocal space mappings, as will be discussed in Section 4.4.3.

The full width at half maximum (FWHM) of the rocking curves in the ω scans around the (002) diffraction planes of the La-$BaSnO_3$ films is also a good indication of the films' crystalline quality [19, 73]. The FWHM is inversely proportional to the size of the grains (crystallites) [74, 75]. The smaller its value, the larger the crystallites size, and the lower the dislocations and scattering by grain boundaries [74]. Figure 4.17 shows the rocking curves with respect to the (002) peaks of the unbuffered and $BaSnO_3$ buffered films that are presented in Figs. 4.14. The rocking curve of the $SrZrO_3$ buffered sample is not shown because it was not measured. As illustrated in the figure, the FWHM values are consistent for all the films and vary from $0.043 \pm 0.001°$ to $0.130 \pm 0.001°$. Considering the FWHM values for the La-doped $BaSnO_3$ thin films listed in Table 4.10, it can be seen that these values are comparable to the values reported in Refs. [10, 17, 34, 35, 52, 76], and smaller than the value in Ref. [53]. However, smaller FWHM values are reported in Refs. [13, 14, 18, 37]. The FWHM values in the present La-doped $BaSnO_3$ thin films are also comparable to the small values varying from 0.015 to 0.400°,

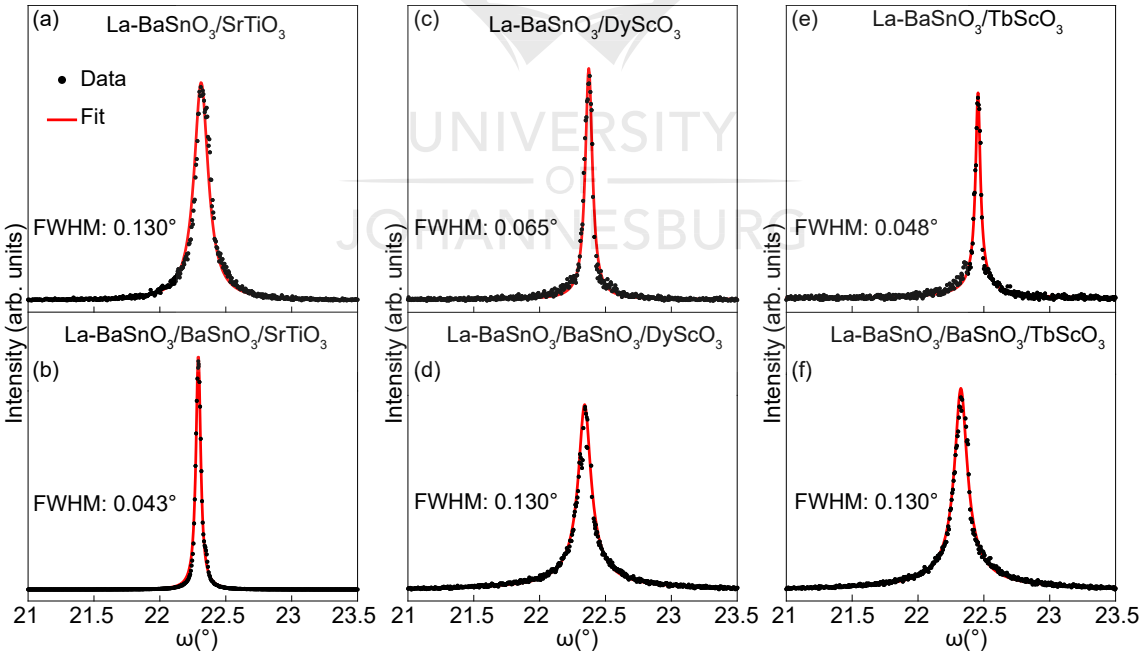

Figure 4.17: Rocking curves in ω scans around the (002) diffraction peaks of the unbuffered and $BaSnO_3$ buffered films grown on (a) and (b) $SrTiO_3$ (001), (c) and (d) $DyScO_3$ (110), and (e) and (f) $TbScO_3$ (110). These are the same samples shown in Fig. 4.14. The curves were fitted using Pearson VII peak function and the FWHM were extracted.

Table 4.10: FWHM values of the 6% La-$BaSnO_3$ films shown in Fig. 4.14 alongside the FWHM values of the La-$BaSnO_3$ films found in literature.

La-$BaSnO_3$ (LBSO) samples	Growth method	FWHM	References
6% LBSO unbuffered on $SrTiO_3$ (001)	PLD	0.130°	This study
6% LBSO unbuffered on $DyScO_3$ (110)	PLD	0.065°	This study
6% LBSO unbuffered on $TbScO_3$ (110)	PLD	0.048°	This study
6% LBSO buffered on $SrTiO_3$ (001)	PLD	0.043°	This study
LBSO buffered on $SrTiO_3$ (001)	MBE	0.048°	Prakash *et al.* [10]
4% LBSO unbuffered on $SrTiO_3$ (001)	PLD	0.086°	Mun *et al.* [17]
7% LBSO unbuffered on $SrTiO_3$ (001)	PLD	0.090°	Kim *et al.* [34]
7% LBSO unbuffered on $SrTiO_3$ (001)	PLD	0.093°	Wadekar *et al.* [35]
7% LBSO unbuffered on $SmScO_3$ (110)	PLD	0.090°	Wadekar *et al.* [35]
7% LBSO nbuffered on $SrTiO_3$ (100)	PLD	0.070°	Niedermeier *et al.* [52]
3% LBSO unbuffered on $SrTiO_3$ (001)	PLD	0.039°	Yu *et al.* [76]
7% LBSO unbuffered on $SrTiO_3$ (001)	PLD	0.570°	Wang *et al.* [53]
LBSO buffered on $DyScO_3$ (001)	MBE	0.016°	Paik *et al.* [13]
4% LBSO buffered on $BaSnO_3$ (001)	PLD	0.029°	Lee *et al.* [14]
0.5% LBSO buffered on $SrTiO_3$ (001)	PLD	0.008°	Shiogai *et al.* [18]
LBSO unbuffered on $TbScO_3$ (110)	MBE	0.006°	Lebens-Higgins *et al.* [37]

reported for PLD grown indium tin oxide thin films [19, 73]. The FWHM values reported here are indeed very small, and indicate a high degree of crystallinity in the films [14, 35, 52, 53]. However, these values are relatively broad compared to the FWHM of the substrates that vary between 0.003 and 0.017° as obtained from previous studies [10, 13, 37, 77]. This can be due to strain relaxations in the epitaxial layers, which are attributed to defects such as grain boundaries and dislocations [10, 17, 78, 79, 80].

4.4.3 Strain State of the Films

Asymmetric X-ray reciprocal space maps measurements provide more information about the strain states of the films, which, as discussed in Section 3.3.1, are mostly indicated by the extracted in-plane lattice constant (a) values. Figure 4.18 shows the reciprocal space mappings for the samples in Fig. 4.14 around the $(\bar{1}03)$ reflections of La-$BaSnO_3$ films peaks, the $(\bar{1}03)$ reflections of $SrTiO_3$ substrates peaks and the $(\bar{1}03)_p$ reflection of $DyScO_3$ and $TbScO_3$ substrates peaks (where the subscript p refers to pseudocubic indices). These data are for samples fabricated on $SrTiO_3$ (001) (Figs. 4.18(a) and 4.18(b)), $DyScO_3$ (110) (Figs. 4.18(c) and 4.18(d)) and $TbScO_3$ (110) (Figs. 4.18(e) and 4.18(f)), without and with $BaSnO_3$ buffer layers, respectively. The lattice parameters (a and c) values extracted from the position of the $(\bar{1}03)$ reflection peaks of the films as described in Section 3.3.1 are summarized in Table 4.11.

From Table 4.11, it can be observed that the unbuffered films are fully strained in the plane direction as their a values are very close to that of the respective substrates, and tetragonally distorted in the out-of-plane direction. The tetragonal distortion is more important for the film grown on $SrTiO_3$ (001), less pronounced for that grown on $DyScO_3$ (110) and almost not existent at all for the film deposited on $TbScO_3$ (110). These different degrees of expansion can be explained by the difference in lattice mismatches between the as-grown film and the respective substrates. For instance, the computed lattice mismatch to the film was found to be 5.70%

with $SrTiO_3$ (001), 4.46% with $DyScO_3$ (110) and 4.00% with $TbScO_3$ (110). Recall that in epitaxial thin films growth, the starting material usually has a larger in-plane lattice parameter (or bulk lattice parameter) compared to that of the substrate on which the thin film has to be grown, hence the lattice mismatch. As already discussed in Section 3.3.1, a pseudomorphic growth occurs when the grown film has an in-plane lattice constant that is equal to that of the underlying substrate. This suggests a lattice compression in the plane direction followed by a distortion in the out-of-plane direction. Thus, considering the a values in Table 4.11 for the unbuffered films for which the reciprocal space maps are shown in Figs. 4.18(a), 4.18(c) and 4.18(e), it is remarkable that pseudomorphic growths were favored over strain relaxations, that were expected to be favored considering the very high lattice mismatches between the as-deposited films and the substrates [12, 13, 16, 37]. This is most probably due to the small thicknesses of the epitaxial layers (25 nm). It can be assumed that at about 25 nm, the growing film layers have not yet reached the critical thickness above which strain relaxations should take place [16, 81, 82, 83, 84, 85]. Moreover, the films compression ratios in the plane which were evaluated as described in Section 3.3.1 are as follows: -1.00% on $SrTiO_3$ (001), -0.48% on $DyScO_3$ (110) and -0.90% on $TbScO_3$ (110). In other words, the in-plane lattice constants of the grown films are respectively 1.00%, 0.48% and 0.90% smaller on $SrTiO_3$ (001), $DyScO_3$ (110) and $TbScO_3$ (110) than the bulk lattice value of 6% La-doped $BaSnO_3$.

Unlike the unbuffered films, all the films containing $BaSnO_3$ buffer layers are strain relaxed (see the values in Table 4.11 and the discussions in Section 3.3.1). In fact, the film deposited on $SrTiO_3$ (001) is completely relaxed as its a and c values are comparable to the bulk lattice parameters of La-doped $BaSnO_3$, and those grown on $DyScO_3$ (110) and $TbScO_3$ (110) are partially relaxed. This observation is substantiated by the estimated relaxation [86], which indicates the strain level of the film with respect to the substrate. Indeed, the calculated relaxations revealed that the film prepared on $SrTiO_3$ (001) was 100.5% relaxed, implying that the film/substrate interface slightly undergoes strain beyond that needed to relieve misfit dislocations; the one deposited on $DyScO_3$ (110) was 95.0% relaxed and that grown on $TbScO_3$ (110) was 94.4% relaxed. Furthermore, the lattice strain (in the direction perpendicular to the surface) induced by lattice mismatches are 0.22% on $SrTiO_3$ (001), -0.05% on $DyScO_3$ (110) and -0.14% on $TbScO_3$ (110). As the lattice strain is a measure of the distribution of lattice constants (out-of-plane) originating from crystal defects, the above ratios would mean that an important amount of residual strain is present in the film grown on $SrTiO_3$ (001) [18, 86]. As a result, this film would contain more structural defects compared to the films prepared on the other two substrates [18, 86]. This is further confirmed in Section 4.5 related to the microstructural analysis. Moreover, the $(\bar{1}03)$ reflection peaks of the buffered films are very

Table 4.11: In-plane (a) and out-of-plane (c) lattice constants extracted from the reciprocal space maps in Fig. 4.18, for epitaxial La-doped $BaSnO_3$ thin films prepared on $SrTiO_3$ (001), $DyScO_3$ (110) and $TbScO_3$ (110) without and with $BaSnO_3$ buffer layers.

Lattice parameters		$SrTiO_3$ (001) 3.905 (Å)	$DyScO_3$ (110) 3.950 (Å)	$TbScO_3$ (110) 3.966 (Å)
Unbuffered films	a	4.080 ± 0.002	4.106 ± 0.002	4.089 ± 0.002
	c	4.167 ± 0.002	4.130 ± 0.002	4.126 ± 0.002
$BaSnO_3$ buffered films	a	4.127 ± 0.002	4.118 ± 0.002	4.117 ± 0.002
	c	4.135 ± 0.002	4.124 ± 0.002	4.120 ± 0.002

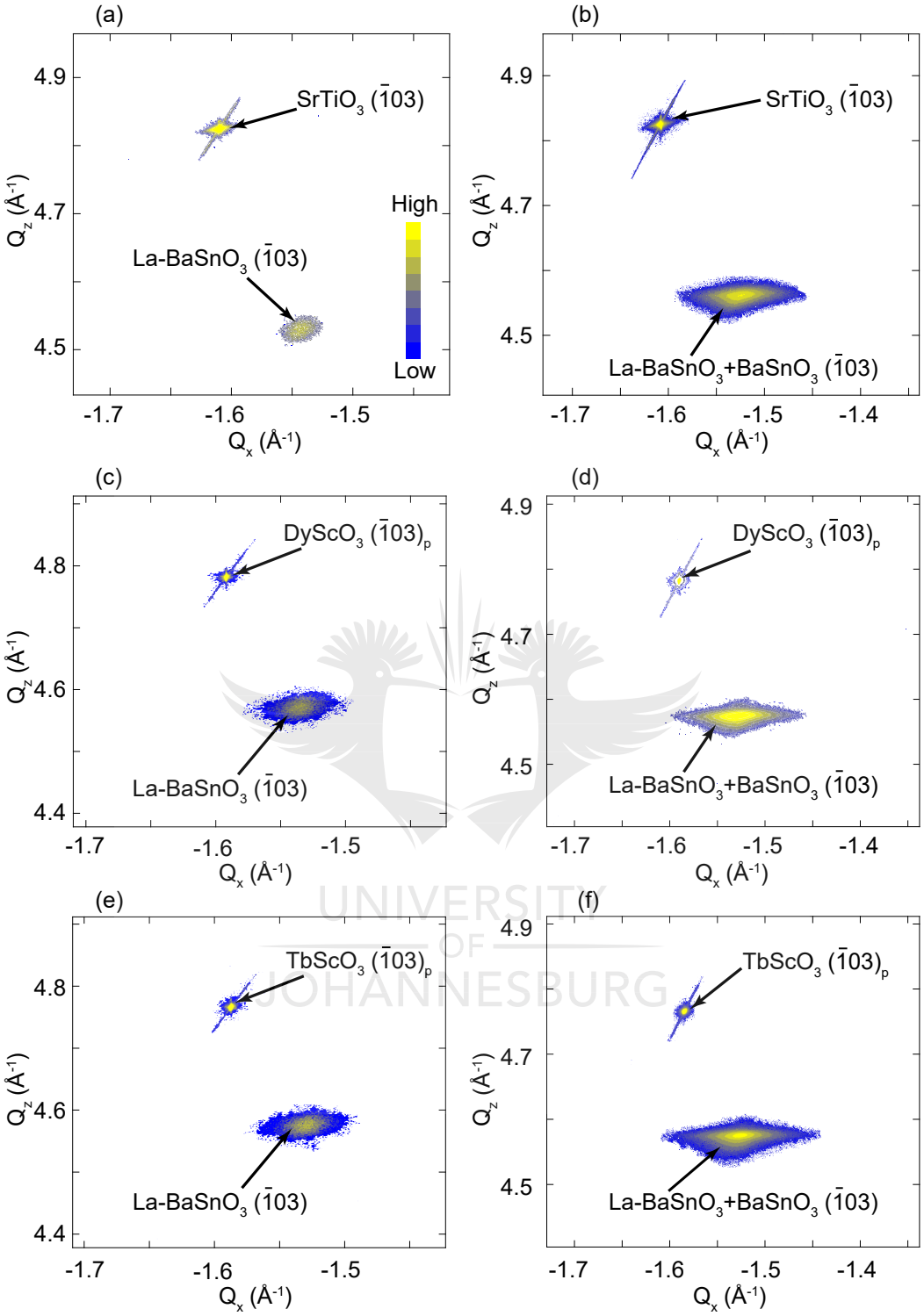

Figure 4.18: Reciprocal space maps around the asymmetric ($\bar{1}03$) La-$BaSnO_3$ and La-$BaSnO_3$+$BaSnO_3$ reflection peaks, the ($\bar{1}03$) reflection peaks of $SrTiO_3$ substrates, and the $(\bar{1}03)_p$ reflection peaks of $DyScO_3$ and $TbScO_3$ substrates, where p refers to pseudocubic indices. These reciprocal space mappings were performed on the samples presented in Fig. 4.14. These are for films grown on (a) and (b) $SrTiO_3$ (001), (c) and (d) $DyScO_3$ (110), and (e) and (f) $TbScO_3$ (110), without and with a $BaSnO_3$ buffer layer, respectively.

broad (also compared to unbuffered films; see Fig. 4.18), suggesting the presence of a large number of dislocation defects in $BaSnO_3$ buffered films [35].

It is well established that improved electronic transport properties are achieved in La-doped $BaSnO_3$ thin films containing adhesion layer(s) (especially made of $BaSnO_3$) between the film layer and the substrate [10, 13, 18, 26, 28, 29, 30, 44]. Thus, the active layer is deposited on a fully matched interface, and establishes epitaxial strain relationship with the host which is a similar material. This is very clearly demonstrated in the buffered films shown in Figs. 4.18(b), 4.18(d) and 4.18(f), where the $(\bar{1}03)$ reflections of the La-doped $BaSnO_3$ films only present a single peak composed of La-$BaSnO_3$ and $BaSnO_3$. However, such structures generally tend to relax due to the thickness [13, 44, 83, 84, 85], resulting in the introduction of defects such as dislocations in the epitaxial layer as demonstrated above. It is good practice to use lattice matched insulating layer(s) to reduce the lattice mismatch with the substrate, but it is preferable to have as low structural defects as possible in the films for functional device applications [10, 13, 18, 26, 28, 29, 30, 44]. In an attempt to address the issue of the large density of defects in La-doped $BaSnO_3$ thin films, an insulating layer of $SrZrO_3$ grown at extremely high temperature, 1300 °C, was inserted between the La-doped $BaSnO_3$ film and the $TbScO_3$ (110) substrate, as already described in Section 4.3. As a result, not only improved electronic transport properties above those reported to date for similar growth technique and without post-growth treatment [38] were achieved, but also a significant reduction of the density of structural defects was simultaneously realized as demonstrated below. In Fig. 4.19, the reciprocal space maps around the $(\bar{1}03)$ reflections of the samples grown with $SrZrO_3$ are shown (same samples as in Fig. 4.15). Figure 4.19(a) shows the $(\bar{1}03)$ reflection of the $SrZrO_3$ film grown at 1300 °C on $TbScO_3$ (110) substrate, and Fig. 4.19(b) shows that of the subsequent La-doped $BaSnO_3$ film deposited on the $SrZrO_3$ layer. The difference in peak broadening can be directly detected when comparing the film reflection in Fig. 4.19(b) with that in Fig. 4.18(f) for the $BaSnO_3$ buffered film grown on $TbScO_3$ (110). As can be clearly seen, the film peak in Fig. 4.18(f) is broad, indicating the presence of an important number of dislocations, whereas that in Fig. 4.19(b) is sharp and suggests fewer defects in the film [35, 87, 88]. Additionally, the La-$BaSnO_3$ film peak and that of the $SrZrO_3$ buffer layer are well separated and located on a perpendicular line to the reciprocal vector Q_x (red dashed line in Fig. 4.19(b)), demonstrating a strained relationship between the film and the buffer layer [30, 83]. This further substantiates the low density of defects in this sample [87, 88].

Table 4.12 summarizes the values of the lattice parameters for the films in Fig. 4.19. Two additional columns are added in the table. A column for the $SrZrO_3$ film layer deposited on $TbScO_3$ (110) at 1400 °C (see Appendix B for its reciprocal space map); and another for the film in Fig. 4.18(f) to allow a direct comparison. In order to follow the discussion below, it should be mentioned that the bulk lattice parameter of cubic $SrZrO_3$ (in its cubic phase above about 1200 °C) is $\approx$ 4.109 Å [45, 46]. Looking at Table 4.12, it can be seen that $SrZrO_3$ films (insulating) grown at 1300 °C and 1400 °C are fully strained to $TbScO_3$ (110) substrates, with subsequent tetragonal distortions in the c direction. As previously mentioned, it can also be seen that the epitaxial La-doped $BaSnO_3$ thin film layer deposited on the substrate template in Fig. 4.19(a) ($SrZrO_3$ layer plus $TbScO_3$ (110) substrate) is fully strained in the a direction and residually strained (or partially relaxed) in the c direction, as opposed to $BaSnO_3$ buffered film which is almost completely relaxed. However, the fact that its c value (4.113 ± 0.002 Å) is smaller than the bulk lattice value of La-doped $BaSnO_3$ ($\approx$ 4.126 Å) should be noted. This is absolutely unexpected in fully strained epitaxial relationships, which originate from

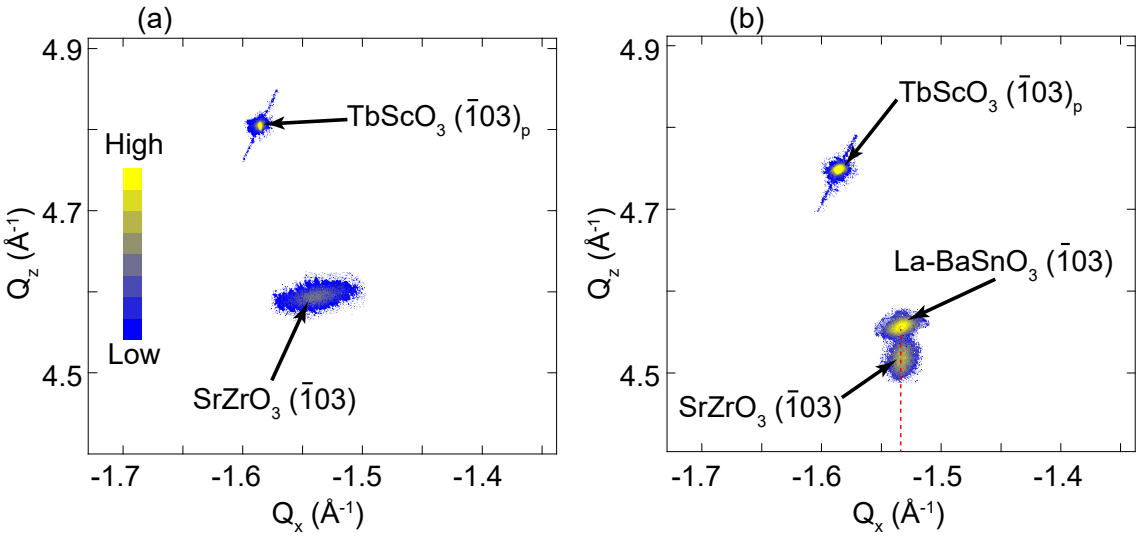

Figure 4.19: Reciprocal space maps for epitaxial thin films grown on $TbScO_3$ (110), around the asymmetric $(\bar{1}03)$ La-$BaSnO_3$ and $SrZrO_3$ reflection peaks, and the $(\bar{1}03)_p$ reflection peaks of $TbScO_3$ substrates, where p refers to pseudocubic indices. These measurements were done on (a) the $SrZrO_3$ film that was grown at 1300 °C, and (b) the 6% La-$BaSnO_3$ thin film that was subsequently deposited on the $SrZrO_3$ layer.

compressive strains in the plane, and are normally accompanied by tetragonal distortions with no strains or stresses in the out-of-plane direction [86]. It is not clear why this is observed in the film, however, it is proposed that the interface defect density or reconstruction effects might dominate the bulk strain considering the fact that the active layer is thin in line with previous reports in literature [81, 82, 83, 84, 85].

To further demonstrate the high structural quality of this sample, the sample with the $SrZrO_3$ buffer layer, the lateral grain size (D) for each of the samples shown in Figs. 4.18 and 4.19 was computed. The values of D were determined by fitting the contour profiles of the $(\bar{1}03)$ reflection spots of the films. These profiles are shown in Fig. 4.20 and represent the distribution of the size of the crystalline domain (crystallites) along the Q_x direction. These correspond to horizontal cuts in the reciprocal space maps, i.e. cuts at fixed Q_y values which give the highest intensities of the peak cross section profiles. Table 4.13 summarizes the extracted values of D. Several remarks can be made, and all are in good agreement with our previous observations. As can be seen in the table, the films prepared on $SrTiO_3$ (001) have the smallest

Table 4.12: In-plane (a) and out-of-plane (c) lattice constants for epitaxial thin films of $SrZrO_3$ and La-doped $BaSnO_3$ which contain $BaSnO_3$ and $SrZrO_3$ buffer layers. All these data are for the samples prepared on $TbScO_3$ (110) for which the reciprocal space map are shown in Fig. 4.19.

	Films deposited on $TbScO_3$ (110) substrates (3.966 Å)			
Lattice parameters	$SrZrO_3$ growth at 1300 °C (Å)	$SrZrO_3$ growth at 1400 °C (Å)	$BaSnO_3$ buffered film (Å)	$SrZrO_3$ buffered film (Å)
a	4.085 ± 0.002	4.093 ± 0.002	4.117 ± 0.002	4.103 ± 0.002
c	4.128 ± 0.002	4.114 ± 0.002	4.120 ± 0.002	4.113 ± 0.002

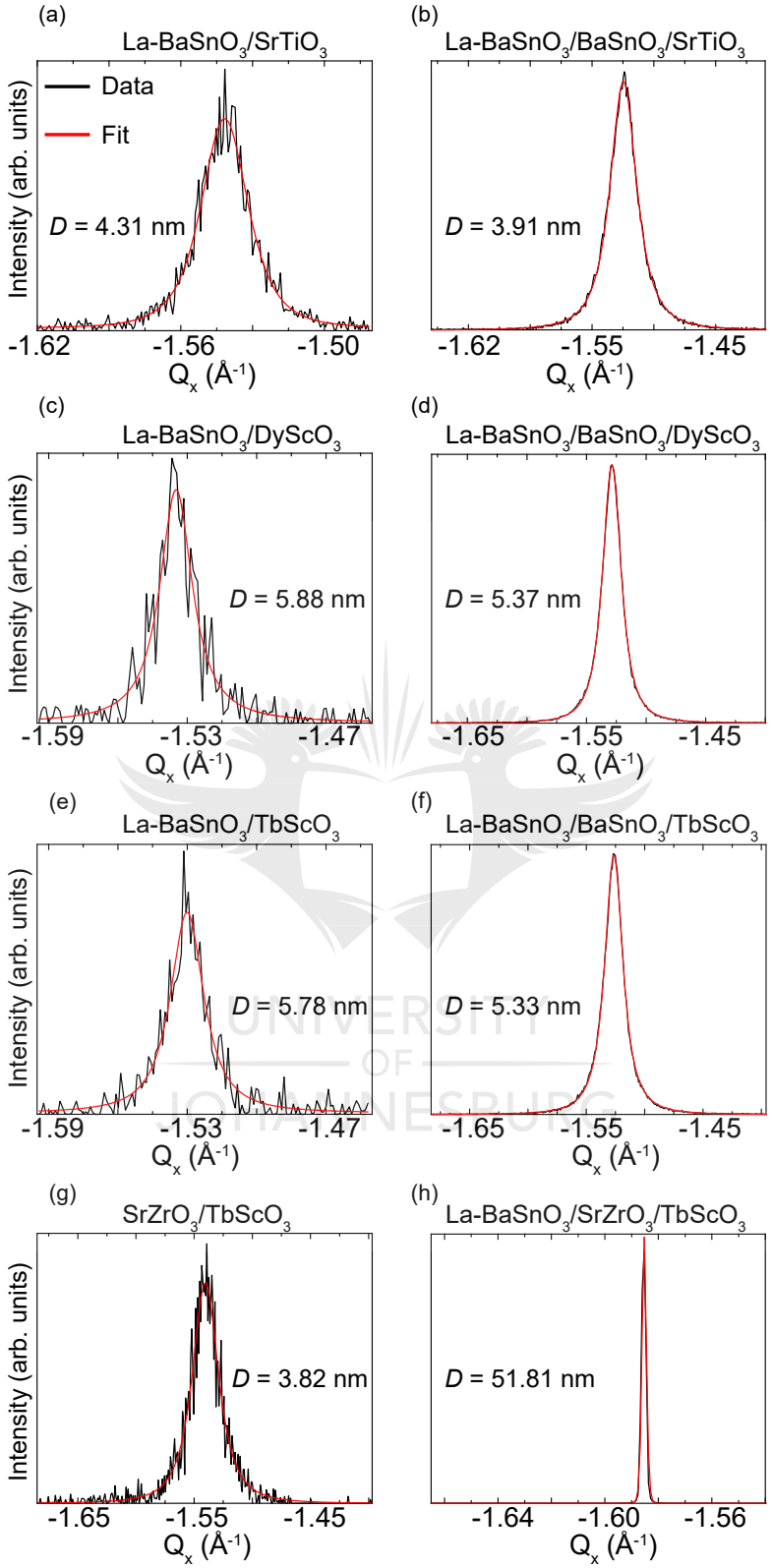

Figure 4.20: Contour profiles of the $(\bar{1}03)$ diffraction spots of the films along the Q_x axis. The profiles are extracted from the reciprocal space maps in Figs. 4.18 and 4.19. The lateral grain sizes D, which are inversely proportional to the FWHM, were determined by peak function fits of the profiles using Pearson VII.

Table 4.13: Lateral grain size D for the unbuffered and $BaSnO_3$ and $SrZrO_3$ buffered films in Figs. 4.18 and 4.19, prepared on $SrTiO_3$ (001), $DyScO_3$ (110) and $TbScO_3$ (110). The values are estimated from the widths of the contour profiles of the $(\bar{1}03)$ diffraction peaks of the La-$BaSnO_3$ films along the Q_x direction in the reciprocal space maps.

Substrates	Unbuffered films D (nm)	$BaSnO_3$ buffered films D (nm)	$SrZrO_3$ buffered film D (nm)
$SrTiO_3$ (001)	4.3 ± 0.1	3.91 ± 0.02	—
$DyScO_3$ (110)	5.9 ± 0.4	5.37 ± 0.02	—
$TbScO_3$ (110)	5.8 ± 0.3	5.33 ± 0.02	52 ± 1

D values, hence would have more grain boundary defects. Also, it appears that D is relatively larger in the unbuffered films, confirming that these films have fewer defects (grain boundaries) compared to the $BaSnO_3$ buffered films. Finally, it can be observed from the table that the size of the crystallites is the largest in $SrZrO_3$ buffered film, about 10 times larger compared to that in $BaSnO_3$ buffered films. This was expected, considering the analyses carried out above. Microstructural investigations that follow in Section 4.5 reveal that the density of defects in this film is greatly reduced.

A correlation was observed between the electronic and structural characteristics of the La-doped $BaSnO_3$ films prepared with $SrZrO_3$ buffer layers grown at various temperatures, from 850 °C to 1600 °C. A synopsis of this correlation is reflected in Table 4.14. Looking at the table, it can be directly observed that all these films are strained in the plane direction and distorted in the out-of-plane direction. However, a strong correlation exists between the RT transport properties (carrier concentration, n, and mobility, μ,) and the in-plane (a) and out-of-plane (c) lattice parameters. For instance, in the films prepared at 1300 °C and 1400 °C, the tetragonal distortions in the c directions are the lowest. The highest RT electron mobilities are then achieved in these films. Also, the films with $SrZrO_3$ buffer layers deposited at 850 °C, 1200 °C and 1600 °C have very similar c values. However, their electronic transport properties are different. Especially, the mobility value for the film grown at 850 °C is about half of the mobility values realized in the films grown at 1200 °C and 1600 °C. Furthermore, the carrier density in the film prepared at 850 °C is reduced by more than half, in comparison with the

Table 4.14: Synopsis of the room temperature electronic transport (carrier density n and mobility μ) and structural (in-plane a and out-of-plane c lattice parameters) properties of different La-$BaSnO_3$ (25 nm)/$SrZrO_3$ (100 nm)/$TbScO_3$ films with respect to the growth temperatures of the $SrZrO_3$ buffer layer.

$SrZrO_3$ growth temperature (°C)	In-plane lattice constant a (Å)	Out-of-plane lattice constant c (Å)	Carrier density at 300 K n ($\times 10^{20}$ cm^{-3})	Mobility at 300 K μ (cm^2 V^{-1} s^{-1})
850	4.090 ± 0.002	4.136 ± 0.002	1.81 ± 0.02	50 ± 1
1200	4.070 ± 0.002	4.140 ± 0.002	4.63 ± 0.06	97 ± 3
1300	4.103 ± 0.002	4.113 ± 0.002	5.21 ± 0.08	140 ± 4
1300	4.103 ± 0.002	4.113 ± 0.002	5.23 ± 0.08	137 ± 4
1400	4.100 ± 0.002	4.115 ± 0.002	4.66 ± 0.06	127 ± 4
1600	4.060 ± 0.002	4.142 ± 0.002	4.95 ± 0.06	101 ± 3

carrier density in the films grown at 1200 °C and 1600 °C. These observations confirm the assumption that low temperature grown buffer layer results in more threading dislocations in the films that lower both the carrier density and electron mobility. In epitaxial thin films, the strong relationship between transport and structural characteristics is even more appreciable at the atomic level, when performing microstructural analysis that will be addressed in Section 4.5.

4.5 Defect Density

Epitaxial thin films generally suffer structural defects originating from several sources such as the growth technique, the surface quality of the host material which is crucial for interfacial interaction with the as-deposited film, as well as the lattice mismatch between the host and the film deposited on top [18, 29, 35, 62, 89]. The major defects found in epitaxially grown thin films are either located at the interface or running across the film thickness, parallel to the growth direction [10, 13, 18, 26, 28, 29, 30, 44]. These defects induce electron scattering centers in the film lattice [10, 90, 91]. It is indeed difficult to talk about structural or microstructural defects in epitaxial thin films without referring to their consequences on the electronic transport properties as demonstrated in Section 2.2.3.

Dislocations are found to be one of the major structural defects influencing the electron mobility in degenerate semiconductors [13, 44, 65, 90, 91, 92, 93, 94]. From TEM measurements, it has been determined that the dislocations in epitaxial thin films, such as conventional *n*-type GaN semiconductors [13, 65, 90, 91, 92, 93] and La-doped $BaSnO_3$ [13, 44, 94], are edge-type threading dislocations. These threading dislocations are traps for electrons as they insert acceptor cores along the dislocation lines, which attract electrons from the conduction band and become negatively charged [90, 91]. The electrons moving across are then scattered, resulting in reduction of electrical mobility [90, 91]. The density of threading dislocations in epitaxial GaN thin films was reported to vary between $\approx 2\times10^{6}$ cm^{-2} and $\approx 2\times10^{10}$ cm^{-2}, although the impact of scattering at charged dislocation lines on the mobility becomes important at densities above 10^{9} cm^{-2} [65, 90, 91, 93, 95, 96, 97]. A higher density, in the range of 10^{11} cm^{-2}, is however reported in MBE and PLD grown epitaxial La-doped $BaSnO_3$ thin films, and could be the origin of the limit threshold of the electronic mobility in this system [13, 44, 94]. In this section, the microstructural data of epitaxial La-doped $BaSnO_3$ thin films that will give an idea of the correlation between structural and electronic properties are discussed. These data are acquired with TEM measurements as described in Section 3.3.2, in conditions where the Burgers vectors were parallel to the film/substrate interfaces.

4.5.1 Microstructural Analysis

The structure of the defects in epitaxial thin films can be revealed at the atomic level using the TEM measurement technique, which provides information about the interface quality, the structure of grain boundaries, the crystallographic orientation and the individual phases [83, 84, 98, 99]. Here, qualitative and quantitative analyses of the data obtained from cross-sectional TEM measurements on the optimized $BaSnO_3$ and $SrZrO_3$ buffered samples prepared on $SrTiO_3$ (001), $DyScO_3$ (110) and $TbScO_3$ (110) substrates will be carried out. The $BaSnO_3$ buffered samples used for the TEM measurements were grown in the same conditions and with the same parameters as the $BaSnO_3$ buffered films presented in Fig. 4.13. It was decided to only perform TEM measurements on the buffered samples because of the need to correlate their microstructure with the high electron mobility achieved in these samples. The results of

the measurements are presented in Figs. 4.21 to 4.25. The TEM images in Fig. 4.21 are for the film deposited on $SrTiO_3$ (001); those in Figs. 4.22 and 4.24 are for the film grown on $DyScO_3$ (110); and the ones in Figs. 4.23 and 4.25 are for the film prepared on $TbScO_3$ (110), with $BaSnO_3$ and $SrZrO_3$ buffer layers, respectively. For clarity, only few contrast details will be represented with arrows or symbols.

In all the films, three types of defects were observed, comparable to those discussed in Section 2.2.3, namely misfit edge dislocations, stacking faults, and threading dislocations. These dislocations are the result of the large lattice mismatch between La-doped $BaSnO_3$ films and the respective substrates [10, 13, 18, 26, 28, 29, 85]. For instance, misfit dislocations are created at or near the film/substrate interface to release lattice mismatch [100, 101, 102, 103], followed by the generation of dislocations which thread across the film layer from the interface to the surface [104, 105]. Interfacial misfit dislocations (white circles) along with threading dislocations (green arrows) and stacking faults (yellow arrows) can be seen in the high resolution TEM (HRTEM) micrographs of the films as shown in Figs. 4.21(a), 4.21(b), 4.22(a), 4.22(b), 4.23(a) and 4.23(b). These misfit dislocations are manifested by the presence of extra atom planes at the interface represented by the $\perp$ symbols in Figs. 4.21(a), 4.22(a) and 4.23(a). The threading dislocations seem to have been created near the interface and propagate to the surface as shown by the green arrows in Figs. 4.21(b), 4.22(b) and 4.23(b). Furthermore, one can observe that the stacking faults (yellow arrows) are more pronounced in the films prepared on $SrTiO_3$ (001) (Fig. 4.21(b)) and $TbScO_3$ (110) (Fig. 4.23(b)) than in that prepared on $DyScO_3$ (110) (Fig. 4.22(b)). Additionally, polygon like shapes whose corners are indicated with thin yellow arrows in Figs. 4.21(a), 4.21(b) and 4.23(a) are also visible in the prepared films. These are believed to be Ruddlesden-Popper faults [94], which are a particular type of stacking faults characterized by their polygonal shape. Indeed, similar defect shapes were recorded in plan-view TEM measurements of PLD grown 0.001% La-$BaSnO_3$/$LaScO_3$/$SrTiO_3$ [94] and MBE grown $BaSnO_3$/$SrTiO_3$ [106] heterostructures, where a high density of stacking faults and threading dislocations were recorded [94].

Moreover, in the medium angle annular dark-field (MAADF) images for the films grown on $SrTiO_3$ (001) and $TbScO_3$ (110), dense defects which are extended in the films and parallel to the interface are revealed, as presented in Figs. 4.21(c), 4.21(d), 4.23(c) and 4.23(d) respectively. The extended defects marked with yellow, thin yellow and green arrows are determined to be stacking faults, Ruddlesden-Popper faults and threading dislocations, respectively; and those parallel to the interface indicated by yellow arrows are stacking faults [13, 94]. On the other hand, the high angle annular dark-field (HAADF) images for the film fabricated on $DyScO_3$ (110) characterize the relaxed interface [13] between the film and the substrate. The relaxed interface is evidenced by the Ruddlesden-Popper faults and extended defects [13] respectively illustrated by thin yellow and green arrows in Figs. 4.22(c) and 4.22(d), and the extra atom planes at the interface in Fig. 4.22(d) suggesting interfacial edge dislocations as indicated by the $\perp$ symbols. One such dislocation delimited by the white rectangle in Fig. 4.22(d) is enlarged and shown in the inset, where structural details at the interface can be seen. It is an interfacial dislocation core with a Burgers circuit drawn around it [13]. The cyan arrow indicates the closure of the circuit with a Burgers vector parallel to the interface.

In summary, the TEM data of the La-doped $BaSnO_3$ thin films grown with $BaSnO_3$ buffer layers on $SrTiO_3$ (001) (Fig. 4.21), $DyScO_3$ (110) (Fig. 4.22) and $TbScO_3$ (110) (Fig. 4.23) substrates showed the presence of misfit dislocations at the film/substrate interfaces, together with parallel (to the interface) and extended (perpendicular to the interface) defects in the

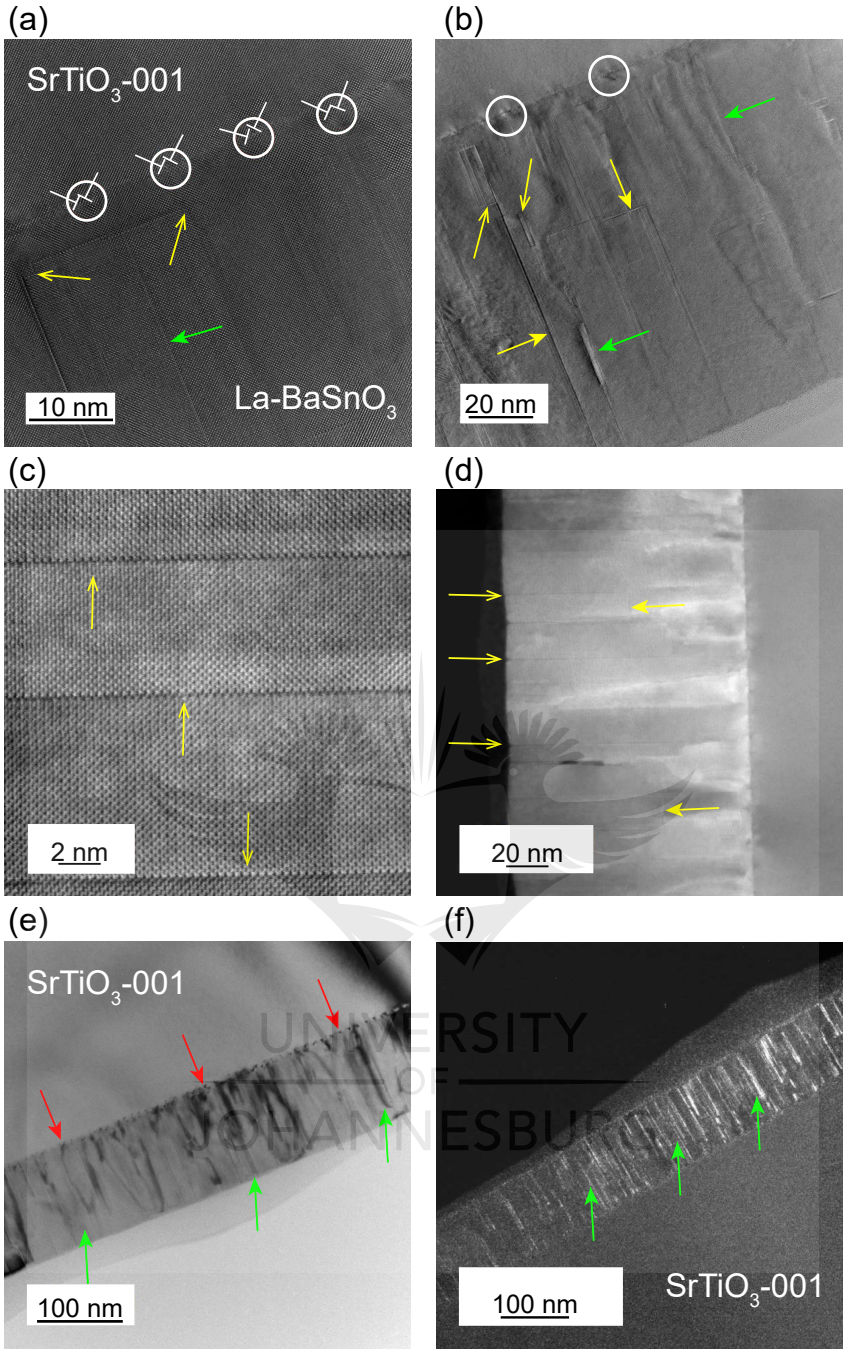

Figure 4.21: Cross-sectional TEM images of a 6% La-$BaSnO_3$ (25 nm)/$BaSnO_3$ (100 nm)/$SrTiO_3$ film. (a) and (b) are HRTEM images of the La-$BaSnO_3$ film and the $SrTiO_3$ (001) substrate, showing misfit dislocations at their interface marked with white circles and $\perp$ symbols; stacking faults and threading dislocations in the film layer respectively marked with yellow and green arrows. The thin yellow arrows point at the corners of the Ruddlesden-Popper faults. MAADF images of the (c) film only and (d) film and substrate, revealing extended defects in the film, Ruddlesden-Popper faults (thin yellow arrows), and sharp defects parallel to the interface (yellow arrows). (e) Bright field TEM image revealing periodic misfit dislocations (dark spots indicated by red arrows) at the interface, spaced by $\approx$ 10 nm; and threading dislocations (vertical dark contrasts indicated by green arrows) in the film. (f) WB-DFTEM image showing threading dislocations (vertical bright contrasts) running across the film from the interface to the surface and represented by green arrows.

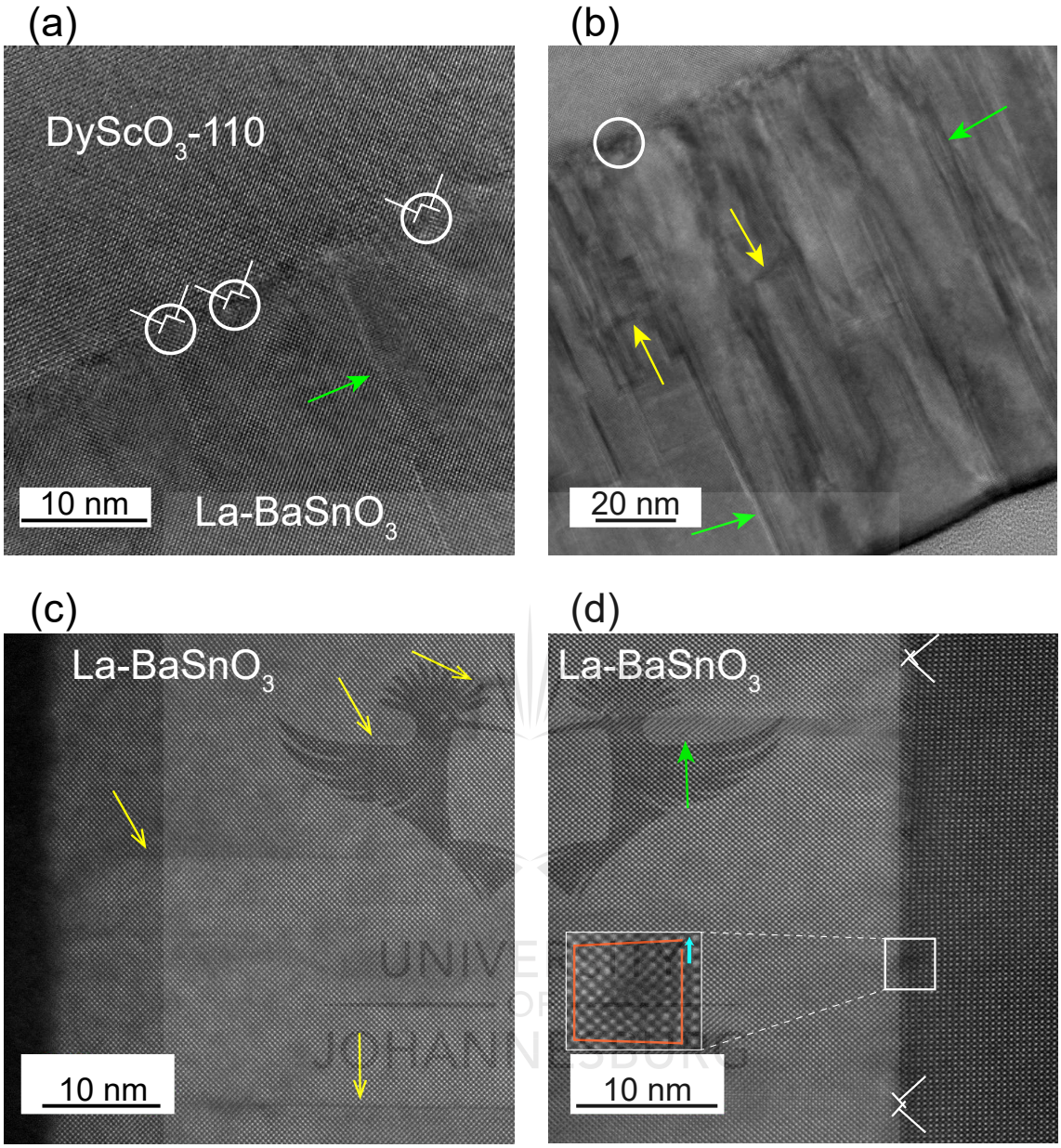

Figure 4.22: Cross-sectional TEM micrographs of a 6% La-$BaSnO_3$ (25 nm)/$BaSnO_3$ (100 nm)/$DyScO_3$ thin film. (a) and (b) are HRTEM images of the La-$BaSnO_3$ film and the $DyScO_3$ (110) substrate, showing misfit dislocations at their interface marked with white circles; stacking faults and threading dislocations in the film layer respectively marked with yellow and green arrows. HAADF images of the (c) film only and (d) film and substrate, revealing Ruddlesden-Popper faults (thin yellow arrows) and an extended defect (green arrows) in the film, and misfit dislocations at the interface indicated by the $\perp$ symbols. The inset in (d) represents a high magnification around one of the misfit dislocations delimited by the white rectangle, where a lack of closure of the Burgers circuit is seen.

films. The presence of these defects in the films and at the interfaces suggests relaxed interfaces between the buffered La-doped $BaSnO_3$ films and the substrates, in agreement with our previous conclusions drawn upon reciprocal space maps data (see Section 4.4.3). These observations are also comparable with the relaxed interfaces reported in La-$BaSnO_3$ thin films grown

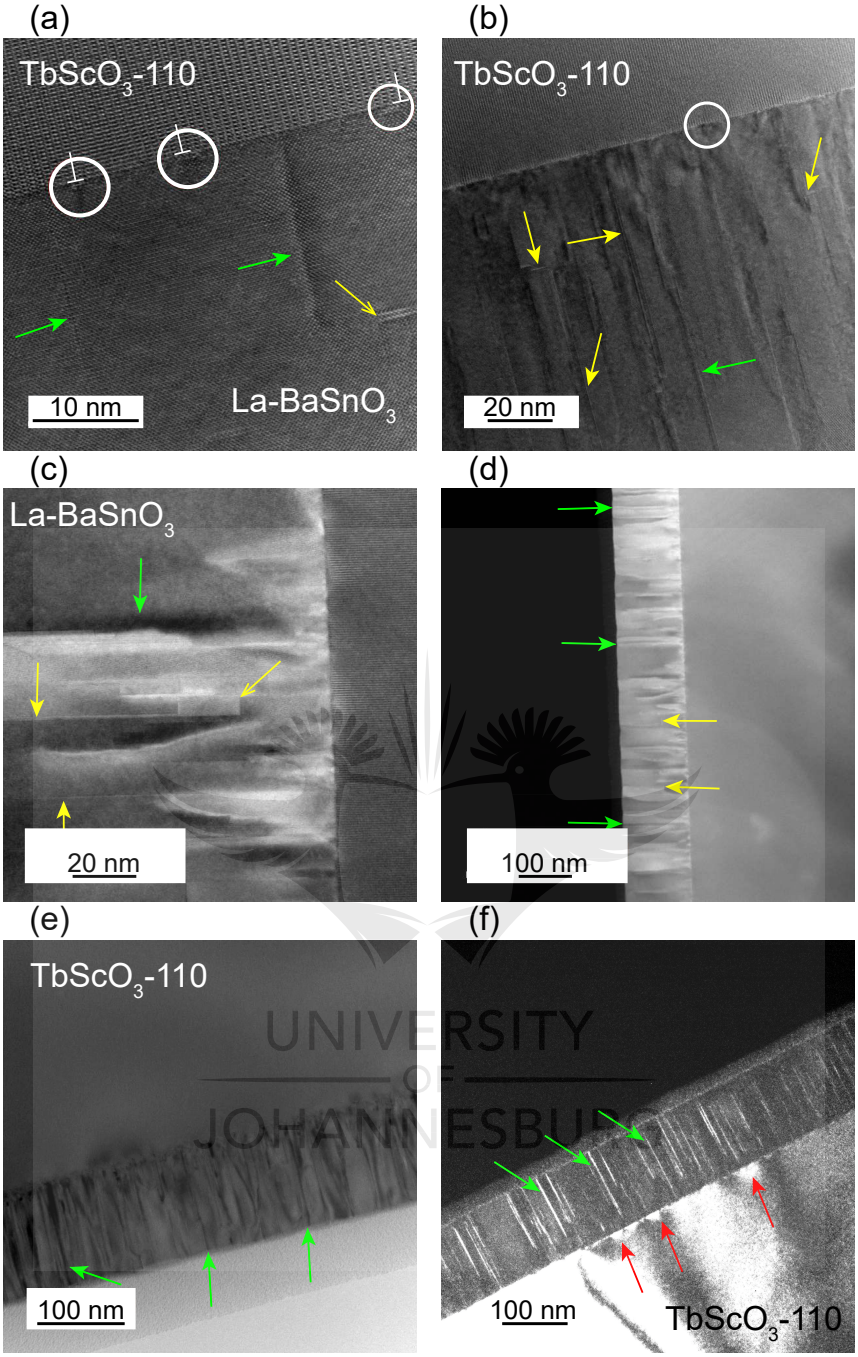

Figure 4.23: Cross-sectional TEM micrographs of a 6% La-$BaSnO_3$ (25 nm)/$BaSnO_3$ (100 nm)/$TbScO_3$ film. (a) and (b) are HRTEM images of the La-$BaSnO_3$ film and the $TbScO_3$ (110) substrate, showing misfit dislocations at their interface marked with white circles and $\perp$ symbols; stacking faults and threading dislocations in the film layer respectively marked with yellow and green arrows. (c) and (d) are MAADF images of the film and substrate, revealing extended defects in the film (yellow and green arrows), and sharp defects parallel to the interface (yellow arrows). The thin yellow arrows in (a) and (c) point at the corners of the Ruddlesden-Popper faults. (e) Bright field TEM image revealing threading dislocations in the film (vertical dark contrasts indicated by green arrows). (f) WB-DFTEM image showing an array of misfit dislocations (bright spots indicated by red arrows) at the interface; and threading dislocations (vertical bright contrasts) running across the film from the interface to the surface and illustrated with green arrows.

by PLD, MBE and high pressure oxygen sputtering on $SrTiO_3$ (001) [12, 16, 30, 52, 94, 106], $DyScO_3$ (001) [13] and $PrScO_3$ (110) [12, 107] substrates.

Quantitative analysis of the defects present in the La-doped $BaSnO_3$ films was carried out by counting the number of contrast details in the bright field TEM and weak beam dark field TEM (WB-DFTEM) micrographs [13, 17, 18, 26, 27, 30] of the films prepared on $SrTiO_3$ (001), $DyScO_3$ (110) and $TbScO_3$ (110) substrates. The bright field TEM images for the films grown on the respective substrates are shown in Figs. 4.21(e), 4.24(a) and 4.23(e); whereas the WB-DFTEM images are shown in Figs. 4.21(f), 4.24(b), 4.24(c), and 4.23(f). In these images, some of the misfit dislocations found at the film/substrate interfaces are marked with red arrows; the stacking faults and threading dislocations found in the epitaxial layers are marked with yellow and green arrows, respectively. It is noteworthy that the theoretical misfit dislocation spacing (d_{misfit}) which is calculated from the in-plane lattice parameters of the film (a) and the substrate (a_s) extracted from the reciprocal space mapping, is given by the formula [52, 108]

$$d_{\text{misfit}} = \frac{a \times a_s}{a - a_s}. \tag{4.1}$$

The dark spots at the La-$BaSnO_3$/$SrTiO_3$ interface in the bright field image (red arrows in Fig. 4.21(e)) are periodic misfit dislocations separated by ≈ 10 nm. This spacing is larger than the expected theoretical d_{misfit} value of 7.26 nm calculated from the in-plane lattice parameter summarized in Table 4.11 for the fully relaxed buffered film prepared on $SrTiO_3$ (001). This discrepancy in the dislocation spacing suggests a large dislocation density in the film. On the other hand, the equidistant misfit dislocations, seen as bright dots at the La-$BaSnO_3$/$DyScO_3$ interface (red arrows in Fig. 4.24(b)), are ≈ 10 nm apart, a value that is in agreement with the calculated value of 9.7 nm obtained from the analytical expression in Equation (4.1) using the lattice parameter value for the partially relaxed buffered film deposited on $DyScO_3$ (110) (see Table 4.11). These bright dots can be seen at the interface in the WB-DFTEM image shown in Fig. 4.24(b). On the contrary, an array of non equally spaced misfit dislocations are observed as bright dots at the La-$BaSnO_3$/$TbScO_3$ interface in the WB-DFTEM image of the film grown on $TbScO_3$ (110) (red arrows in Fig. 4.23(f)). The experimental and calculated values reported above are consistent with those found in literature for La-doped $BaSnO_3$ thin films deposited on $SrTiO_3$ (001) [12, 16, 27, 52, 108, 109, 110] and $DyScO_3$ (001) [13] substrates. The d_{misfit} values reported in this present study are summarized in Table 4.15 alongside the d_{misfit} values found in literature.

As for the threading dislocations, it can be seen (Figs. 4.21(f), 4.23(f) and 4.24(c)), at first glance, that these are denser in the film grown on $SrTiO_3$ (001) in comparison with the films deposited on the other two substrates. This observation is sustained by the density of the vertical bright contrasts indicated by the green arrows in the WB-DFTEM micrographs shown in Figs. 4.21(f) ($SrTiO_3$ (001)), 4.24(c) ($DyScO_3$ (110)) and 4.23(f) ($TbScO_3$ (110)). In fact, in a 16 nm thick specimen grown on $SrTiO_3$ (001), 80 dislocation lines within 500 nm in the specimen were counted, resulting in a dislocation density of 10×10^{11} cm^{-2}. On the other hand, 37 and 39 dislocation lines were counted within the same distance in 14 nm and 16 nm thick specimens respectively prepared on $DyScO_3$ (110) and $TbScO_3$ (110), giving a dislocation density of 5×10^{11} cm^{-2} for both specimens. It is therefore evident that there are twice as many dislocations in the film deposited on $SrTiO_3$ (001) than in the films deposited on

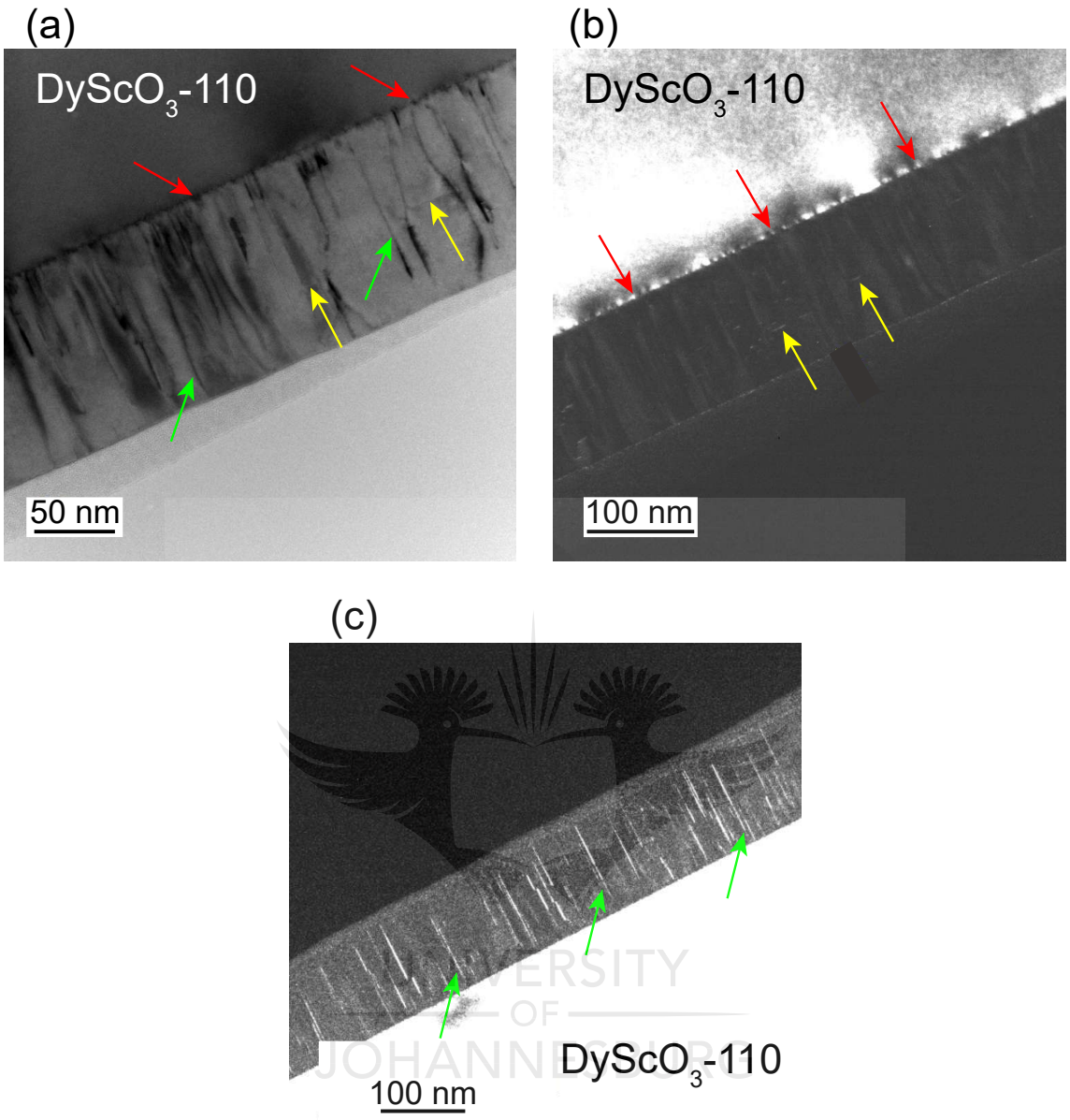

Figure 4.24: (a) Bright field, and (b) and (c) WB-DF cross-sectional TEM micrographs of a 6% La-$BaSnO_3$ (25 nm)/$BaSnO_3$ (100 nm)/$DyScO_3$ thin film. Arrays of equidistant misfit dislocations, dark dots in (a) and bright dots in (b) are visible at the interface and marked by red arrows. Their average distance is $\approx$ 10 nm. Few sharp and short defects parallel and perpendicular to the interface (yellow arrows) are also visible, probably representing stacking faults. Many threading dislocations (vertical dark contrasts in (a) and vertical bright contracts in (c)) are indicated by green arrows.

$DyScO_3$ (110) and $TbScO_3$ (110). These dislocation densities are recapitulated in Table 4.16, together with previously reported dislocation density values in La-doped $BaSnO_3$ thin films. As can be seen from the table, the dislocation densities in the grown films are consistent with those reported in unbuffered and buffered La-doped $BaSnO_3$ films grown by PLD on MgO [26, 27], and by MBE on $DyScO_3$ (001) [13] and Si (001) [30] substrates; and are one order of magnitude higher than those reported in unbuffered and buffered La-doped $BaSnO_3$ films

Table 4.15: Synopsis of the theoretical and experimental values of the misfit dislocation spacing (d_{misfit}) in the La-doped $BaSnO_3$ films grown with $BaSnO_3$ buffer layer on $SrTiO_3$ (001), $DyScO_3$ (110) and $TbScO_3$ (110) substrates, shown in Figs. 4.21 to 4.24. The d_{misfit} values found in literature are given for comparison. CSD stands for chemical solution deposition and OSD stands for oxygen sputter-deposition.

Substrates	Growth method	Theoretical d_{misfit} (nm)	Experimental d_{misfit} (nm)	References
$SrTiO_3$ (001)	PLD	7.26	10.00	This study
$SrTiO_3$ (001)	PLD	—	7.30	Sanchela *et al.* [27]
$SrTiO_3$ (001)	PLD	—	7.40	Sanchela *et al.* [110]
$SrTiO_3$ (001)	PLD	—	8.00	Ismail-Beigi *et al.* [109]
$SrTiO_3$ (001)	CSD	7.39	7.30	Wei *et al.* [108]
$SrTiO_3$ (001)	OSD	7.50	7.00–8.00	Ganguly *et al.* [16]
$SrTiO_3$ (001)	MBE	8.00	8.00	Raghavan *et al.* [12]
$SrTiO_3$ (001)	PLD	7.90	7.70	Niedermeier *et al.* [52]
$DyScO_3$ (110)	PLD	9.70	10.00	This study
$DyScO_3$ (110)	MBE	—	9.50	Paik *et al.* [13]

grown by PLD on $SrTiO_3$ (001) [17, 18, 27]. These dislocations are edge-type threading dislocations, since they contrast perpendicularly to the interface [13, 17, 18, 26, 27, 30] in the bright field TEM and WB-DFTEM images recorded with g-vector parallel to the interface (see the green arrows in Figs. 4.21(e), 4.21(f), 4.23(e) 4.23(f), 4.24(a) and 4.24(c)). Note that g-vector is the vector pointing (in reciprocal space) to the reflection used for imaging. The edge character is confirmed when the beam condition is changed, with g-vector perpendicular to the interface. This is seen in the WB-DFTEM image in Fig. 4.24(b), where only sharp and short defects parallel to the interface indicated by yellow arrows (also in Fig. 4.24(a)) are visible, and the vertical dark contrasts previously observed in Fig. 4.24(a) have disappeared. These sharp defects are probably stacking faults [94], and the other defects (vertical) are undoubtedly

Table 4.16: Summary of the dislocation density values calculated from the TEM micrographs of the La-doped $BaSnO_3$ films grown with $BaSnO_3$ buffer layer on $SrTiO_3$ (001), $DyScO_3$ (110) and $TbScO_3$ (110) substrates, shown in Figs. 4.21(f), 4.24(c) and 4.23(f), respectively. The dislocation density values reported in literature for La-doped $BaSnO_3$ thin films are given for comparison.

La-$BaSnO_3$ (LBSO) samples	Growth method	Density (cm^{-2})	References
6% LBSO buffered on $SrTiO_3$ (001)	PLD	10×10^{11}	This study
6% LBSO buffered on $DyScO_3$ (110)	PLD	5×10^{11}	This study
6% LBSO buffered on $TbScO_3$ (110)	PLD	5×10^{11}	This study
2% LBSO buffered on MgO (001)	PLD	2×10^{11}	Shin *et al.* [26]
2% LBSO unbuffered on MgO (001)	PLD	2.5×10^{11}	Sanchela *et al.* [27]
LBSO buffered on $DyScO_3$ (001)	MBE	1.2×10^{11}	Paik *et al.* [13]
LBSO buffered on Si (001)	MBE	1.3×10^{11}	Wang *et al.* [30]
4% LBSO unbuffered on $SrTiO_3$ (001)	PLD	4.9×10^{10}	Mun *et al.* [17]
0.5% LBSO unbuffered on $SrTiO_3$ (001)	PLD	2.1×10^{10}	Shiogai *et al.* [18]
2% LBSO unbuffered on $SrTiO_3$ (001)	PLD	1.4×10^{10}	Sanchela *et al.* [27]

threading edge dislocations [13, 17, 18, 26, 27, 30].

The vertical contrasts in Figs. 4.21(e) and 4.23(e) are similar to the columnar structures observed in La-doped $BaSnO_3$ thin films grown by PLD on $SrTiO_3$ (001) [94], and by high pressure oxygen sputtering on $PrScO_3$ (001), where they were associated with low-angle rotation at grain boundaries resulting in planes twist and tilt around the growth direction and the in-plane direction, respectively [107]. However, it is noteworthy that the TEM results discussed in this present study do not show any evidence for grain boundaries in the grown films. All HRTEM images show good epitaxial growth, although few extra atom planes are detected. Such columnar structures have also been reported in GaN thin films, which were qualitatively characterized as a mixture of threading edge, screw and mixed dislocations [93]. In the present work, however, a complete analysis of their distribution would have required at least two acquisition conditions with different types of Burgers vectors. But this was unfortunately not done in the framework of this thesis. Nevertheless, the high defect density reported in the $BaSnO_3$ buffered films above has been considerably reduced when using a $SrZrO_3$ buffer layer instead.

The microstructure of the 6% La-$BaSnO_3$ (25 nm)/$SrZrO_3$ (100 nm)/$TbScO_3$ sample was also analyzed, in order to examine the role of microstructural defects in limiting the electrical mobility in thin films fabricated with a buffer layer grown a extremely high temperature. The cross-sectional TEM measurements of the sample showing the film, the substrate, and the details at the interface are presented in Fig. 4.25. The HRTEM images in Figs. 4.25(a) and 4.25(b), the bright field TEM and WB-DFTEM images, respectively in Figs. 4.25(c) and 4.25(d), were all recorded in the condition whereby the g-vectors were parallel to the interface. As can be clearly seen, this film has a lower defect density compared to the films with $BaSnO_3$ buffer layer grown at 850 °C as presented in Figs. 4.21 to 4.23. An interface free of misfit dislocation is clearly visible in the HRTEM images in Figs. 4.25(a) and 4.25(b). However, the detailed contrasts at the interface in Fig. 4.25(b) could suggest extra atomic planes. But the inset (Fig. 4.25(b)) representing a magnification of the interface region delimited by the white rectangle shows a perfect cube-on-cube epitaxial relationship between the film and the $SrZrO_3/TbScO_3$ substrate, consistent with a fully strained film [84, 85] as also reported in the XRD analysis in Section 4.4.3.

In the bright field TEM and WB-DFTEM micrographs on the other hand, arrays of equidistant misfit dislocations indicated by red arrows are seen as dark and bright spots in Figs. 4.25(c) and 4.25(d), respectively. Their average distance is $\approx$ 13 nm, consistent with the expected 12 nm value for the fully strained film calculated from Equation (4.1) and using the in-plane lattice parameters of the La-doped $BaSnO_3$ film and $TbScO_3$ (110) substrate, summarized in Table 4.12. It is remarkable that the array of periodic misfit defects at the interface did not result in dislocations running across the film as was previously seen in the $BaSnO_3$ buffered films. In fact, 5 threading dislocations (two of which are marked with green arrows in Fig. 4.25(c)) were counted within 500 nm of a specimen as thick as 205.5 nm, giving a density of 4.9×10^9 cm^{-2}. This value is two orders of magnitude smaller than the densities found in this study in $BaSnO_3$ buffered films grown on $SrTiO_3$ (001), $DyScO_3$ (110) and $TbScO_3$ (110), and consistent with the concentration of $\approx 4\times10^9$ cm^{-2} reported in PLD grown 0.5% La-$BaSnO_3$ (80 nm)/$BaSnO_3$ (80 nm)/$BaSnO_3$ (130 nm)/(Sr,Ba)SnO_3 (10 nm)/$SrTiO_3$ heterostructure [18]. This result implies that the highest mobility sample grown on $SrZrO_3/TbScO_3$ substrate template, could have great potential for the next generation of electronic and optoelectronic devices, since it exhibits a defect density in the 10^9 cm^{-2} range similarly found in GaN [93, 95, 97] and indium tin oxide [73, 111], thin films.

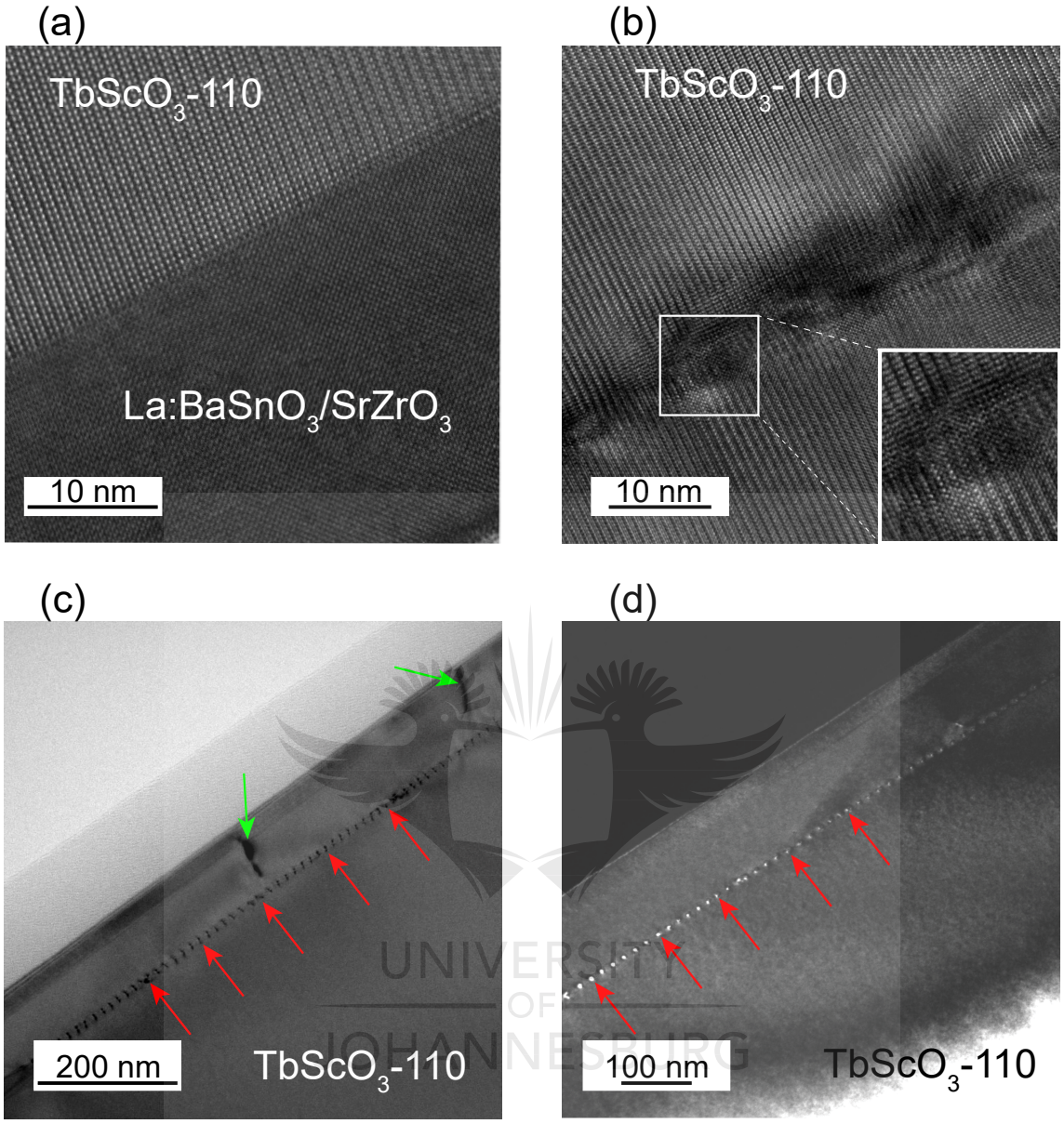

Figure 4.25: Cross-sectional TEM micrographs of a 6% La-$BaSnO_3$ (25 nm)/$SrZrO_3$ (100 nm)/$TbScO_3$ thin film. (a) and (b) are HRTEM images of the La-$BaSnO_3$ film and the $TbScO_3$ (110) substrate showing the film/substrate interface free of apparent defects. Although some contrast are visible at the interface in (b), there are no extra atom planes as can be seen in the inset showing the enlargement of an interface region delimited by the white rectangle. (c) Bright field TEM and (d) WB-DFTEM images revealing the presence of periodic misfit dislocations (dark and bright dots, respectively) at the interface, indicated by red arrows, with average distance of $\approx$ 13 nm. Threading dislocations, vertical dark contrasts in (c), are visible as indicated by the green arrows.

There are several explanations to the low threading dislocation density realized in the $SrZrO_3$ buffered film. The first and straightforward reason is the extremely high temperature growth of $SrZrO_3$ buffer layer. Indeed, as illustrated before in the case of epitaxial GaAs thin films fabricated on Si substrates, the density of threading dislocations is effectively reduced upon high thermal stresses, which increase the velocity of their glide motion as well as climb motion

due to reaction with point defects produced by atom diffusion [112, 113]. It was reported that the glide motion velocity and the concentration of vacancies that enhance the climb motion increase exponentially with temperature [114, 115, 116]. Thus, the dislocation density reduction in the $SrZrO_3$ buffered La-doped $BaSnO_3$ thin film was expected since the $SrZrO_3$ buffer layer was grown at extremely high temperature, even above that for thermal treatments in GaAs prepared on Si which resulted in significant reduction of the threading dislocation density. The fact that extended defects perpendicularly crossing the film from the interface to the surface as in $BaSnO_3$ buffered films (Figs 4.21 to 4.24) could not be observed in the $SrZrO_3$ buffered film (Fig. 4.25) could therefore be supported by the appearance of dislocations climb motion after high temperature growth [112, 114, 115, 116].

Furthermore, the thermal strain originating from the difference in thermal expansion coefficients between $SrZrO_3$ and $TbScO_3$ which also enhances the dislocations glide motion would explain the dislocation density reduction in the $SrZrO_3$ buffered film. The average thermal expansion coefficient of $SrZrO_3$ and $TbScO_3$ are 2.61×10^{-5} K^{-1} and 0.82×10^{-5} K^{-1}, respectively, giving a difference of ≈ 3 times [48, 71]. This difference, together with the fact that $SrZrO_3$ undergoes phase transition from tetragonal to cubic symmetry at ≈ 830 °C and ≈ 1170 °C [71], respectively, suggest epitaxial strain at the interface during cool down, and as a consequence, a reduction of the lattice mismatch. Indeed, the theoretical lattice mismatch between $SrZrO_3$ and $TbScO_3$ is about 3.7% [45, 48]; this value is reduced to $\approx 3\%$ after the deposition of $SrZrO_3$ at 1300 °C as can be seen in Table 4.12.

4.6 Concluding Remarks

The structural characteristics of the grown La-$BaSnO_3$/$SrZrO_3$/$TbScO_3$ heterostructure have significant impact on its electrical properties as demonstrated in Section 4.3. The structural and transport characteristics of this sample are essential for high performance in functional device applications. The present results demonstrate that $SrZrO_3$ layer grown on perovskite substrates, such as $SrTiO_3$ (001), $DyScO_3$ (110), $TbScO_3$ (110) and non-perovskite substrate such as MgO (001) at high temperature, can be employed as a substrate template for subsequent fabrication of high mobility La-doped $BaSnO_3$ films with fewer dislocation defects.

It has been demonstrated that $SrZrO_3$ buffer layer deposited at high temperature between La-doped $BaSnO_3$ film layer and $TbScO_3$ (110) substrate, results in an outstanding enhancement of the electron mobility (brown curve in Fig 4.13(b)), associated with a considerable reduction of the density of threading dislocations. However, the following observations should be made. It is well known that scattering at threading dislocations not only lowers the electrical mobility by scattering the charges travelling across, but also reduces the concentration of free carriers which are trapped at the dislocation lines due to the important density of dangling bonds along the lines [17, 90, 91]. Thus, it is not expected that the samples with the higher dislocation densities have higher carrier concentrations. This can be perceived in Fig 4.13(a) when comparing the $BaSnO_3$ buffered samples prepared on $DyScO_3$ (110) (green diamonds) and $TbScO_3$ (110) (blue diamonds) with the $SrZrO_3$ buffered sample (brown diamonds). It would be assumed that, given the fact that the active epitaxial layer in the film is thin (25 nm), the lower density of free charge in the highest mobility $SrZrO_3$ buffered sample (with the lowest defect density) implies that not only the threading dislocations are trapping electrons, but also effects such as surface scattering or interface traps are reducing the concentration of mobile carriers. For the samples with the highest defect densities ($BaSnO_3$ buffered films, blue and green diamonds

in Fig 4.13(a)), these contributions are expected to be less pronounced as the buffer layer ($BaSnO_3$) and the active layer consist of the same material.

Bibliography

[1] S. Kasap, and P. Capper, *Springer Handbook of Electronic and Photonic Materials* (Springer, Gewerbestraße, 2017).

[2] D. K. Schroder, *Semiconductor Material and Device Characterization* (John Wiley & Sons, Inc., Hoboken, 2006).

[3] E. N. Kaufmann, *Characterization of Materials* (John Wiley & Sons, Inc., Hoboken, 2012).

[4] N. Reyren, S. Thiel, A. D. Caviglia, L. F. Kourkoutis, G. Hammerl, C. Richter, C. W. Schneider, T. Kopp, A.-S. Rüetschi, D. Jaccard, M. Gabay, D. A. Muller, J.-M. Triscone, and J. Mannhart, Science **317**, 1196 (2007).

[5] D. Stornaiuolo, D. Massarotti, R. Di Capua, P. Lucignano, G. P. Pepe, M. Salluzzo, and F. Tafuri, Phys. Rev. B **95**, 140502 (2017).

[6] S. Thiel, G. Hammerl, A. Schmehl, C. W. Schneider, and J. Mannhart, Science **313**, 1942 (2006).

[7] Ariando, X. Wang, G. Baskaran, Z. Q. Liu, J. Huijben, J. B. Yi, A. Annadi, A. R. Barman, A. Rusydi, S. Dhar, Y. P. Feng, J. Ding, H. Hilgenkamp, and T. Venkatesan, Nat. Commun. **2**, 188 (2011).

[8] J.-S. Lee, Y. W. Xie, H. K. Sato, C. Bell, Y. Hikita, H. Y. Hwang, and C.-C. Kao, Nat. Mater. **12**, 703 (2013).

[9] J. Choi, C. B. Eom, G. Rijnders, H. Rogalla, and D. H. A. Blank, Appl. Phys. Lett. **79**, 1447 (2001).

[10] A. Prakash, P. Xu, A. Faghaninia, S. Shukla, J. W. Ager, C. S. Lo, and B. Jalan, Nat. Commun. **8**, 15167 (2017).

[11] A. Prakash, J. Dewey, H. Yun, J. S. Jeong, K. A. Mkhoyan, and B. Jalan, J. Vac. Sci. Technol. A **33**, 060608 (2015).

[12] S. Raghavan, T. Schumann, H. Kim, J. Y. Zhang, T. A. Cain, and S. Stemmer, APL Mater. **4**, 016106 (2016).

[13] H. Paik, Z. Chen, E. Lochocki, H. Ariel Seidner, A. Verma, N. Tanen, J. Park, M. Uchida, S. Shang, B. C. Zhou, M. Brützam, R. Uecker, Z. K. Liu, D. Jena, K. M. Shen, D. A. Muller, and D. G. Schlom, APL Mater. **5**, 116107 (2017).

[14] W.-J. Lee, H. J. Kim, E. Sohn, T. H. Kim, J.-Y. Park, W. Park, H. Jeong, T. Lee, J. H. Kim, K.-Y. Choi, and K. H. Kim, Appl. Phys. Lett. **108**, 082105 (2016).

[15] H. Hosono, Thin Solid Films **515**, 6000 (2007).

[16] K. Ganguly, P. Ambwani, P. Xu, J. S. Jeong, K. A. Mkhoyan, C. Leighton, and B. Jalan, APL Mater. **3**, 062509 (2015).

[17] H. Mun, U. Kim, H. Min Kim, C. Park, T. Hoon Kim, H. Joon Kim, K. Hoon Kim, and K. Char, Appl. Phys. Lett. **102**, 252105 (2013).

[18] J. Shiogai, K. Nishihara, K. Sato, and A. Tsukazaki, AIP Adv. **6**, 065305 (2016).

[19] H. Ohta, M. Orita, and M. Hirano, J. Appl. Phys. **91**, 3547 (2002).

[20] H. Kim, A. Piqué , J. S. Horwitz, H. Mattoussi, H. Murata, Z. H. Kafafi, and D. B. Chrisey, Appl. Phys. Lett. **74**, 3444 (1999).

[21] H. Kim, C. M. Gilmore, A. Piqué, J. S. Horwitz, H. Mattoussi, H. Murata, Z. H. Kafafi, and D. B. Chrisey, J. Appl. Phys. **86**, 6451 (1999).

[22] F. Sánchez, M. V. García-Cuenca, C. Ferrater, M. Varela, G. Herranz, B. Martínez, and J. Fontcuberta, Appl. Phys. Lett. **83**, 902 (2003).

[23] W.-J. Lee, H. Lee, K.-T. Ko, J. Kang, H. J. Kim, T. Lee, J.-H. Park, and K. H. Kim, Appl. Phys. Lett. **111**, 231604 (2017).

[24] R. Bachelet, F. Valle, I. C. Infante, F. Sánchez, and J. Fontcuberta, Appl. Phys. Lett. **91**, 251904 (2007).

[25] K. Sudoh, and H. Iwasaki, Phys. Rev. Lett. **87**, 216103 (2001).

[26] J. Shin, Y. M. Kim, Y. Kim, C. Park, and K. Char, Appl. Phys. Lett. **109**, 262102 (2016).

[27] A. V. Sanchela, M. Wei, H. Zensyo, B. Feng, J. Lee, G. Kim, H. Jeen, Y. Ikuhara, and H. Ohta, Appl. Phys. Lett. **112**, 232102 (2018).

[28] C. Park, U. Kim, C. J. Ju, J. S. Park, Y. M. Kim, and K. Char, Appl. Phys. Lett. **105**, 203503 (2014).

[29] C. A. Niedermeier, S. Rhode, K. Ide, H. Hiramatsu, H. Hosono, T. Kamiya, and M. A. Moram, Phys. Rev. B **95**, 161202 (2017).

[30] Z. Wang, H. Paik, Z. Chen, D. A. Muller, and D. G. Schlom, APL Mater. **7**, 022520 (2019).

[31] H. L. Hartnagel, A. L. Dawar, A. K. Jain, and C. Jagadish, *Semiconducting Transparent Thin Films* (Institute of Physics, Bristol, 1995).

[32] N. Taga, Y. Shigesato, and M. Kamei, J. Vac. Sci. Technol. A **18**, 1663 (2000).

[33] S. Sallis, D. O. Scanlon, S. C. Chae, N. F. Quackenbush, D. A. Fischer, J. C. Woicik, J.-H. Guo, S.-W. Cheong, and L. F. J. Piper, Appl. Phys. Lett. **103**, 042105 (2013).

[34] H. J. Kim, U. Kim, T. H. Kim, J. Kim, H. M. Kim, B. G. Jeon, W. J. Lee, H. S. Mun, K. T. Hong, J. Yu, K. Char, and K. H. Kim, Phys. Rev. B **86**, 165205 (2012).

[35] P. V. Wadekar, J. Alaria, M. O'Sullivan, N. L. O. Flack, T. D. Manning, L. J. Phillips, K. Durose, O. Lozano, S. Lucas, J. B. Claridge, and M. J. Rosseinsky, Appl. Phys. Lett. **105**, 052104 (2014).

[36] A. Prakash, P. Xu, X. Wu, G. Haugstad, X. Wang, and B. Jalan, J. Mater. Chem. C **5**, 5730 (2017).

[37] Z. Lebens-Higgins, D. O. Scanlon, H. Paik, S. Sallis, Y. Nie, M. Uchida, N. F. Quackenbush, M. J. Wahila, G. E. Sterbinsky, D. A. Arena, J. C. Woicik, D. G. Schlom, and L. F. Piper, Phys. Rev. Lett. **116**, 027602 (2016).

[38] D. Yoon, S. Yu, and J. Son, NPG Asia Mater. **10**, 363 (2018).

[39] H. Amano, N. Sawaki, I. Akasaki, and Y. Toyada, Appl. Phys. Lett. **48**, 353 (1986).

[40] H. Amano, J. Akasaki, K. Hiramatsu, N. Koide, and N. Sawaki, Thin Solid Films **163**, 415 (1988).

[41] H. Amano, M. Kito, K. Hiramatsu, and I. Akasaki, Jpn. J. Appl. Phys. **28**, L2112 (1989).

[42] S. Nakamura, Jpn. J. Appl. Phys. **30**, L1705 (1991).

[43] Y. Huang, X. D. Chen, S. Fung, C. D. Beling, C. C. Ling, Z. F. Wei, S. J. Xu, and C. Y. Zhi, J. Appl. Phys. **96**, 1120 (2004).

[44] A. P. Nono-Tchiomo, W. Braun, B. P. Doyle, W. Sigle, P. Van Aken, J. Mannhart, and P. Ngabonziza, APL Mater. **7**, 041119 (2019).

[45] E. Mete, R. Shaltaf, and Ş. Ellialtıoğlu, Phys. Rev. B **68**, 035119 (2003).

[46] A. J. Smith and A. J. E. Welch, Acta Cryst. **13**, 653 (1960).

[47] H. J. Kim, U. Kim, H. M. Kim, T. H. Kim, H. S. Mun, B. G. Jeon, K. T. Hong, W. J. Lee, C. Ju, K. H. Kimy, and K. Char, Appl. Phys. Express **5**, 061102 (2012).

[48] R. Uecker, B. Velickov, D. Klimm, R. Bertram, M. Bernhagen, M. Rabe, M. Albrecht, R. Fornari, and D. Schlom, J. Cryst. Growth **310**, 2649 (2008).

[49] W. Braun, J. Cryst. Growth **477**, 34 (2017).

[50] W. Braun, J. Cryst. Growth **477**, 50 (2017).

[51] M. Jäger, A. Teker, J. Mannhart, and W. Braun, Appl. Phys. Lett. **112**, 111601 (2018).

[52] C. A. Niedermeier, S. Rhode, S. Fearn, K. Ide, M. A. Moram, H. Hiramatsu, H. Hosono, and T. Kamiya, Appl. Phys. Lett. **108**, 172101 (2016).

[53] H. F. Wang, Q. Z. Liu, F. Chen, G. Y. Gao, and W. Wu, J. Appl. Phys. **101**, 106105 (2007).

[54] Q. Liu, J. Liu, B. Li, H. Li, G. Zhu, K. Dai, Z. Liu, P. Zhang, and J. Dai, Appl. Phys. Lett. **101**, 241901 (2012).

[55] Q. Liu, J. Dai, Z. Liu, X. Zhang, G. Zhu, and G. Ding, J. Phys. D: Appl. Phys. **43**, 455401 (2010).

[56] Q. Liu, J. Dai, H. Li, B. Li, Y. Zhang, K. Dai, and S. Chen, J. Alloys Compd. **647**, 959 (2015).

[57] Q. Liu, J. Dai, Y. Zhang, H. Li, B. Li, Z. Liu, and W. Wang, J. Alloys Compd. **655**, 389 (2016).

[58] K. Ganguly, A. Prakash, B. Jalan, and C. Leighton, APL Mater. **5**, 056102 (2017).

[59] H.-H. Wang, D.-F. Cui, S.-Y. Dai, H.-B. Lu, Y.-L. Zhou, Z.-H. Chen, and G.-Z. Yang, J. Appl. Phys. **90**, 4664 (2001).

[60] A. Leitner, C. T. Rougers, J. C. Price, D. A. Herman, and D. R. Herman, Appl. Phys. Lett. **72**, 3065 (1998).

[61] J. H. Cho, and H. J. Cho, Appl. Phys. Lett. **79**, 1426 (2001).

[62] U. Kim, C. Park, T. Ha, R. Kim, H. S. Mun, H. M. Kim, H. J. Kim, T. H. Kim, N. Kim, J. Yu, K. H. Kim, J. H. Kim, and K. Char, APL Mater. **2**, 056107 (2014).

[63] D. C. Look, and R. J. Molnar, Appl. Phys. Lett. **70**, 3377 (1997).

[64] D. C. Look, D. C. Reynolds, J. W. Hemsky, J. R. Sizelove, R. L. Jones, and R. J. Molnar, Phys. Rev. Lett. **79**, 2273 (1997).

[65] D. C. Look, C. E. Stutz, R. J. Molnar, K. Saarinen, and Z. Liliental-Weber, Solid State Commun. **117**, 571 (2001).

[66] T. Makino, Y. Segawa, A. Tsukazaki, A. Ohtomo, and M. Kawasaki, Appl. Phys. Lett. **87**, 022101 (2005).

[67] K. Ellmer, and R. Mientus, Thin Solid films **516**, 5829 (2007).

[68] R. Engel-Herbert, *Molecular Beam Epitaxy of Complex Oxides*, Molecular Beam Epitaxy, edited by H. Mohamed (Elsevier, Amsterdam, 2013), p. 417–449.

[69] R. S. Roth, J. Res. Natl. Bur. Stand. **58**, 75 (1957).

[70] W. Ma, X. Li, X. Meng, Y. Xue, Y. Bai, W. Chen, and H. Dong, J. Therm. Spray. Tech. **27**, 1056 (2018).

[71] D. de Ligny, and P. Richet, Phys. Rev. B **53**, 3013 (1996).

[72] T. Huang, T. Nakamura, M. Itoh, Y. Inaguma, and O. Ishiyama, J. Mater. Sci. **30**, 1556 (1995).

[73] H. Ohta, M. Orita, M. Hirano, H. Tanji, H. Kawazoe, and H. Hosono, Appl. Phys. Lett. **76**, 2740 (2000).

[74] J. I. Langford, and A. J. C. Wilson, J. Appl. Cryst. **11**, 102 (1978).

[75] P. Scherrer, Nachr. Ges. Wiss. Göttingen **26**, 98 (1918).

[76] S. Yu, D. Yoon, and J. Son, Appl. Phys. Lett. **108**, 262101 (2016).

[77] Q. Z. Liu, H. F. Wang, F. Chen, and W. Wu, J. Appl. Phys. **103**, 093709 (2008).

[78] B. Heying, X. H. Wu, S. Keller, Y. Li, D. Kapolnek, B. P. Keller, S. P. DenBaars, and J. S. Speck, Appl. Phys. Lett. **68**, 643 (1996).

[79] H. Heinke, V. Kirchner, S. Einfeldt, and D. Hommel, Appl. Phys. Lett. **77**, 2145 (2000).

[80] S. R. Lee, A. M. West, A. A. Allerman, K. E. Waldrip, D. M. Follstaedt, P. P. Provencio, D. D. Koleske, and C. R. Abernathy, Appl. Phys. Lett. **86**, 241904 (2005).

[81] P. R. Berger, K. Chang, P. Bhattacharya, J. Singh, and K. K. Bajaj, Appl. Phys. Lett. **53**, 684 (1988).

[82] D. A. King, and D. P. Woodruff, *Growth and Properties of Ultrathin Epitaxial Layers* (Elsevier, North Holland, 1997).

[83] M. Kneiß, P. Storm, A. Hassa, D. Splith, H. von Wenckstern, M. Lorenz, and M. Grundmann, APL Mater. **8**, 051112 (2020).

[84] J. P. Bosco, G. M. Kimball, N. S. Lewis, and H. A. Atwater, J. Cryst. Growth **363**, 205 (2013).

[85] M. Huijben , G. Koster , D. H. A. Blank, and G. Rijnders, Phase Transit. **81**, 703 (2008).

[86] P. Kidd, *XRD of gallium nitride and related compounds: strain, composition and layer thickness*, (Panalytical: Almelo, Netherlands, 2009).

[87] G. V. Hansson, H. H. Radamsson, and W.-X. Ni, J. Mater. Sci. Mater. Electron. **6**, 292 (1995).

[88] M. R. Sardela, H. H. Radamsson, W.-X. Ni, J.-E. Sundgren, and G. V. Hansson, Jpn. J. Appl. Phys. **33**, 417 (1994).

[89] K. Hiramatsu, J. Phys.: Condens. Matter **13**, 6961 (2001).

[90] N. G. Weimann, L. F. Eastman, D. Doppalapudi, H. M. Ng, and T. D. Moustakas, J. Appl. Phys. **83**, 3656 (1998).

[91] H. M. Ng, D. Doppalapudi, T. D. Moustakas, N. G. Weimann, and L. F. Eastman, Appl. Phys. Lett. **73**, 821 (1998).

[92] A. Chatterjee, S. K. Khamari, V. K. Dixit, S. M. Oak, and T. K. Sharma, J. Appl. Phys. **118**, 175703 (2015).

[93] J. Jasinski, and Z. Liliental-Weber, J. Electron. Mater. **31**, 429 (2002).

[94] W. Y. Wang, Y. L. Tang, Y. L. Zhu, J. Suriyaprakash, Y. B. Xu, Y. Liu, B. Gao, S. W. Cheong, and X. L. Ma, Sci. Rep. **5**, 16097 (2015).

[95] S. D. Lester, F. A. Ponce, M. G. Craford, and D. A. Steigerwald, Appl. Phys. Lett. **66**, 1249 (1995).

[96] D. Kapolnek, X. H. Wu, B. Heying, S. Keller, B. P. Keller, U. K. Mishra, S. P. DenBaars, and J. S. Speck, Appl. Phys. Lett. **67**, 1541 (1995).

[97] F. A. Ponce, B. S. Krusor, J. S. Major, Jr. W. E. Plano, and D. F. Welch, Appl. Phys. Lett. **67**, 410 (1995).

[98] N. V. Richardson, and S. Holloway, *Handbook of Surface Science: Physical Structure. Ed. by W. N. Unertl* (Elsevier, North Holland, 1996).

[99] A. Patané, and N. Balkan, *Semiconductor Research* (Springer, New York, 2012).

[100] H. P. Sun, W. Tian, X. Q. Pan, J. H. Haeni, and D. G. Schlom, Appl. Phys. Lett. **84**, 3298 (2004).

[101] Y. L. Zhu, X. L. Ma, D. X. Li, H. B. Lu, Z. H. Chen, and G. Z. Yang, Acta Mater. **53**, 1277 (2005).

[102] Y. L. Zhu, X. Wang, M. J. Zhuo, Y. Q. Zhang, and X. L. Ma, Phil. Mag. Lett. **90**, 323 (2010).

[103] Y. L. Tang, Y. L. Zhu, H. Meng, Y. Q. Zhang, and X. L. Ma, Acta Mater. **60**, 5975 (2012).

[104] I. B. Misirlioglu, A. L. Vasiliev, M. Aindow, S. P. Alpay, and R. Ramesh, Appl. Phys. Lett. **84**, 1742 (2004).

[105] H. P. Sun, X. Q. Pan, J. H. Haeni, and D. G. Schlom, Appl. Phys. Lett. **85**, 1967 (2004).

[106] H. Yun, M. Topsakal, A. Prakash, K. Ganguly, C. Leighton, B. Jalan, R. M. Wentzcovitch, K. A. Mkhoyan, and J. S. Jeong, J. Vac. Sci. Technol. A **36**, 031503 (2018).

[107] H. Yun, K. Ganguly, W. Postiglione, B. Jalan, C. Leighton, K. A. Mkhoyan, and J. S. Jeong, Sci. Rep. **8**, 10245 (2015).

[108] R. H. Wei, X. W. Tang, Z. Z. Hui, X. Luo, J. M. Dai, J. Yang, W. H. Song, L. Chen, X. G. Zhu, X. B. Zhu, and Y. P. Sun, Appl. Phys. Lett. **106**, 101906 (2015).

[109] S. Ismail-Beigi, F. J. Walker, S.-W. Cheong, K. M. Rabe, and C. H. Ahn, APL Mater. **3**, 062510 (2015).

[110] A. V. Sanchela, T. Onozato, B. Feng, Y. Ikuhara, and H. Ohta, Phys. Rev. Mater. **1**, 034603 (2017).

[111] I. A. Rauf, J. Appl. Phys. **79**, 4057 (1996).

[112] Y. Takagi, H. Yonezu, Y. Hachiya, and K. Pak, Jpn. J. Appl. Phys. **33**, 3368 (1994).

[113] D. Deppe, N. Holonyak Jr, K. Hsieh, D. Nam, W. Plano, R. Matyi, and H. Shichijo, Appl. Phys. Lett. **52**, 1812 (1988).

[114] I. Yonenaga, and K. Sumino, J. Appl. Phys. **62**, 1212 (1987).

[115] S. K. Choi, M. Mihara, and T. Ninomiya, Jpn. J. Appl. Phys. **16**, 737 (1977).

[116] J. A. Van Vechten, J. Electrochem. Soc. **122**, 419 (1975).

5. *Ex Situ* Spectroscopic Analysis of La-Doped $BaSnO_3$ Thin Films

5.1 Introduction

Several material properties including oxidation state, corrosion and electronic characteristics are strongly governed by the chemical composition of the material's surfaces and interfaces [1, 2, 3, 4, 5]. Thus, surface analysis techniques such as electron spectroscopies (allowing sampling at the atomic layer scale) were developed. Photoemission spectroscopy is one of the most widely used methods for surface studies. It is effective for elemental identification, chemical bond detection, and oxidation state determination in compounds, solids or molecules. In this chapter, we report on the structural and electronic properties of epitaxial La-doped $BaSnO_3$ thin films obtained from spectroscopic measurements. More precisely, the surface atomic composition and electronic band structure of the La-doped $BaSnO_3$ thin films acquired with XPS and ARPES are presented.

As mentioned earlier, this research project was built around two major ideas. Firstly, the idea of preparing epitaxial thin films of La-doped $BaSnO_3$ featuring remarkable electronic transport properties. Secondly, the idea of linking these transport characteristics to the electronic band structure of La-doped $BaSnO_3$, which at the time the project was defined was still not well understood, at least experimentally (see Chapter 2). Thus, two important points should be highlighted at the beginning of this section of the thesis.

Firstly, as described in Section 3.3.4, the electronic band structure in materials is assessed by ARPES, which is a surface sensitive technique, meaning that only a few atomic layers underneath the surface can be probed. As also stated in Sections 3.2.2 and 3.3.4, the La-doped $BaSnO_3$ samples were grown at the Max-Planck Institute (MPI) for Solid State Research in Stuttgart (Germany), and transported at ambient conditions for spectroscopic measurements at the University of Johannesburg (UJ) in South Africa. For these two reasons, the surfaces of the samples required thorough cleaning in UHV prior to conducting the spectroscopic measurements. The sample cleaning involved annealing and proved to be challenging. This implies that the trial and error approach had to be followed. In certain cases, the samples were annealed at very high temperatures, resulting in the surface being damaged, as evidenced by the XPS data shown in Appendix C.1. Hence, several sample surfaces, including the highest mobility sample prepared with a $BaSnO_3$ buffer layer (Table 4.6 in Section 4.2.3), were destroyed in the cleaning process until an optimal cleaning procedure was established. The optimized cleaning recipe is described in Section 3.3.4. The highest mobility sample prepared with a $SrZrO_3$ buffer layer grown at 1300 °C (see Section 4.3) was not measured as it was used for TEM measurements. Nevertheless, the XPS data of the sample prepared with $SrZrO_3$ buffer layer grown at 1400 °C (see Table 4.14) of which the surface was also believed to have been damaged is shown in Appendix C.4.

Secondly, as demonstrated in Chapter 4, optimized transport characteristics were achieved in 2% and 6% unbuffered and buffered La-doped $BaSnO_3$ thin films. Therefore, only the XPS and ARPES data of the samples with the highest mobility, unbuffered and $BaSnO_3$ buffered as presented in Table 4.6 will be discussed in this chapter. However, since the surface of the $BaSnO_3$ buffered samples was damaged by annealing as mentioned above, the data of a

sample grown with the same parameters (substrate, film and buffer layer thicknesses) in the same conditions will be addressed instead, for completeness of the data analysis. The XPS and ARPES data of the highest mobility $BaSnO_3$ buffered sample presented in Table 4.6 are given in Appendix C.1. The XPS data of a 4% La-doped $BaSnO_3$ sample prepared with $BaSnO_3$ buffer layer (lower mobility) is also given in Appendix C.2 as additional data.

This chapter is structured into two sections. In the first section, the chemical composition of the surface of the films is addressed. The fitted XPS data for both as-inserted and cleaned surfaces are presented, and the origin of the different peak components is discussed. In the second section, a combined analysis of the valence band states of the films is conducted. The XPS and ARPES valence band spectra are shown, and the electronic band structure of the films is investigated.

5.2 Stoichiometry

In this section, the XPS data for as-inserted and cleaned surfaces are presented. The survey and core level spectra shown were acquired with the analyzer pass energies of 60 and 20 eV, respectively, using a monochromatized Al K_α excitation source, emitting photons of energy of 1486.71 eV. All the elements constituting the surface of La-doped $BaSnO_3$ films are identified. A thorough analysis of the angle-dependent XPS data helps to clarify the origin of the multiple components found in the primary core levels.

5.2.1 Chemical Composition of the Surface

With the use of XPS measurements, the surface composition of the epitaxially grown La-doped $BaSnO_3$ thin films was investigated. Here, the XPS data for 2% and 6% La-doped $BaSnO_3$ (25 nm thick) thin films directly deposited on $TbScO_3$ (110) and $SrTiO_3$ (001) substrates, respectively, are presented. The electrical transport properties of these samples were addressed in Section 4.2.3, with their RT electronic data given in Table 4.6. These data were as follows: an electron mobility (μ) of 75 ± 2 cm^2 V^{-1} s^{-1} with an associated carrier density (n) of $(1.35 \pm 0.02) \times 10^{20}$ cm^{-3} achieved in the 2% La-$BaSnO_3$ (25 nm)/$TbScO_3$ film; and 91 ± 2 cm^2 V^{-1} s^{-1} with $n = (4.05 \pm 0.05) \times 10^{20}$ cm^{-3} realized in the 6% La-$BaSnO_3$ (25 nm)/$SrTiO_3$ sample.

It is noteworthy that the choice of carrying out a comparative analysis of the spectroscopic data of samples with different doping levels was not made randomly. The different amount of La doping affected the electronic structure of the samples in terms of binding energy shifts, peak broadenings an/or changes in the line shape of the core levels [6, 7, 8]. Hence, the effects of different doping levels in these two films, which are interpreted as different levels of perturbation or disorder introduced into the original (pristine) lattice, was probed by XPS.

It should also be noted that these two films are grown on different single crystal substrates. As mentioned in Section 5.1 above, the electronic properties of materials are strongly correlated to the chemical composition of their surfaces [1, 2, 3, 4, 5]. Although the 2% and 6% films described here are grown on different substrates, the comparative analysis of the spectroscopic data of their surfaces holds. This can be supported by two arguments. The first argument is that the thickness (25 nm) of the active La-doped $BaSnO_3$ film layers is enough (with respect to surface spectroscopy) for the thin films to be viewed as "bulk" by a surface sensitive measurement technique, as demonstrated in Section 3.3.4. It is therefore highly unlikely to have

an interfacial contribution in the resulting photoelectron signals [9]. The choice of the substrate is however determinant for optimal electronic performance in thin film growth as demonstrated in Chapters 2 and 4. The second argument is that any of the changes mentioned above would not be attributed to change in the chemical environment of the core electrons since it was demonstrated in Section 4.4.1 that the La-doped $BaSnO_3$ thin films were epitaxially grown (single crystalline) on either of these substrates, with no formation of secondary phases or randomly oriented grains.

The spectroscopic data of these two samples were acquired both on the samples as-inserted and after they were thoroughly cleaned in vacuum following the procedure described in Section 3.3.4. It should be highlighted that the 2% La-$BaSnO_3$/$TbScO_3$ sample was pre-annealed in vacuum at a very low filament current of 1.6 A (without high voltage on) and for a short period of time (15 minutes). The temperature indicated by the pyrometer (spot on the sample holder) was about 300 °C. This was near the limit of the measuring range of the pyrometer so this value could be incorrect. However, the surface was still not clean, judging from the measured core level spectra such as O 1s and C 1s, as will be shown further in this section. Therefore, for better comparison of the spectra, this surface will be referred to as "as-inserted". The cleanliness of the samples was monitored by recording the LEED patterns directly after an annealing cycle in the preparation chamber, as well as by measuring the C 1s signal after the samples were transferred into the analysis chamber.

Evidence of a clean surface can be seen in Fig. 5.1 representing typical LEED pattern images for a clean La-$BaSnO_3$ (001) surface taken at various electron energies. The surface depicted in the figure exhibits a stable 1×1 surface structure, comparable to that obtained in $BaSnO_3$ thin films annealed at 600 °C in oxygen [10]. Similar structure was also reported in related perovskite systems such as $BaTiO_3$ and $SrTiO_3$ [11, 12, 13]. Following the description in Section 3.3.1, it can be observed that the diffraction spots in Fig. 5.1 form square lattices in reciprocal space which correspond to the cubic lattice structure of $BaSnO_3$ in real space. These reciprocal lattices, one of which is drawn on the image taken at 48 eV, indicate the high crystallinity of the films [10, 11, 12, 13].

The cleanliness of the surfaces can also be seen in Fig. 5.2 showing the XPS scans in the wide energy range consistent with the excitation energy of a standard laboratory source (photons of 1486.71 eV emitted from the Al K_α anode). As can be seen in the figure, all the expected core electron levels (accessible with the source) originating from La, Ba, Sn and O are present in the survey scans. However, a signal located at a binding energy of 285.95 eV attributed to C 1s is detected in the as-inserted samples portrayed by the light green and orange curves in Fig. 5.2. In addition, the C KLL Auger peak is present at 1224 eV. These samples are therefore not clean, since the presence of a foreign element (adventitious carbon) means that there is surface contamination. Upon annealing, this contamination is systematically eliminated, resulting in clean surfaces as depicted by the blue and red curves in Fig. 5.2.

The most intense (see Fig. 5.2) and informative spectroscopic regions are Sn 3d, O 1s and Ba 3d. The photoemission spectra of these core electrons were analyzed/fitted following the description given in Section 3.3.4. Knowing that the 3d energy level is split into $3d_{\frac{5}{2}}$ and $3d_{\frac{3}{2}}$ due to the spin orbit coupling, the area ratio ($3d_{\frac{3}{2}}$/ $3d_{\frac{5}{2}}$) of both Ba and Sn 3d core levels (since the number of states in the degenerate $\frac{5}{2}$ and $\frac{3}{2}$ levels are different) was fixed to 0.667 during the fits. Also, the spin orbit splitting (energy separation of the doublet consecutive to the splitting of the 3d energy level) was fixed at 15.323 eV for Ba 3d and 8.423 eV for Sn 3d

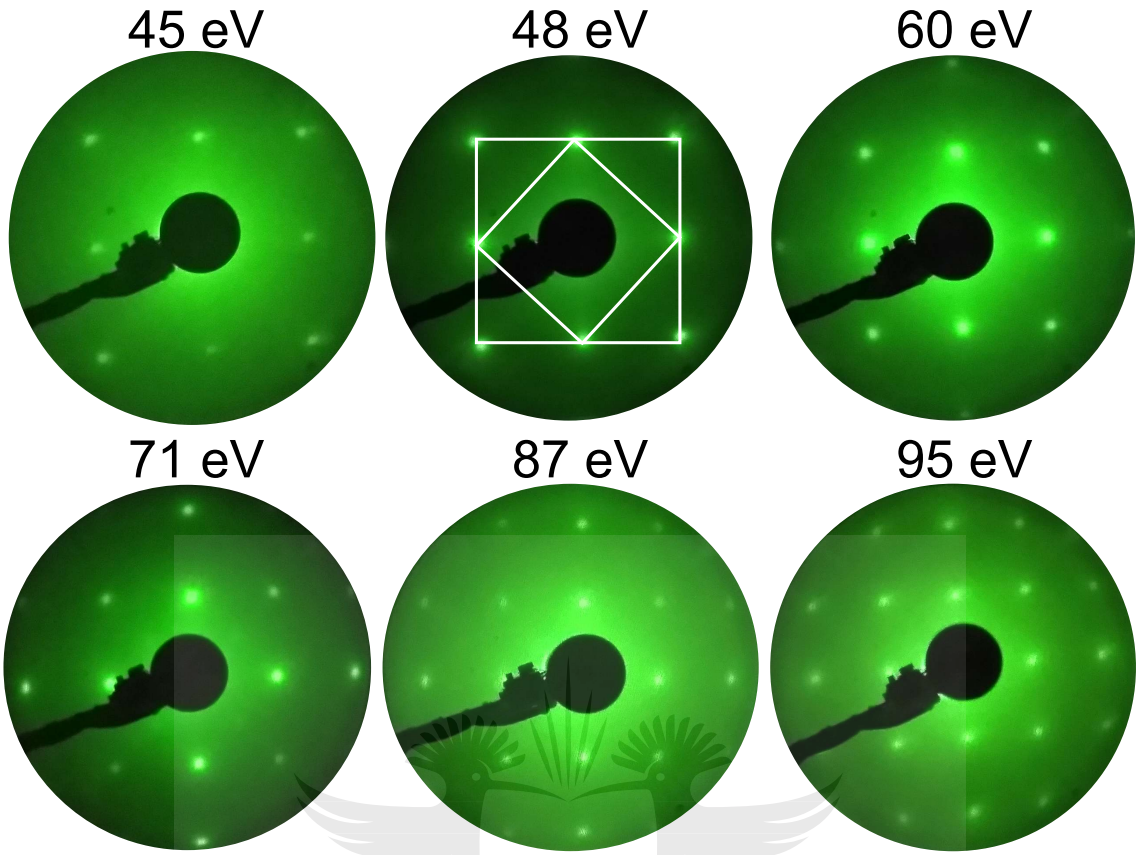

Figure 5.1: Typical LEED images of the La-$BaSnO_3$ (001) surface taken at various electron energies indicated in the figure for each image. The white squares drawn on the image recorded at 48 eV illustrate the square lattice of $BaSnO_3$. Note that at the electron energy of 48 eV, the diffraction pattern shows only first order diffraction spots. When the energy is approximately doubled to 95 eV, the pattern shows all the second order spots.

[14, 15]. Both core levels were asymmetric and deconvoluted with multiple components. Fits of the spectra of these regions and the spectra of the O 1s core levels for both as-inserted and cleaned surfaces are presented in Figs. 5.3, 5.4 and 5.5, and the fitted parameters after background (Bgrd) subtraction are given in Tables 5.1, 5.2 and 5.3 for Sn 3d, O 1s and Ba 3d, respectively. It should be noted that the data for La 3d core levels whose signals were detectable but very weak as can be seen in the binding energy range 820 eV to 860 eV in Fig. 5.2 are not shown. However, combined XPS data for La 3d regions with respect to the La doping concentration is provided in Appendix C.3 as supplemental information.

a) Sn 3d Core Level

Figure 5.3 represents the fitted spectra of the Sn 3d core levels. The parameters obtained from the fits of the spectra are summarized in Table 5.1. Figures 5.3(a) and 5.3(b) are the Sn 3d core electrons of the 2% La-$BaSnO_3$/$TbScO_3$ sample ($n = 1.35 \times 10^{20}$ cm^{-3}) whereas Figs. 5.3(c) and 5.3(d) are those of the 6% La-$BaSnO_3$/$SrTiO_3$ sample ($n = 4.05 \times 10^{20}$ cm^{-3}). As mentioned above, the Sn 3d core regions were asymmetric on the higher binding energy side. The asymmetry of the photoemission spectra of Sn 3d was previously reported in La-doped $BaSnO_3$ [16, 17], $BaSnO_3$ [18] and SnO_2 [19] thin films, as well as in Sb-doped SnO_2

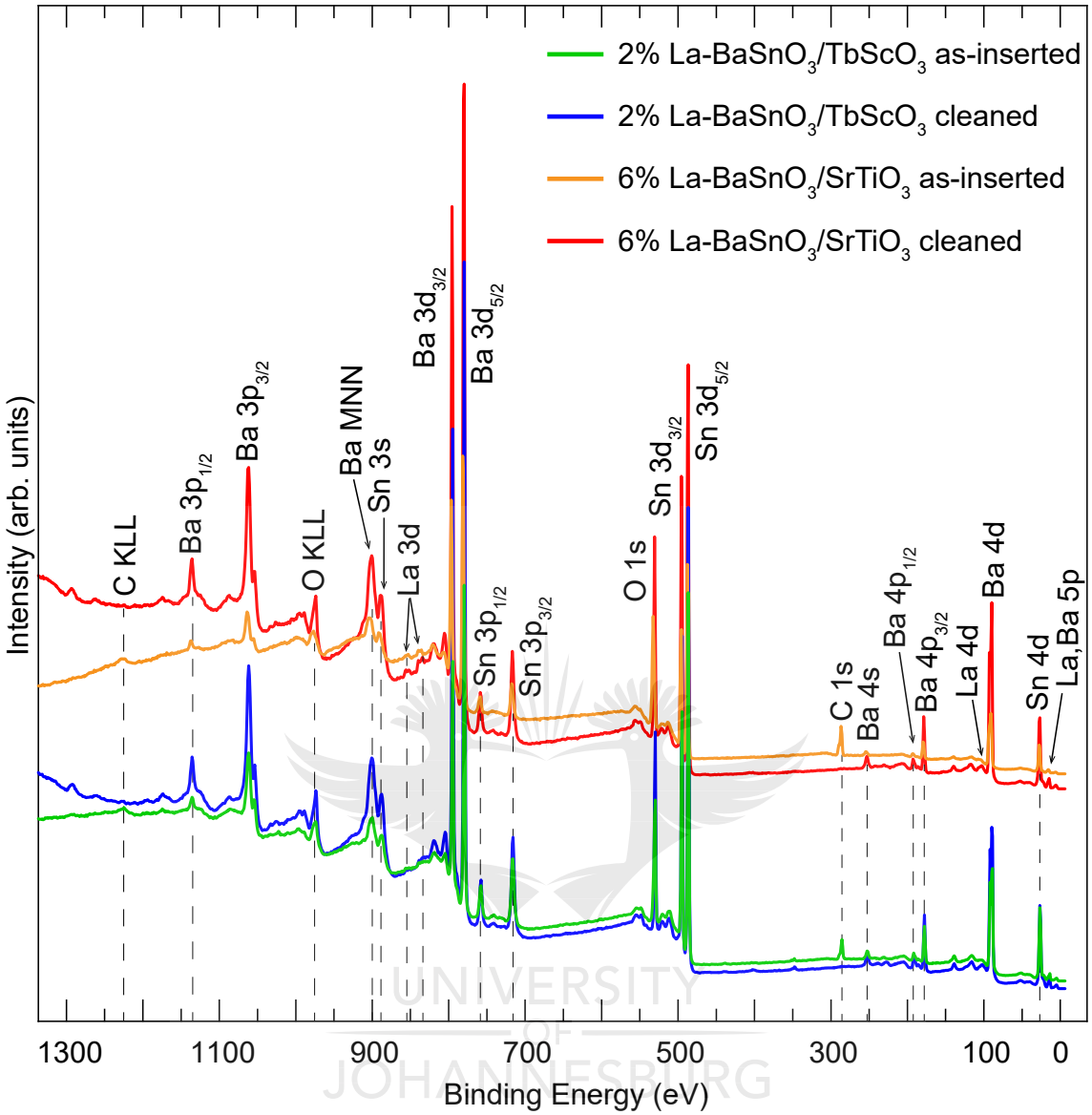

Figure 5.2: XPS survey scans for as-inserted (light green and orange curves) and cleaned (blue and red curves) 2% La-$BaSnO_3$ (25 nm)/$TbScO_3$ and 6% La-$BaSnO_3$ (25 nm)/$SrTiO_3$ samples. All the core levels from La, Ba, Sn and O elements can be seen in the spectra. The C 1s signal originating from surface contamination with the associated C KLL Auger electron peak are also visible. The spectra were acquired with an experimental resolution of 0.90 eV using the Al K_α excitation source.

[20, 21, 22] ceramics. It was also reported that this asymmetry is a function of the amount of band filling [17, 20, 22], as the Sn 3d core of the undoped materials shows a highly symmetric peak [16, 20, 22], while that of the doped materials shows an asymmetry toward the high binding energy side of the core peak that greatly increases with the level of doping [17, 20, 22]. As discussed in Section 3.3.4, the asymmetry in core photoemission spectra of metallic systems arises from intrinsic plasmon excitations, which result in an additional component satellite to the main core line associated with an unscreened final state [20, 22]. As was also discussed in Section 3.3.4, an intrinsic plasmon is a localized trap state created by the Coulomb potential

of the core hole [23, 24]. The localized trap state is created by pulling out an electron from the conduction band [8]. Thus, the effect of doping on the line shape of the Sn 3d core level can be perceived in terms of a screening response of the conduction electron introduced by doping [22]. Based on these observations (which are also discussed in detail in Section 3.3.4), two doublet components were used to fit the Sn 3d spectra assuming that the Koopmans' state (excited state after the removal of a core electron from an atom) is projected into screened and unscreened final eigenstates [22].

As can be seen in Fig. 5.3, Sn 3d core lines are fitted to two Voigt components which give an excellent description of the overall line shape of the spectra. It should be noted that the Gauss-Lorentz ratio was allowed to vary freely during the fits. In each spectrum in the figure, the main component is the peak at low binding energy labeled "screened". This peak has a dominant Gaussian line shape. The component at high binding energy labeled "unscreened" is dominantly Lorentzian. As stated above, this component is a satellite associated with intrinsic plasmon excitations. Thus, large Lorentzian line width, would mean short core hole lifetime, and large Gaussian would imply small Lorentzian width and long core hole lifetime. Similar satellite structure was strongly observed in the Sn 3d and In 3d core photoemission spectra of transparent conducting oxides (TCOs) such as Sb-doped SnO_2 [20, 21, 22], In_2O_3–ZnO [25] and Sn-doped In_2O_3 [8, 26]. However, it is remarkable that a completely different peak assignment was made for the Sn 3d regions in $BaSnO_3$ thin films [18] as described in Section 2.4.2, as well as in SnO_2 thin films [19, 27, 28]. In those reports, Sn showed mixed valence states and the Sn 3d core levels were fitted with three components associated with Sn^{4+}, Sn^{2+} and Sn metal (Sn^0). A mix of oxidation states suggests a non-pristine surface. In this present study, however, the valence state of Sn is 4+ as indicated by the binding energy of the screened component in all the Sn 3d spectra [29, 30].

Looking at Table 5.1, it can be seen that the spectra of the 6% La doping ($n = 4.05 \times 10^{20}$ cm^{-3}) are shifted to high binding energies as compared with the spectra of the 2% La doping ($n = 1.35 \times 10^{20}$ cm^{-3}). Considering the screened components, the shift is 0.62 eV in the XPS spectrum of the as-inserted surface. This shift decreases to 0.12 eV after the surface is cleaned. Binding energy shifts of the 3d orbital with increasing carrier density were also reported in the photoemission spectra of other TCOs. For instance, shifts of 0.05 and 0.10 eV were reported in the Sn 3d core XPS spectra of Sb-doped SnO_2 ceramics [20, 22]; a shift of 0.30 eV was observed in the HAXPES Cd 3d core of CdO thin films [31]; shifts up to 0.19 eV were recorded in the HAXPES In 3d spectra of In_2O_3–ZnO thin films [25]; and a shift of 0.78 eV was reported in the In 3d core XPS and HAXPES spectra of Sn-doped In_2O_3 thin

Table 5.1: Fitted parameters of Sn 3d regions for the as-inserted and cleaned samples shown in Fig. 5.3. The peak position (P), the relative intensity (R) and the FWHM (F) are given.

		As-inserted			Cleaned		
	Error	P (eV) (±0.05)	R (%) (±1)	F (eV) (±0.05)	P (eV) (±0.05)	R (%) (±1)	F (eV) (±0.05)
2% 1.35×10^{20} cm^{-3}	Screened	486.67	52	1.17	486.68	54	1.15
	Unscreened	487.18	48	1.43	487.19	46	1.34
6% 4.05×10^{20} cm^{-3}	Screened	487.29	68	1.31	486.80	57	1.06
	Unscreened	487.99	32	1.53	487.50	43	1.34

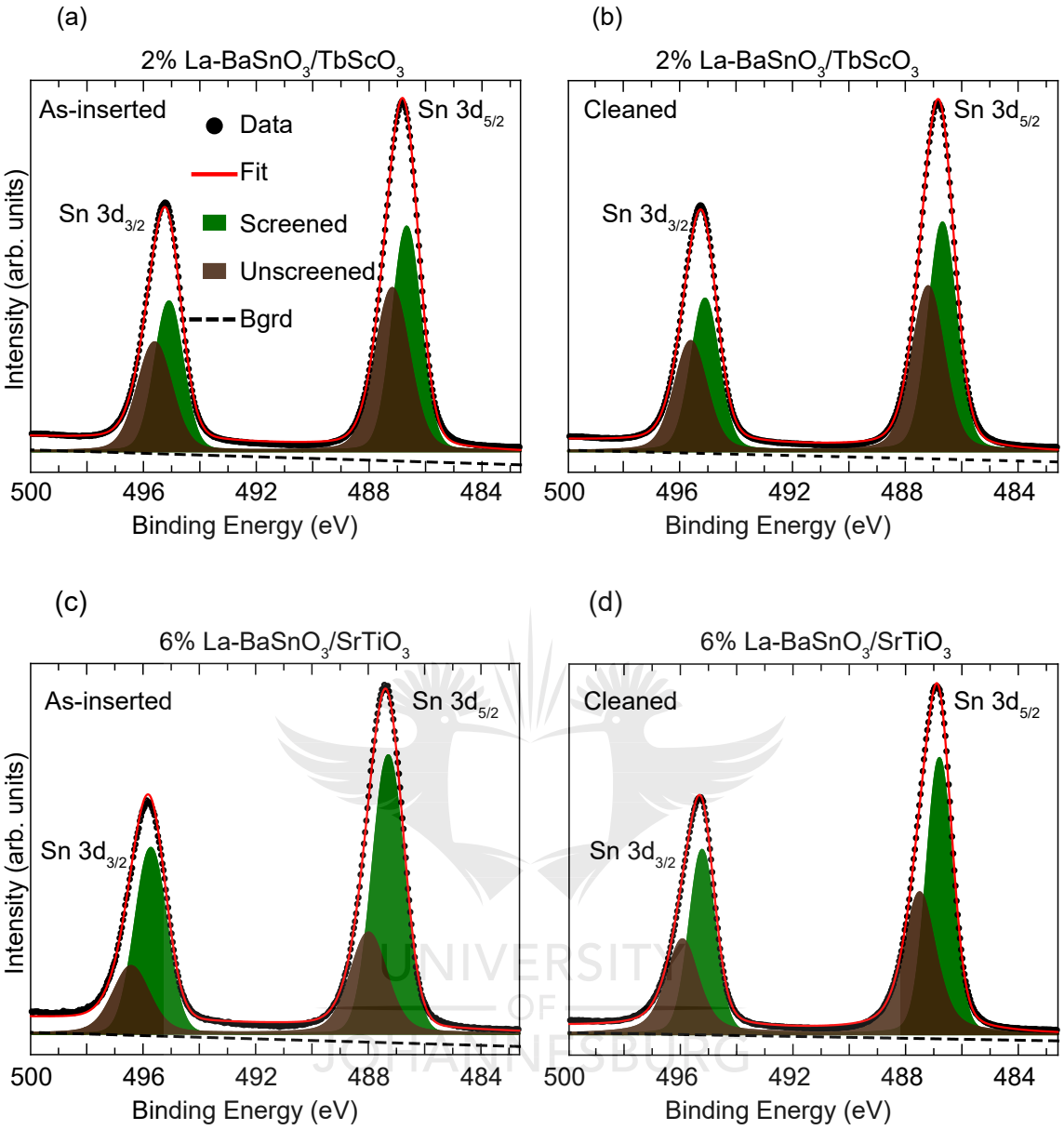

Figure 5.3: Fits of the XPS spectra around the Sn 3d regions for as-inserted and cleaned 2% La-$BaSnO_3/TbScO_3$ and 6% La-$BaSnO_3/SrTiO_3$ samples. The Sn 3d spectra are fitted with two Voigt doublet components labeled screened and unscreened. The data were acquired with an experimental resolution of 0.58 eV. The peak heights are normalized for all four figures for easier comparison. In this figure and most following XPS spectra, the background and fit components are shifted vertically to make the figures clearer.

films [8]. These shifts were related to the shifts in the conduction band due to doping as will be also addressed in Section 5.3. It should be noted that the positions of the screened and unscreened peaks as shown in Table 5.1 are consistent with those in Refs. [20, 22].

It is important to highlight that during the fits, boundaries were set for the energy separation between the screened peak and its satellite. These constraints were applied to the lower limit of the position of the unscreened peak such that the satellite energy (energy separation

between screened and unscreened peaks) would be ≈ 0.5 eV in the sample with the carrier density $n = 1.35 \times 10^{20}$ cm^{-3} (2% doped film), ≈ 0.7 eV in that with the electron density $n = 4.05 \times 10^{20}$ cm^{-3} (6% doped sample). These choices were made considering two important results reported in literature. First, the satellite energy corresponds to the plasmon energy, especially the surface plasmon energy, and increases with the carrier density n [8, 20, 22, 32, 33]. Since the surface plasmon energy is proportional to the carrier density [20, 26], it was decided on the satellite energy values reported for the photoemission of the 3d orbital in Sb-doped SnO_2, In_2O_3–ZnO and Sn-doped In_2O_3 [8, 20, 22, 25], that were associated with carrier density values comparable to the carrier densities achieved in the samples.

The second important result that guided this choice is that in TCOs, the surface plasmon energy is around 0.7 eV, comparable with intrinsic plasmon core level line widths [20, 25]. Hence, based on the above considerations, there could be some variations in the choice made for the satellite energy. Nevertheless, this choice tends to be in agreement with the Langreth model [23, 34] described in Section 3.3.4. Indeed, according to the plasmon model developed by Langreth, the relative intensity of the unscreened high binding energy component should increase with decreasing carrier density, as can be clearly seen in Table 5.1, when comparing the relative intensities of the unscreened peaks for the 6% and 2% doped samples. Concomitantly, the relative intensity of the screened low binding energy peak decreases, consistent with previous reports [8, 20, 22, 25]. Furthermore, as also reported in literature, the unscreened peak is broader than the screened component [8, 20, 22, 25], as evidenced by their FWHM values contained in Table 5.1. This parameter was not constrained in the fits; and the fact that a narrower low binding energy peak and a broader high binding energy peak are consistently observed in the fits, only confirms the applicability of the plasmon model to the analysis of the Sn 3d core XPS spectra in these films.

b) O 1s Core Level

The fitted XPS spectra of the O 1s core regions are depicted in Fig. 5.4. Considering the figures, it can be seen that the O 1s peaks are asymmetric, presenting a shoulder on the high binding energy side. This shoulder is more pronounced in the as-inserted surfaces (Figs 5.4(a) and 5.4(c)). The shape of the peaks indicates several oxygen related components at the surface. Hence, four and three symmetric Voigt peaks of same FWHM were used for the deconvolution of the as-inserted and cleaned spectra, respectively. The main component which is labeled O_{lat} is attributed to lattice oxygen in a BaO environment. The peak labeled O_{vac} is associated with the formation of oxygen vacancies. This peak represents the change in the local electronic density of the other lattice oxygen atoms when an oxygen is removed [35, 36, 37, 38, 39, 40]. Oxygen vacancies are common native point defects in oxide materials [41, 42, 43, 44], and have been often reported in O 1s spectra of these materials [18, 43, 45, 46, 47, 48]. In the case of epitaxial $BaSnO_3$ and La-doped $BaSnO_3$ thin films, it has been reported that oxygen vacancies are created during the deposition of the film, and upon annealing of the grown film in vacuum or in forming gasses [43, 44, 47, 49]. As for the peaks labeled $-$OH and C-O, both are related to contamination, associated with adsorbed oxygen (chemisorbed) resulting from the dissociation of water on the sample surface [45, 46, 47, 50, 51, 52], and oxygen attached to organic residues or carbonates [45, 50], respectively.

The results of the parameters employed for the fits of the spectra shown in Fig. 5.4 are provided in Table 5.2. As can be seen from the table, the O 1s signals from the 6% doped sample are shifted to higher binding energies, consistent with the shifts observed in the Sn 3d

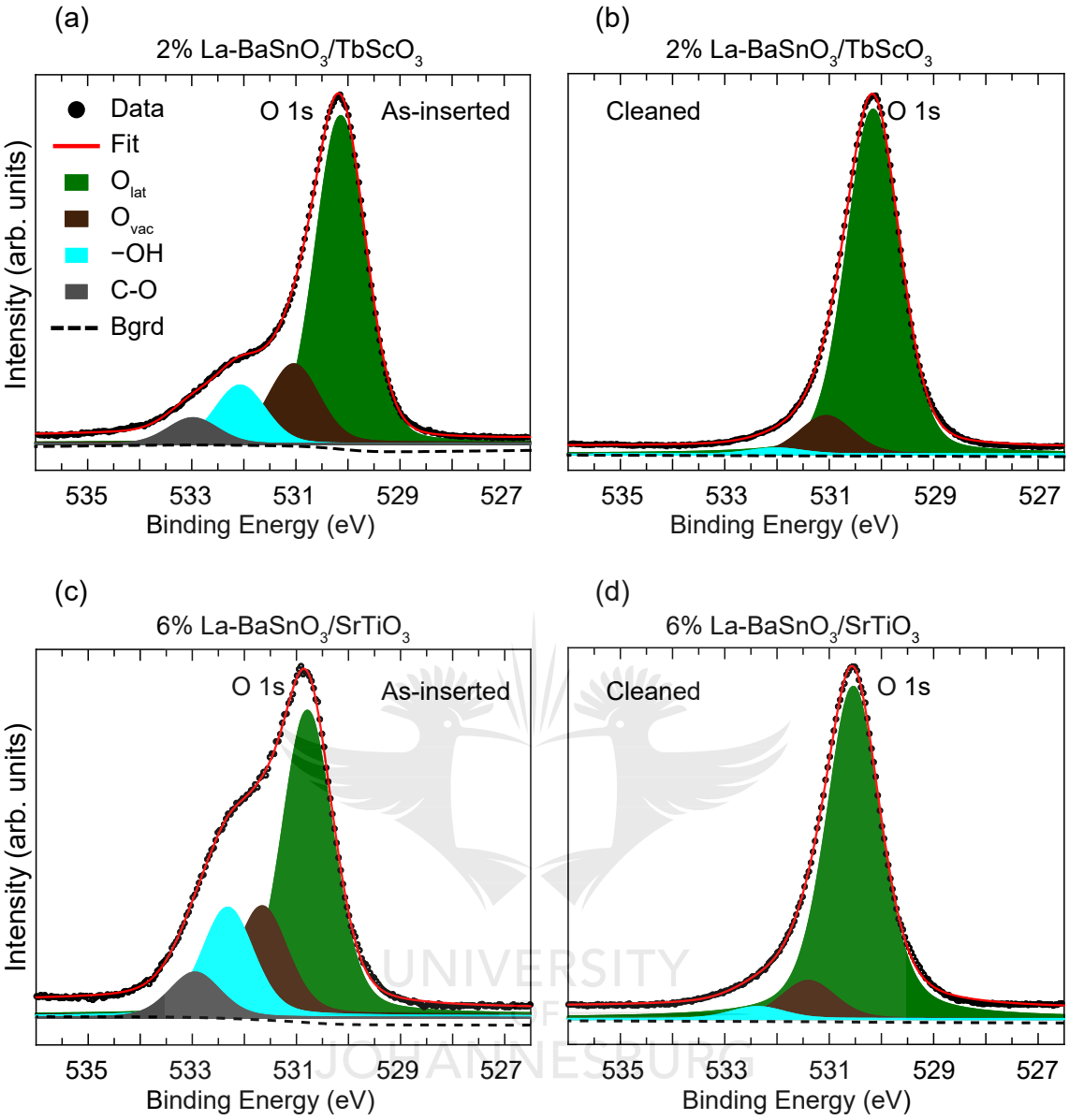

Figure 5.4: Fits of the XPS spectra of the O 1s core levels for as-inserted and cleaned 2% La-$BaSnO_3/TbScO_3$ and 6% La-$BaSnO_3/SrTiO_3$ samples. The O 1s core electrons are fitted with (a) and (c) four, and (b) and (d) three Voigt singlet components. The data were acquired with an experimental resolution of 0.58 eV. The peak heights are normalized.

core spectra above. These shifts are therefore associated with the doping effect. Similar shifts with increases in La doping, that increase the carrier density, were previously reported in the HAXPES spectra of O 1s core levels of MBE grown La-$BaSnO_3/TbScO_3$ thin films [17]. For the as-inserted spectrum shown in Fig. 5.4(c), O_{lat} is shifted by 0.65 eV. The shift is reduced to 0.38 eV in the spectrum of the cleaned surface shown in Fig. 5.4(d). The C-O component which is only identified in the as-inserted samples presented in Figs. 5.4(a) and 5.4(c) disappears after the treatment of the surfaces as clearly illustrated in Figs. 5.4(b) and 5.4(d). The −OH component (hydroxyl groups [45, 50]) originates from sample exposure to air. Note that like the C-O component, the −OH peak is less intense in the as-inserted surface

Table 5.2: Fitted parameters of O 1s regions for as-inserted and cleaned surfaces shown in Fig. 5.4. The peak position (P), the relative intensity (R) and the FWHM (F) are given.

		As-inserted			Cleaned		
	Error	P (eV) (±0.05)	R (%) (±1)	F (eV) (±0.05)	P (eV) (±0.05)	R (%) (±1)	F (eV) (±0.05)
2% 1.35×10^{20} cm^{-3}	O_{lat}	530.14	67	1.13	530.16	89	1.19
	O_{vac}	531.04	16	1.13	531.06	10	1.19
	−OH	532.07	12	1.13	532.01	2	1.19
	C-O	532.98	5	1.13	—	—	—
6% 4.05×10^{20} cm^{-3}	O_{lat}	530.79	54	1.15	530.54	88	1.21
	O_{vac}	531.66	19	1.15	531.40	9	1.21
	−OH	532.32	19	1.15	532.37	3	1.21
	C-O	532.95	8	1.15	—	—	—

presented in Fig. 5.4(a) compared with the as-inserted surface depicted in Fig. 5.4(c) (see also Table 5.2). The comparatively low intensities of the contaminant components in the surface shown in Fig. 5.4(a) are most probably related to the fact that this surface was pre-annealed. Furthermore, the relative intensity of the −OH component is lower in the cleaned spectrum in Fig. 5.4(b) (compared with that in Fig. 5.4(d)) as indicated in Table 5.2. This could be because both samples (surfaces) were measured (prepared) two years apart (the sample in Fig. 5.4(a) was measured first), under perhaps different vacuum conditions. Although the base pressures were similar in both cases, the composition of the residual molecules in the vacuum could easily have been different. Indeed, as can be seen in Figs. 5.4(b) and 5.4(d), −OH could not be completely removed from the surfaces, probably because the preparation chamber contained too much H_2O, and even more so when the spectra in Fig. 5.4(d) was prepared (the surfaces were annealed at ≈ 700 °C at a pressure of ≈ 7×10^{-6} mbar oxygen). Nevertheless, its relative intensity is considerably reduced in the cleaned surfaces, confirming its contaminant character. The surface-related character of the −OH component will be further addressed in Section 5.2.2.

Interestingly, the relative intensities of the O_{lat} peaks increase whereas those of the O_{vac} components decrease after the surfaces are cleaned (see Table 5.2). The relative intensity of the O_{vac} component in the as-inserted surfaces (Figs. 5.4(a) and 5.4(c)) is probably amplified with surface contamination (C-O). In the cleaned surfaces (Figs. 5.4(b) and 5.4(d)), O_{vac} is almost in the same proportion. Its relative intensity is slightly smaller in the cleaned surface shown in Fig. 5.4(d) where the component due to water (−OH) is more intense (as compared with the cleaned surface depicted in Fig. 5.4(b)). This could lead to the conclusion that the relative intensity of the O_{vac} peak is affected by contamination, where the carbonate component (C-O) has an amplifying effect and the hydroxyl component (−OH) has a reducing effect.

c) Ba 3d Core Level

The fits of the XPS spectra of the Ba 3d core electrons for the as-inserted and cleaned surfaces are reported in Fig. 5.5. The Ba 3d spectra also showed asymmetric line shapes and were fitted with two symmetric Voigt doublets. Table 5.3 summarizes the fitted parameters of the Ba 3d core levels. The FWHM of the Voigt peaks were set to be the same in each spectrum. Again,

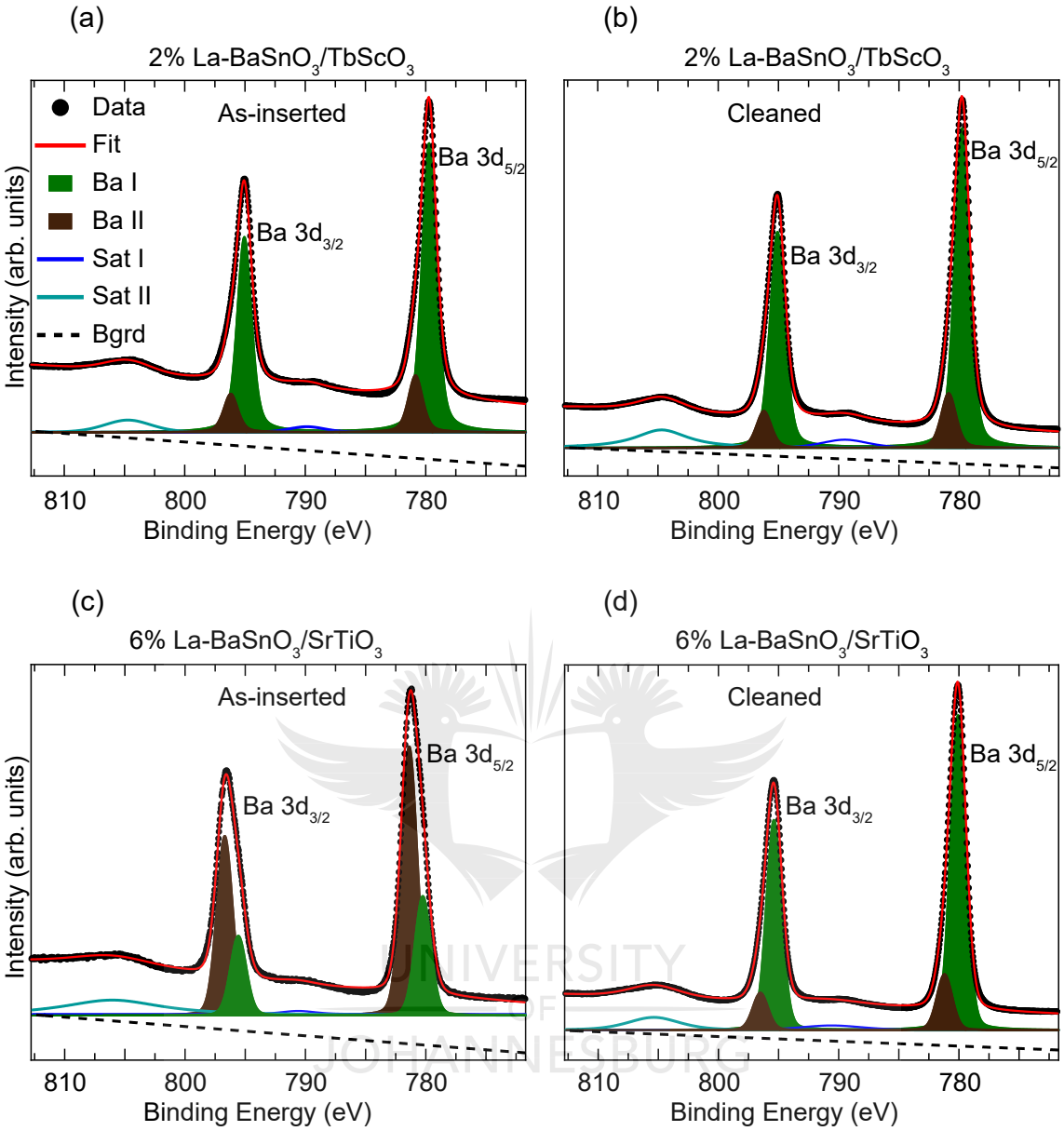

Figure 5.5: Fits of the XPS spectra of the Ba 3d core regions for as-inserted and cleaned 2% La-$BaSnO_3/TbScO_3$ and 6% La-$BaSnO_3/SrTiO_3$ samples. The Ba 3d core spectra are fitted with two Voigt doublet peaks, Ba I and Ba II. The spectra were acquired with an experimental resolution of 0.58 eV. Peak heights normalized.

the spectra of the 6% doped sample are shifted to high binding energies (with respect to the spectra of the 2% doped sample) due to the increase in the concentration of the electrons [17]. Such shifts were also observed in the HAXPES spectra of the Ba 3d core levels of the La-$BaSnO_3/TbScO_3$ thin films [17]. The main doublet labeled Ba I, which is assigned to lattice barium in the Ba^{2+} state, is shifted by 0.53 eV for the as-inserted sample and by 0.32 eV for the cleaned sample. The valence state of Ba, 2+, as identified by the binding energy of the Ba I component, is consistent with previous spectroscopic results on powder and epitaxial thin films of $BaSnO_3$ [18, 51], as described in Section 2.4.2. The second doublet labeled

Table 5.3: Fitted parameters of Ba 3d regions for as-inserted and cleaned spectra presented in Fig. 5.5. The peak position (P), the relative intensity (R) and the FWHM (F) are given.

		As-inserted			Cleaned		
	Error	P (eV) (±0.05)	R (%) (±1)	F (eV) (±0.05)	P (eV) (±0.05)	R (%) (±1)	F (eV) (±0.05)
2%	Ba I	779.72	84	1.42	779.75	85	1.48
1.35×10^{20} cm^{-3}	Ba II	780.85	16	1.42	780.88	15	1.48
6%	Ba I	780.25	31	1.57	780.07	85	1.51
4.05×10^{20} cm^{-3}	Ba II	781.38	69	1.57	781.20	15	1.51

Ba II is either due to under-coordinated barium as assigned in several reports on epitaxial $BaTiO_3$ thin films [11, 53, 54, 55, 56], or to contamination. As shown in Table 5.3, the relative intensities of the Ba II doublets decrease after the treatment of the surfaces while those of the Ba I doublets increase. This trend suggests that Ba II doublet could be a surface component related to contamination. Moreover, the very high proportion of Ba II in the as-inserted sample portrayed in Fig. 5.5(c) would then be related to the high level of contamination observed in the corresponding O 1s spectrum presented in Fig. 5.4(c). The drastic decrease of the Ba II proportion in the cleaned surface, depicted in Fig. 5.5(d), further supports its surface character associated with contamination. The origin and nature of the Ba II peak are carefully investigated in Section 5.2.2 by carrying out a systematic analysis of its fraction with respect to the probing depth. It is to be noted that the energy separation between Ba I and Ba II components was constrained to vary between 1 eV and 1.5 eV, as reported in literature for $BaSnO_3$ and $BaTiO_3$ thin films [18, 53, 54, 55, 57, 58]. For all the fits shown in Fig. 5.5, this energy separation was consistently found to be 1.13 eV (see Table 5.3).

Two satellite features labeled Sat I and Sat II are also detected in the XPS spectra of Ba 3d regions as can be seen in Fig. 5.5. These are satellites resulting from shake-up processes involving Ba 3d photoelectrons and valence electrons, as was described in Section 3.3.4. These satellites are located at the high binding energy side of the associated Ba $3d_{\frac{5}{2}}$ and Ba $3d_{\frac{3}{2}}$ peaks. These satellites are broad, and their energy separation from the main peak, 10 eV on average, is consistent with literature [59].

It is noteworthy that the Ba 3d and O 1s core lines slightly broaden with increasing carrier density, but neither of them exhibit a pronounced asymmetry variation with increasing La doping as observed in the Sn 3d core spectra. This discrepancy can be understood considering that the conduction band minimum in $BaSnO_3$ and La-doped $BaSnO_3$ is predominantly of Sn 5s orbital character [17, 60, 61, 62]. As stated in Section 2.2.2, the key elements for the high electron mobility in La-doped $BaSnO_3$ are the cubic structure of $BaSnO_3$ which features a perfect 180° angle of the O—Sn—O bonds in the SnO_6 octahedra, as well as the highly dispersive Sn 5s derived conduction band [61]. This highlights the key role of the Sn in the structural and electronic transport characteristics of La-doped $BaSnO_3$ thin films.

It is also important to note that the loss of Ba:Sn stoichiometry in the nominal ratio 1:1 could result in additional defects in the films and hinder the desired electrical properties [17, 63]. The Ba:Sn stoichiometry in the grown epitaxial La-doped $BaSnO_3$ thin films was examined by investigating the oxidation state of the Sn. To investigate the valence state of the Sn in the

samples, EELS measurements were performed within a transmission electron microscope on a 6% La-doped $BaSnO_3$ (25 nm) sample grown on a $DyScO_3$ (110) substrate with a 100 nm thick $BaSnO_3$ buffer layer. This is the optimized sample studied in Sections 4.2.2 to 4.5. The EELS data were acquired during the TEM measurements at the Max Planck Institute in Stuttgart, and represents a typical example in this study. For reference, the microstructural properties of this sample investigated by analyzing the TEM data are shown in Figs. 4.22 and 4.24. The EELS measurements were performed on a cross-section of the sample, and the electron beam was focused on the $BaSnO_3$ buffer layer and the La-doped $BaSnO_3$ film layer regions. Spectra from areas without and with La could then be compared, to see whether the doping alters or changes the oxidation state of the Sn.

As discussed in Section 3.3.2, EELS is an analytical technique based on the inelastic scattering of the electrons emitted from the source with those of the specimen (atomic electrons). This interaction results in loss of energy by the electron beam. The energy dispersion gives detailed information of the local environment of the atomic electrons, and consequently of the chemical properties of the specimen. In Fig. 5.6(a), the signal intensities in the EELS spectrum are plotted. This figure shows the distribution of the elements (atomic distribution) in the sample, forming a total layer thickness of 120 nm, with a 24 nm thick La-doped layer. For better understanding, dashed orange lines are used to divide the signal into regions indicated as (1) to (4). In the region labeled (1), intensities of Dy, O, and Sc are visible, whereas Sn, Ba and La are basically zero (the residual color in the La plot is noise). This is the substrate. In the middle, indicated as (2), Sn, O, and Ba show non-zero intensities, and, as expected, Dy, Sc, and La are zero. This is the $BaSnO_3$ area (buffer layer). On the right side, region (3), La

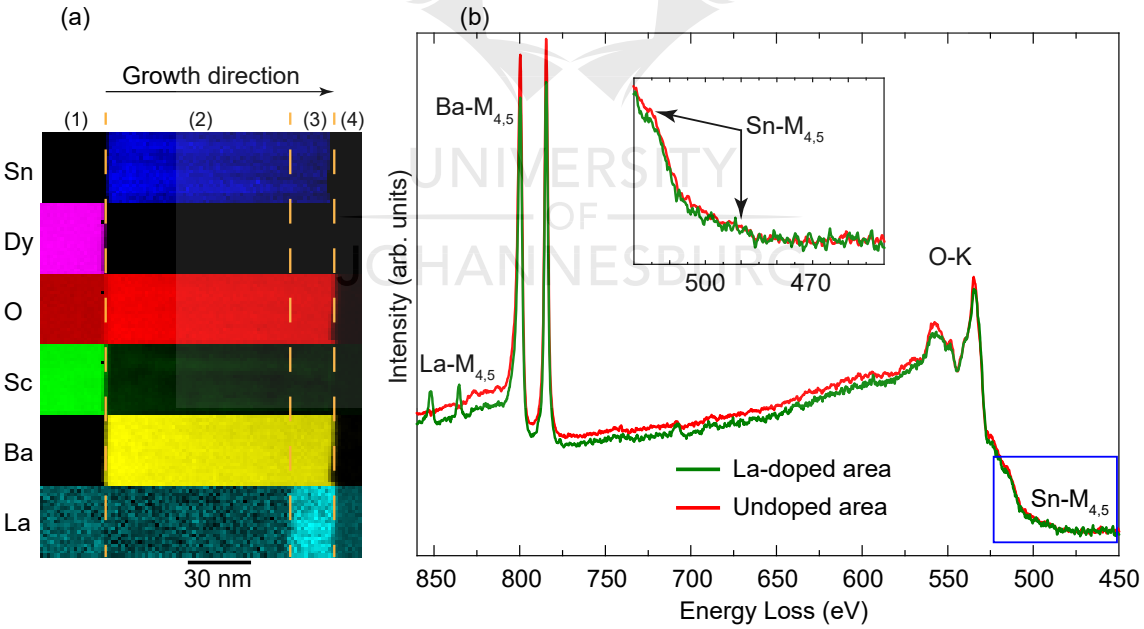

Figure 5.6: EELS data of the 6% La-$BaSnO_3$/$BaSnO_3$/$DyScO_3$ sample acquired with a transmission electron microscope. (a) Elemental mapping which shows the atomic layer distribution, 120 nm thick, where the La-doped layer is 24 nm. The dashed orange lines serve to indicate different regions of the sample. (b) Electron energy loss spectra for two regions in the specimen, an area with only $BaSnO_3$ (red curve) and another with only La-$BaSnO_3$ (green curve). The inset shows the enlargement of the region around the Sn-$M_{4,5}$ ionized edge delimited by the blue rectangle.

becomes non-zero along with Sn, O, and Ba. This is the La-doped part of the $BaSnO_3$ layer. On the very right, region depicted as (4), all signals are zero because there is no specimen in this area. Note that the intensities are very homogeneous. There is a gradual loss of intensity from left to right (from (1) to (4)). This is due to the fact that the specimen becomes thinner along this direction, i.e. it is not a material property.

In Fig. 5.6(b), the ionized core La-$M_{4,5}$, Ba-$M_{4,5}$ and Sn-$M_{4,5}$ corresponding to the excitation of 3d states, as well as O-K corresponding to the excitation of the 1s state, are presented. It can be seen that the spectra of the $BaSnO_3$ (red curve) and La-doped $BaSnO_3$ (green curve) are very similar, apart from the presence of La peaks in the latter. Most importantly, this can be seen in the area around the Sn-$M_{4,5}$ core edge indicated by the arrows in the inset. This implies that the valence state of the Sn in $BaSnO_3$ and La-doped $BaSnO_3$ are the same, ensuring good stoichiometry in these films [63]. Although the peak at $\approx$ 490 eV is barely detectable in this present study, the two arrows in the inset point at two very weak peaks at $\approx$ 490 eV (M_5) and $\approx$ 515 eV (M_4), which are in good agreement with those reported for Sn-$M_{4,5}$ EELS edge in SnO_2 [64]. This indicates that the Sn in the epitaxial films grown in this study essentially has an oxidation state of 4+, consistent with the XPS data shown in Fig 5.3, as well as with the previous EELS reports on epitaxial La-doped $BaSnO_3$ thin films [63, 65].

5.2.2 Angle-Dependent XPS

To obtain more insights into the origin of the multiple components observed in the XPS spectra of the core electrons shown in Figs. 5.3, 5.4 and 5.5, XPS acquisitions at two different electron take-off angles θ (angle between the analyzer and the sample surface) were performed. Firstly, the measurements were done in the configuration used to obtain the data shown in Figs. 5.3, 5.4 and 5.5, which corresponds to a take-off angle of 90° (normal emission). Secondly, the configuration was changed by rotating the manipulator polar angle to obtain a take-off angle of 35°. In these two configurations, the spectra were acquired with photons emitted from Al K_α anode (photon energy of 1486.71 eV) and the experimental resolution during acquisition was 0.58 eV. It is well known that the effective probing depth (herein called ζ) is dependent on the photoelectron escaping angle, and both are related by the expression $\zeta \approx 3\lambda \sin\theta$, where λ is the mean attenuation length [54, 66, 67, 68]. This means that at the take-off angle of 35°, the photoelectrons emitted originate from a region nearer the surface, whereas at the take-off angle of 90° these photoelectrons are emitted from a deeper depth within the sample. This is because at normal emission, electrons from a given depth have a shorter path to travel through the sample than those at 35°, and are therefore attenuated less. Additionally, to excite electrons more from the bulk, the Ag L_α anode (at normal emission) which produces photons of much higher energy (2984.31 eV) was used. This permitted to conclusively fingerprint each component. With this photon source, the data were acquired with an experimental resolution of 0.96 eV. It is noteworthy that the experimental resolution with the Ag anode is worse since the monochromatization of this anode is not as effective as with the Al anode. Thus, for accurate comparison of the data, a rescaling of the FWHM values is performed considering the resolution with the Al anode.

For the angle-dependent XPS analysis, a 6% La-$BaSnO_3$ (25 nm)/$BaSnO_3$ (100 nm)/$TbScO_3$ sample with a carrier density of $n = 4.92 \times 10^{20}$ cm^{-3} was used. As mentioned in the introductory section (Section 5.1), this sample was chosen as a replacement of the highest mobility $BaSnO_3$ buffered sample shown in Table 4.6, as the surface of the original sample was

believed to have been damaged (see Appendix C.1). In Section 5.2.1, the XPS data of two high mobility unbuffered samples with carrier densities of 1.35×10^{20} cm^{-3} and 4.05×10^{20} cm^{-3} were discussed. Thus, having another sample with different electrical properties is convenient for qualitative and quantitative discussions of the core levels and valence band electrons.

The above sample was cleaned following the procedure described in Section 3.3.4, and then exposed to contamination in the load lock on purpose, to investigate how the hydroxide layer would affect the states in the valence band region. The core orbitals and valence bands of these two surfaces are presented in Figs. 5.7 to 5.11. The spectra of the clean surface (core levels and valence bands) were taken for about 30 hours in the analysis chamber maintained in good vacuum ($\approx 5\times10^{-10}$ mbar). After these measurements, no carbon signal was detected and the sample was transferred into the load lock (average pressure of 1×10^{-8} mbar) to allow for absorption of carbonate and hydroxyl groups on the sample surface. After 1 day in the load lock, a more defined carbon peak could be detected. It is to be noted that this carbon peak was anyway more than two orders of magnitude less intense than the signal from the sample as-inserted. Measuring the core levels associated with surface exposure helped track the changes induced in the respective orbitals and enabled a correlation with the features in the valence band. All the spectra associated with the contaminated surface were collected with the Al K_α anode at take-off angles of 35° and 90° as shown in Figs. 5.7, 5.8 and 5.9.

Figure 5.7 shows the XPS angle-dependent spectra for the Sn 3d core line. In the figure, the measurement gets more bulk sensitive as the photoelectron take-off angle increases from 35° to 90°, and as the excitation source is changed from Al K_α (Al) to Ag L_α (Ag). Only the spectrum in Fig. 5.7(c) was taken with the Ag anode to probe bulk electrons and ensure a systematic comparison of the surface sensitive and bulk sensitive data [66, 67, 68]. As for the analysis of the Sn 3d core electrons shown in Fig. 5.3, two Voigt doublets associated with screened and unscreened final eigenstates were used to fit the spectra. Considering that the carrier density in this sample is $n = 4.92 \times 10^{20}$ cm^{-3}, the satellite energy was fixed at 0.8 eV, consistent with the reported energy separation (for comparable carrier concentration) between the screened and unscreened components of the In 3d core lines in In_2O_3–ZnO [25] and Sn-doped In_2O_3 [8] thin films. It should be noted that this satellite energy value is closer to the bulk plasmon energy [25]. The parameters of the fits are summarized in Table 5.4. Again, the variation of the relative intensity of the unscreened component for the clean surfaces in Tables 5.1 and 5.4 (at 90°, Al anode) provide support for the Langreth model. As can be seen from the tables, the value of relative intensity of the unscreened state increases as the carrier density decreases following the sequence 4.92×10^{20} cm^{-3}, 4.05×10^{20} cm^{-3} and 1.35×10^{20} cm^{-3}.

Consider the clean surface presented in Figs. 5.7(a) to 5.7(c). As can be seen in Table 5.4, as the measurement becomes more bulk sensitive (from Fig. 5.7(a) to Fig. 5.7(c)), the relative intensity of the low binding energy screened state decreases whereas that of the high binding energy unscreened satellite increases. This indicates that the satellite is more a bulk feature. Similarly for the spectrum measured with the Ag anode as shown in Fig. 5.7(c), the unscreened signal is in a higher proportion compared with the screened component. The bulk nature of the satellite suggests that the core holes considerably depend on the neighboring bulk atoms of the ionized atom [69]. In Section 3.3.4 it was discussed that the screening mechanism is a response to the creation of a core hole during the photoionization process [20, 22, 23, 24]. In this model, a localized state is created and can be filled (screened state) by an electron from the conduction band or left empty (unscreened state) such as discussed in Section 3.3.4. Thus, the line width of the unscreened final state is governed by the time scale for the conduction

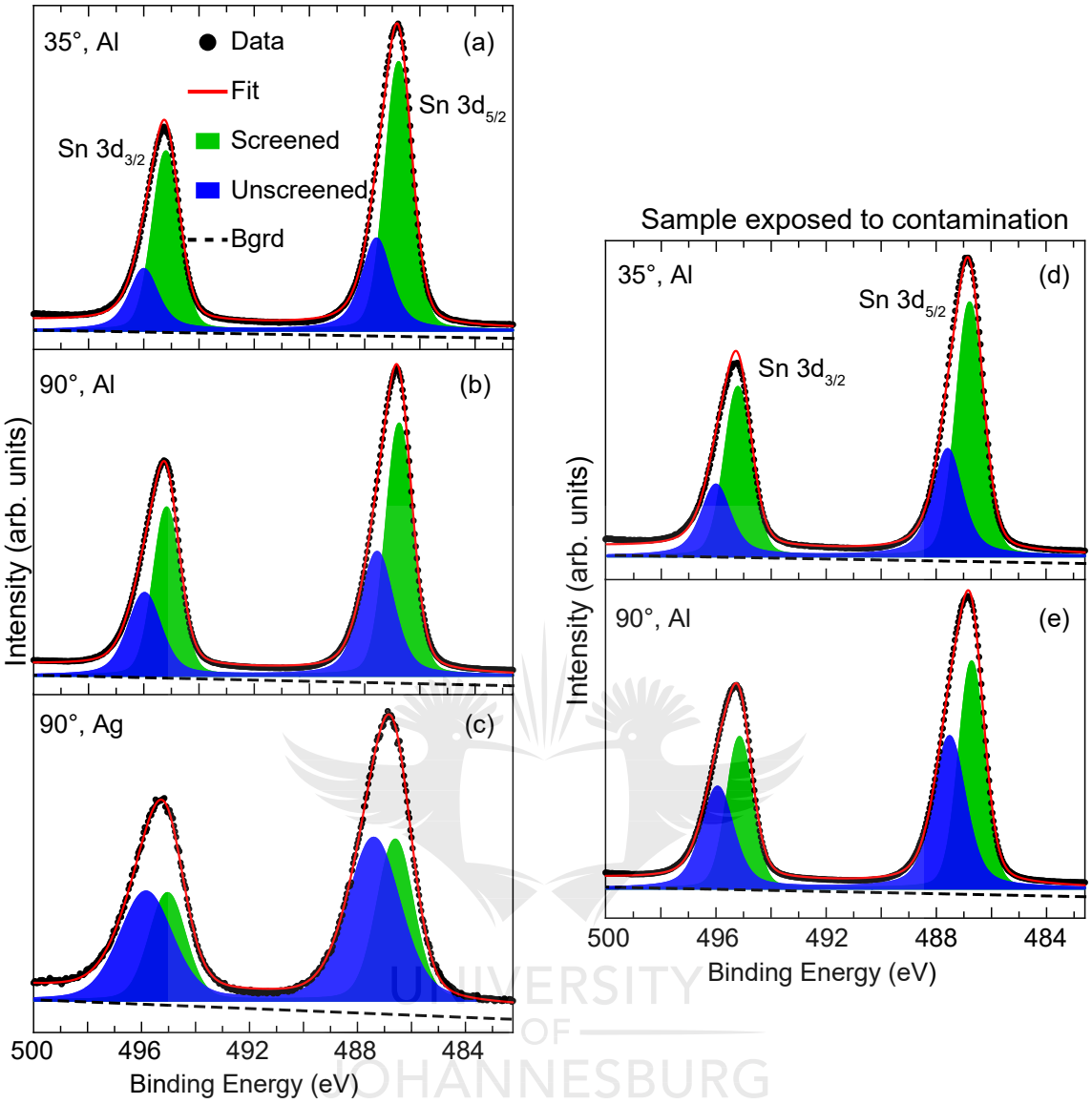

Figure 5.7: Fits of the angle-dependent XPS spectra around the Sn 3d region of the 6% La-$BaSnO_3/BaSnO_3/TbScO_3$ film. The take-off angle of the electrons is varied to collect electrons from a region near the surface (35°) and also from a deeper region (90°). The spectra in (a)-(c) are for the clean surface, and those in (d) and (e) are for the surface voluntarily exposed to contamination in the load lock. The data in (a), (b), (d) and (e) were collected while exciting the sample with an Al K_α anode (Al) at 35° and 90° take-off angles, whereas for the spectrum in (c) an Ag L_α anode (Ag) was used at 90° electron take-off angle. Peak heights were normalized.

electrons to screen the core hole [8, 20]. For the situation depicted in Fig. 5.7(c), where the unscreened component has the largest FWHM value in the bulk of 2.21 eV (Table 5.4), this implies that the core holes are less screened in the bulk. This could be assuming that the mobile conduction electrons are more localized to the surface.

The situation portrayed in Fig. 5.7(c) whereby the relative intensity of the unscreened final state is higher than that of the screened state is similar to that observed previously by HAXPES and XPS [8, 22, 25]. More precisely, this situation was also encountered in the HAXPES spectra of

Table 5.4: Peak ratios for angle-dependent XPS of the Sn 3d spectra shown in Fig. 5.7. The peak position (P), the relative intensity (R) and the FWHM (F) are given. The FWHM values in brackets are the ones rescaled for the resolution of the Al anode.

		Clean surface			Contaminated surface		
	Error	P (eV) (±0.05)	R (%) (±1)	F (eV) (±0.05)	P (eV) (±0.05)	R (%) (±1)	F (eV) (±0.05)
35° Al anode	Screened	486.77	69	1.13	486.94	64	1.14
	Unscreened	487.57	31	1.24	487.74	36	1.25
90° Al anode	Screened	486.75	60	1.12	486.86	52	1.08
	Unscreened	487.55	40	1.40	487.66	48	1.35
90° Ag anode	Screened	486.60	40	1.56 (1.46)			
	Unscreened	487.40	60	2.28 (2.21)			

the In 3d of In_2O_3–ZnO thin films doped at 2.35×10^{20} cm^{-3} [25], in the Sn 3d XPS of SnO_2 thin film doped with Sb at 3.5×10^{20} cm^{-3} [22], and in the In 3d XPS spectra of undoped In_2O_3 thin films [8]. For the case of the undoped In_2O_3 film, the unusual presence of both screened and unscreened (dominant) states was attributed to surface carrier accumulation [8]. Indeed, it was found that surface band bending in intrinsic semiconductors induces carrier accumulation close to the surface which results in a space charge region of about 5 nm [8, 70, 71]. However, in conventional photoemission, with an excitation energy of ≈ 1496 eV for example, 97% of the photoexcited electrons originate from a region of about 2 nm [8, 72]. Thus, in the case of In_2O_3, the XPS signal acquired using Al K_α is dominated by the space charge region, hence the presence of the screened state [8, 73].

As for the contaminated surface presented in Fig. 5.7(d) and 5.7(e), a similar behavior as in the case of the clean surface is observed. In fact, considering Table 5.4, it can be seen that the fraction of the screened state decreases, while that of the unscreened state increases when the sampling becomes more bulk sensitive (from Fig. 5.7(d) to Fig. 5.7(e)). The unscreened signal is consistently amplified in the two measurement configurations after the surface is contaminated. This can be seen when comparing the data of the clean and contaminated surfaces (at 35° and 90° acquisition, respectively) in the table, and also when comparing Figs 5.7(a) and 5.7(d) on one hand and Figs 5.7(b) and 5.7(e) on the other hand. In addition to this increase, peak shifts to high binding energies are observed. The screened components are shifted by 0.17 eV and 0.11 eV for the measurements at 35° and 90°, respectively. The increase in the relative intensity of the unscreened state and the shift of the components upon surface contamination in the load lock could be linked to the resulting rise of the intensity of the states in the conduction band [8, 17, 25]. This is comprehensively addressed in Section 5.3.

Figure 5.8 represents the fits of the angle-dependent XPS spectra of the O 1s core level, for clean (Figs. 5.8(a) to 5.8(c)) and contaminated (Figs. 5.8(d) and 5.8(e)) surfaces. Again, similar to the fits presented in Fig. 5.4, the spectra are fitted to four symmetric Voigt peaks identified as oxygen attached to Ba in lattice BaO (O_{lat}), to oxygen vacancies (O_{vac}), to a surface component or hydroxyl groups (−OH), and to surface contamination (C-O). The parameters of the fits are provided in Table 5.5. As can be seen from Fig. 5.8 and Table 5.5, the ratio of the −OH component consistently decreases with increasing sampling depth, both

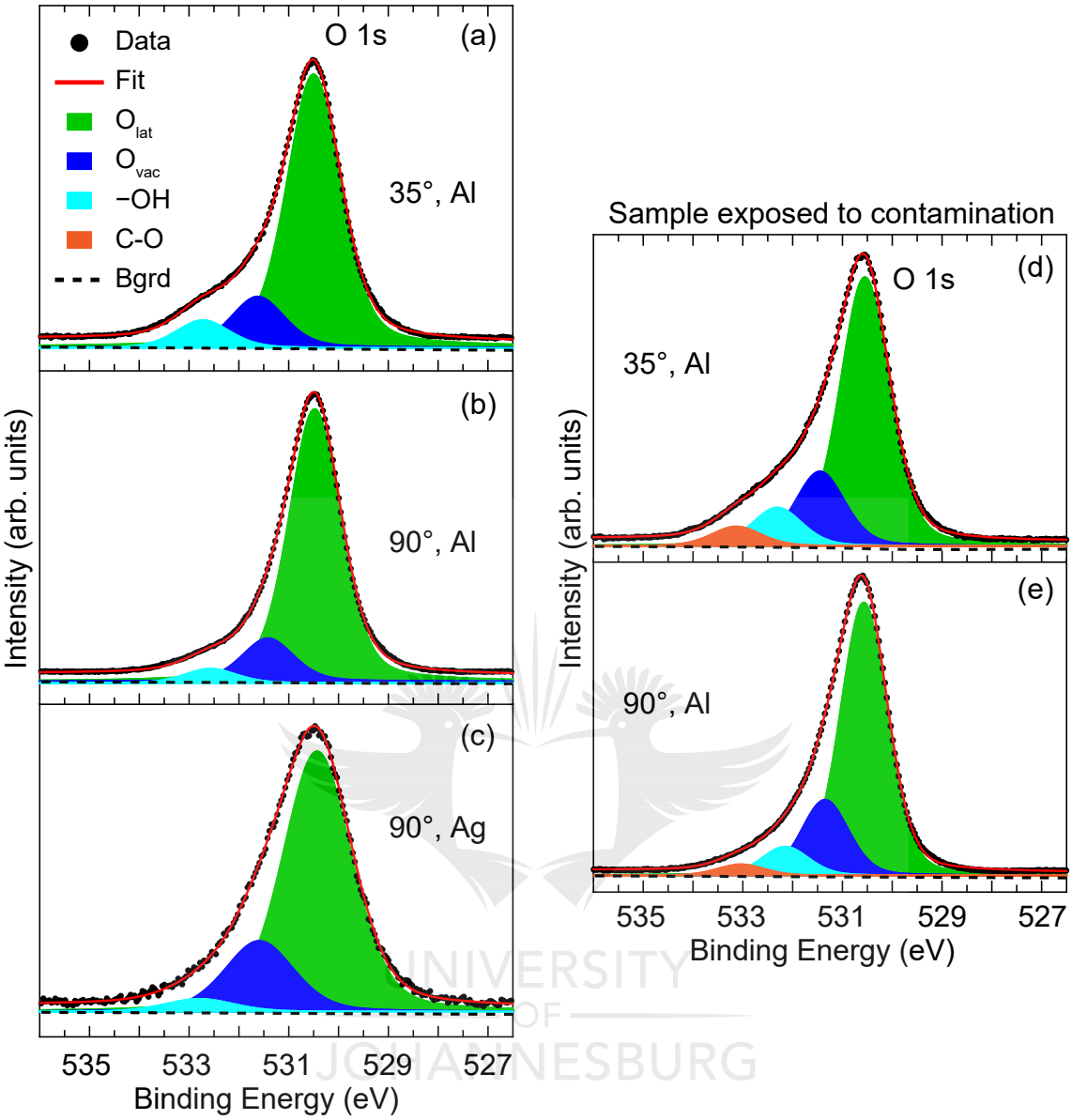

Figure 5.8: Fits of the angle-dependent XPS spectra around the O 1s region of a 6% La-$BaSnO_3$/$BaSnO_3$/$TbScO_3$ sample. (a)-(c) The measurements are done on a clean surface. (d) and (e) The data are acquired on the surface voluntarily exposed to contamination in the load lock. The take-off angle of the electrons is varied such that those collected by the analyzer are from a region near the surface (35°) and also from a deeper region in the bulk (90°). The spectra in (a), (b), (d) and (e) were recorded with an Al anode at 35° and 90° take-off angles, whereas that in (c) was taken with an Ag anode at 90°. Peak heights were normalized.

in clean and contaminated spectra. This is expected as the −OH groups are only present on the surface. Additionally, an increase in the relative intensity of the hydroxide component is noticeable when comparing the clean and contaminated spectra in both acquisition configurations (see Table 5.5). These observations confirm the assumption made in Section 5.2.1 that −OH peak which is located at the highest binding energy side of the main peak in the clean spectra is a surface component.

Table 5.5: Peak ratios for angle-dependent XPS of the O 1s spectra shown in Fig. 5.8. The peak position (P), the relative intensity (R) and the FWHM (F) are given. The FWHM values in brackets are the ones rescaled for the resolution of the Al anode.

		Clean surface			Contaminated surface		
	Error	P (eV) (±0.05)	R (%) (±1)	F (eV) (±0.05)	P (eV) (±0.05)	R (%) (±1)	F (eV) (±0.05)
35° Al anode	O_{lat}	530.41	77	1.28	530.55	66	1.17
	O_{vac}	531.54	15	1.28	531.45	19	1.17
	−OH	532.63	8	1.28	532.31	10	1.17
	C-O	—	—	—	533.1	5	1.17
90° Al anode	O_{lat}	530.48	83	1.23	530.57	70	1.11
	O_{vac}	531.42	13	1.23	531.35	20	1.11
	−OH	532.57	4	1.23	532.15	7	1.11
	C-O	—	—	—	533.04	3	1.11
90° Ag anode	O_{lat}	530.52	76	1.63 (1.53)			
	O_{vac}	531.69	21	1.63 (1.53)			
	−OH	532.90	3	1.63 (1.53)			
	C-O	—	—	—			

As for the O_{vac} signal, it can be seen looking at Table 5.5 that its relative intensity increases in the clean surface with bulk sensitivity, i.e. from the measurement at 35° with Al anode (Fig 5.8(a)) to the measurement at 90° with Ag anode (Fig 5.8(c)). However, a discrepancy is observed in the measurement at 90° with Al anode (Fig 5.8(b)), as the ratio is slightly smaller compared with the measurement at 35°. One would have expected a higher value for consistency, as the measurement becomes less surface sensitive. Nevertheless, this small difference is within the sensitivity of XPS spectra fitting. Therefore, O_{vac} ratios in Figs 5.8(a) and 5.8(b) respectively for measurements at 35° and 90° can be considered the same. It can also be seen that O_{vac} is sensitive to contamination, as its ratio increases in the contaminated surface for measurements both at 35° and 90°. Thus, based on the above, it can be concluded that O_{vac} component shows both surface and bulk character [74, 75]. However, it has been largely reported that oxygen vacancies are mostly surface related defects in oxide materials, since their low formation energy favors their diffusion through the surface [76, 77, 78, 79, 80].

Also, looking at Table 5.5, an inconsistency is noticeable for the O_{lat} component. Its relative intensity first increases for acquisitions from 35° to 90° using Al anode (from Fig 5.8(a) to Fig 5.8(b)) suggesting a bulk sensitivity of the component, then decreases again when Ag anode is used (Fig 5.8(c)). The rescaled FWHM values given in the table indicate that this discrepancy cannot be related to peak broadening associated with the experimental resolution with Ag anode. A possible explanation could be that the bulk signal of the O_{lat} component is probably reduced by the residual −OH on the surface region. Indeed, it can be observed from the table that O_{lat} shows sensitivity to contamination as its ratio is reduced when the surface is exposed to contamination. Again, this can be seen comparing the data of the clean and contaminated surfaces for acquisitions at 35° and 90°. These are consistent with the observation in Section 5.2.1 (see Fig. 5.5) where the fraction of the O_{lat} peak increased in the

surface where the contamination was removed.

As for Ba 3d core regions, their angle-dependent XPS are shown in Fig. 5.9, to elucidate the origin of the multiple components. Again, as for the fits of Ba 3d core lines shown in Fig 5.5, two symmetric Voigt doublets, Ba I and Ba II, are used to fit the spectra. The fitted data are given in Table 5.6. As can be observed in the table, the ratio of Ba II considerably decreases with bulk sensitivity measurement. This decrease is consistent for both clean (Figs. 5.9(a) to 5.9(c)) and contaminated (Figs. 5.9(d) and 5.9(e)) surfaces. In the clean surface, the rate

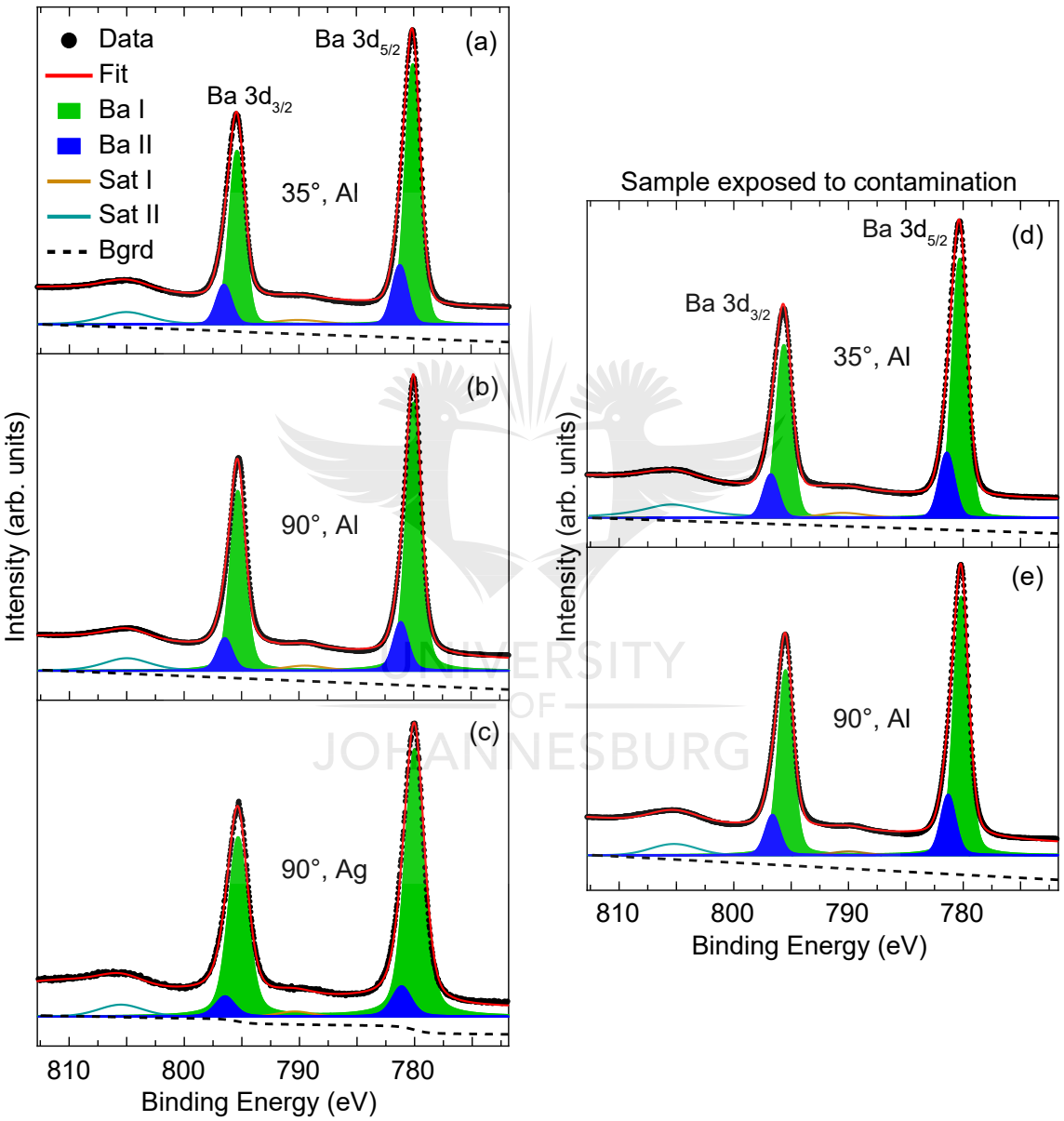

Figure 5.9: Fits of the angle-dependent XPS spectra of the Ba 3d core level in a 6% La-$BaSnO_3/BaSnO_3/TbScO_3$ sample. In (a)-(c) the spectra are for the clean surface. In (d) and (e) the data are for the surface exposed to contamination. The spectra in (a), (b), (d) and (e) were acquired with an Al anode at 35° and 90° take-off angles, whereas that in (c) was measured with an Ag anode at 90° take-off angle. Peak heights were normalized.

Table 5.6: Peak ratios for angle-dependent XPS of the Ba 3d spectra shown in Fig. 5.9. The peak position (P), the relative intensity (R) and the FWHM (F) are given. The FWHM values in brackets are the ones rescaled for the resolution of the Al anode.

		Clean surface			Contaminated surface		
	Error	P (eV) (±0.05)	R (%) (±1)	F (eV) (±0.05)	P (eV) (±0.05)	R (%) (±1)	F (eV) (±0.05)
35° Al anode	Ba I	780.08	82	1.58	780.30	80	1.56
	Ba II	781.21	18	1.58	781.43	20	1.56
90° Al anode	Ba I	780.00	85	1.53	780.18	81	1.50
	Ba II	781.13	15	1.53	781.31	19	1.50
90° Ag anode	Ba I	780.00	90	1.97 (1.89)			
	Ba II	781.13	10	1.97 (1.89)			

of the decrease suggests that Ba II feature would disappear at a certain depth, confirming its surface state character, as discussed in Section 5.2.1. In similar analyses of angle-dependent XPS measurements on $BaTiO_3$ systems, it has been reported that Ba II component which was also located at the higher binding energy side in the core level, is a surface component associated with $BaCO_3$ [11, 53, 54, 55, 56, 57, 58]. It is noteworthy that apart from the carbon signal that was removed from the surface of the samples after annealing, no other unexpected signals were recorded in the survey scans (see Fig 5.2). Furthermore, the XRD patterns of these samples only showed pure $BaSnO_3$ with no evidence of secondary phases. In $BaTiO_3$ thin films however, it has been hypothesized that the Ba II component could more likely be the consequence of the polar discontinuity at the TiO_2 surface terminated upon Pt electrode patterning [11]. Yet, the origin and the nature of Ba II peak is still unknown and subject to controversy. Considering the clean and contaminated surfaces in Fig. 5.9, it is clearly seen that there is no additional surface related component upon exposure of the surface to contamination, and no change in the line shapes of the spectra, although the peaks are shifted to high binding energies (see Table 5.6). However, it can be observed from Table 5.6 that Ba II signal is intensified with contamination in both measurement configurations. All these observations plus the analysis conducted for the spectra in Figs. 5.5, where it was observed a decrease in the relative intensity of the Ba II component after surface cleaning, are consistent with the consideration that Ba II is a surface component, potentially attached to carbonate. As for the Ba I component, it can be clearly seen from Table 5.6 that in the clean surface, its ratio increases with bulk sensitivity measurements (Figs. 5.9(a) to 5.9(c)), indicating its bulk character. It can also be seen that its relative intensity slightly decreases after the surface exposed to contamination.

5.3 Analysis of the Valence Band Structure

As previously mentioned in Section 5.1, one of the goals of this study was to correlate the high transport properties in the epitaxially grown La-doped $BaSnO_3$ thin films with the electronic band structure. The structural results reported in Chapter 4 showed that the electron mobility in the films is limited by defects. Hence, it is expected to observe features due to these in the band structure. A direct way of accessing the electronic band structure of materials is

by measuring their valence band using spectroscopic techniques such as XPS and ARPES. XPS samples the density of states (DOS), whereas ARPES maps the electronic bands in the Brillouin zone [81, 82].

For the analysis of the valence band of the films using XPS, the samples investigated in Sections 5.2.1 and 5.2.2 and presented in Fig. 5.3 to Fig. 5.9 were used. These samples are: 2% La-$BaSnO_3$/$TbScO_3$ with $n = 1.35 \times 10^{20}$ cm^{-3}, 6% La-$BaSnO_3$/$SrTiO_3$ with $n = 4.05 \times 10^{20}$ cm^{-3}, and 6% La-$BaSnO_3$/$BaSnO_3$/$TbScO_3$ with $n = 4.92 \times 10^{20}$ cm^{-3}. As for the study of the band structure, only the ARPES data of the 2% La-$BaSnO_3$/$TbScO_3$ sample will be discussed.

Figures 5.10 and 5.11 represent the XPS spectra of the valence bands associated with the primary core levels presented in Figs 5.3, 5.4 and 5.5 for the cleaned surface, and in Figs 5.7, 5.8 and 5.9 for the clean and contaminated surfaces, excited with Al K_α at normal emission. In Fig. 5.10, the legend of the curves is given in terms of the carrier density to identify the samples as presented above. The cyan curve represents the valence band spectrum of the sample with the carrier density of 4.92×10^{20} cm^{-3} after this sample is intentionally exposed to contamination in the load lock. To see whether the shifts observed in the core electrons would also reflect in the valence bands, no offset in energy was applied to align the peaks. Looking at Fig. 5.10, it can be seen that the valence band is mainly composed of three features. Firstly, a mixture of Sn 5s and bonding O 2p orbitals located at 10.6 eV; secondly, the states at 8.3 eV originating from hybridized Sn 5p and O 2p orbitals; and thirdly, the bands at binding energies between 4 and 6 eV associated with O 2p bonding or anti-bonding character. The assignment of the peaks was conducted according to preliminary DFT calculations (not shown here) done by one of the collaborators of our research group, Dr Robert Warmbier (affiliated with the University of Johannesburg), and also based on the details provided in Refs. [27, 83, 84, 85].

Note that the features associated with Sn 5p states are weaker in the blue and red curves (Fig. 5.10). Additionally, when comparing the spectrum of the clean surface represented by the red curve and that of the corresponding contaminated surface represented by the cyan curve in Fig. 5.10, it is observed that there is no change in the line shape of the Sn 5s peaks. This agrees with the surface being Ba-rich, and justifies the peak assignments in the O 1s spectra where the most intense signal was attributed to BaO. Furthermore, shifts of the valence band leading edge to high binding energies upon increasing carrier density can be seen. These are clearly indicated by the magenta arrow in Fig. 5.10. As described in Section 2.4.3, this observation is in agreement with the optical absorption edge and valence band shifts observed in La-doped $BaSnO_3$ systems respectively by spectroscopic ellipsometry and HAXPES measurements, and suggests an increase in the optical band gap [17, 86, 87, 88]. Interestingly, as also discussed in Section 2.4.3, an opposite trend, i.e., shift of the valence band spectra toward lower binding energies with increases in La doping, was reported by ARPES experiments [49]. This is in clear contrast to the present result, and can be associated with the surface sensitivity of the measurement technique, since this opposite trend was attributed to the opposite evolution of surface and bulk chemical potentials [49]. The valence band shifts in this present study can be correlated to the shifts in the core levels, especially to the asymmetry in the Sn 3d core lines as discussed in Sections 5.2.1 and 5.2.2. Similarly, it was observed in CdO, Sb-doped SnO_2, In_2O_3–ZnO, and Sn-doped In_2O_3 thin films that the increase in the concentration of the conduction electrons leads to shifts of the valence band features toward high binding energies [8, 22, 25, 31]. These shifts were attributed to the increasing occupation of the states in the conduction band of the degenerately doped materials [8, 22, 25].

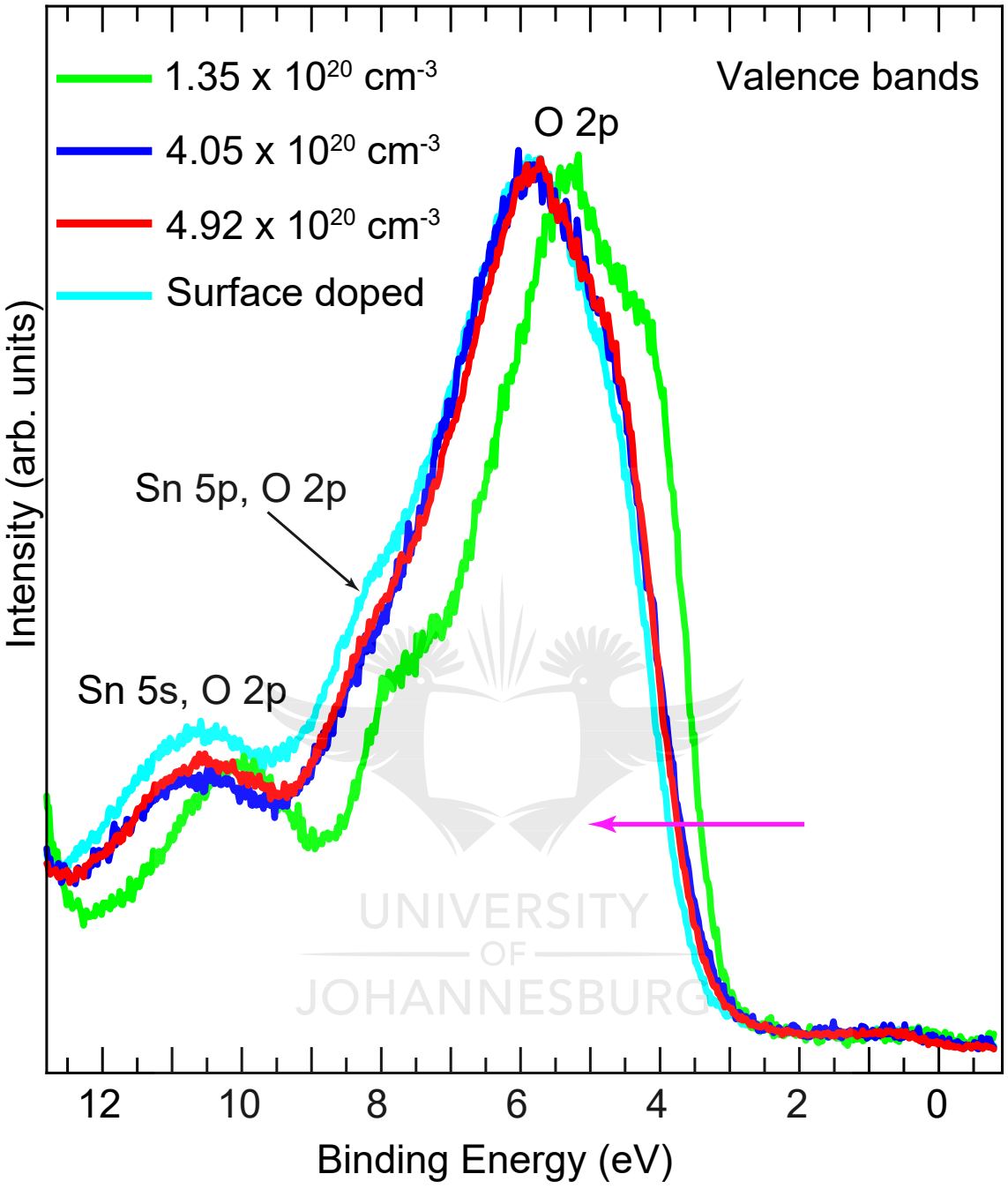

Figure 5.10: Valence band spectra of the 2% La-$BaSnO_3$/$TbScO_3$ (green curves), 6% La-$BaSnO_3$/$SrTiO_3$ (blue curves), and 6% La-$BaSnO_3$/$BaSnO_3$/$TbScO_3$ (red and cyan curves) samples. The cyan curve is the spectra of the surface exposed to contamination in the load lock. In the figure, the samples are indicated in terms of their carrier densities. The blue, green and cyan curves are normalized to the maximum intensity of the red curve. The magenta arrow indicates the shift of the valence band with increasing carrier density.

To identify the features arising from occupation of the conduction bands in the grown samples, scans around the valence band leading edges were performed as shown in Fig. 5.11. In the figure, only the blue and green curves are normalized to the intensity of the red curve. As

mentioned before, each spectrum in the figure was acquired over a period of about 20 hours by adding several scans to achieve an adequate signal to noise ratio and enhance the details in the region close to the Fermi energy (E_F). As also mentioned before, after the acquisition of the red, blue and green spectra, the samples remained clean as no C 1s peak was detected; and to obtain the cyan spectrum, the sample with the carrier density of 4.92×10^{20} cm^{-3} (red) was exposed to contamination in the load lock for 1 day. Looking at Fig. 5.11, it is observed that each spectrum presents a peak at about 4 eV deriving from O 2p orbitals [44, 49]. The presence of a band at 4 eV is confirmed by the first derivative of the spectra shown in the left inset in Fig. 5.11, although the band is considerably weak in the samples indicated by the blue and green curves. Moreover, a shift to higher binding energy of about 0.23 eV is clearly visible for the valence band leading edge spectrum of the contaminated surface (cyan curve). Additionally, a bump is detectable in all the spectra in the region around 2 eV to 0 eV (E_F). This region which is delimited by a rectangle as depicted in Fig. 5.11 is enlarged and shown in the right inset. The enlargement shows that all the spectra contain a weak structure close to E_F which terminates in a sharp Fermi edge. This structure is associated with occupied states in the conduction band, and clearly peaked at ≈ 0.9 eV in the red and cyan spectra. These states have Sn 5s orbital character with a small contribution from O 2p orbital [17, 60]. Note that the conduction bands straddle zero binding energy, E_F, indicated by the vertical dashed line in the right inset [8, 20, 25]. This is a confirmation of an accurate binding energy calibration.

As indicated by the green and blue curves in the right inset in Fig. 5.11, the conduction band structure is weaker for the samples with carrier densities of 1.35×10^{20} cm^{-3} and 4.05×10^{20} cm^{-3}, respectively. In the sample with the carrier density of 4.92×10^{20} cm^{-3} (red curve), the conduction band structure is more developed and suggests a conduction band minimum (CBM) located at about 0.87 eV below E_F. The intensity of the CBM peak is increased in the contaminated surface as evidenced by the cyan curve. Thus, one could argue that exposure of the surface to contamination results in doping of the sample (electrons being added to the conduction band). This is because this increase in intensity is associated with the shift of the valence band edge as addressed above, and is also related to the shift and increase in the relative intensity of the components in the Sn 3d core level shown in Fig. 5.7. Indeed, as previously mentioned for the case of CdO, In_2O_3–ZnO, Sn-doped In_2O_3 and La-doped $BaSnO_3$ thin films, the valence band shifts associated with the increasing density of electrons occupying the conduction band were reported to result in the increase of the intensity of the conduction band feature [8, 17, 25, 31, 86, 87, 88]. Based on the above, it can be concluded with certainty that the contamination results in sample doping, as increasing occupied states in the conduction band upon surface contamination could be identified. However, to accurately identify the states in the valence and conduction bands, and determine the precise position of both the valence band maximum (VBM) and the CBM, ARPES experiments are required.

Figure 5.12 shows the ARPES data of the valence band region of the sample with the carrier density of 1.35×10^{20} cm^{-3}, measured at room temperature with a photon energy of 21.2 eV (He I). Figure 5.12(a) illustrates a typical 2D ARPES map of the valence band in the binding energy range from -2.50 eV to 10.62 eV. This mapping is resolved in the $\bar{\Gamma}\bar{X}$ direction in momentum space. Valence band states are observed from about 3.10 eV to 10.62 eV, although the bands are not well resolved. These bands can be more clearly seen in Fig. 5.12(b) representing the density of states (DOS) integrated from the ARPES map in Fig. 5.12(a). In fact, Fig. 5.12(b) represents the energy distribution curve (EDC) which is obtained by integrating the ARPES map over the entire momentum space (from -0.47 Å^{-1} to 0.47 Å^{-1}). This EDC

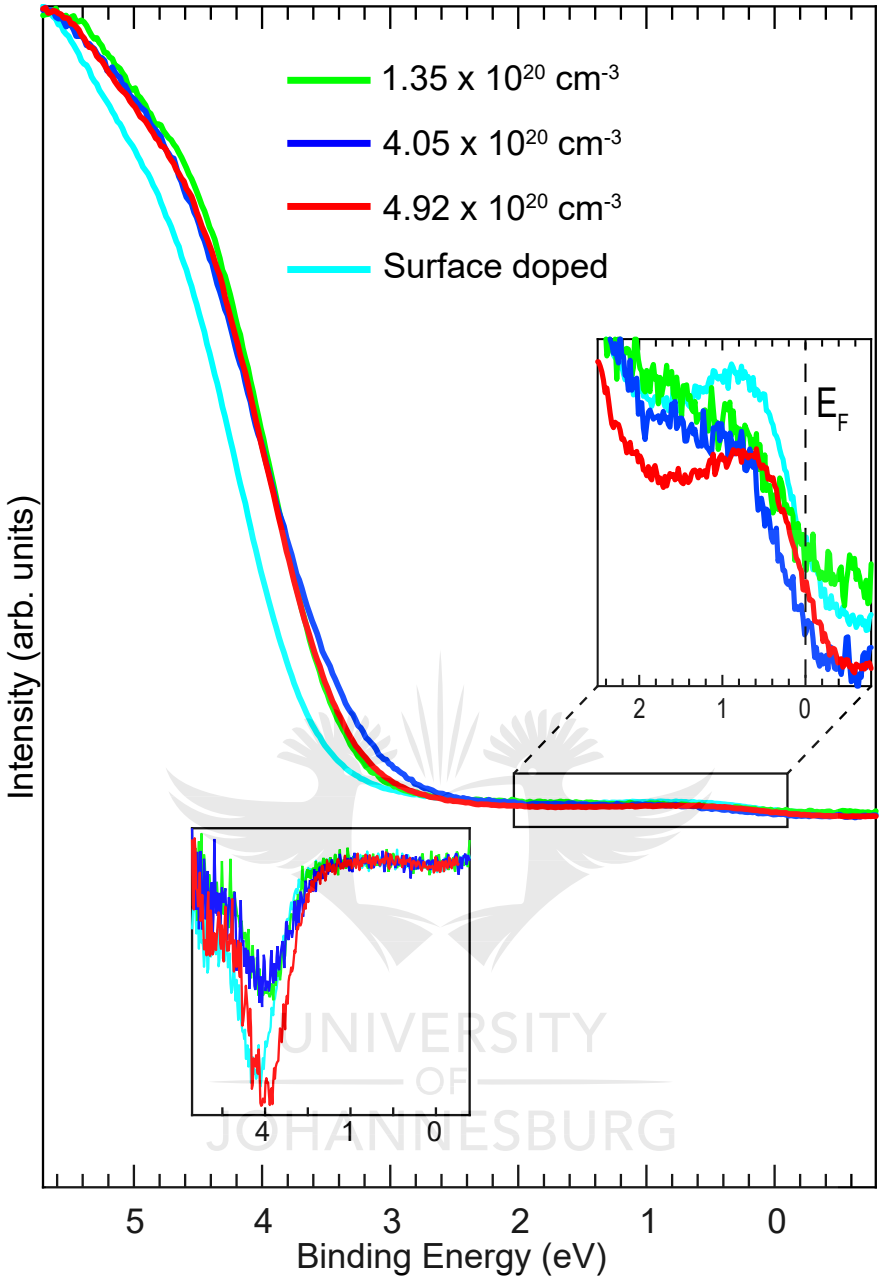

Figure 5.11: Valence band leading edge spectra of the samples in Fig. 5.10. The cyan curve is the spectra of the surface exposed to contamination in the load lock. The blue and green curves are normalized to the intensity of the red curve. The inset on the left shows the derivative of the spectra. The cyan curve is magnified $\times 18$, the blue and green curves are magnified $\times 40$. The inset on the right shows the enlargement of the region around E_F delimited by the black rectangle.

is very similar to the valence band spectra obtained with XPS, as shown in Fig. 5.10, with the only difference that the EDC has a better resolution and the bands are clearer. However, as can be seen in the inset (Fig. 5.12(b)), the conduction band feature is not developed in the EDC, but the Fermi-Dirac edge that straddles 0 eV is visible. A linear extrapolation of the valence band leading edge illustrated by the black dashed line in Fig. 5.12(b) reveals that

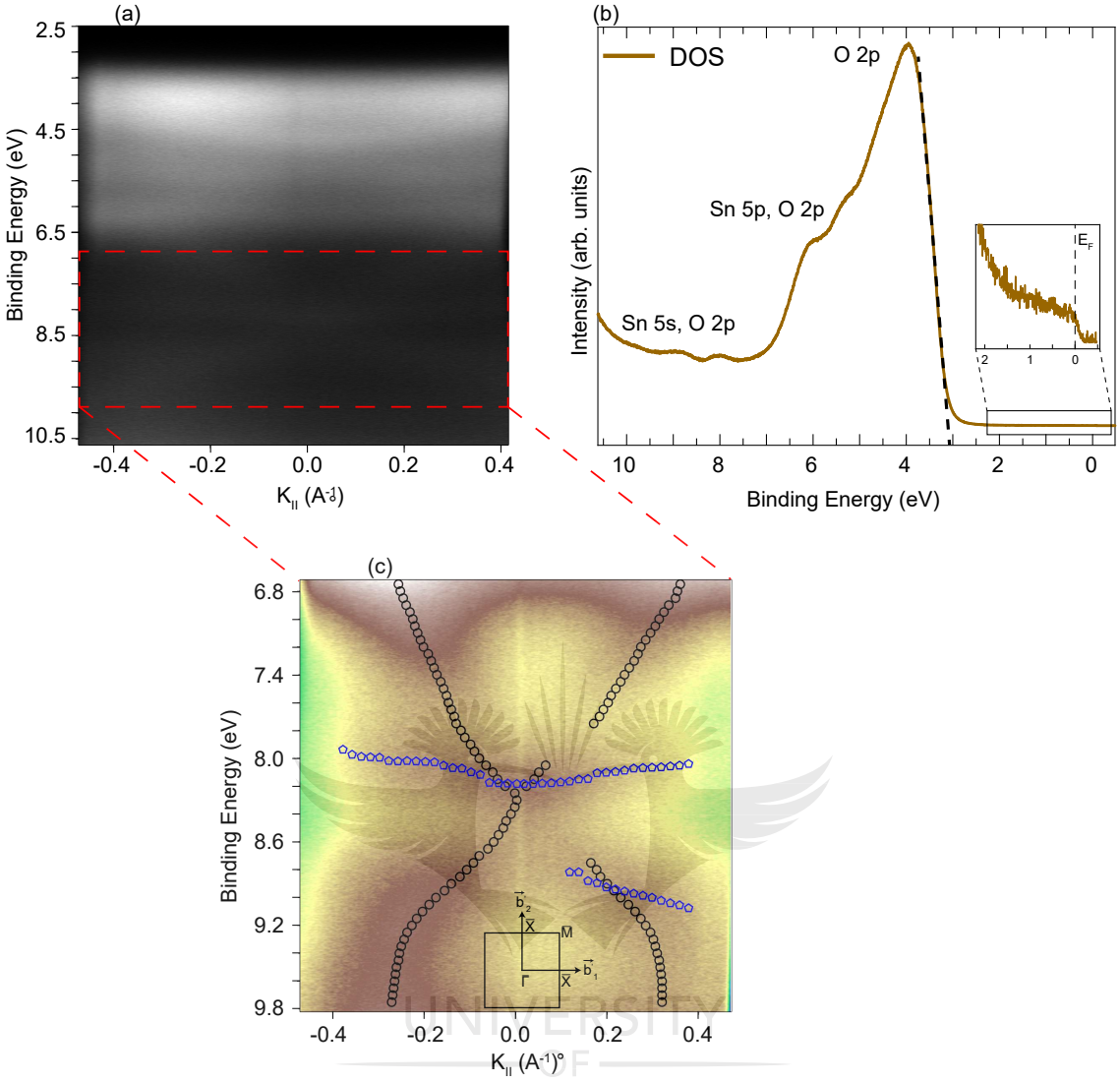

Figure 5.12: (a) 2D ARPES map of the valence band measured from a 2% La-$BaSnO_3$/$TbScO_3$ sample at room temperature in the $\bar{\Gamma}\bar{X}$ direction. (b) EDC integrated over the entire momentum space from the ARPES map in (a). The black dashed line represents a linear fit of the leading edge. (c) ARPES map of the region indicated by the red dashed rectangle in (a). A few bands are visible and fitted with black and blue markers as shown. The black markers are the fits of the bands with MDCs and the blue markers are the fits with EDCs. The inset in (c) shows the La-$BaSnO_3$ (001) Brillouin zone.

the VBM is situated at about 3.1 eV. This value is consistent with theoretical calculations [41, 60], and close to the value of 3.5 eV [49] reported for La-doped $BaSnO_3$ thin films, and the values of 3.7 eV [44] and 3.3 eV [10] reported for $BaSnO_3$ thin films, all recorded from ARPES valence band spectra.

The image in Fig. 5.12(c) represents a 2D ARPES map of the region indicated by the red dashed rectangle in Fig. 5.12(a). This image corresponds to a scan in the binding energies ranging from 6.7 eV to 9.8 eV around the hybridized Sn 5s and O 2p states seen in the EDC shown in Fig. 5.12(b). Few highly dispersive bands are resolved as indicated by black and

blue markers. The black markers represent the fits of the bands to peaks in the momentum distribution curves (MDCs), whereas the blue markers represent the bands fitted to peaks in the energy distribution curves (EDCs). As can be observed, the EDCs fit well the flat band located in the middle of the image, but tend not to be the best choice for the fitting of the other bands.

The large size of the 1st Brillouin zone limited the proportion of the reciprocal space that could be accessed with the equipment used for ARPES experiments. Since $BaSnO_3$ has a FCC lattice structure, the (001) surfaces form square lattices, implying that the surface Brillouin zone analogue to the 1st Brillouin zone in the bulk is also square as shown in the inset in Fig. 5.12(c). The magnitude of the associated reciprocal lattice vectors $\vec{b'}_1$ and $\vec{b'}_2$ is equal to $|\vec{b'}_1| = |\vec{b'}_2| = \frac{2\pi\sqrt{2}}{a}$, with $a = 4.126$ Å the lattice constant. It follows that the corresponding distances in the high symmetry directions are equal to $\bar{\Gamma}\bar{X} = \bar{M}\bar{X} = 1.077$ Å^{-1} and $\bar{\Gamma}\bar{M} = 1.522$ Å^{-1}. The ARPES setup, more precisely the He I photon energy, allows measurement to a maximum of 0.470 Å^{-1} in one direction in momentum space, which also corresponds to the maximum value of the parallel component of the momentum K accessible with the equipment. As a consequence, only $\approx$ 44% of $\bar{\Gamma}\bar{X}$ and $\approx$ 31% of $\bar{\Gamma}\bar{M}$ could be accessed.

The ARPES data reported in Figs. 5.12(a) and 5.12(b) are comparable to previous ARPES experiments reported in Refs. [44, 49]. However, it should be emphasized that the 2D ARPES map and the EDCs reported by these authors exhibit more features than those seen in Figs. 5.12(a) and 5.12(b). This can be in part explained by the fact that the samples in this study were grown overseas and transported in air before ARPES acquisitions whereas these authors report *in situ* ARPES measurements. For example, as described in Section 2.4.2, an in-gap state, β, located at -1.75 eV, and occupied states in the conduction band (with the CBM situated at -0.15 eV) were seen in the EDCs extracted at the high symmetry points in the raw 2D ARPES spectra of $BaSnO_3$ thin films [44]. It should be highlighted that since $BaSnO_3$ is electrically insulating, the authors associated the states in the conduction band with doping induced by oxygen vacancies or antisite defects. Similarly, as also described in Section 2.4.3, features such as the β state, a state labeled α located at 4 eV, occupied conduction band states as well as a metallic state at the CBM were reported in the EDCs measured from La-doped $BaSnO_3$ thin films [49]. Resolved and highly dispersive bands were also reported in the 2D ARPES map of these films in the binding energy range from 3.5 eV to 10 eV [49]. The authors attributed the states α and β to oxygen adsorption and oxygen vacancies, respectively, and the metallic state to the increase in the concentration of carriers at the surface of the films, since it was reported that this state develops after surface illumination.

For the ARPES data presented in this present study, the major difficulty encountered in resolving the bands was associated with the preparation of the surface prior to ARPES measurements. Collaborators at the Interface Analysis Service Group at the Max-Planck Institute (MPI) in Stuttgart were approached. At the MPI, the ARPES measurements were also done on samples transferred through air, and several optimizations of the surface preparation were attempted, including minimizing air contamination while transferring the samples from the growth chamber to the ARPES chamber. From the data acquired at the MPI (presented in Appendix C.5), it is evident that the collaborators had the same challenges as the efforts to resolve the bands were unfortunately unsuccessful.

In preparing the chapters for this thesis, we came across another report on the electronic band

structure of $BaSnO_3$ thin films studied by ARPES [10] (published in May 2020). It is interesting that the authors initially used almost the same high vacuum surface preparation as followed in the present study. In fact, the $BaSnO_3$ (10 nm)/$La_{0.04}Ba_{0.96}SnO_3$ (100 nm)/$SrTiO_3$ samples studied in their report were grown in a PLD chamber and were *ex situ* transferred into an UHV chamber where the surfaces were prepared and the ARPES data were taken. After annealing the grown samples in UHV at temperatures up to 400 °C, the 2D ARPES spectra were similar to that shown in Fig 5.12(a). However, after an annealing cycle in a tube furnace for 1 hour at 400 °C in 1×10^3 mbar of O_2, followed by subsequent UHV annealing cycles (1 hour each) at temperatures up to 700 °C, very clear and dispersive bands could be seen from 3.3 eV to 12 eV in the 2D ARPES map taken at low temperature, between 7 to 12K (refer Fig. 3 in Ref. [10]). Moreover, the authors established a correlation between the surface and electronic band structures associated with the surface treatment. It was observed that the LEED pattern of surfaces prepared in UHV at temperatures up to 550 °C showed a 1×1 structure with non-dispersive bands. However, at the temperature of 700 °C, the surfaces reconstruct into a $\sqrt{2} \times \sqrt{2}R45°$ structure. The authors emphasized that this latter structure was associated with the highly dispersive valence bands. This could be a hint as to why these bands could not be observed in this present study since the LEED patterns only showed 1×1 structures (see Fig. 5.1). Unfortunately, at this point, a breakage of the UV source used in the ARPES experiments prevented attempts using the same surface preparation.

To our knowledge, the three reports above (Refs. [10, 44, 49]) are the only available literature to date on the ARPES study of the electronic structure of $BaSnO_3$ and La-doped $BaSnO_3$ thin films. All three together provide a complementary understanding of the electronic band structure (nature and size of the band gap), the conduction mechanism and the effect of surface reconstruction on the structure of the bands. The one outstanding piece of information is a correlation between electronic structure and mobility.

5.4 Conclusion

In this chapter, the elemental composition of the surface of the epitaxially grown La-doped $BaSnO_3$ thin films was determined. This was systematically achieved through fitting of the peaks in the core regions. In particular, the Sn 3d core level presented an asymmetry variation with the carrier density and was fitted to two components, a main component screened, and its associated unscreened satellite. It was observed that the proportion of the components in the core levels varies depending on whether the surface is measured as-inserted or cleaned. From angle-dependent XPS experiments, it was determined which of the components of the core spectra show either a surface character or a bulk character. The valence bands of the films were also measured. The valence band was found to shift to higher binding energy as the concentration of electrons introduced into the conduction band increases. It was also observed that contamination of the surface could result in a doping mechanism as an increase in the conduction band states was noted in a surface intentionally exposed to contamination. The structure of the bands in the valence and conduction bands could not be well explored. Only a few valence bands far from E_F could be resolved and fitted with EDCs and MDCs. This was understood in terms of the need for a very particular surface treatment.

Bibliography

[1] R. W. Cahn, and P. Haasen, *Interfacial and Surface Microchemistry* (Physical Metallurgy, 4th edition, Elsevier, Amsterdam, 1996).

[2] M. D. Siao, W. C. Shen, R. S. Chen, Z. W. Chang, M. C. Shih, Y. P. Chiu, and C.-M. Cheng, Nature Commun. **9**, 1442 (2018).

[3] H. Schmidt, F. Giustiniano, and G. Eda, Chem. Soc. Rev. **44**, 7715 (2015).

[4] D. J. Late, B. Liu, H. S. S. R. Matte, V. P. Dravid, and C. N. R. Rao, ACS Nano **6**, 5635 (2012).

[5] G. R. Berdiyorov, EPL **111**, 67002 (2015).

[6] G. Greczynski, and L. Hultman, Prog. Mater. Sci. **107**, 100591 (2020).

[7] E. Korin, N. Froumin, and S. Cohen, ACS Biomater. Sci. Eng. **3**, 882 (2017).

[8] C. Körber, V. Krishnakumar, A. Klein, G. Panaccione, P. Torelli, A. Walsh, J. L. F. Da Silva, S.-H. Wei, R. G. Egdell, and D. J. Payne, Phys. Rev. B **81**, 165207 (2010).

[9] D. Cabrera-German, G. Gomez-Sosa, and A. Herrera-Gomez, Surf. Interface Anal. **48**, 252 (2016).

[10] S. Soltani, S. Hong, B. Kim, D. Kim, J. K. Jung, B. Sohn, T. W. Noh, K. Char, and C. Kim, Phys. Rev. Mater. **4**, 055003 (2020).

[11] J. E. Rault, G. Agnus, T. Maroutian, V. Pillard, Ph. Lecoeur, G. Niu, B. Vilquin, M. G. Silly, A. Bendounan, F. Sirotti, and N. Barrett, Phys. Rev. B **87**, 155146 (2013).

[12] R. Courths, Phys. Status Solidi B **100**, 135 (1980).

[13] C. Chen, J. Avila, E. Frantzeskakis, A. Levy, and M. C. Asensio, Nat. Commun. **6**, 8585 (2015).

[14] D. Briggs, and J. T. Grant, *Surface Analysis by Auger and X-ray Photoelectron Spectroscopy* (IM Publications, Chichester, 2003).

[15] J. F. Moulder, W. F. Stickle, P. E. Sobol, and K. D. Bomben, *Handbook of X-ray Photoelectron Spectroscopy* (Perkin-Elmer Corp, Eden Prairie, MN, 1992).

[16] S. A. Chambers, T. C. Kaspar, A. Prakash, G. Haugstad, and B. Jalan, Appl. Phys. Lett. **108**, 152104 (2016).

[17] Z. Lebens-Higgins, D. O. Scanlon, H. Paik, S. Sallis, Y. Nie, M. Uchida, N. F. Quackenbush, M. J. Wahila, G. E. Sterbinsky, D. A. Arena, J. C. Woicik, D. G. Schlom, and L. F. Piper, Phys. Rev. Lett. **116**, 027602 (2016).

[18] H. M. Jaim, S. Lee, X. Zhang, and I. Takeuchi, Appl. Phys. Lett. **111**, 172102 (2017).

[19] M. Kwoka, L. Ottaviano, M. Passacantando, S. Santucci, G. Czempik, and J. Szuber, Thin Solid Films **490**, 36 (2005).

[20] R. G. Egdell, T. J. Walker, and G. Beamson, J. Electron Spectrosc. Relat. Phenom. **128**, 59 (2003).

[21] P. A. Cox, R. G. Egdell, C. Harding, A. F. Orchard, W. R. Patterson, and P. J. Tavener, Solid State Commun. **44**, 837 (1982).

[22] R. G. Egdell, J. Rebane, T. J. Walker, and D. S. L. Law, Phys. Rev. B **59**, 1792 (1999).

[23] J. N. Chazalviel, M. Campagna, and G. K. Wertheim, Phys. Rev. B **16**, 697 (1977).

[24] M. Campagna, G. K. Wertheim, H. R. Shanks, F. Zumsteg, and E. Banks, Phys. Rev. Lett. **34**, 738 (1975).

[25] J. Jia, N. Oka, and Y. Shigesato, J. Appl. Phys. **113**, 163702 (2013).

[26] V. Christou, M. Etchells, O. Renault, P. J. Dobson, O. V. Salata, G. Beamson, and R. G. Egdell, J. Appl. Phys. **88**, 5180 (2000).

[27] J.-M. Themlin, M. Chtaïb, L. Henrard, P. Lambin, J. Darville, and J.-M. Gilles, Phys. Rev. B **46**, 2460 (1992).

[28] M. Kwoka, N. Waczyńska, P. Kościelniak, M. Sitarz, and J. Szuber, Thin Solid Films **520**, 913 (2011).

[29] B. V. Cris, *Handbook of Monochromatic XPS Spectra: The Elements of Native Oxides* (Wiley, Chichester, 2000).

[30] W. E. Morgan, and J. R. Van Wazer, J. Phys. Chem. **77**, 964 (1973).

[31] J. J. Mudd, T.-L. Lee, V. Muñoz-Sanjosé, J. Zúñiga-Pérez, D. Hesp, J. M. Kahk, D. J. Payne, R. G. Egdell, and C. F. McConville, Phys. Rev. B **89**, 035203 (2014).

[32] D. J. Payne, R. G. Egdell, W. Hao, J. F. Foord, A. Walsh, and G. W. Watson, Chem. Phys. Lett. **411**, 181 (2005).

[33] P. A. Glans, T. Learmonth, K. E. Smith, J. Guo, A. Walsh, G. W. Watson, F. Terzi, and R. G. Egdell, Phys. Rev. B **71**, 235109 (2005).

[34] D. C. Langreth, Nobel Symp. **24**, 210 (1973).

[35] C. Aruta, G. Balestrino, A. Tabano, G. Ghiringhelli, and N. B. Brooker, Europhys. Lett. **80**, 37003 (2007).

[36] M. Sirena, N. Haberkorn, M. Granada, L. B. Steren, and J. Guimpel, J. Appl. Phys. **105**, 033902 (2009).

[37] J. Rubio-Zuazo, L. Onandia, P. Ferrer, and G. R. Castro, Appl. Phys. Lett. **104**, 021604 (2014).

[38] K. Wang, Y. Ma, and K. Betzler, Phys. Rev. B **76**, 144431 (2007).

[39] S. V. Trukhanov, N. V. Kasper, I. O. Troyanchuk, M. Tovar, H. Szymczak, and K. Bärner, J. Solid State Chem. **169**, 85 (2002).

[40] H. Guo, J.-o. Wang, X. He, Z. Yang, Q. Zhang, K.-j. Jin, C. Ge, R. Zhao, L. Gu, Y. Feng, W. Zhou, X. Li, Q. Wan, M. He, C. Hong, Z. Guo, C. Wang, H. Lu, K. Ibrahim, S. Meng, H. Yang, and G. Yang, Adv. Mater. Interfaces **3**, 1500753 (2016).

[41] D. O. Scanlon, Phys. Rev. B **87**, 161201 (2013).

[42] L. Liu, Z. Mei, A. Tang, A. Azarov, A. Kuznetsov, Q.-K. Xue, and X. Du, Phys. Rev. B **93**, 235305 (2016).

[43] D. Yoon, S. Yu, and J. Son, NPG Asia Mater. **10**, 363 (2018).

[44] B. S. Joo, Y. J. Chang, L. Moreschini, A. Bostwick, E. Rotenberg, and M. Han, Curr. Appl. Phys. **17**, 595 (2017).

[45] J. Zhuang, S. Weng, W. Dai, P. Liu, and Q. Liu, J. Phys. Chem. C **116**, 25354 (2012).

[46] K. A. Bogle, M. N. Bachhav, M. S. Deo, N. Valanoor, and S. B. Ogale, Appl. Phys. Lett. **95**, 203502 (2009).

[47] H. J. Cho, T. Onozato, M. Wei, A. Sanchela, and H. Ohta, APL Mater. **7**, 022507 (2019).

[48] A. P. Nono-Tchiomo, G. Babu-Geetha, E. Carleschi, P. Ngabonziza, and B. P. Doyle, Surf. Sci. Spectra **25**, 024001 (2018).

[49] E. B. Lochocki, H. Paik, M. Uchida, D. G. Schlom, and K. M. Shen, Appl. Phys. Lett. **112**, 181603 (2018).

[50] J. C. Yu, J. Yu, H. Y. Tanga, and L. Zhang, J. Mater. Chem. **12**, 81 (2002).

[51] G. Larramona, C. Gutiérrez, I. Pereira, M. R. Nunes, and F. M. A. da Costa, J. Chem. Soc. Faraday Trans. 1 **85**, 907 (1989).

[52] A. Fujishima, X. Zhang, and D. A. Tryk, Surf. Sci. Rep. **63**, 515 (2008).

[53] D. G. Popescu, N. Barrett, C. Chirila, I. Pasuk, and M. A. Husanu, Phys. Rev. B **92**, 235442 (2015).

[54] X. L. Li, B. Chen, H. Y. Jing, H. B. Lu, B. R. Zhao, Z. H. Mai, and Q. J. Jia, Appl. Phys. Lett. **87**, 222905 (2005).

[55] S. Sengupta, A. Ghatak, S. Sett, M. Sreemany, S. Bysakh, B. Ghosh, and A. K. Raychaudhuri, J. Phys. D: Appl. Phys. **51**, 085304 (2018).

[56] X. L. Li, H. B. Lu, Ming Li, Zhenhong Mai, Hyunjung Kim, and Q. J. Jia, Appl. Phys. Lett. **92**, 012902 (2008).

[57] W. H. Zhang, L. Chen, Y. T. Tao, W. H. Zhang, J. Chen, and J. X. Zhang, Physica B **406**, 4630 (2011).

[58] L. T. Hudson, R. L. Kurtz, and S. W. Robey, Phys. Rev. B **47**, 10832 (1993).

[59] C. G. Allen, and P. M. Tucker, Chem. Phys. Lett. **43**, 254 (1976).

[60] S. Sallis, D. O. Scanlon, S. C. Chae, N. F. Quackenbush, D. A. Fischer, J. C. Woicik, J.-H. Guo, S.-W. Cheong, and L. F. J. Piper, Appl. Phys. Lett. **103**, 042105 (2013).

[61] H. Mizoguchi, H. W. Eng, and P. M. Woodward, Inorg. Chem. **43**, 1667 (2004).

[62] H. J. Kim, U. Kim, T. H. Kim, J. Kim, H. M. Kim, B. G. Jeon, W. J. Lee, H. S. Mun, K. T. Hong, J. Yu, K. Char, and K. H. Kim, Phys. Rev. B **86**, 165205 (2012).

[63] H. Paik, Z. Chen, E. Lochocki, H. Ariel Seidner, A. Verma, N. Tanen, J. Park, M. Uchida, S. Shang, B. C. Zhou, M. Brützam, R. Uecker, Z. K. Liu, D. Jena, K. M. Shen, D. A. Muller, and D. G. Schlom, APL Mater. **5**, 116107 (2017).

[64] M. S. Moreno, R. F. Egerton, and P. A. Midgley, Phys. Rev. B **69**, 233304 (2004).

[65] W. Y. Wang, Y. L. Tang, Y. L. Zhu, J. Suriyaprakash, Y. B. Xu, Y. Liu, B. Gao, S. W. Cheong, and X. L. Ma, Sci. Rep. **5**, 16097 (2015).

[66] K. Siegbahn, U. Gelius, H. Siegbahn, and E. Olson, Phys. Lett. A, **32**, 221 (1970).

[67] C. J. Fadley, R. J. Baird, W. Siekhaus, T. Novakov, and S. A. L. Bergstrom, J. Electron Spectrosc. Relat. Phenom. **4**, 93 (1974).

[68] H. Iwasaki, R. Nishitani, and S. Nakamura, Jpn. J. Appl. Phys. **17**, 1519 (1978).

[69] J. A. Leiro, and M. H. Heinonen, Surf. Sci. **346**, 73 (1996).

[70] P. D. C. King, T. D. Veal, D. J. Payne, A. Bourlange, R. G. Egdell, and C. F. McConville, Phys. Rev. Lett. **101**, 116808 (2008).

[71] Z. Zhang, and J. T. Yates Jr, Chem. Rev. **112**, 5520 (2012).

[72] M. P. Seah, and W. A. Dench, Surf. Interface Anal. **1**, 2 (1979).

[73] K. Zhang, D. Payne, R. Palgrave, V. Lazarov, W. Chen, A. Wee, C. McConville, P. King, T. Veal, G. Panaccione, P. Lacovig, and R. G. Egdell, Chem. Mater. **21**, 4353 (2009).

[74] H. Li, Y. Guo, and J. Robertson, J. Phys. Chem. C **119**, 18160 (2015).

[75] P. Scheiber, M. Fidler, O. Dulub, M. Schmid, U. Diebold, W. Hou, U. Aschauer, and A. Selloni, Phys. Rev. Lett. **109**, 136103 (2012).

[76] J. Carrasco, N. Lopez, F. Illas, and H.-J. Freund, J. Chem. Phys. **125**, 074711 (2006).

[77] G. Pacchioni, ChemPhysChem **4**, 1041 (2003).

[78] R. Schaub, E. Wahlström, A. Rønnau, E. Laegsgaard, I. Stensgaard, and F. Besenbacher, Science **299**, 377 (2003).

[79] S. Kim, K. C. Ko, J. Y. Lee, and F. Illas, Phys. Chem. Chem. Phys. **18**, 23755 (2016).

[80] A. Sakar, and G. G. Khan, Nanoscale, **11**, 3414 (2019).

[81] A. Damascelli, Phys. Scr. **T109**, 61 (2004).

[82] J. A. C. Santana, *Quantitative Core Level Photoelectron Spectroscopy*, (Morgan & Claypool Publishers, San Rafael, USA, 2016).

[83] J. M. Themlin, R. Sporken, J. Darville, R. Caudano, J. M. Gilles, and R. L. Johnson, Phys. Rev. B **42**, 11914 (1990).

[84] S. K. Vasheghani Farahani, T. D. Veal, J. J. Mudd, D. O. Scanlon, G. W. Watson, O. Bierwagen, M. E. White, J. S. Speck, and C. F. McConville, Phys. Rev. B **90**, 155413 (2014).

[85] L. Kövér, G. Moretti, Zs. Kovács, R. Sanjinés, I. Cserny, G. Margaritondo, J. Pálinkás, and H. Adachi, J. Vac. Sci. Technol. A **13**, 1382 (1995).

[86] C. A. Niedermeier, S. Rhode, K. Ide, H. Hiramatsu, H. Hosono, T. Kamiya, and M. A. Moram, Phys. Rev. B **95**, 161202 (2017).

[87] Q. Liu, J. Liu, B. Li, H. Li, G. Zhu, K. Dai, Z. Liu, P. Zhang, and J. Dai, Appl. Phys. Lett. **101**, 241901 (2012).

[88] D. Seo, K. Yu, Y. Jun Chang, E. Sohn, K. Hoon Kim, and E. J. Choi, Appl. Phys. Lett. **104**, 022102 (2014).

6. Future Perspectives: Probing the Interface of Oxide Heterostructures

6.1 Introduction

In the work presented in Chapters 4 and 5 of this thesis, oxide heterostructures (OHs) were fabricated by directly growing an epitaxial thin film of La-doped $BaSnO_3$ on a single crystal substrate, or by firstly depositing an insulating buffer layer on the substrate and then growing the active La-doped $BaSnO_3$ film on top. These OHs were optimized to achieve higher electronic transport characteristics in La-doped $BaSnO_3$ thin films prepared on $SrTiO_3$ (001), $DyScO_3$ (110) and $TbScO_3$ (110) using $BaSnO_3$ and $SrZrO_3$ buffer layers. As addressed in Chapter 2, OHs based La-doped $BaSnO_3$ thin films are scientifically and industrially important. More generally, OHs are promising as they offer a wide range of opportunities, not only for applications in the next generation of transparent electronics, optoelectronic and spintronic devices [1, 2, 3, 4, 5, 6, 7, 8], and in energy storage and utilization [4, 5, 7, 8, 9], but also for the exploration of novel physics phenomena at oxide heterointerfaces [10, 11, 12, 13, 14, 15, 16, 17]. In particular, the heterointerfaces with $SrTiO_3$ substrates are known to possess a wide spectrum of fascinating properties such as superconductivity [13, 14], metal-to-insulator transitions [15] as well as different types of magnetic ordering [16, 17] and many more. These characteristics are enclosed into a two dimensional conductive sheet, the two dimensional electron system (2DES), which is generated at the heterointerface under specific conditions [13, 15]. Understanding the physics of complex OHs is an active field of current research.

This chapter presents the preliminary results obtained from a project dedicated to thermally evaporating pure Al metal on $SrTiO_3$ substrates and probing the heterointerface. More precisely, it addresses the formation of a 2DES at the surfaces of cleaned $SrTiO_3$ substrates. This chapter is composed of three sections. In the first section, the interest of growing the $Al/SrTiO_3$ heterostructure and investigating the properties of the interface is presented. In the second section, recent efforts oriented towards creating a 2DES at the interface of OHs and analyzing its properties are explored. In the last section, the XPS data obtained from the preparation of $SrTiO_3$ substrates prior to subsequent Al layer evaporation are discussed.

6.2 Why Study $Al/SrTiO_3$ Heterostructures?

Over the past few decades, technical advances in the fabrication of 2DES in OHs have been mainly achieved through an epitaxially grown layer of $LaAlO_3$ on a $SrTiO_3$ substrate, using either PLD, MBE or sputtering at relatively high growth temperatures [18, 19, 20, 21, 22, 23, 24]. Amorphous layers of Al_2O_3 and $LaAlO_3$ grown by an atomic layer deposition (ALD) process on $SrTiO_3$ have also been exploited to create 2DES by generating oxygen vacancies in the $SrTiO_3$ substrate [25, 26]. The growth of a $LaAlO_3$ layer to generate a 2DES using either PLD or MBE imposes a critical thickness of at least 4 unit cells that itself drastically restricts the control of the 2DES properties [15, 27]. Although the creation of the 2DES at the $LaAlO_3/SrTiO_3$ heterointerface has been widely studied, the production of $LaAlO_3/SrTiO_3$ at an industrial level is problematic because of its high cost and complexity. Another approach, which is to directly fabricate a two-dimensional sheet of conductive electrons at the surface of $SrTiO_3$, requires an intense ultraviolet (UV) light or X-ray synchrotron source to create

oxygen vacancies [28, 29, 30, 31]. This process is conducted in ultrahigh vacuum (UHV) and under oxygen pressure, in order to control the vacancies, and thus control the properties of the 2DES. Out of the vacuum, the surface vacancies are filled and the material thus becomes not usable for applications at ambient conditions [32, 33]. Hence, there is a need to obtain oxide materials that retain the properties of the 2DES at the heterointerface regardless of the conditions (in vacuum or air).

The thermal deposition (or evaporation) of a thin layer of pure Al on $SrTiO_3$ could be the solution, which surmounts the limits encountered in previous heterostructures. Indeed, the redox reaction between the metal layer of aluminium and the oxide surface constitutes a simple and cheap way of generating a 2DES. Moreover, this technique is convenient for industrial production and the realization of mesoscopic devices, and has so far been used in fabricating $Al/SrTiO_3$ and $Al/Fe/SrTiO_3$ heterostructures and creating 2DES at the metal/substrate interfaces [32, 33]. The $Al/SrTiO_3$ heterostructure is particularly promising for device applications as it is candidate for achieving a high-mobility channel layer. However, little is known on the mechanism, fabrication and electronic band structure of this system, and a proper electronic transport characterization of the interface has not yet been carried out. Therefore, for future directions, a method to design and control the 2DES at the interface of the $Al/SrTiO_3$ heterostructure should be established; also, a study of its novel complex phenomena in both the band structure and on fabricated quantum devices should be conducted. The complexity in designing this system lies in the critical thickness of the evaporated Al layer, which should not be too thick to prevent probing of the conductive interface, and not too thin to result in a complete insulating interface [32, 33]. Additionally, for quantum device fabrication purposes, the 2DES feature at the interface should exhibit a high electron mobility and low carrier density at room temperature.

6.3 Overview of the Two Dimensional Electron System

The electronic transport properties (high electron mobility and superconductivity, for example), as well as large magnetoresistance found in 2DES systems are promising to motivate the use of oxide materials for the fabrication of novel devices. The use of oxide materials in various technological applications such as the fabrication of optoelectronic and spintronic devices promises that it can replace its semiconductor counterparts [34]. Notably, the 2DES system formed at the Al and $SrTiO_3$ interface has attracted our attention for two reasons: 1- it has not yet been extensively investigated, unlike the $LaAlO_3/SrTiO_3$ interface; 2- it is promising for the investigation of novel physics phenomena in quantum devices that exploit the property of the interface. ARPES spectra, as reported in Ref. [32], reveal the existence of the 2DES at the $Al/SrTiO_3$ interface, and are to our knowledge, the only data available so far for such a heterostructure, although a 2DES was recently reported in an $Al/Fe/SrTiO_3$ heterostructure where the Al served as capping layer [33]. Thus, for the purpose of giving an extensive background on oxide heterointerfaces, it is worthwhile to first refer to $LaAlO_3/SrTiO_3$ [18, 19, 20, 21, 22, 23], and thereafter to $SrTiO_3$ [28, 29, 30, 31], as prototypical materials in which the interfacial 2DES has been largely investigated.

6.3.1 Origin

The mechanism by which the 2DES occurs at the interface remains controversial [35, 36, 37]. One wants to understand how an insulator surface becomes metallic. To date, two

theoretical approaches have been considered. The first one, which applies only to the polar $LaAlO_3$ and non-polar $SrTiO_3$ heterostructure, is based on an intrinsic mechanism known as electronic reconstruction in the case of perfectly stoichiometric $SrTiO_3$ and $LaAlO_3$ layers [20, 22]. $SrTiO_3$ has two neutral layers in the unit cell, i.e. SrO and TiO_2. On the contrary, $LaAlO_3$ has LaO and AlO_2 layers with $+1$ and -1 charge, respectively [35]. Thus, when $LaAlO_3$ is grown on top of $SrTiO_3$, an electrostatic potential that rapidly increases as a function of the number of $LaAlO_3$ unit cells is accumulated. This potential would diverge in an infinite crystal, giving rise to the so-called polarization catastrophe [36]. A redistribution of electrons can reduce the electrostatic potential created at the $LaAlO_3$ surface and $LaAlO_3/SrTiO_3$ interface due to the unbalanced charge, and thus prevent the polarization catastrophe. Figure 6.1 illustrates an example of layer stacking in the case of the *n*-type interface in which $SrTiO_3$ is TiO_2 terminated and $LaAlO_3$ is AlO_2 terminated. In the case portrayed in the figure, there will be an electrostatic stabilization due to a transfer of -0.5 charge from the AlO_2 layer at the surface to the TiO_2 layer at the interface [36]. The same process holds in the case of *p*-type interfaces, i.e. where $SrTiO_3$ is SrO terminated and $LaAlO_3$ is LaO terminated [36]. The 2DES carrier density strongly depends on the thickness of the $LaAlO_3$ layers, due to the competition between electronic reconstruction and polar distortion [37]. However, the electronic reconstruction that contributes to the formation of the 2DES at a critical thickness

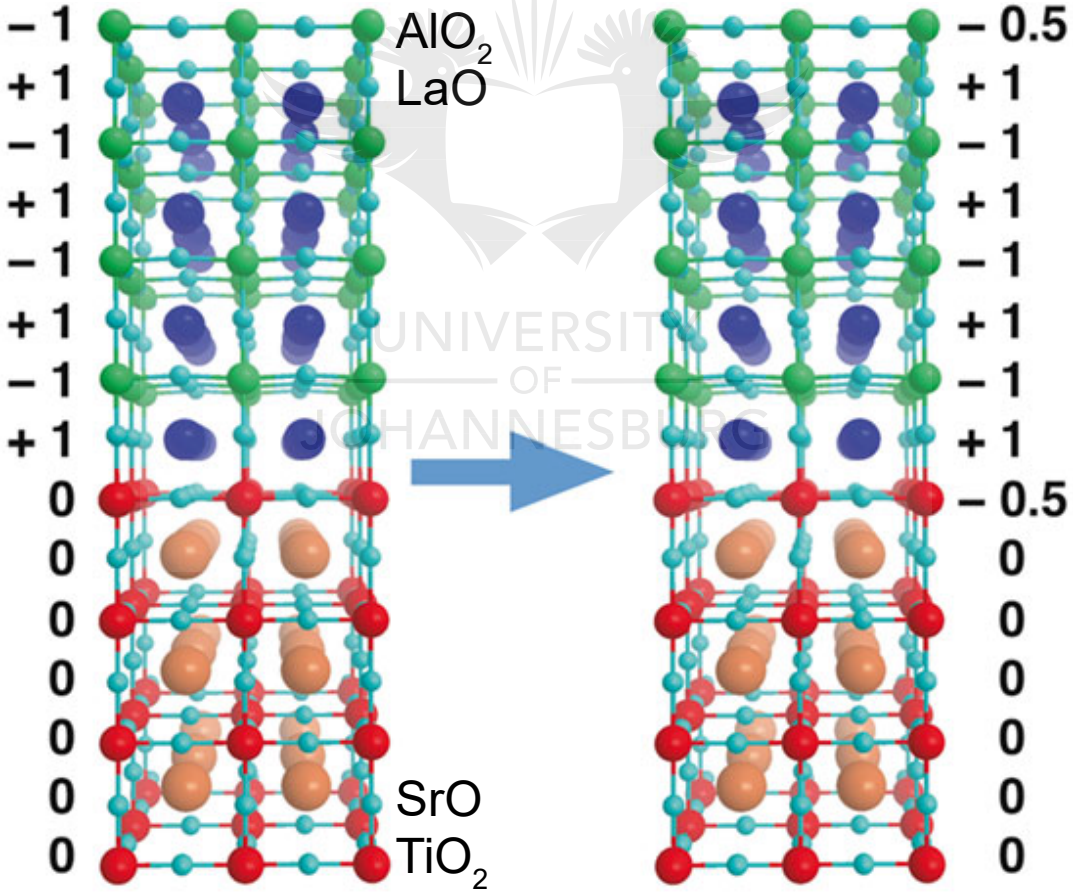

Figure 6.1: Layer stacking in *n*-type $LaAlO_3/SrTiO_3$ heterostructure. The formal charge of each layer is indicated on the sides together with the transfer of -0.5 charge which ensures electrostatic stabilization. This image was adapted from Ref. [36].

of the $LaAlO_3$ layer is favoured by the variable valence of the transition metal titanium ions [38]. While the intrinsic electrical field in the $LaAlO_3$ layer is likely essential to create a 2DEG at the $LaAlO_3/SrTiO_3$ interface, many experimental investigations have shown that this cannot apply to bare $SrTiO_3$, since it is an insulator [29, 30, 31, 34].

The second approach, that has been suggested by many authors as responsible for the formation of the 2DES at the interface of $LaAlO_3/SrTiO_3$, relies on an extrinsic mechanism attributed to structural defects known as oxygen vacancies, applicable to all OHs [18, 19, 20, 21, 22, 23, 35]. Oxygen vacancies are created during the deposition of the $LaAlO_3$ layers, as a result of high-energy particle bombardment during the growth process [21]. The conducting properties of the layer at the $LaAlO_3/SrTiO_3$ interface strongly depend on the oxidation conditions under which they are made. It is shown that the growth of the heterostructure under different atomic oxygen pressure reduces the carrier density at the interface [21], resulting in a change of the $SrTiO_3$ colour, from transparent white to grey, which is a characteristic of oxygen reduced $SrTiO_3$ [19].

On the other hand, based on experimental results, researchers postulated that it is not necessary to grow a polar material (like $LaAlO_3$) on top of the $SrTiO_3$ surface to obtain a 2DES [29, 30, 31, 34]. Recent ARPES experiments have shown that the surface of $SrTiO_3$ fully supports a 2DES when it is irradiated with intense UV light. After exposure of the surface to a small amount of oxygen, the 2DES feature completely disappears. The irradiation of the surface creates oxygen vacancies and its sudden exposure to either atomic or molecular oxygen flow leads to the occupation of the vacancies by oxygen electrons and the suppression of the 2DES. This phenomenon has been observed in both Nb-doped $SrTiO_3$ (111) and La-doped $SrTiO_3$ (001) materials [29, 30]. It also appears that the intensity and energy of the UV source play a role in controlling the 2DES charge density. Nevertheless, the 2DES carrier density increases with the irradiation dose but reaches a limit beyond which there is no increase in conduction electrons.

6.3.2 Two Dimensional Electron System at the Al/$SrTiO_3$ Interface

Recently, a new and cost-effective method to generate 2DES in functional oxides has been proposed [32]. The method consists of depositing an atomically thin layer of pure Al on $SrTiO_3$ by thermal evaporation at room temperature and in UHV [32]. Al acts as a reducing element, and due to the redox reaction, it oxidises, which creates oxygen vacancies and forms a 2DES in the first atomic planes of the oxide. This process is more efficient as the evaporated Al homogeneously reduces the oxygen in the whole surface, while the intense UV source used to create 2DES at $SrTiO_3$ surface locally creates oxygen vacancies. The momentum distribution curves (MDCs) at E_F measured at different positions on the Al/$SrTiO_3$ (001) interface as shown in Fig. 6.2(a), reveal that the Fermi momenta given by the MDCs peak positions are invariant with respect to the measurement point (see inset in Fig. 6.2(a)). Thus, the quality of the 2DES, attributed to the evaporated Al is much better, and the Fermi surface areas as well as the carrier density are much larger [32]. Furthermore, contrary to the $LaAlO_3/SrTiO_3$ system where a critical thickness of the $LaAlO_3$ layer is fundamental, the evaporation of 2 Å of the Al layer is sufficient to absorb oxygen from the surface of the oxide, because the carrier density already saturates at this thickness (see Fig. 6.2(b)).

Furthermore, ARPES measurements performed on the 2 Å Al/$SrTiO_3$ (111) and (001) heterostructures at a photon energy of 47 eV at 8 K reveal concentric circular Fermi surfaces as

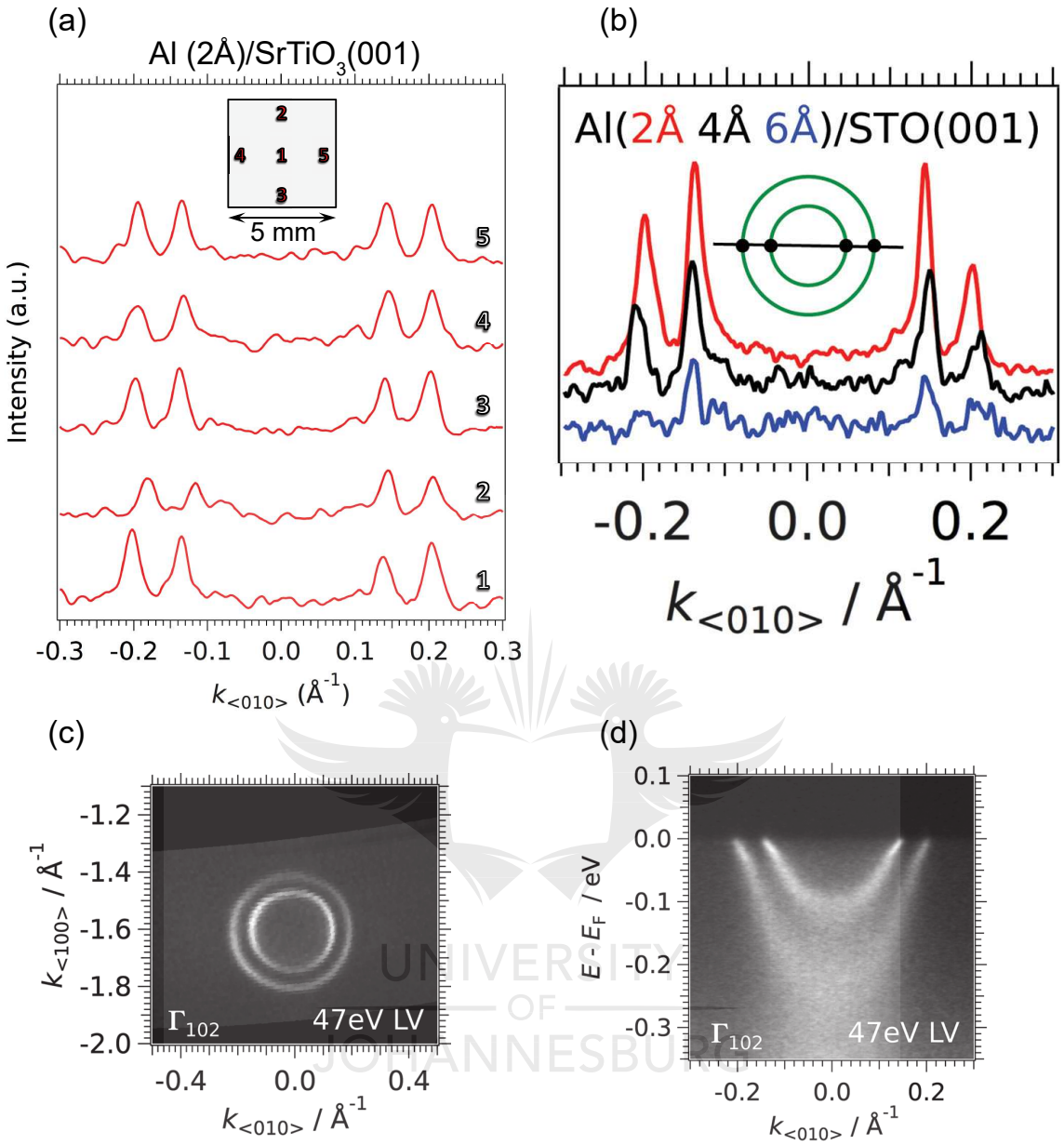

Figure 6.2: (a) Momentum distribution curves (MDCs) at the Fermi energy, E_F, measured at various positions at the Al/$SrTiO_3$ interface as shown in inset. (b) Influence of the Al layer thickness on the 2DES evidenced by the Fermi momenta peaks intensities in the MDCs at E_F. The inset shows the Fermi surface cut. (c) Fermi surface and (d) energy-momentum intensity maps at the 2 Å Al/$SrTiO_3$ (001) interface. These images were adapted from Ref. [32].

can be seen in Fig. 6.2(c) [32]. A kink and a change in intensity in the dispersion of the two light bands (d_{xy}-orbital character) at about -30 meV is also observed in the energy-momentum intensity map (see Fig. 6.2(d)). It was also demonstrated that the temperature affects the electronic structure of the 2DES. Indeed, as can be seen in Fig. 6.3, as the temperature increases up to about 303 K, the line widths of the bands increase and become large enough that the bands mix with each other. However, that spectral weight around E_F shows that the 2DES is still present and stable at room temperature. Furthermore, from the values of the

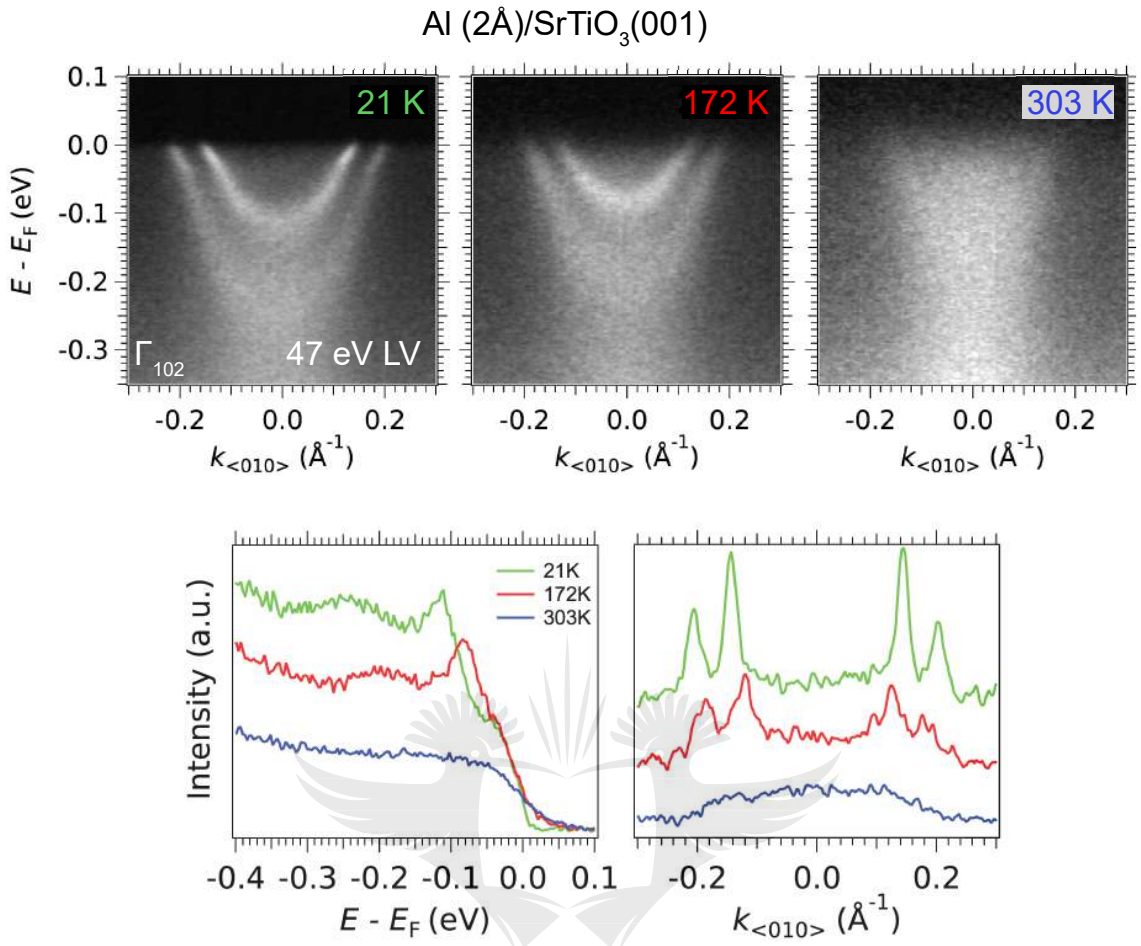

Figure 6.3: Energy-momentum intensity maps and corresponding EDCs and MDCs at the 2 Å Al/$SrTiO_3$ (001) interface as a function of temperature. These images were adapted from Ref. [32].

Fermi momenta of the peaks in the MDCs and those of the binding energies of the peaks in the energy distribution curves (EDCs) at different temperatures and at E_F, it appears that the carrier density slightly decreases as the temperature increases.

Moreover, it was observed that a natural oxidized layer (Al_2O_x) at the surface of Al metal is about 12.4 Å thick [40]. Hence, exposure of the Al/$SrTiO_3$ (001) material to ambient conditions raises the issue of the passivation of the Al surface against re-oxidation of the interface. The oxidized metallic Al increases the layer thickness. Thus, the deposition of 10 Å Al layer corresponds to an oxidized layer of about 12.5 Å, which is close to the limiting thickness for the passivation of Al found in Ref. [40]. The stability of the 2DES upon exposure of Al/$SrTiO_3$ (001) sample with an aluminium-capping layer of 10 Å to air for about thirty minutes was tested with the help of soft X-ray resonant ARPES (photon energy of 459.5 eV) conducted at low temperature [32]. The probed interface demonstrated the existence of the 2DES, but the peak shape of the Al 2p orbital showed that the aluminium is completely oxidized. Nevertheless, for electronic transport measurements purposes, the capping layer must be thick enough (a critical thickness) to prevent both oxygen from diffusing through the oxidized layer and metallic aluminium from contributing to the measurements.

As it is intended to conduct further investigations including systematic electronic transport, two points should be highlighted. First, with a systematic growth of Al/$SrTiO_3$ and characterization of the 2DES at interface, it is expected to achieve a high electron mobility (preferentially with a low carrier density), comparable, or much better than that of $LaAlO_3/SrTiO_3$. Second, it is expected that this interface would also exhibit fascinating properties such as superconductivity [13], magnetism [41], Rashba spin-orbit coupling [42, 43] and the coexistence superconductivity and magnetism [44].

6.4 Vacuum Treatment Induced 2DES at the $SrTiO_3$ Surface

Here, the preparation of the surfaces of $SrTiO_3$ (100) substrates, which precedes the thermal evaporation of metal Al layers is discussed. For epitaxial growth of multifunctional layers and heterointerface tailoring purposes, $SrTiO_3$ which has a wide band gap (3.25 eV) and a large dielectric constant [39] has been the material of choice owing to its interesting characteristics. Indeed, it has a cubic structure at room temperature, but undergoes an antiferrodistortive phase transition to a tetragonal structure at about 105 K [45, 46]. Hence, it exhibits para-electric properties at room temperature that transit to intrinsic quantum paraelectric below about 4 K [45, 46]. Upon mechanical stresses, $SrTiO_3$ also displays ferroelectric properties [47, 48, 49]. Furthermore, as a perovskite compound, $SrTiO_3$ was found to be structurally compatible in heteroepitaxial growth with a wide range of related compound, mostly due to its lattice parameter which allows lattice matching. Thus, it has been extensively employed in the epitaxial growth of quantum materials exhibiting novel topological states of matter. Due to its high dielectric constant at low temperature, $SrTiO_3$ has also been used as a back-gate dielectric in many electronic devices [50, 51, 52, 53].

However, in heterostructures such as Al/$SrTiO_3$, the characteristics of the heterointerface described above strongly depend on the surface properties of the $SrTiO_3$ substrate, which in turn are extremely sensitive to treatment conditions [29, 30, 31, 34]. Prior to the thermal deposition of Al, it was proceeded with a systematic vacuum preparation of the surface of $SrTiO_3$ (100)[1]. The preparation took several cycles of sputtering and annealing. The sputtering processes were achieved at a pressure of 1.38×10^{-5} mbar using argon ions. The optimized parameters used during these processes were as follows: a 30 minute bombardment of the surface with argon ions emitted at a current of 6 mA and accelerated to a maximum energy of 0.8 keV. As for the annealing processes, they were performed in vacuum kept at pressures below about 7×10^{-9} mbar. These were carried out using an electron beam heater, that heats the substrate from the back side of the molybdenum sample holder on which it was glued. The annealing was operated by electrons emission current, controlled to a power of 30 W, and followed with subsequent flashes (2 to 3 times) to the highest temperature for approximately 10 s. The substrate temperature during annealing was around 700 to 800 °C, estimated by the red color of both substrate and sample holder.

Figures 6.4 to 6.6 represent the fitted spectra of some core levels of $SrTiO_3$ (100) including Sr 3p, O 1s and Ti 2p, for the substrates as-received and cleaned (sputter-annealed). The peak fitting parameters of these respective core electrons are summarized in Tables 6.1 to 6.3. These core spectra were excited with an Al K_α source, and the experimental resolution for

[1] The XPS data of these samples were compiled into a paper entitled: *Surface characterization of clean $SrTiO_3$(100) substrates by x-ray photoelectron spectroscopy*, A. P. Nono Tchiomo *et al.*, Surf. Sci. Spectra 25, 024001 (2018).

the acquisition was 0.78 eV. The core electrons are presented together with their satellites. In $SrTiO_3$, most of these satellites emanate from charge transfer shake-up processes [54]. In the case of the O 1s spectrum, theoretical calculations along with high resolution spectra have allowed a proper identification of the excitations responsible for its satellites [55]. Those seen in the spectra presented in this study are as follows: the satellite located 11.6 eV from the main peak comes from the excitation of O 2p electrons to unoccupied Sr 5s levels; that at the energy difference of 14.1 eV, O 2p electrons to unoccupied Sr 4d levels; and the one 19.3 eV away from the main core electron, O 2p electrons to unoccupied Ti 4sp states.

Figure 6.4 shows the Sn 3p core electrons for as-received (Fig. 6.4(a)) and sputter-annealed (Fig. 6.4(b)) surfaces. The peak splitting in Sn $3p_{\frac{3}{2}}$ and Sn $3p_{\frac{1}{2}}$ is clearly seen along with the signal originating from C 1s. As can be observed from Table 6.1, the Sn 3p core level is located at $\approx$ 270 eV binding energy. Furthermore, it can also be seen that the intensity of the carbon peak which is a surface contamination is drastically reduced by a factor of approximately 5 after sputtering and annealed steps. This points to an improvement of the surface cleanliness with substrate treatment. As a result, the shoulder in the high binding energy side of the main O 1s region presented in Fig. 6.5(a) that was associated with contamination disappears, as can

Table 6.1: Fitted parameters of Sr 3p spectra Shown in Fig. 6.4 for as-received and cleaned $SrTiO_3$ (100) substrates. The peak position (P), the peak intensity (I) and the FWHM (F) are given. Cts stands for counts, Dbl stands for doublet.

	As received			Sputter-annealed		
	P (eV)	I (Cts/s)	F (eV)	P (eV)	I (Cts/s)	F (eV)
Error	($\pm$0.05)	($\pm$0.01)	($\pm$0.05)	($\pm$0.05)	($\pm$0.01)	($\pm$0.05)
Sr 3p Dbl	270.35	5.82×10^6	2.25	269.65	6.42×10^6	2.4
C 1s	286.62	4.90×10^5	1.6	285.33	1.00×10^5	2.7

Table 6.2: Fitted parameters of O 1s core spectra shown in Fig. 6.5 for as-received and cleaned $SrTiO_3$ (100) substrates. The peak position (P), the peak intensity (I) and the FWHM (F) are given. Cts stands for counts, Contamin stands for contamination, and Oxy Vac stands for oxygen vacancy.

	As received			Sputter-annealed		
	P (eV)	I (Cts/s)	F (eV)	P (eV)	I (Cts/s)	F (eV)
Error	($\pm$0.07)	($\pm$0.01)	($\pm$0.07)	($\pm$0.07)	($\pm$0.01)	($\pm$0.07)
O 1s	531.25	4.76×10^6	1.31	530.61	5.82×10^6	1.64
Contamin	532.98	5.88×10^5	2.15	—	—	—
Oxy Vac	—	—	—	531.49	7.43×10^5	3

Table 6.3: Fitted parameters of Ti 2p core levels presented in Fig. 6.6 for as-received and cleaned $SrTiO_3$ (100) substrates. The peak position (P), the peak intensity (I) and the FWHM (F) are given. Cts stands for counts, Dbl stands for doublet.

	As received			Sputter-annealed		
	P (eV)	I (Cts/s)	F (eV)	P (eV)	I (Cts/s)	F (eV)
Error	($\pm$0.04)	($\pm$0.01)	($\pm$0.04)	($\pm$0.04)	($\pm$0.01)	($\pm$0.04)
Ti^{4+} Dbl	460.14	4.63×10^6	1.21	459.33	7.10×10^6	1.50
Ti^{3+} Dbl	—	—	—	457.17	7.00×10^5	1.67

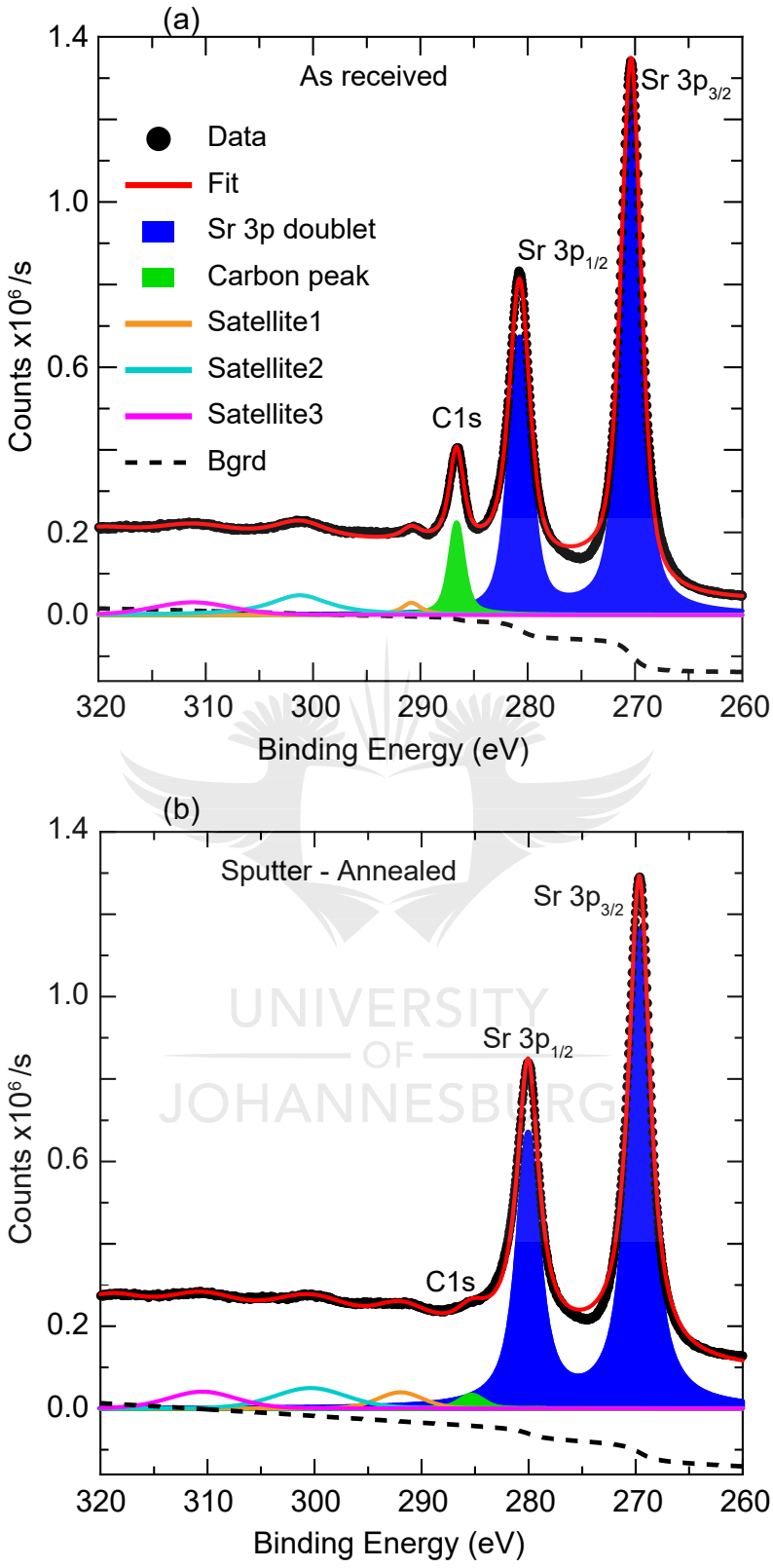

Figure 6.4: Fits of Sr 3p core spectra for (a) as-received and (b) sputter-annealed surfaces of $SrTiO_3$ (100) substrates. The spectra are fitted with doublet Voigt components and the satellites with single Voigt components.

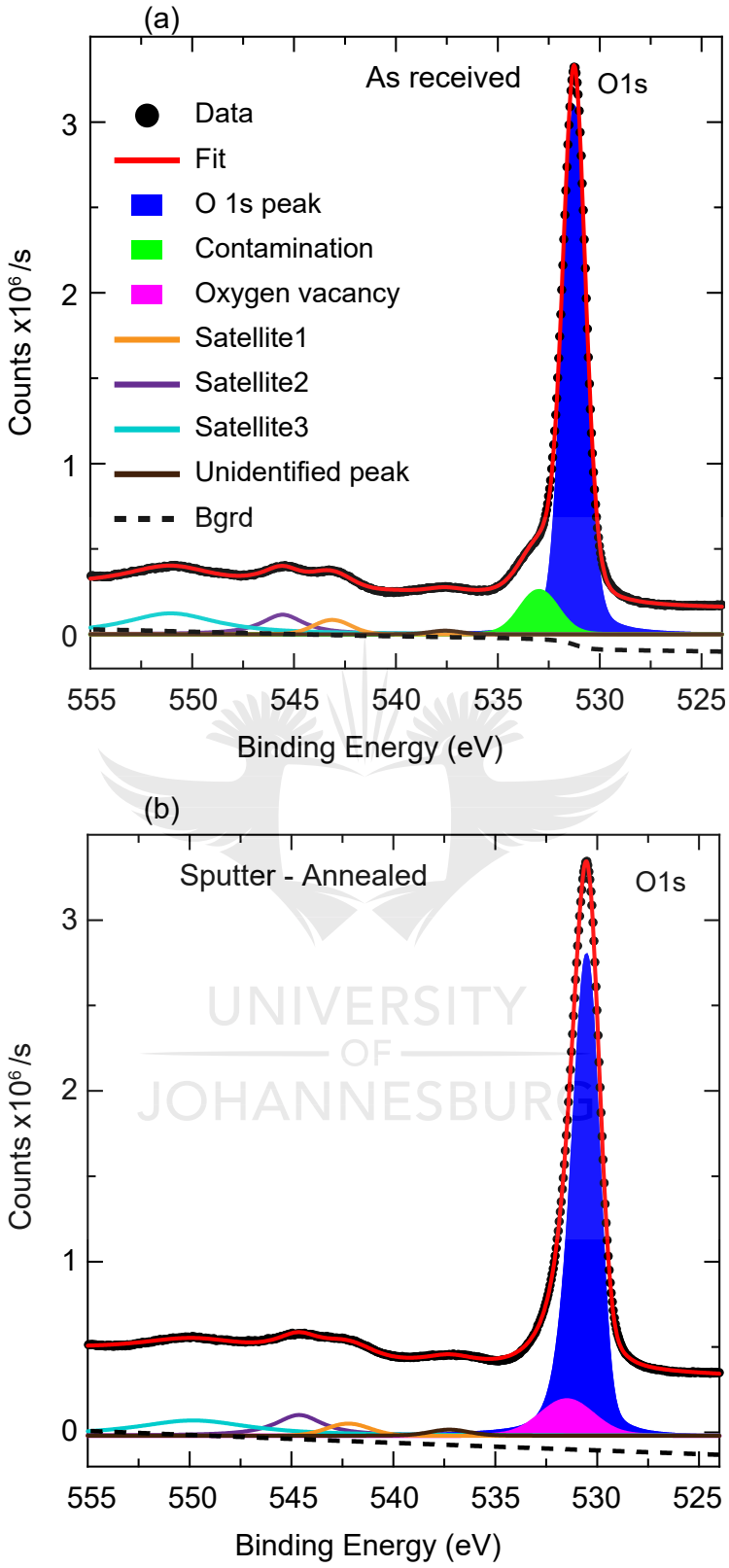

Figure 6.5: Fits of O 1s core level for (a) as-received and (b) sputter-annealed surfaces of $SrTiO_3$ (100) substrates. The core spectra are fitted to two singlet Voigt components. The satellites are likewise fitted by singlet Voigts.

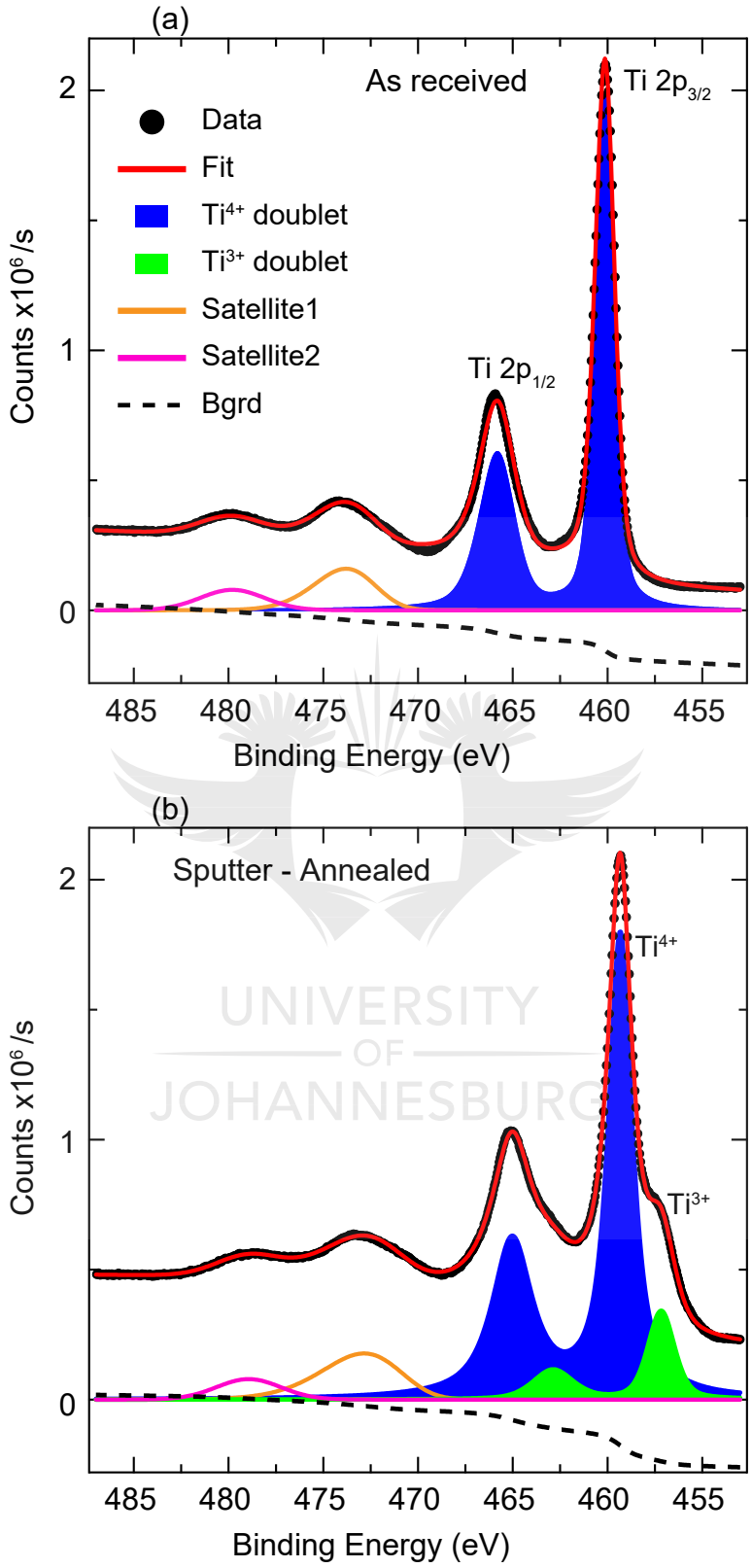

Figure 6.6: Fits of Ti 2p core electrons for (a) as-received and (b) sputter-annealed surfaces of $SrTiO_3$ (100) substrates. The spectra are fitted to (a) a Voigt doublet and (b) two Voigt doublets. The satellites are fitted with Voigt singlets.

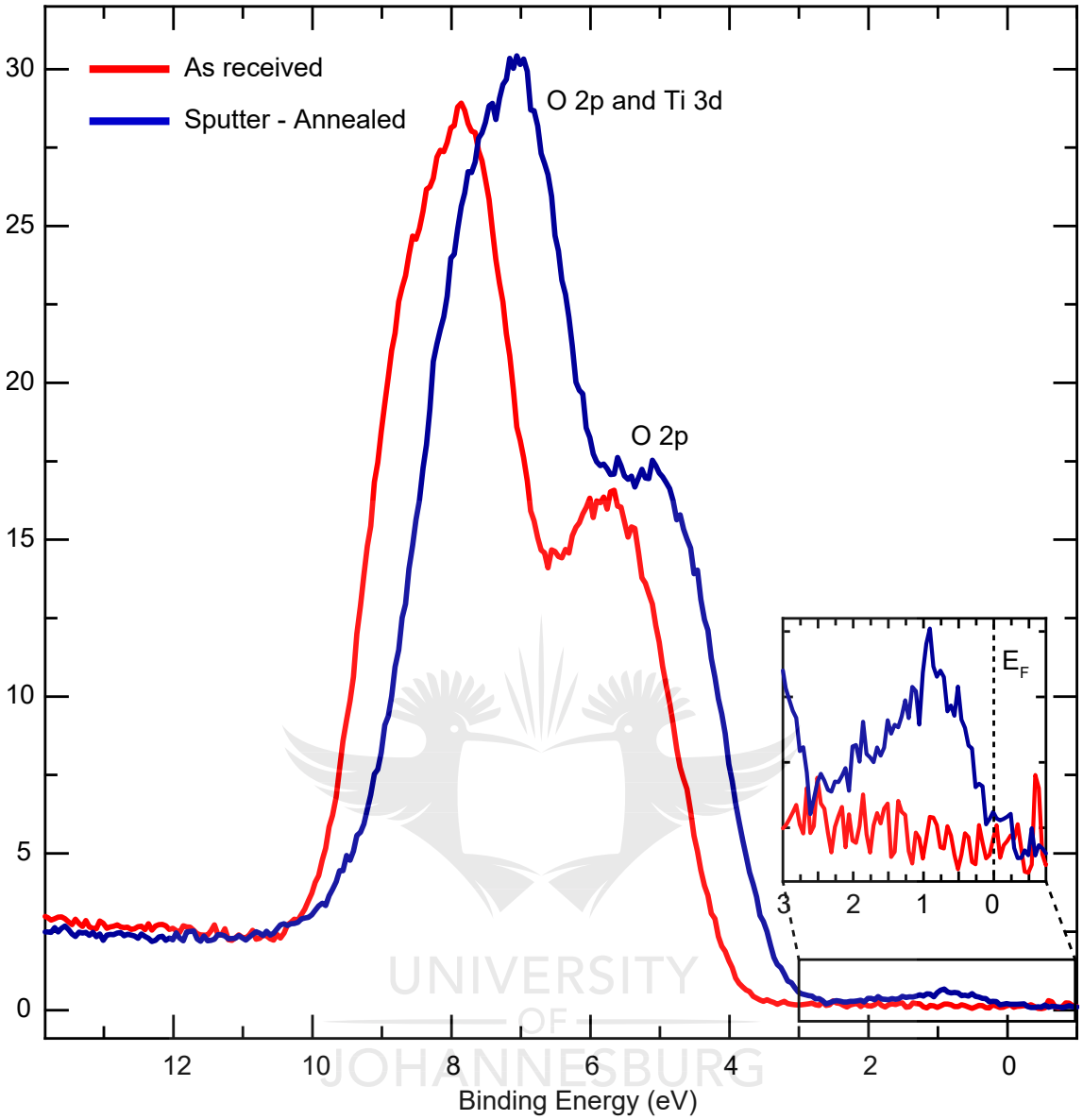

Figure 6.7: Valence band regions for as-received and sputter-annealed $SrTiO_3$ (100) substrates. The inset shows the enlargement of the region indicated by the black rectangle.

be seen in the spectrum of the clean O 1s surface shown in Fig. 6.5(b). Concomitantly, a peak related to oxygen vacancies appears at 531.49 eV in the clean spectrum, 0.92 eV away from the O^{2-} peak. This energy difference is comparable to the values reported in the literature [56, 57, 58].

Figures. 6.6(a) and 6.6(b) depict the Ti 2p core spectra for as-received and sputter-annealed surfaces, respectively. As can be observed in the figures, apart from the Ti^{4+} doublet due to spin-orbit splitting situated at 460 eV, a new feature emerging at the low binding energy side of the main peak attributed to Ti^{3+} states develops. This feature which reveals substantial changes at the surface with treatment is due to the formation of oxygen vacancy induced at the surface by Ar^{+} sputtering and UHV annealing. Indeed, it is well established that the surface

valence state of Ti in $SrTiO_3$ becomes Ti^{3+} when oxygen defects appear in the material, different from the bulk Ti^{4+} of the pristine compound [59, 60, 61, 62]. Based on the data from Table 6.3, the ratio Ti^{3+}/Ti^{4+} sites gives 0.099, meaning $\approx$ 10% of redistribution from Ti^{4+} to Ti^{3+} states. This low rate can be explained assuming that the surface is only partially cleaned and also that vacancies do not form as deeply as XPS probes. The presence of Ti^{3+} indicates the formation of a metallic surface state on $SrTiO_3$ (100), notably a 2DES. This result is consistent with the reports of the formation of 2DES at the surface of $SrTiO_3$ irradiated in UHV [28, 29], or at the interface of $LaAlO_3/SrTiO_3$ [63], evidenced by the appearance of Ti^{3+} suggesting additional electrons in the otherwise empty 3d shell of Ti^{4+}. This is further demonstrated in Fig. 6.7 which represents the XPS spectra of the valence band for as-received and sputter-annealed surfaces. As can be seen in the figure, a peak (metallic state) in the band gap of the valence band region of the clean surface features occupied states near E_F. These in-gap states are clearly visible in the inset showing a magnification of the valence bands of both as-received and sputter-annealed surfaces around E_F.

6.5 Concluding Remarks

It is noteworthy that the surface preparation was extremely challenging. This was in part due to the way the substrates were attached onto the sample holder. In fact, at the time the data presented in Figs 6.4 to 6.7 were acquired, a silver-based conductive paste was used to glue the substrates on the sample holder. Once loaded in vacuum and heated to a very small current, it was noted that the ensemble (substrate and holder) considerably degassed, although this was cured in air on a hot plate for 30 min at 80 °C before being introduced into the preparation chamber. A more effective way of attaching the substrate on the holder has been developed since then. It consists of using a clamp that applies an homogeneous force at the corners of the substrate and therefore prevent crystal breakage due to intense heat. This has proved to be efficient, not time consuming and resulted in well prepared surfaces as evidenced by the data presented in Chapter 5. Hence, the Al metal would be evaporated on a surface devoid of any contamination. It should also be mentioned that for deposition purposes, the surface should be prepared in an oxygen environment in order to compensate for the vacancies induced by annealing, so that the evaporation is done on a surface which is not oxygen deficient for more controllability. This project is part of the current research interests ongoing in the research unit at the University of Johannesburg.

Bibliography

[1] A. P. Ramirez, Science **315**, 1377 (2007).

[2] A. Ohtomo, D. A. Muller, J. L. Grazul, and H. L. Hwang, Nature **419**, 378 (2002).

[3] P. Barquinha, L. Pereira, R. Martins, and E. Fortunato, *Transparent Oxide Electronics: from Materials to Devices* (Wiley, New York, 2012).

[4] B. G. Lewis, and D. C. Paine, MRS Bull. **25**, 22 (2000).

[5] T. Minami, MRS Bull. **25**, 38 (2000).

[6] T. J. Coutts, D. L. Young, and X. Li, MRS Bull. **25**, 58 (2000).

[7] D. S. Ginley, C. Bright, and G. Editors, MRS Bull. **25**, 15 (2000).

[8] E. Fortunato, D. Ginley, H. Hosono, and D. C. Paine, MRS Bulletin **32**, 242 (2007).

[9] A. J. Freeman, K. R. Poeppelmeier, T. O. Masson, R. P. H. Chang, and T. J. Marks, MRS Bull. **25**, 45 (2000).

[10] H. Y. Hwang, Y. Iwasa, M. Kawasaki, B. Keimer, N. Nagaosa, and Y. Tokura, Nature Mater. **11**, 103 (2012).

[11] J. Chakhalian, A. J. Millis, and J. Rondinelli, Nature Mater. **11**, 92 (2012).

[12] Nature Mater. **11**, 91 (2012).

[13] N. Reyren, S. Thiel, A. D. Caviglia, L. F. Kourkoutis, G. Hammerl, C. Richter, C. W. Schneider, T. Kopp, A.-S. Rüetschi, D. Jaccard, M. Gabay, D. A. Muller, J.-M. Triscone, and J. Mannhart, Science **317**, 1196 (2007).

[14] D. Stornaiuolo, D. Massarotti, R. Di Capua, P. Lucignano, G. P. Pepe, M. Salluzzo, and F. Tafuri, Phys. Rev. B **95**, 140502 (2017).

[15] S. Thiel, G. Hammerl, A. Schmehl, C. W. Schneider, and J. Mannhart, Science **313**, 1942 (2006).

[16] Ariando, X. Wang, G. Baskaran, Z. Q. Liu, J. Huijben, J. B. Yi, A. Annadi, A. R. Barman, A. Rusydi, S. Dhar, Y. P. Feng, J. Ding, H. Hilgenkamp, and T. Venkatesan, Nat. Commun. **2**, 188 (2011).

[17] J.-S. Lee, Y. W. Xie, H. K. Sato, C. Bell, Y. Hikita, H. Y. Hwang, and C.-C. Kao, Nat. Mater. **12**, 703 (2013).

[18] S. Y. Moon, C. W. Moon, H. J. Chang, T. Kim, C.-Y. Kang, H.-J. Choi, J.-S. Kim, S.-H. Baek, and H. W. Jang, Electron. Mater. Lett. **12**, 243 (2016).

[19] A. Kalabukhov, R. Gunnarsson, J. Börjesson, E. Olsson, T. Claeson, and D. Winkler, Phys. Rev. B **75**, 121404 (2007).

[20] Z. Q. Liu, C. J. Li, W. M. Lü, X. H. Huang, Z. Huang, S. W. Zeng, X. P. Qiu, L. S. Huang, A. Annadi, J. S. Chen, J. M. D. Coey, T. Venkatesan, and Ariando, Phys. Rev. X **3**, 021010 (2013).

[21] W. Siemons, G. Koster, H. Yamamoto, W. A. Harrison, G. Lucovsky, T. H. Geballe, D. H. A. Blank, and M. R. Beasley, Phys. Rev. Lett. **98**, 196802 (2007).

[22] Y.-L. Han, Y.-W. Fang, Z.-Z. Yang, C.-J. Li, L. He, S.-C. Shen, Z.-Z. Luo, G.-L. Qu, C.-M. Xiong, R.-F. Dou, X. Wei, L. Gu, C.-G. Duan, and J.-C. Nie, Phys. Rev. B **92**, 115304 (2015).

[23] Y. Segal, J. H. Ngai, J. W. Reiner, F. J. Walker, and C. H. Ahn, Phys. Rev. B **80**, 241107 (2009).

[24] J. P. Podkaminer, T. Hernandez, M. Huang, S. Ryu, C. W. Bark, S. H. Baek, J. C. Frederick, T. H. Kim, K. H. Cho, J. Levy, M. S. Rzchowski, and C. B. Eom, Appl. Phys. Lett. **103**, 071604 (2013).

[25] S. W. Lee, J. Nanomater. **2016**, 1 (2016).

[26] S. W. Lee, Y. Liu, J. Heo, and R. G. Gordon, Nano Lett. **12**, 4775 (2012).

[27] N. C. Plumb, M. Kobayashi, M. Salluzzo, E. Razzoli, C. E. Matt, V. N. Strocov, K. J. Zhou, M. Shi, J. Mesot, T. Schmitt, L. Patthey, and M. Radović, Appl. Surf. Sci. **412**, 271 (2017).

[28] N. C. Plumb, M. Salluzzo, E. Razzoli, M. Månsson, M. Falub, J. Krempasky, C. E. Matt, J. Chang, M. Schulte, J. Braun, H. Ebert, J. Minár, B. Delley, K.-J. Zhou, T. Schmitt, M. Shi, J. Mesot, L. Patthey, and M. Radović, Phys. Rev. Lett. **113**, 086801 (2014).

[29] S. M. Walker, F. Y. Bruno, Z. Wang, A. de la Torre, S. Riccó, A. Tamai, T. K. Kim, M. Hoesch, M. Shi, M. S. Bahramy, P. D. C. King, and F. Baumberger, Adv. Mater. **27**, 3894 (2015).

[30] S. M. Walker, A. de la Torre, F. Y. Bruno, A. Tamai, T. K. Kim, M. Hoesch, M. Shi, M. S. Bahramy, P. D. C. King, and F. Baumberger, Phys. Rev. Lett. **113**, 177601 (2014).

[31] W. Meevasana, P. D. C. King, R. H. He, S.-K. Mo, M. Hashimoto, A. Tamai, P. Songsiriritthigul, F. Baumberger, and Z.-X. Shen, Nat. Mater. **10**, 114 (2011).

[32] T. C. Rödel, F. Fortuna, S. Sengupta, E. Frantzeskakis, P. Le Fèvre, F. Bertran, B. Mercey, S. Matzen, G. Agnus, T. Maroutian, P. Lecoeur, and A. F. Santander-Syro, Adv. Mater. **28**, 1976 (2016).

[33] L.-D. Anh, S. Kaneta, M. Tokunaga, M. Seki, H. Tabata, M. Tanaka, and S.u Ohya Adv. Mater. **32**, 1906003 (2020).

[34] Z. Wang, Z. Zhong, X. Hao, S. Gerhold, B. Stöger, M Schmid, J. Sánchez-Barriga, A. Varykhalov, C. Franchini, K. Held, and U. Diebold, Pro. Nat. Ac. Sci. **111**, 3933 (2014).

[35] N. C. Bristowe, P. Ghosez, P. B. Littlewood, and E. Artacho, J. Phys.: Condens. Matter **26**, 143201 (2014).

[36] P. Mele, T. Endo, S. Arisawa, C. Li, T. Tsuchiya, *Oxide Thin Films, Multilayers, and Nanocomposites* (Springer, Switzerland, 2015).

[37] N. Sivadas, H. Dixit, V. R. Cooper, and D. Xiao, Phys. Rev. B **89**, 075303 (2014).

[38] R. Pentcheva, and W. E. Pickett, Phys. Rev. Lett. **102**, 107602 (2009).

[39] R. W. Wyckoff, *The Structure of Crystals* (The Chemical Catalog Company, Inc., New York, 1935).

[40] N. Cai, and G. Zhou, Phys. Rev. Lett. **107**, 035502 (2011).

[41] A. Brinkman, M. Huijben, M. van Zalk, J. Huijben, U. Zeitler, J. C. Maan, W. G. van der Wiel, G. Rijnders, D. H. A. Blank, and H. Hilgenkamp, Nature Mater. **6**, 493 (2007).

[42] A. D. Caviglia, M. Gabay, S. Gariglio, N. Reyren, C. Cancellieri, and J. M. Triscone, Phys. Rev. Lett. **104**, 126803 (2010).

[43] Y. A. Bychkov, and E. I. Rashba, J. Phys. C: Solid State Phys. **17**, 6039 (1984).

[44] J. A. Bert, B. Kalisky, C. Bell, M. Kim, Y. Hikita, H. Y. Hwang, and K. A. Moler, Nature Phys. **7**, 767 (2011).

[45] L. Rimai, and G. A. deMars, Phys. Rev. **127**, 702 (1962).

[46] K. A. Muller, Phys. Rev. B **19**, 3593 (1979).

[47] K. A. Muller, W. Berlinger, and J. C. Slonczewski, Phys. Rev. Lett. **25**, 734 (1970).

[48] H. Uwe, and T. Sakudo, Phys. Rev. B **13**, 271 (1976).

[49] W. J. Burke, and R. J. Pressley, Solid State Commun. **9**, 191 (1971).

[50] P. Ngabonziza, R. Heimbuch, N. de Jong, R. A. Klaassen, M. P. Stehno, M. Snelder, A. Solmaz, S. V. Ramankutty, E. Frantzeskakis, E. van Heumen, G. Koster, M. S. Golden, H. J. W. Zandvliet, and A. Brinkman, Phys. Rev. B **92**, 035405 (2015).

[51] C. X. Quintela, N. Campbell, D. F. Shao, J. Irwin, D. T. Harris, L. Xie, T. J. Anderson, N. Reiser, X. Q. Pan, E. Y. Tsymbal, M. S. Rzchowski, and C. B. Eom, APL Mater. **5**, 096103 (2017).

[52] Y. Nakazawa, M. Uchida, S. Nishihaya, M. Kriener, Y. Kozuka, Y. Taguchi, and M. Kawasaki, Sci. Rep. **8**, 2244 (2018).

[53] P. Ngabonziza, M. P. Stehno, H. Myoren, V. A. Neumann, G. Koster, and A. Brinkman, Adv. Electron. Mater. **2**, 1600157 (2016).

[54] K. S. Kim, and N. Winograd, Chem. Phys. Lett. **31**, 312 (1975).

[55] B. Mayer, S. Mähl, and M. Neumann, Z. Phys. B **101**, 85 (1996).

[56] B. Santara, P. K. Giri, K. Imakita, and M. Fujii, Nanoscale **5**, 5476 (2013).

[57] K. A. Bogle, M. N. Bachhav, M. S. Deo, N. Valanoor, and S. B. Ogale, Appl. Phys. Lett. **95**, 203502 (2009).

[58] J. Zhuang, S. Weng, W. Dai, P. Liu, and Q. Liu, J. Phys. Chem. C **116**, 25354 (2012).

[59] B. Bharti, S. Kumar, H.-N. Lee, and R. Kumar, Sci. Rep. **6**, 32355 (2016).

[60] J. Jun, J.-H. Shin, and M. Dhayal, Appl. Surf. Sci. **252**, 3871 (2006).

[61] Z. Q. Zheng, and X. P. Zhou, J. Am. Ceram. Soc. **96**, 3504 (2013).

[62] J.-L. Maurice, G. Herranz, C. Colliex, I. Devos, C. Carrétéro, A. Barthélémy, K. Bouzehouane, S. Fusil, D. Imhoff, É. Jacquet, F. Jomard, D. Ballutaud, and M. Basletic, Europhys. Lett. **82**, 17003 (2008).

[63] M. Sing, G. Berner, K. Goß, A. Müller, A. Ruff, A. Wetscherek, S. Thiel, J. Mannhart, S. A. Pauli, C. W. Schneider, P. R. Willmott, M. Gorgoi, F. Schäfers, and R. Claessen, Phys. Rev. Lett. **102**, 176805 (2009).

7. General Conclusion and Outlook

7.1 Summary of the Study

In this thesis, a combined study of the growth and characterization, and electronic transport and electronic band structure of epitaxial La-doped $BaSnO_3$ thin films was conducted. Thin films of La-doped $BaSnO_3$ have shown to have the potential for application in the vast industry of electronic and optoelectronic devices.

In the introductory chapter of this study, Chapter 1, the features that place La-doped $BaSnO_3$ material as a suitable candidate for transparent conducting oxide (TCO) technology were presented. In Chapter 2, a summary of recent research efforts dedicated to improving the electron mobility in epitaxial La-doped $BaSnO_3$ thin films was given. This chapter constitutes a literature review on the topic. The structural, physical and electrical characteristics of $BaSnO_3$ and La-doped $BaSnO_3$ materials were described in more detail. More precisely, their crystallographic structure, the different types of defects and scattering mechanisms that are found to influence the electron mobilities in both single crystal and epitaxial thin film forms, and the potential origins of these high mobilities were presented. In the case of epitaxially grown La-doped $BaSnO_3$ thin films, experimental evidence points to scattering at line dislocations as the principal source responsible for mobility reduction, since these lines act as scattering centers and diminish the density of free carriers.

For the contribution of the present study to this active field of research, the PLD technique was used to prepare epitaxial thin films of La-doped $BaSnO_3$ on various oxide single crystal substrates including $SrTiO_3$ (001), $DyScO_3$ (110), $TbScO_3$ (110), $GdScO_3$ (110) and MgO (001). All the preliminary steps preceding the film deposition as well as all the techniques that were adopted to characterize these films were described in the experimental section, Chapter 3. Therein, the preparation steps that are essential for the successful fabrication of high quality epitaxial films were presented. These steps include *ex situ* and *in situ* substrate preparation, as well as target cleaning. Also, comprehensive explanations of the working principles of both PLD and the characterization techniques were provided. These characterization methods are grouped into categories of techniques including diffraction (RHEED, LEED and XRD), microscopy (AFM and TEM), magnetotransport and spectroscopy (XPS and ARPES). Without going deeply into the theory, substantial elements necessary for the understanding of the physics behind each of these techniques was given. RHEED and AFM were used to analyze the surface properties of the grown films; XRD and TEM were employed to study their structural and microstructural properties, respectively; Hall effect measurements were adopted for the investigation of the electrical transport characteristics of these films; and XPS and ARPES were respectively used to analyze the elemental composition/chemical state of the near-surface and study the electronic band structure of the films.

As reported in Chapter 4, the growth was optimized to achieve the highest electronic mobility in the films. Firstly, the deposition pressure and temperature were optimized, and were found to be $\sim 1 \times 10^{-1}$ mbar and 850 °C, respectively. Secondly, the film and buffer layer thicknesses were optimized, with values of 25 and 100 nm, respectively. Finally, both the substrate employed for the growth and the La doping level were optimized. In a comparative study of the transport properties of unbuffered and $BaSnO_3$ buffered films, it was found that the best electrical properties are realized in films with 6% La-doping, prepared on $TbScO_3$ (110)

substrates with an insulating $BaSnO_3$ buffer layer (grown at 850 °C). In those samples, the room temperature electron mobility was as high as 117 ± 3 cm^2 V^{-1}s^{-1} with an associated carrier density value of $(5.95 \pm 0.08) \times 10^{20}$ cm^{-3}. This mobility value is found to be limited by a high density of line dislocations in the films. Together with stacking faults and Ruddlesden-Popper faults, these are the most prominent structural defects encountered in such films. In TEM images, the line dislocations were observed as vertical contrasts threading across the film layer from the interface to the surface, generated by the misfit dislocations that are created at the film/substrate interface due to the large lattice mismatch. The stacking faults were recognized as the much sharper contrasts both parallel and perpendicular to the film plane; and the Ruddlesden-Popper faults are identified by the polygonal shape of the contrasts.

To reduce the density of defects, in particular, the density of threading dislocations in the grown La-doped $BaSnO_3$ thin films and subsequently enhance the electron mobility, an insulating $SrZrO_3$ buffer layer grown at extremely high temperature was inserted between the active film layer and the $TbScO_3$ (110) substrate. This is a new approach developed as part of this project to enhance the electron mobility in TCO systems. The growth temperature of the $SrZrO_3$ buffer layer was optimized by preparing several La-$BaSnO_3$/$SrZrO_3$ heterostructures with $SrZrO_3$ grown at temperatures varying between 850 °C and 1600 °C. In the film prepared with the $SrZrO_3$ buffer layer grown at 1300 °C, the optimal electron mobility value of 140 ± 4 cm^2 V^{-1}s^{-1} at a carrier density of $(5.21 \pm 0.08) \times 10^{20}$ cm^{-3} was reached. This value constitutes the highest room temperature mobility value reported to date for as-grown La-doped $BaSnO_3$ thin films using the PLD technique. This is explained by the significant reduction of the threading dislocations, due to the high temperature growth of the $SrZrO_3$ buffer layer. In particular, quantitative analyses of the TEM data show a reduction of the dislocation defects by two orders of magnitude in $SrZrO_3$ buffered samples in comparison with the density of dislocation in $BaSnO_3$ buffered films.

Moreover, structural investigations show that $SrZrO_3$ buffered films are fully strained to the substrate in the plane direction whereas $BaSnO_3$ buffered films are relaxed. This strained relationship with the substrate results in a considerable reduction of the lattice mismatch, and therefore, in the diminution of the misfit dislocations originating at the interface, yielding the low density of structural defects observed in these films. Furthermore, it was also observed that all the films prepared as part of this thesis (unbuffered films, and $BaSnO_3$ and $SrZrO_3$ buffered films) grew epitaxially on all the substrates named above, and exhibited a high degree of crystallinity. These films are stoichiometric, as evidenced by the EELS measurements. The analysis of the surface growth dynamics, the surface morphology and the surface structure of all these samples showed that the surfaces are flat, smooth, and possess ordered structures. These surface and structural characteristics are comparable to those of the successful TCO indium tin oxide, and thus make these films suitable for applications in electronic devices.

The results of both the analysis of the chemical composition of the surface region and the study of the electronic band structure of the grown samples are presented in Chapter 5 of this thesis. With the help of combined XPS and angle-dependent XPS studies, the origins of the components constituting the primary core levels Sn 3d, O 1s and Ba 3d in La-doped $BaSnO_3$ films were thoroughly examined through systematic fits. It was also determined that the ratio of these components varies with the treatment of the surfaces. The Sn 3d core spectra exhibit an asymmetry to the high binding energy side of the peak. This asymmetry consistently increases with the amount of conduction band filling, i.e., with the concentration of the free carriers. On the other hand, O 1s and Ba 3d core lines do not show a pronounced asymmetry variation

with increasing doping level, but were found to slightly broaden. Moreover, Sn 3d, O 1s and Ba 3d spectra shift toward high binding energies as the carrier density increases. These shifts were also detected in the valence band regions with increasing carrier density. The valence band spectra allowed the detection of the occupied states in the conduction bands. Furthermore, it was determined that surface contamination could potentially induce surface carrier accumulation. This is supported by the increase in the intensity of the conduction band minimum that was detected in the valence band spectrum of a surface intentionally exposed to contamination in the load lock. The electronic structure of both the valence and conduction bands was not fully studied. This was due to several challenges including the preparation of the surfaces for spectroscopic experiments and instrument breakages. However, a few valence bands in a region far from E_F are resolved. These bands were subsequently fitted with energy distribution curves (EDCs) and momentum distribution curves (MDCs).

7.2 Future Projects

For all the work carried out in this thesis, the optimized highest electron mobility in the epitaxial La-doped $BaSnO_3$ thin films is realized for films prepared on $TbScO_3$ (110) substrates with a $SrZrO_3$ buffer layer grown at 1300 °C.

Future experiments would consist of exploring the growth of La-doped $BaSnO_3$ thin films with an extremely high temperature grown $SrZrO_3$ buffer layer also on $SrTiO_3$ (001), $DyScO_3$ (110), $GdScO_3$ (110) and MgO (001) single crystal substrates, using the optimized growth parameters. In a bid to increase the electron mobility in these films, a combined PLD and MBE growth could also be conducted. This is because MBE is known to produce La-doped $BaSnO_3$ thin films with better mobility compared to PLD. Since extremely high substrate temperatures cannot be used in MBE, the $SrZrO_3$ buffer layer would thus be grown at a very high temperature using PLD, and the active film layer would be subsequently deposited by MBE. Thin film transistor devices could then be fabricated based on these high mobility samples. Furthermore, more ARPES measurements on these samples (at room and low temperatures) would be also needed in order to resolve the valence and conduction bands, and provide a complete ARPES description of the electronic band structure of La-doped $BaSnO_3$.

The direction toward another project related to the fabrication of the heterostructure formed by thermally evaporating Al on $SrTiO_3$ substrates is given in Chapter 6. Therein, the technological importance of such heterostructures is described and comprehensive background knowledge on the topic is provided. The XPS data of the Sr 3p, Ti 2p and O 1s core electrons and the valence band regions of the surfaces of both pristine and heat-treated $SrTiO_3$ (100) substrates are discussed. These results open up the path to mastering the preparation of the surface of the substrates prior to subsequent Al layer deposition. Although some preliminary results were presented, there still exists scope for in-depth studies such as probing the $Al/SrTiO_3$ heterointerface using ARPES, as well as conducting a systematic electronic transport characterization of the interface.

Acknowledgements

A PhD study is a serious commitment engaging all the components of a life. I would not have made it through without the support and love of so many people. All of them contributed separately, but their efforts together accompanied me in this lifetime journey. I would like to take this opportunity to thankfully convey my respect and recognition to all these wonderful people. I might not be able to name each one of them, but I acknowledge them in the lines below.

I would like to say thank you to my supervisor Prof. Bryan Doyle, as well as Prof. Emanuela Carleschi for welcoming me in their research unit as a PhD student. Thank you for trusting me with your new acquired ARPES equipment and for the training you provided to shape me as a serious scientist. I would like to thank my co-supervisors Prof. Aletta R.E. Prinsloo for her sharp guidance and her experience that were extremely helpful and crucial in shaping this thesis; and Dr Prosper Ngabonziza for his expertise in this research field. I particularly thank you Prosper. You have been a pillar in this project. You introduced me to almost all the tools and techniques that I used to complete this project. Being close to you, I learned a lot as a young scientist and researcher. Thank you for giving me the opportunity to spend time close to you and also to spare some of your time to train and work with me.

I am particularly grateful to Prof. Dr. Jochen Mannhart for agreeing to the collaboration and giving me this unique opportunity in a lifetime to carry out research activities in his outstanding facilities at the Max-Planck Institute for Solid State Research in Stuttgart. Prof, you welcomed me in your Department and supported my stay in Germany for almost a year. You allowed me to use your state-of-the-art equipment and gather all the data that I needed to realize this project. I am deeply grateful for all your support Prof.

For the financial support, I would like to acknowledge the support from the South African National Research Foundation, the African Institute for Mathematical Sciences, the University of Johannesburg and the Max-Planck Institute for Solid State Research in Stuttgart. This PhD project would not have been possible without these supports.

I would like to address my deepest thanks to Dr Helga Hoier, Dr Wilfried Sigle and Dr Marion Hagel for their technical assistance respectively in X-ray diffraction and transmission electron microscopy measurements, and samples wire bonding. Also, thank you to Dr Kathrin Küster and the Interface Analysis Service Group at the Max-Planck Institute in Stuttgart for the additional spectroscopic measurements. I would like to thank Prof. Darrell G. Schlom and Dr Hans Boschker for the valuable discussions which were really determinant in understanding some key concepts of the project.

I would like to express my sincere gratitude to Dr Susan Jacobs for making time to proofread this document, to Mrs Renate Zimmermann and Mrs Birgit King for organizing all the necessary paper work for my coming to Germany and also for the work at the Max-Planck Institute for Solid State Research in Stuttgart.

Thank you to my friends and colleagues both at the University and Johannesburg and at the Max-Planck Institute in Stuttgart. Wonderful people! You made the working environment healthy and provided the support needed in difficult situations both in the lab and outside the working environment.

I would like to express my deepest gratitude to my family. Their supports have been priceless during this journey and specially during the tough times. A special thanks to my wife, Mrs Javeline Aurelie Enonguene Simapi, who has accepted to sacrifice 4 years of her life which she spent without me. I know my love that this was even tougher on you than it was on me. I know the future will reward you above what you lost. Thank you darling for giving me Abimael Jesse Nono, our little boy, who brought so much light in my life and gave me the strength to continue working on my project. Thank you to my parents and siblings for always encouraging me and believing in me.

Appendix A. Additional Surface Properties

A.1 La-Doped $BaSnO_3$ Growth on MgO (001) and $GdScO_3$ (110) Substrates

In addition to the samples discussed in Chapter 4, epitaxial thin films of La-doped $BaSnO_3$ on MgO (001) (Figs. A.1(a)-(c)) and $GdScO_3$ (110) (Fig. A.1(d)) substrates have also been fabricated. Their growth characteristics are presented in Figs. A.1 and A.2. Figures A.1(a) and A.1(b) are the RHEED images for 4% La-doped $BaSnO_3$ thin films of 50 nm directly deposited on the substrate and 100 nm thick grown with a 25 nm $BaSnO_3$ buffer layer, respectively. These were prepared (films and buffer layer) at the temperature of 850 °C, at 1 pulse per second and 1.5 J cm^{-2}, in 1.33×10^{-2} mbar of O_2. Figure A.1(c) represents the RHEED image of a 6% La-doped $BaSnO_3$ thin film prepared with a 100 nm $BaZrO_3$ buffer layer, which was deposited at 900 °C in 1.35×10^{-2} mbar of O_2 at the laser rate of 4 Hz and energy density of 2 J cm^{-2}. The 25 nm top layer was grown at 850 °C, 1 Hz and 1.5 J cm^{-2}, in 1.07×10^{-1} mbar of O_2. Figure A.1(d) is the RHEED image of a 2% La-doped $BaSnO_3$ thin film prepared without a buffer layer at 850 °C, 1 Hz and 1.5 J cm^{-2} in 1.05×10^{-1} mbar of O_2 pressure. A summary of the growth parameters for all these films is given in Table A.1. Considering Fig. A.1, it can be observed that the film surfaces are flat and single crystalline, indicated by the sharp diffraction spots in all the images.

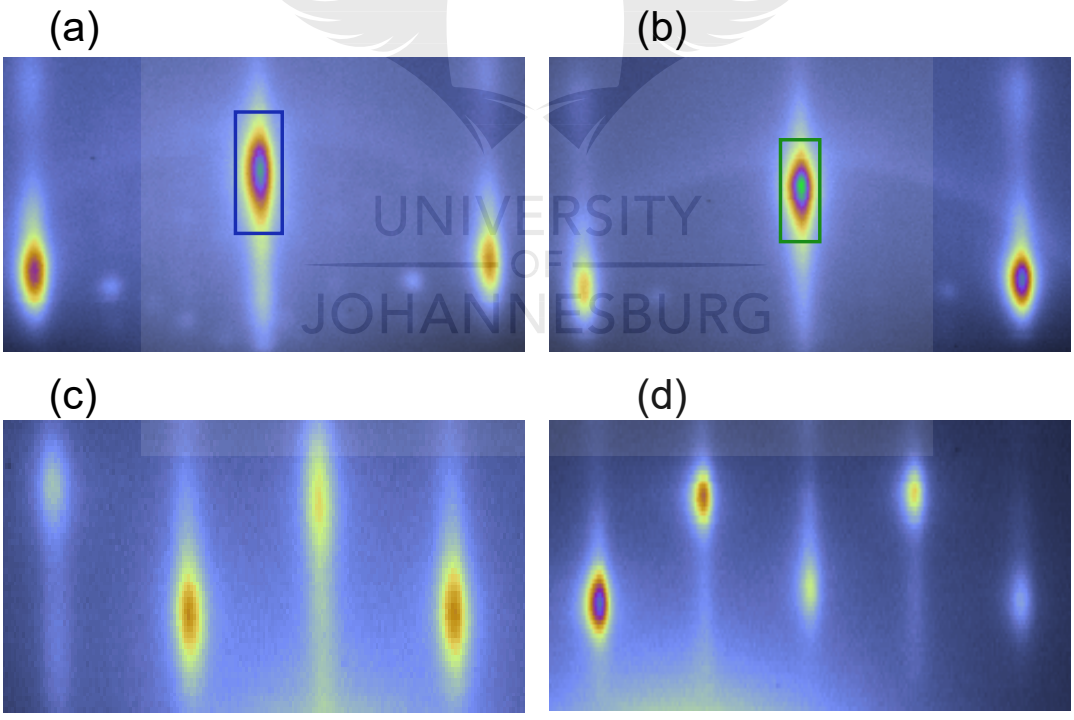

Figure A.1: RHEED patterns viewed along the [110] azimuth for films grown at 850 °C on (a)-(c) MgO (001), and (d) $GdScO_3$ (110). 4% La-doped $BaSnO_3$ thin films grown (a) without buffer layer and (b) with $BaSnO_3$ buffer layer. (c) 6% La-doped $BaSnO_3$ thin film prepared with $BaZrO_3$ buffer layer. (d) 2% La-doped $BaSnO_3$ thin film grown without buffer layer. The rectangles represent the regions over which the integrated intensity shown on the following page are measured.

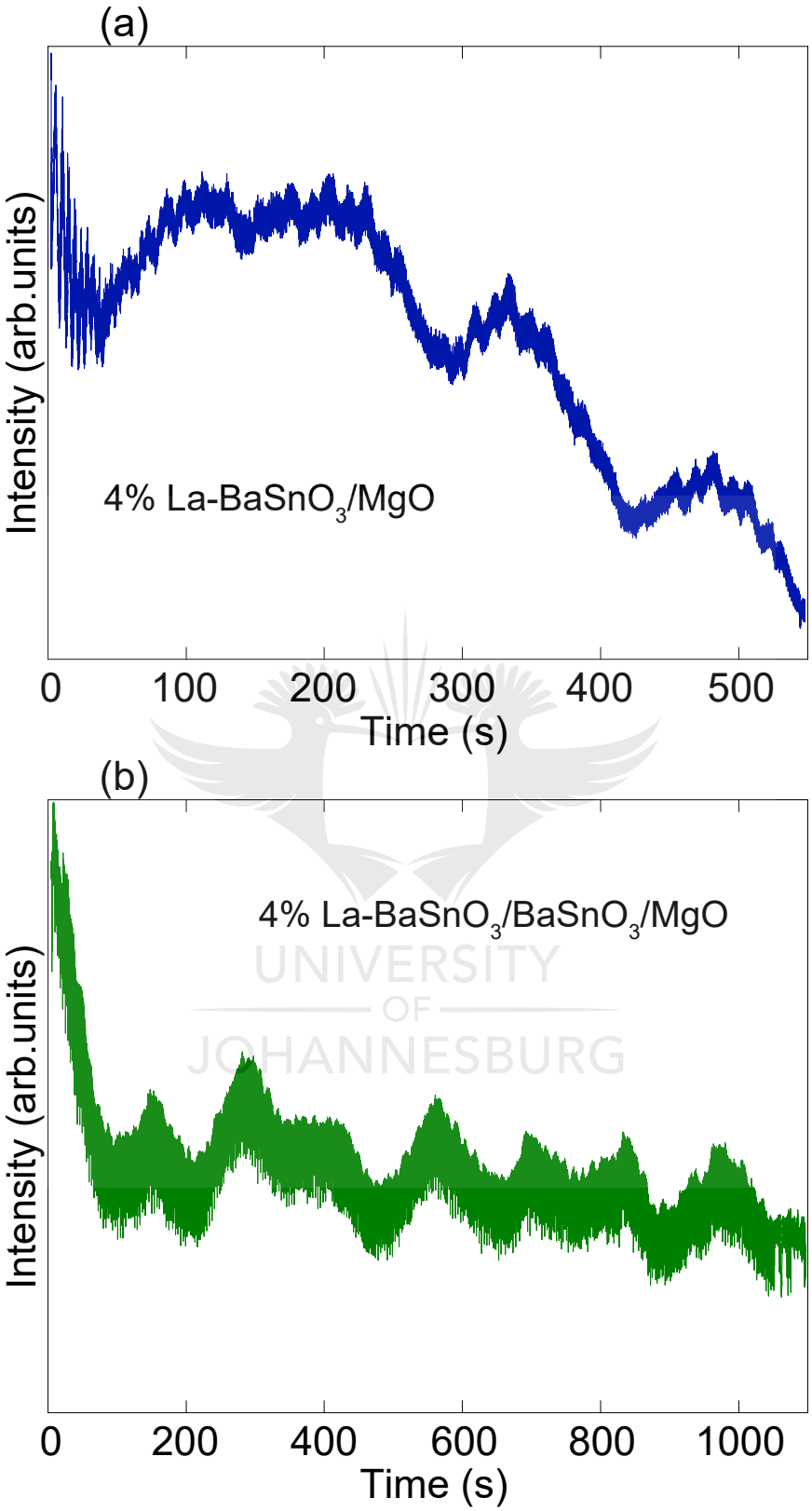

Figure A.2: Time dependent RHEED intensity oscillations for 4% La-doped $BaSnO_3$ thin films prepared on MgO (001), (a) without a buffer layer and (b) with $BaSnO_3$ buffer layer. The curves are extracted from the areas indicated in Fig. A.1(a) and A.1(b), respectively.

Table A.1: Growth parameters for La-doped $BaSnO_3$ thin films presented in Fig. A.1, prepared on MgO (001) and $GdScO_3$ (110) without and with $BaSnO_3$ buffer layer.

	Samples from Fig. A.1	Substrate temperature (°C)	O_2 partial pressure (mbar)	Laser fluence (J cm^{-2})	Laser repetition rate (Hz)	Thickness (nm)
(a)	4% La-$BaSnO_3$	850	1.33×10^{-2}	1.5	1	50
(b)	$BaSnO_3$ layer	850	1.33×10^{-2}	1.5	1	25
	4% La-$BaSnO_3$ layer	850	1.33×10^{-2}	1.5	1	100
(c)	$BaZrO_3$ layer	900	1.35×10^{-2}	2	4	100
	6% La-$BaSnO_3$ layer	850	1.07×10^{-1}	1.5	1	25
(d)	2% La-$BaSnO_3$	850	1.05×10^{-1}	1.5	1	25

The RHEED intensity oscillations in Fig. A.2 also suggest smooth and epitaxial growth [1, 2]. Although the intensity in Fig. A.2(a) is not constant, oscillations are seen from the very beginning of the growth till the end, with drops in the intensity. This irregularity in the intensity of the oscillations could probably be due to the crystallographic differences of the two materials (perovskite La-$BaSnO_3$ and non-perovskite MgO). It could also be created by the interaction of the electron beam with the film being deposited and the substrate [2]. On the other hand, after inserting a $BaSnO_3$ buffer layer between the film layer and the substrate, regular oscillations are obtained (see Fig. A.2(b)). This last observation tends to confirm the latter hypothesis that the irregularity of the RHEED intensity oscillations are created by the interaction of the electron beam with the MgO (001) substrate and the growing La-$BaSnO_3$ film.

A.2 RHEED Images for the Samples Used to Optimize the Pressure and the Temperature

Table A.2: Growth parameters of the 4% La-doped $BaSnO_3$ thin films that were used to optimize the oxygen background pressure and the temperature of the substrates on $SrTiO_3$ (001) substrates. These samples were discussed in Section 4.2.1 of the main text.

	Samples from Fig. 4.1	Substrate temperature (°C)	O_2 partial pressure (mbar)	Laser fluence (J cm^{-2})	Laser repetition rate (Hz)	Thickness (nm)
(a)	4% La-$BaSnO_3$	850	1.33×10^{-3}	1.5	1	25
(b)	4% La-$BaSnO_3$	850	1.33×10^{-1}	1.5	1	25
(c)	4% La-$BaSnO_3$	750	1.08×10^{-1}	1.5	1	25
(d)	$BaSnO_3$ layer	750	1.1×10^{-1}	1.5	1	25
	4% La-$BaSnO_3$ layer	750	1.1×10^{-1}	1.5	1	100
(e)	$BaSnO_3$ layer	850	1.1×10^{-1}	1.5	1	50
	4% La-$BaSnO_3$ layer	850	1.1×10^{-1}	1.5	1	100
(f)	$BaSnO_3$ layer	950	1.1×10^{-1}	1.5	1	25
	4% La-$BaSnO_3$ layer	950	1.1×10^{-1}	1.5	1	100

As mentioned in the main text in Section 4.2.1, the RHEED image of the sample that was used

to optimize the pressure and grown at the temperature of 850 °C in the oxygen background pressure of 1.33×10^{-2} mbar is shown in Fig. A.3(a); that of the sample used to optimize the substrate temperature and grown at the optimized pressure of 1.33×10^{-1} mbar at the temperature of 950 °C is shown in Fig. A.3(b). The surfaces of these films are flat and smooth, judging from the diffraction spots. However, the surface in Fig. A.3(a) might contain small out-of-phase domains since the diffraction patterns are elongated (streaks). This is perhaps not surprising since it was grown at a non-optimal pressure. Table A.2 summarizes the growth parameters of all the samples employed to optimized both the substrate temperature and the deposition pressure.

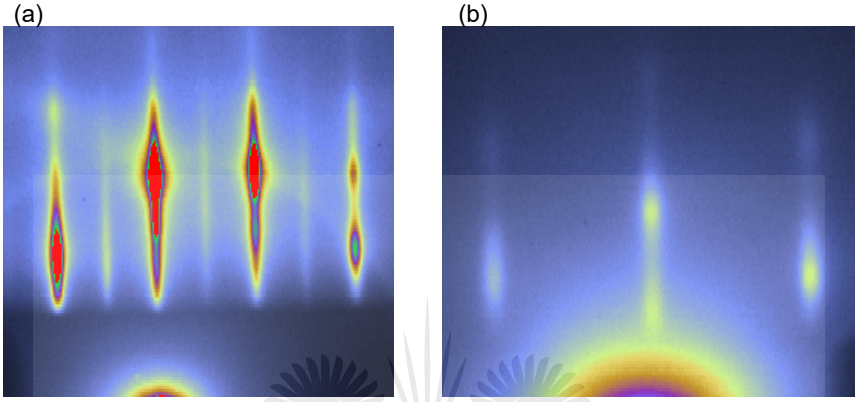

Figure A.3: (a) and (b) RHEED images for 4% La-$BaSnO_3$(25 nm)/$SrTiO_3$ samples used for the optimization of (a) the pressure and (b) the substrates temperature. The sample in (a) was deposited at 850 °C, at the pressure of 1.33×10^{-2} mbar. The sample in (b) was grown at the optimized pressure of 1.33×10^{-1} mbar at the temperature of 950 °C.

A.3 RHEED Image of the 1000 nm La-$BaSnO_3$ Thin Film

As mentioned in Section 4.2.2 of the main text, the RHEED image of the 6% La-doped $BaSnO_3$ (1000 nm thick) thin film grown with a 100 nm $BaSnO_3$ buffer layer on $TbScO_3$ (110) substrate is presented in Fig. A.4. The surface of this sample is flat, smooth and single crystalline, as indicated by the sharp diffraction spots.

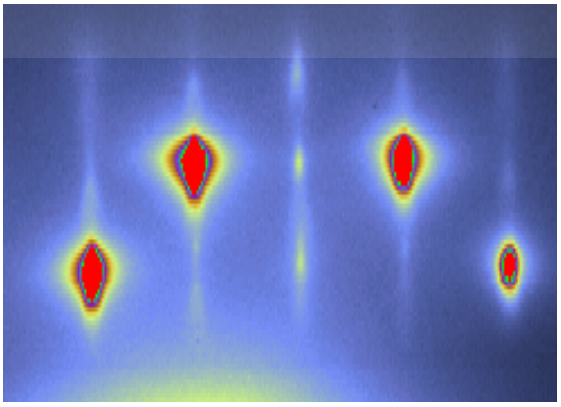

Figure A.4: RHEED image of a 6% La-$BaSnO_3$ (1000 nm)/$BaSnO_3$ (100 nm)/$TbScO_3$ film. This sample was grown for the optimization of the film thickness.

A.4 Surface Properties of Optimized Unbuffered and $BaSnO_3$ Buffered Samples

The surface properties of some of the samples discussed in Section 4.2.3 of the main text are presented in Figs. A.5, A.6, A.7 and A.8. These data are provided here in addition to the RHEED and AFM data of the optimized samples discussed in Section 4.2.2. For each sample, the RHEED image is shown on top and the AFM image at the bottom. On the bottom-right, the extracted height profile is shown, together with the roughness profile (lower panel). The profiles are measured along the green solid lines drawn on the AFM image. The samples in Fig. A.5 are 2% La-$BaSnO_3$ (25 nm)/$SrTiO_3$ (Fig. A.5(a)), 6% La-$BaSnO_3$ (25 nm)/$SrTiO_3$ (Fig. A.5(b)) and 6% La-$BaSnO_3$ (25 nm)/$BaSnO_3$ (100 nm)/$SrTiO_3$ (Fig. A.5(c)). The films in Fig. A.6 are 2% (Fig. A.6(a)) and 6% (Fig. A.6(b)) La-$BaSnO_3$ (25 nm)/$DyScO_3$. It should be mentioned that the data for the 2% La-doped buffered sample grown on $SrTiO_3$ (001) and $DyScO_3$ (110) are not available and these are not shown. The samples displayed in Fig. A.7 are 2% La-$BaSnO_3$ (25 nm)/$TbScO_3$ (Fig. A.7(a)) and 2% La-$BaSnO_3$ (25 nm)/$BaSnO_3$ (100 nm)/$TbScO_3$ (Fig. A.7(b)). These samples have flat, smooth and single crystalline surfaces, as indicated by their RHEED diffraction spots [3, 4], and the values of their surface roughness parameters are summarized in Tables A.3, A.4 and A.5, respectively.

Table A.3: Surface roughness parameters from height profiles of La-doped $BaSnO_3$ samples prepared on $SrTiO_3$ (001). These parameters are extracted from Fig. A.5. The values in the table are given with a precision of the order of $\pm 10^{-3}$ nm.

Samples from Fig. A.5	Scan area (μm^2)	Average roughness R_a (nm)	Root mean square roughness R_q (nm)	Maximum roughness peak height R_p (nm)	Step height (Å)
(a)	3×3	0.013	0.017	0.056	—
(b)	5×5	0.033	0.041	0.127	—
(c)	10×10	0.082	0.097	0.249	4

Table A.4: Surface roughness parameters from height profiles of La-doped $BaSnO_3$ samples prepared on $DyScO_3$ (110). These parameters are extracted from Fig. A.6. The values in the table are given with a precision of the order of $\pm 10^{-3}$ nm.

Samples from Fig. A.6	Scan area (μm^2)	Average roughness R_a (nm)	Root mean square roughness R_q (nm)	Maximum roughness peak height R_p (nm)	Step height (Å)
(a)	6.8×6.8	0.033	0.042	0.122	3.9
(b)	9.2×9.2	0.025	0.032	0.096	3.6

From the areas marked with rectangles in Figs. A.5(c) and A.7(a), the RHEED intensity oscillations as a function of time were extracted as shown in Figs. A.8(a) and A.8(c), respectively. These are typical RHEED intensity oscillations [1, 2], although it was not always possible to record intensity oscillations over the entire deposition window as those observed in Figs. A.8(a) and A.8(b). The RHEED intensity oscillations for most samples resembled those presented in Fig. A.8(c). The intensity oscillations presented in Fig. A.8(a) were recorded during the growth of the $BaSnO_3$ layer (buffer layer) on $SrTiO_3$ (001). A drop in intensity is observed the moment the attenuator opens. Then, after several monolayers, the intensity increases and the

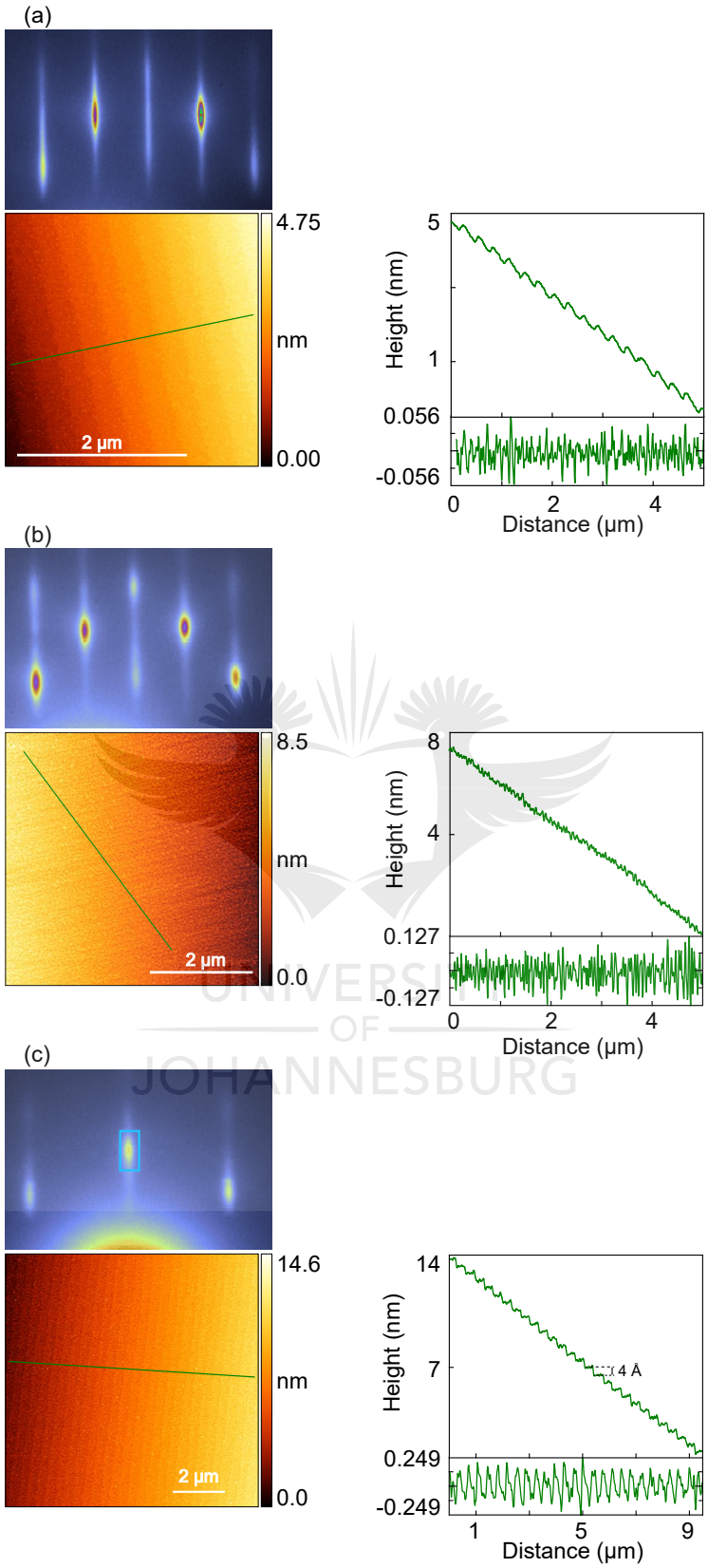

Figure A.5: RHEED and AFM images for 2% and 6% La-doped films prepared on $SrTiO_3$ (001) substrates. The height and surface roughness profiles extracted along the green solid lines are given on the right hand side of the images. The samples are (a) 2% La-$BaSnO_3$ (25 nm)/$SrTiO_3$, (b) 6% La-$BaSnO_3$ (25 nm)/$SrTiO_3$ and (c) 6% La-$BaSnO_3$ (25 nm)/$BaSnO_3$ (100 nm)/$SrTiO_3$.

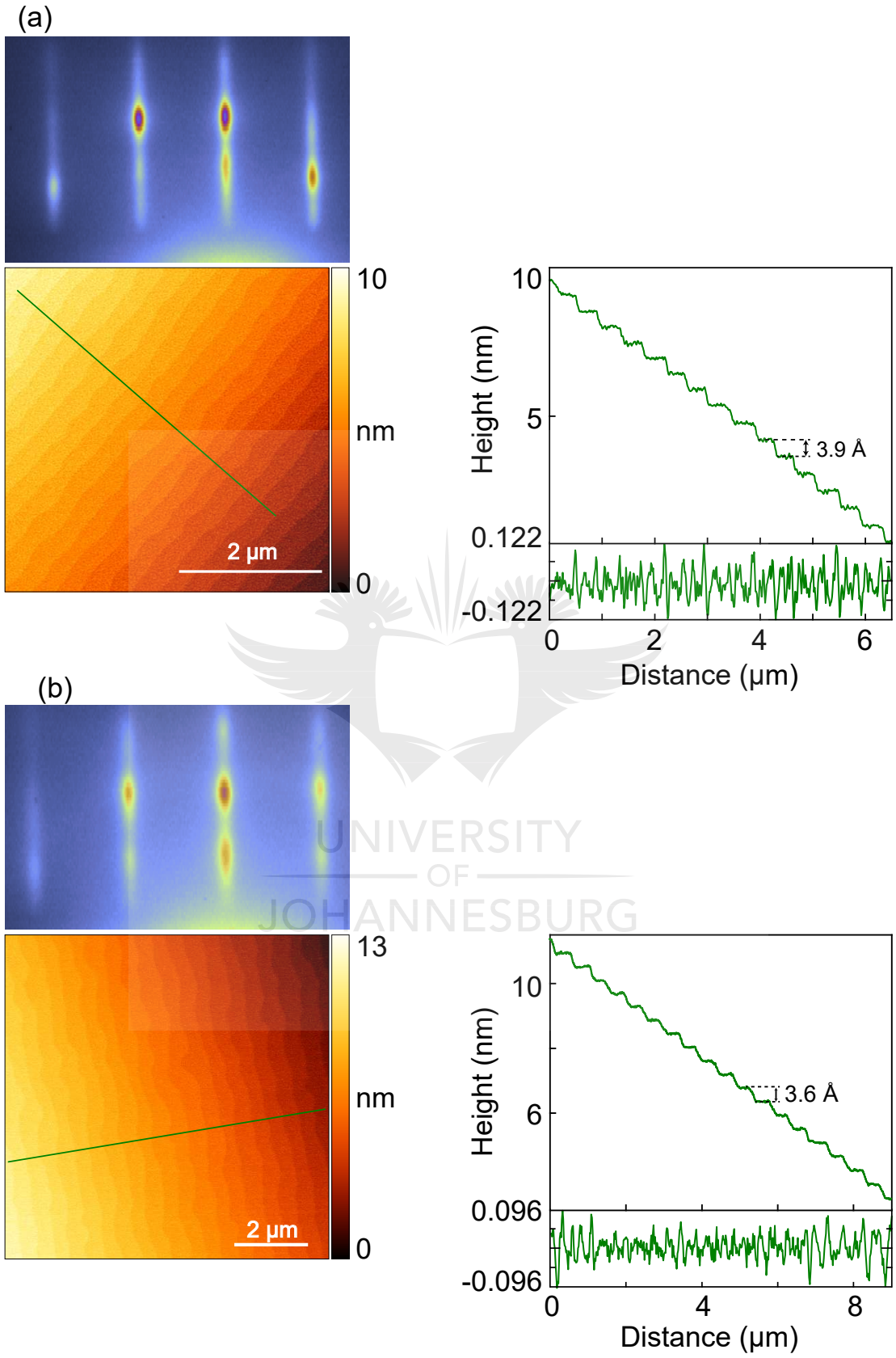

Figure A.6: RHEED and AFM images for (a) 2% and (b) 6% La-$BaSnO_3$ (25 nm)/$DyScO_3$ samples. The height and surface roughness profiles extracted along the green solid lines across the AFM images are given on the right hand side of the images.

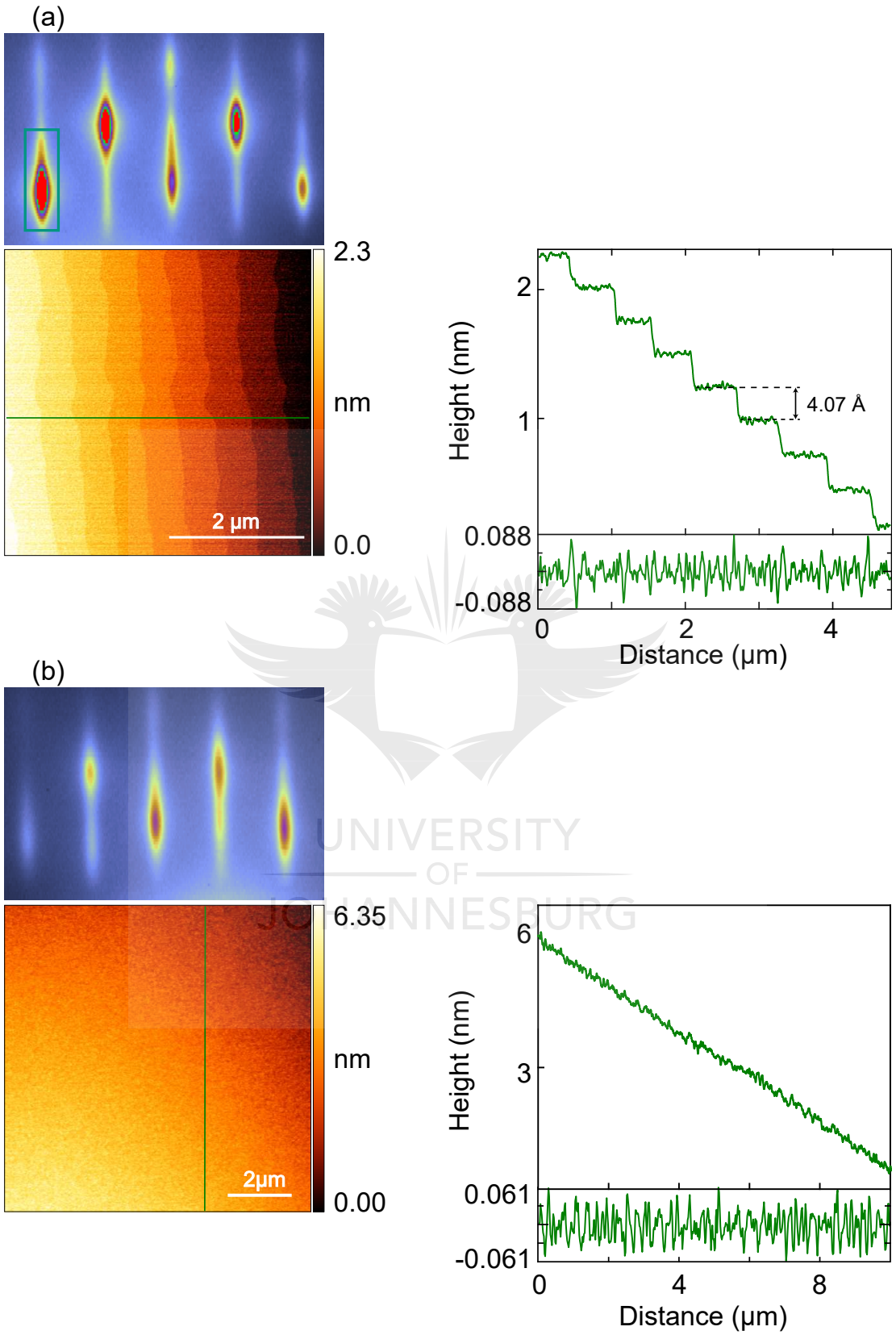

Figure A.7: RHEED and AFM images for (a) 2% La-$BaSnO_3$ (25 nm)/$TbScO_3$ and (b) 2% La-$BaSnO_3$ (25 nm)/$BaSnO_3$ (100 nm)/$TbScO_3$ samples. The height and surface roughness profiles extracted along the green solid lines across the AFM images are given on the right hand side of the images.

Table A.5: Surface roughness parameters from height profiles of La-doped $BaSnO_3$ samples prepared on $TbScO_3$ (110). These parameters are extracted from Fig. A.7. The values in the table are given with a precision of the order of $\pm 10^{-3}$ nm.

Samples from Fig. A.7	Scan area (μm^2)	Average roughness R_a (nm)	Root mean square roughness R_q (nm)	Maximum roughness peak height R_p (nm)	Step height (Å)
(a)	5×5	0.020	0.025	0.088	4.07
(b)	10×10	0.018	0.022	0.061	—

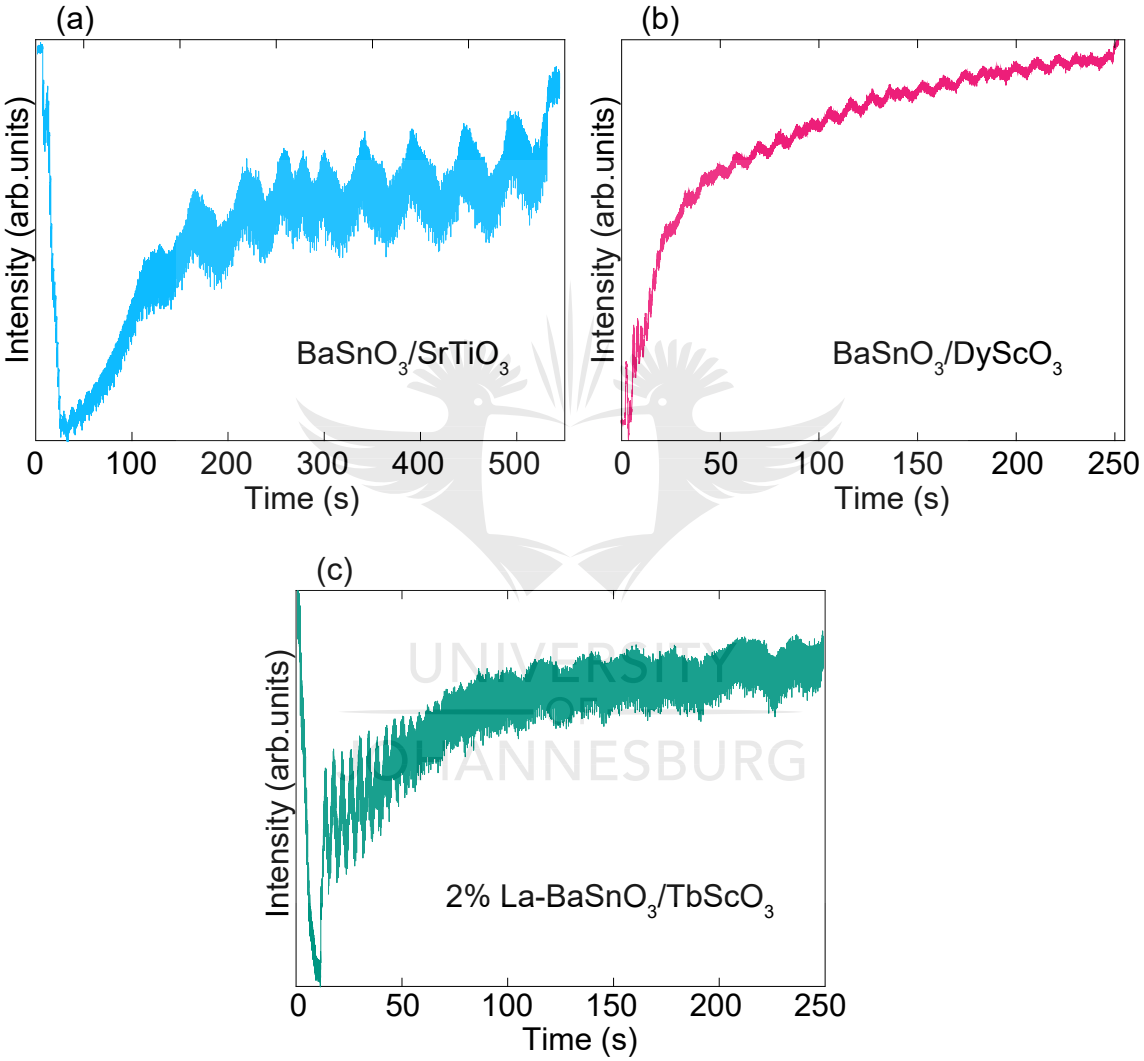

Figure A.8: RHEED intensity oscillations as a function of time. (a) Deposition of a layer of $BaSnO_3$ film on $SrTiO_3$ (001). The intensity oscillations were recorded during the growth of the $BaSnO_3$ buffer layer from the area indicated with a rectangle in Fig. A.5(c). (b) RHEED intensity oscillations for the deposition of a $BaSnO_3$ buffer layer on $DyScO_3$ (110). (c) RHEED intensity oscillations recorded from the area marked with a rectangle in Fig. A.7(a) during the growth of a 2% La-doped $BaSnO_3$ thin film directly on $TbScO_3$ (110). The films in (a), (b) and (c) are grown in a layer-by-layer mode, whereas that in (c) follows a layer-by-layer growth mode at the beginning, but transits to step-flow mode during the deposition.

oscillations become regular till the end of the growth, with a constant amplitude. The intensity drop at the beginning of the growth was also reported for undoped $BaSnO_3$, grown by MBE on $DyScO_3$ (001), followed by oscillations amplitude decay towards the end of the growth [1]. Considering Fig. A.8(a), from the moment the intensity oscillations become regular, 9 oscillations, corresponding to the deposition of 9 unit cells of $BaSnO_3$, can be counted. On the other hand, the deposition of about 25 unit cells of $BaSnO_3$ on $DyScO_3$ (110) can be evaluated in Fig. A.8(b). These are the RHEED intensity oscillations corresponding to the growth of a $BaSnO_3$ buffer layer on $DyScO_3$ (110). The oscillations are barely visible at the beginning of the deposition, but after few monolayers, more regular oscillations of identical amplitude are seen till the end of the growth. These clear intensity oscillations indicate a two-dimensional (2D) layer-by-layer deposition mode, and an epitaxial growth of these buffer layers [5].

Figure A.8(c) represents the RHEED intensity oscillations for a La-doped $BaSnO_3$ thin film directly grown on $TbScO_3$ (110). As can be observed, clear and regular oscillations are visible at the beginning of the growth, after the drop and the stabilization of the intensity. However, the width of the intensity oscillations starts to increase at a certain time during the growth, rendering the appreciation of the features difficult. This could be explained by observing the corresponding diffraction pattern which is relatively broad and slightly elongated (see Fig. A.7(a)). Thus, it can be pointed out that there exist two regions. A first region where clear and regular oscillations are visible, and a second region that looks more like a steady state. This could be suggesting a growth mode transition from layer-by-layer (first region) to step-flow (second region), following relaxations introduced in the film due to lattice mismatch [1, 4]. Nonetheless, it should be noted that this hypothesis is not sufficient because this phenomenon was not observed for the films grown on $SrTiO_3$ (001) and $DyScO_3$ (110). As demonstrated in Section 4.4.3 of the main text, these substrates have larger lattice mismatches with La-doped $BaSnO_3$ compared to $TbScO_3$ (110).

Appendix B. Reciprocal Space Maps of the $SrZrO_3$ Buffered Films

In this section, the reciprocal space map data of the La-doped $BaSnO_3$ thin films prepared on $TbScO_3$ (110) substrates with $SrZrO_3$ buffer layers grown at various temperatures ranging from 850 °C to 1600 °C are shown. These data are shown here in addition to the data presented in the main text in Section 4.4.3. Figure B.1 shows the reciprocal space maps around the $(\bar{1}03)$ La-$BaSnO_3$ and $SrZrO_3$ reflection peaks, and the $(\bar{1}03)_p$ reflection peaks of $TbScO_3$. The $SrZrO_3$ buffer layer is grown at 850 °C (Fig. B.1(a)), 1200 °C (Fig. B.1(b)), 1400 °C

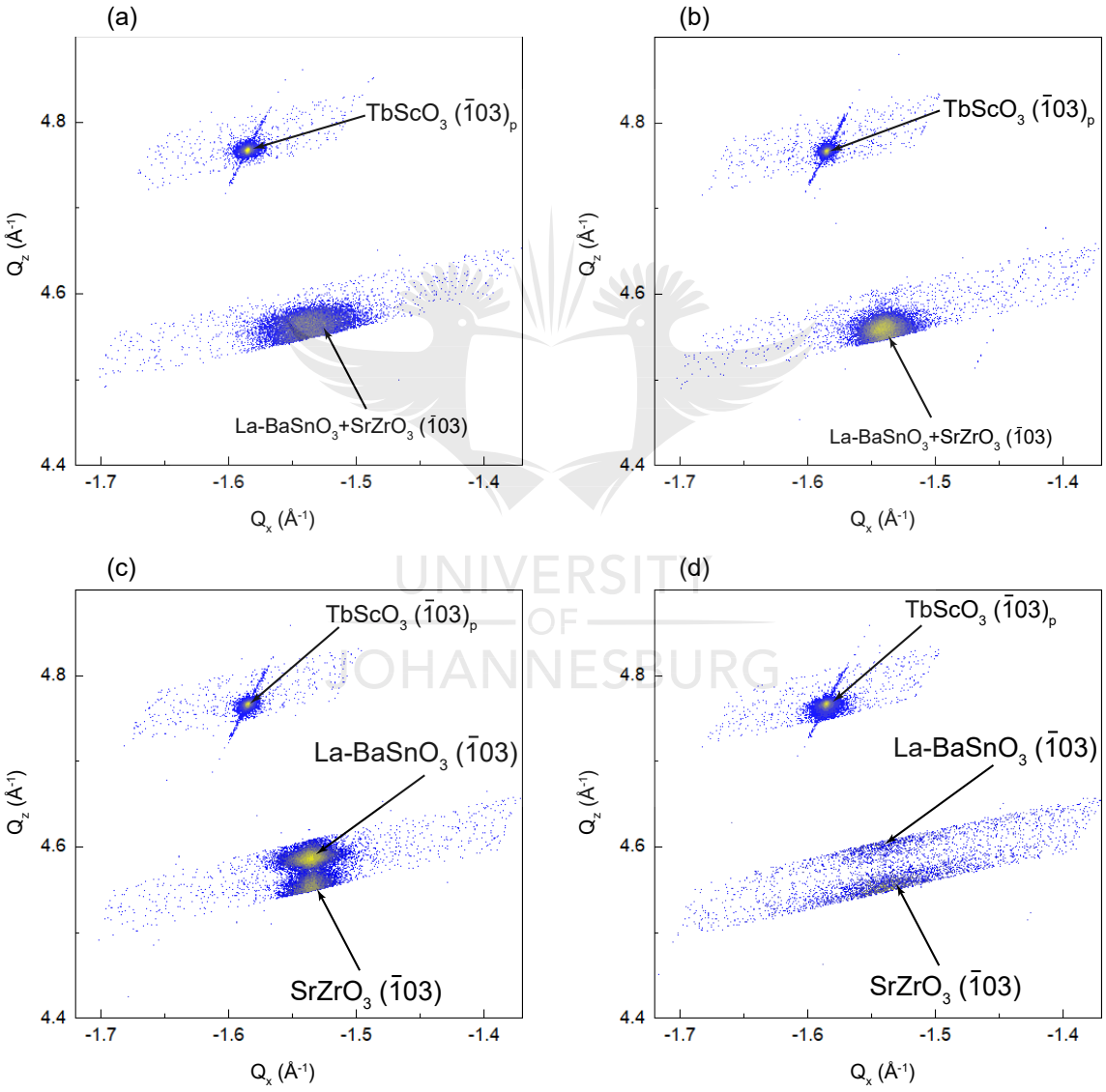

Figure B.1: Reciprocal space maps around the asymmetric $(\bar{1}03)$ La-$BaSnO_3$ and $SrZrO_3$ reflection peaks, and the $(\bar{1}03)_p$ reflection peaks of $TbScO_3$ for epitaxial La-doped $BaSnO_3$ thin films grown on $TbScO_3$ (110) substrates with $SrZrO_3$ buffer layers. The subscript p refers to pseudocubic indices. The $SrZrO_3$ buffer layers were grown at (a) 850 °C, (b) 1200 °C, (c) 1400 °C and (d) 1600 °C.

(Fig. B.1(c)) and 1600 °C (Fig. B.1(d)). The contour profiles of the ($\bar{1}03$) diffraction spots of the La-$BaSnO_3$ films along the Q_x axis are given in Fig. B.2, respectively for the maps in Figs. B.1(a), B.1(b) and B.1(c). The contour profile of the film with $SrZrO_3$ grown at 1600 °C could not be extracted since the ($\bar{1}03$) reflection of the film is incomplete (cut) as can be seen in Fig. B.1(d). The values of the lateral grain size D are estimated from the integral breadth of the contour profiles. As can be seen in Fig. B.2, the value of D increases with the growth temperature. This is consistent with the assumption that high temperature grown $SrZrO_3$ results in reduced grain boundary defects.

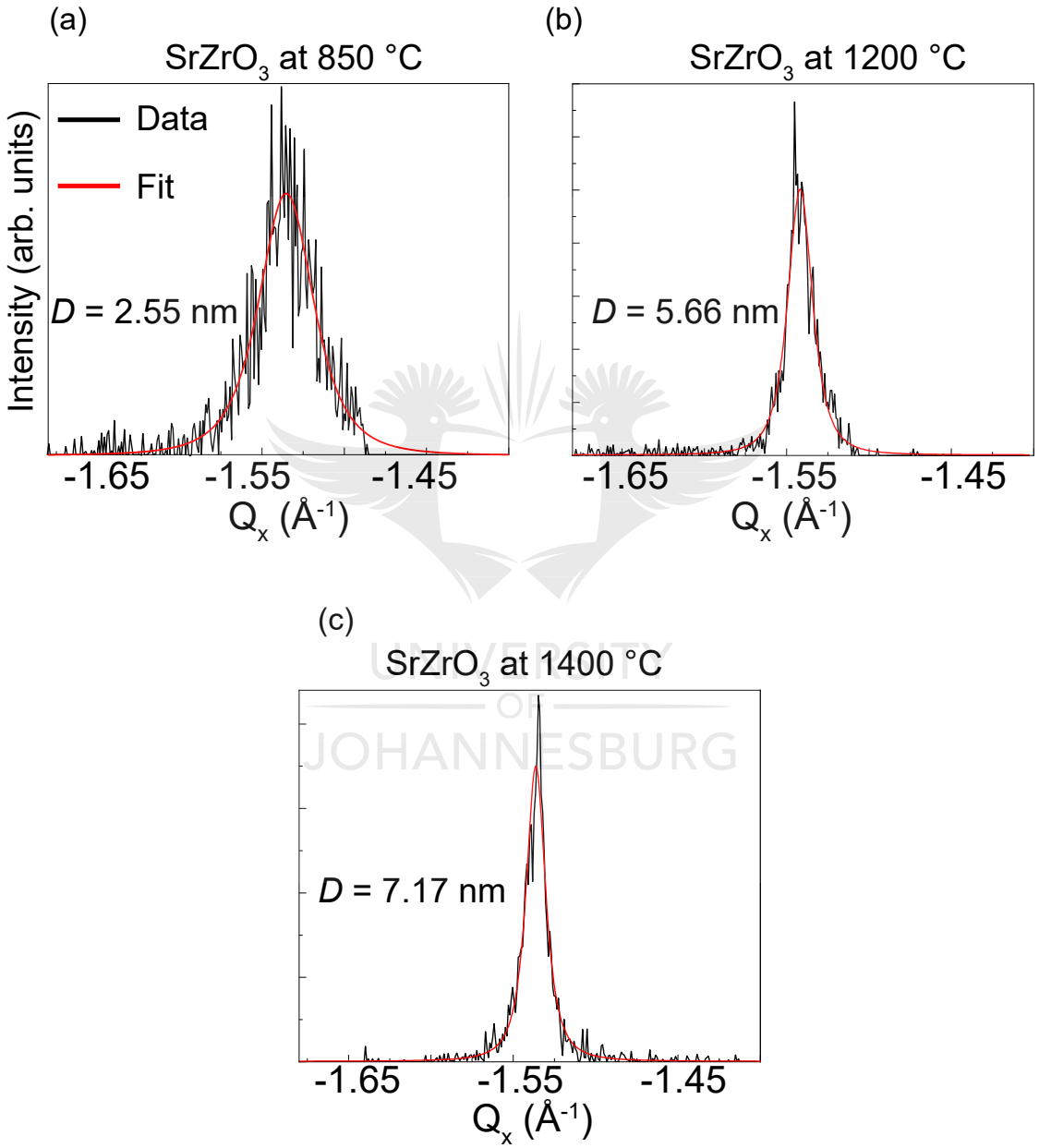

Figure B.2: Contour profiles of the ($\bar{1}03$) diffraction spots of the films along the Q_x axis. The profiles are extracted from the reciprocal space maps in Fig. B.1 for the films with $SrZrO_3$ grown at (a) 850 °C, (b) 1200 °C and (c) 1400 °C. The lateral grain sizes D, which are inversely proportional to the FWHM, were determined by fitting the profiles using Pearson VII peak function.

Appendix C. Additional Spectroscopic Data

C.1 Spectroscopic Data of the Higher Electron Mobility Sample Grown with $BaSnO_3$ Buffer Layer

This section presents the XPS and ARPES data of the 6% La-$BaSnO_3$ (25 nm)/$BaSnO_3$ (100 nm)/$TbScO_3$ sample with the mobility of 117 ± 3 cm^2 V^{-1} s^{-1} and the carrier density of $(5.95 \pm 0.08) \times 10^{20}$ discussed in Sections 4.2.2 to 4.4. This sample was annealed at temperatures up to about 1100°C in 7×10^{-7} mbar of O_2. Figures C.1, C.2 and C.3 show the angle-dependent XPS data of the Sn 3d, O 1s and Ba 3d core spectra, measured at take off angles of 35°, 45° and 90°. The fitted parameters are summarized in Tables C.1, C.2 and C.3. The data were acquired with an experimental resolution of 0.78 eV using the Al K_α excitation source. This surface was damaged as the ratio of the peaks vary inconsistently for all the core electrons, if compared with the data presented in Section 5.2.2 of the main text. Additionally, shifts of the peaks to higher binding energies by more than 1 eV in the spectra taken at 45° and 90° should be noted. These shifts are more pronounced in the Sn 3d and O 1s core levels. This could indicate charging effects, as the clamp used to hold and ground the sample might have not made good contact with the sample surface. It is important to mention that this sample was previously annealed in vacuum at 1000° for 30 minutes (at the Max Planck Institute). However, these do not explain why only the data recorded at 45° and 90° are shifted. Furthermore, it should be observed that the O 1s spectra (see Fig. C.2) are fitted with two components (see Table C.2), compared to three components used to fit the cleaned O 1s spectra in the main text as discussed in Chapter 5. The $-$OH component associated with residual water on the surface as reported in surfaces prepared at lower temperatures in the main text is completely removed from the surface. This is to be expected, as $-$OH groups desorb more easily at higher temperatures.

Figure C.4 shows the 2D ARPES maps of the valence band measured in various binding energy ranges at room temperature, with a photon energy of 21.2 eV along the $\bar{\Gamma}\bar{X}$ direction in momentum space. As can be seen, the bands are not resolved. This is attributed to damage from the high temperature annealing cycles.

Table C.1: Peak ratios for angle-dependent XPS of the Sn 3d spectra shown in Fig. C.1. The peak position (P), the relative intensity (R) and the FWHM (F) are given.

		P	R	F
	Error	(±0.05 eV)	(±1 %)	(±0.05 eV)
35°	Screened	486.37	78	1.37
	Unscreened	487.26	22	1.74
45°	Screened	487.60	85	1.58
	Unscreened	488.49	15	2.02
90°	Screened	487.49	77	1.40
	Unscreened	488.38	23	1.76

Table C.2: Peak ratios for angle-dependent XPS of the O 1s spectra shown in Fig. C.2. The peak position (P), the relative intensity (R) and the FWHM (F) are given.

		P	R	F
	Error	(±0.05 eV)	(±1 %)	(±0.05 eV)
35°	O_{lat}	530.02	93	1.72
	O_{vac}	531.86	7	1.72
45°	O_{lat}	531.22	90	1.98
	O_{vac}	532.92	10	1.98
90°	O_{lat}	531.23	97	1.92
	O_{vac}	533.24	3	1.92

Table C.3: Peak ratios for angle-dependent XPS of the Ba 3d spectra shown in Fig. C.3. The peak position (P), the relative intensity (R) and the FWHM (F) are given.

		P	R	F
	Error	(±0.05 eV)	(±1 %)	(±0.05 eV)
35°	Ba I	780.02	88	1.66
	Ba II	781.15	12	1.72
45°	Ba I	780.99	85	1.71
	Ba II	782.12	15	1.71
90°	Ba I	781.01	86	1.81
	Ba II	782.14	14	1.81

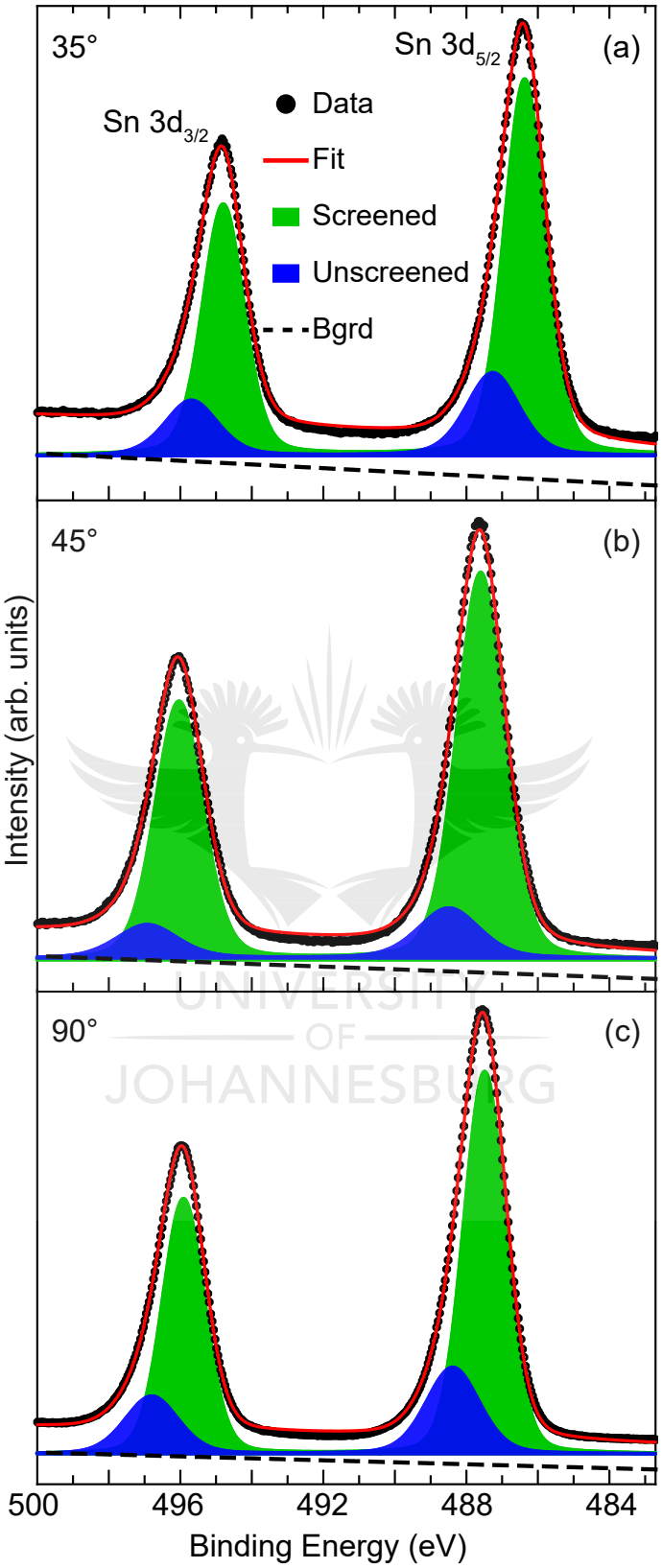

Figure C.1: Fits of the XPS spectra of the Sn 3d region. The Sn 3d spectra are fitted with two Voigt doublet components labeled screened and unscreened. The spectra were acquire at take-off angles of (a) 35°, (b) 45° and (c) 90°.

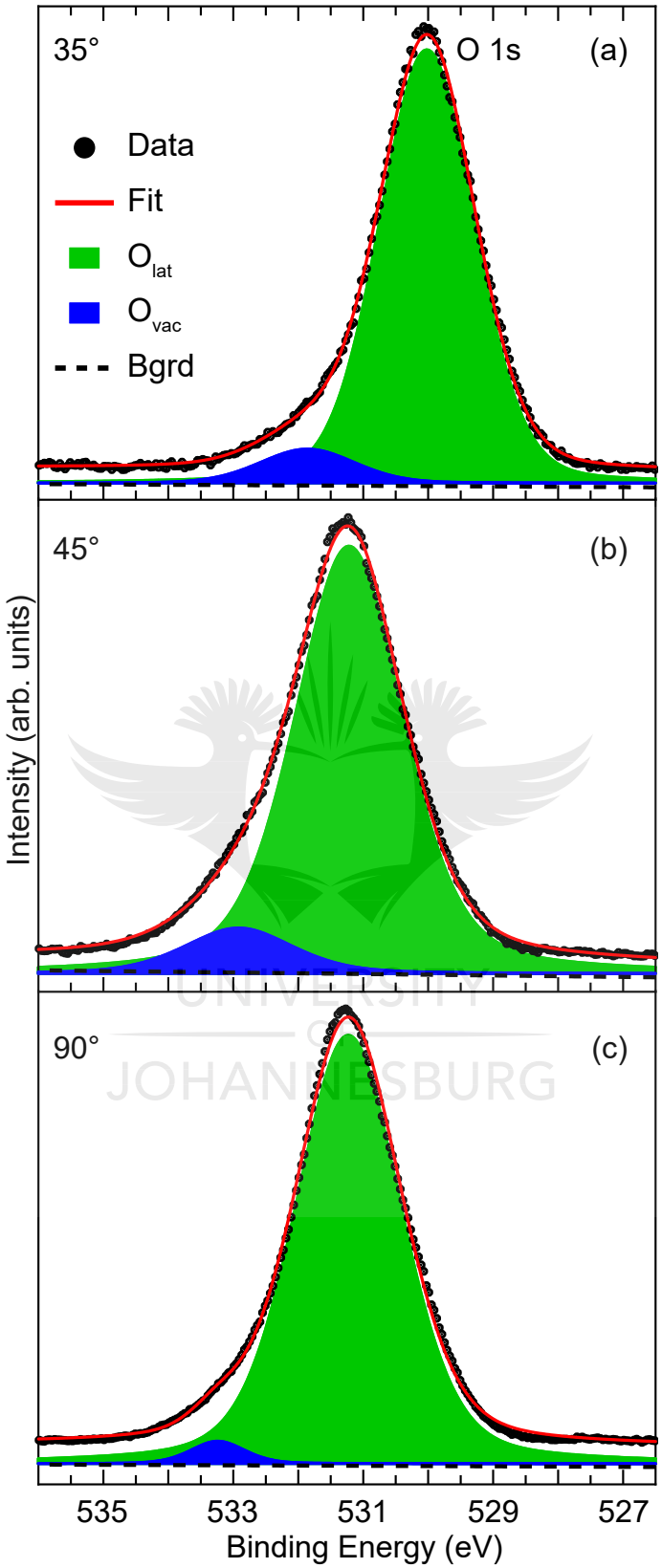

Figure C.2: Fits of the XPS spectra of the O 1s core level. The O 1s spectra are fitted with two single Voigt components labeled O_{lat} and O_{vac}. The spectra were acquire at take-off angles of (a) 35°, (b) 45° and (c) 90°.

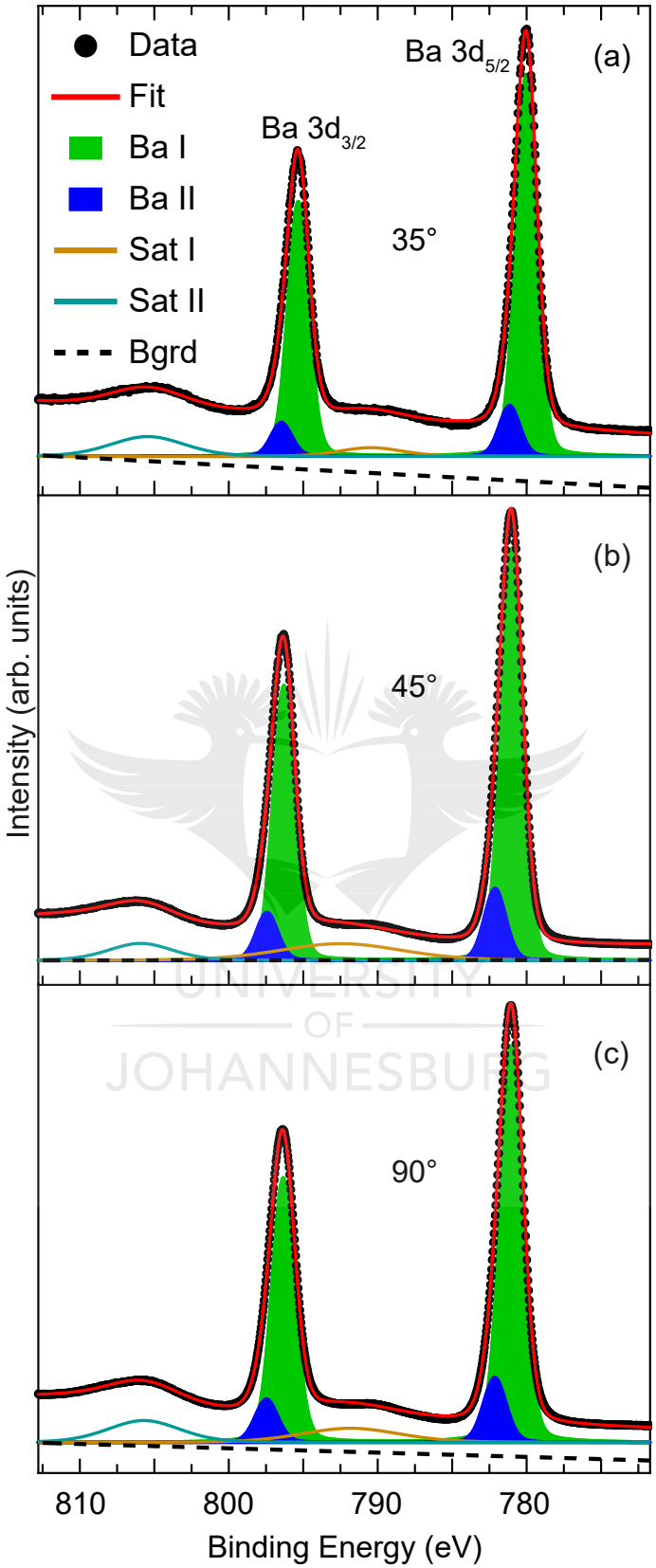

Figure C.3: Fits of the XPS spectra of the Ba 3d core electron. The Ba 3d spectra are fitted with two Voigt doublet components Ba I and Ba II. The spectra were acquire at take-off angles of (a) 35°, (b) 45° and (c) 90°.

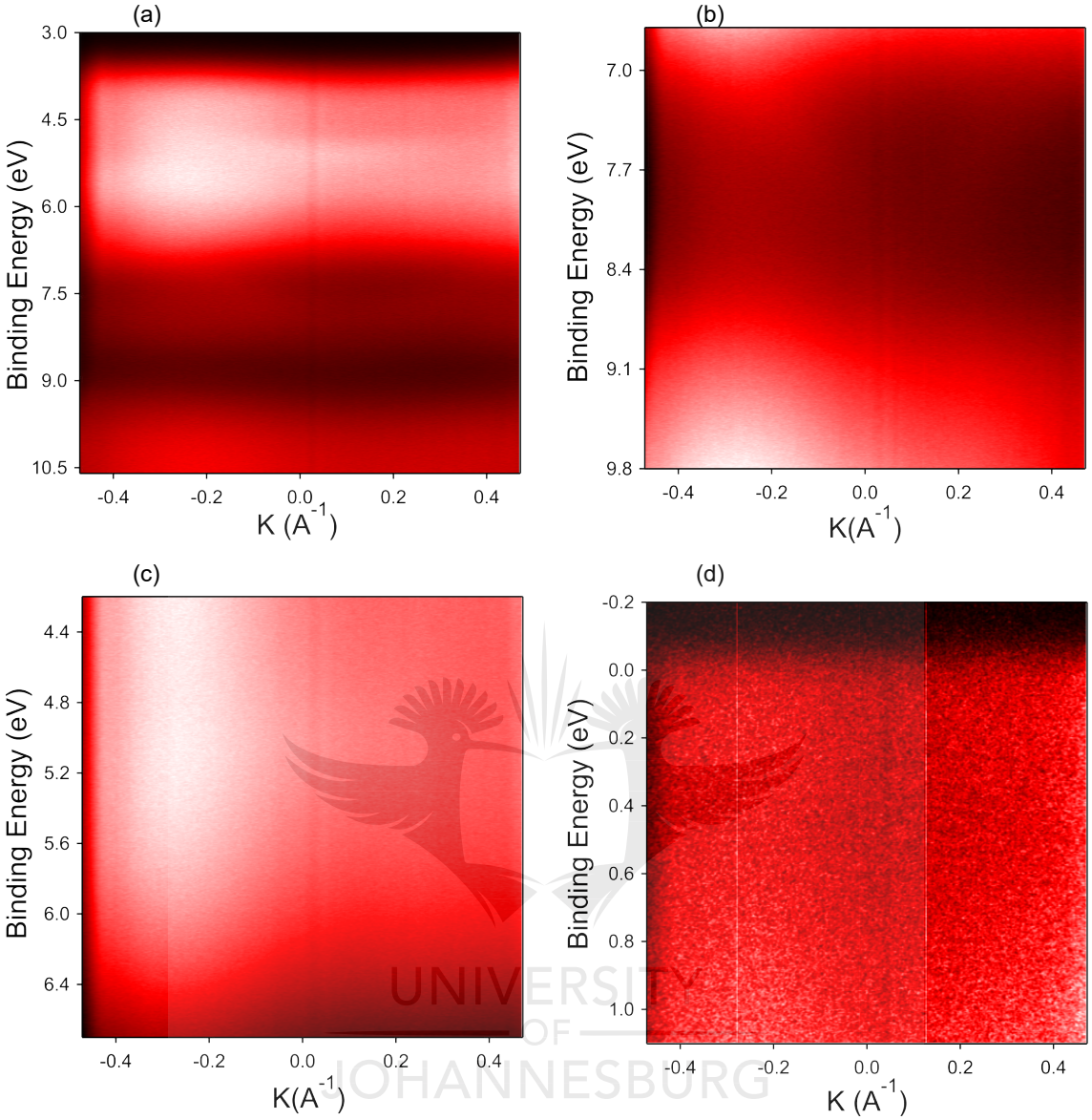

Figure C.4: 2D ARPES maps of the valence band of 6% La-$BaSnO_3$ (25 nm)/$BaSnO_3$ (100 nm)/$TbScO_3$ sample with the mobility of 117 $cm^2\ V^{-1}\ s^{-1}$. The data were recorded at room temperature in the $\bar{\Gamma}\bar{X}$ direction. (a) The full scan of the valence band region. (b)-(d) Scans around selected regions of the map in (a) indicated by the range of the vertical axis. This sample was annealed at about 1100°C in 7×10^{-7} mbar of O_2 for 10 minutes. The bands are not visible.

C.2 XPS Data of a 4% La-Doped $BaSnO_3$ Sample Grown with $BaSnO_3$ Buffer Layer

XPS data of the 4% La-$BaSnO_3$ (100 nm)/ $BaSnO_3$ (25 nm)/$SrTiO_3$ sample with the mobility of $18.35\pm0.11\ cm^2\ V^{-1}\ s^{-1}$ and the carrier density of $(0.781\pm0.002)\times10^{20}\ cm^{-3}$. The core electrons were excited with the Al K_α source and recorded with an experimental resolution of 0.78 eV. This sample was used to optimize the substrate temperature and the deposition pressure in Section 4.2.1 of the main text, and was grown at the temperature of 850 °C in

1.33×10^{-1} mbar of oxygen.Figures C.5, C.6 and C.7 show the fits of the Sn 3d, O 1s and Ba 3d spectra, respectively, for as-inserted and cleaned surfaces. The surface was cleaned following the procedure described in Section 3.3.4. Tables C.4, C.5 and C.6 summarized the parameters used to fit these spectra. It can be observed that the ratio of the peaks vary in proportions comparable to those reported in Tables 5.1, 5.2 and 5.3 in the main text for these core levels. Figure C.8 shows the XPS valence band region. The valence band leading edge (blue curve) was acquired over a period of 20 hours in order to enhance the feature around E_F. As can be seen in the inset, the conduction band minimum is not visible for this sample.

Table C.4: Fitted parameters of Sn 3d regions for the as-inserted and cleaned sample shown in Fig. C.5. The peak position (P), the relative intensity (R) and the FWHM (F) are given.

	As-inserted			Cleaned		
Error	P (eV) (±0.05)	R (%) (±1)	F (eV) (±0.05)	P (eV) (±0.05)	R (%) (±1)	F (eV) (±0.05)
Screened	486.90	60	1.18	486.76	66	1.11
Unscreened	487.32	40	1.57	487.18	34	1.61

Table C.5: Fitted parameters of O 1s regions for as-inserted and cleaned surfaces shown in Fig. C.6. The peak position (P), the relative intensity (R) and the FWHM (F) are given.

	As-inserted			Cleaned		
Error	P (eV) (±0.05)	R (%) (±1)	F (eV) (±0.05)	P (eV) (±0.05)	R (%) (±1)	F (eV) (±0.05)
O_{lat}	530.42	54	1.17	530.37	90	1.26
O_{vac}	531.65	20	1.17	531.36	8	1.26
−OH	532.52	20	1.17	531.96	2	1.26
C-O	533.53	6	1.17	—	—	—

Table C.6: Fitted parameters of Ba 3d regions for as-inserted and cleaned surfaces presented in Fig. C.7. The peak position (P), the relative intensity (R) and the FWHM (F) are given.

	As-inserted			Cleaned		
Error	P (eV) (±0.05)	R (%) (±1)	F (eV) (±0.05)	P (eV) (±0.05)	R (%) (±1)	F (eV) (±0.05)
Ba I	780.00	60	1.52	779.88	84	1.43
Ba II	781.13	40	1.52	781.01	16	1.43

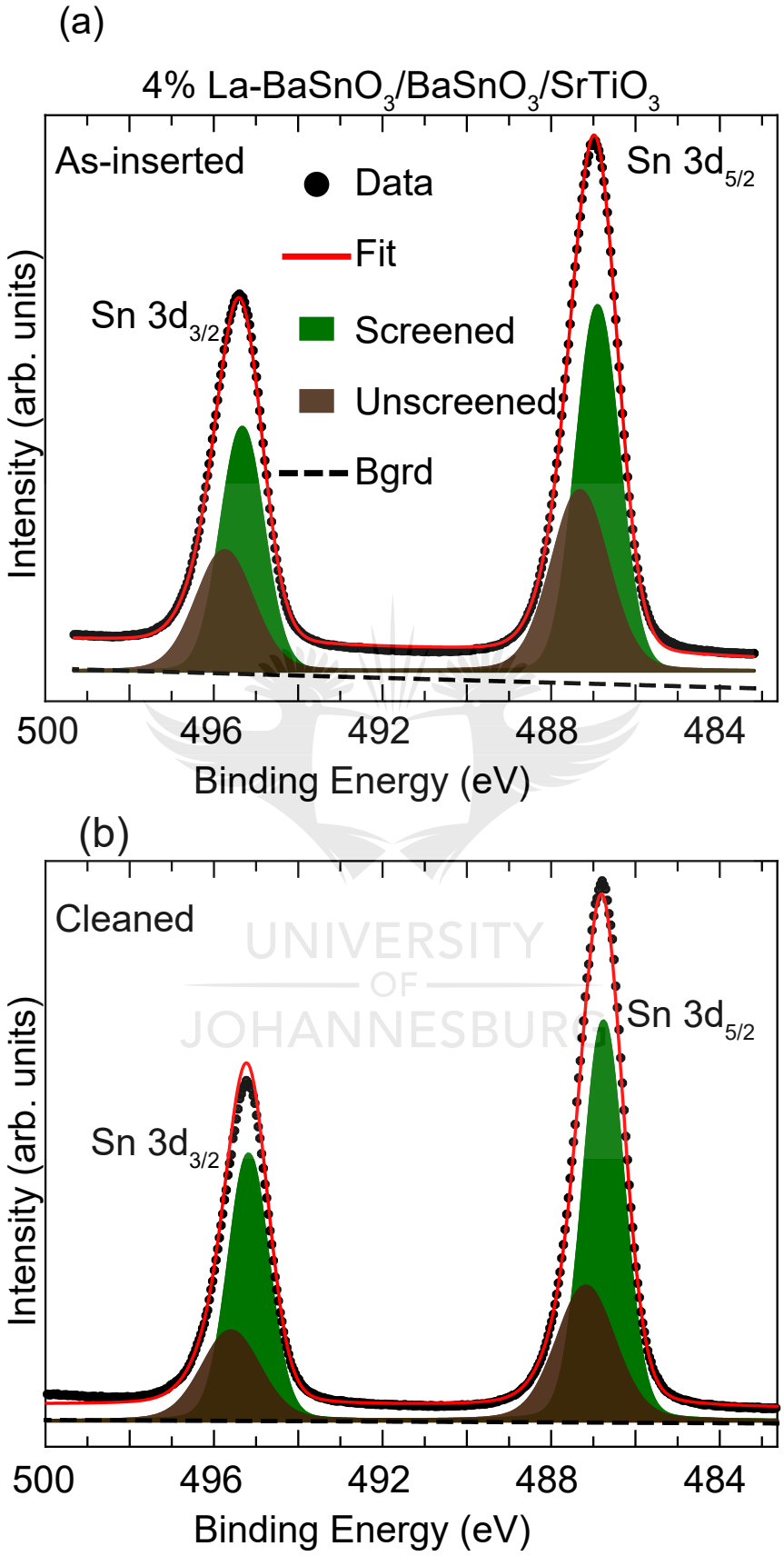

Figure C.5: XPS Sn 3d core regions for the (a) as-inserted and (b) cleaned 4% La-$BaSnO_3$ (100 nm)/ $BaSnO_3$ (25 nm)/$SrTiO_3$ sample. Two Voigt doublet components are used to fit the core spectra.

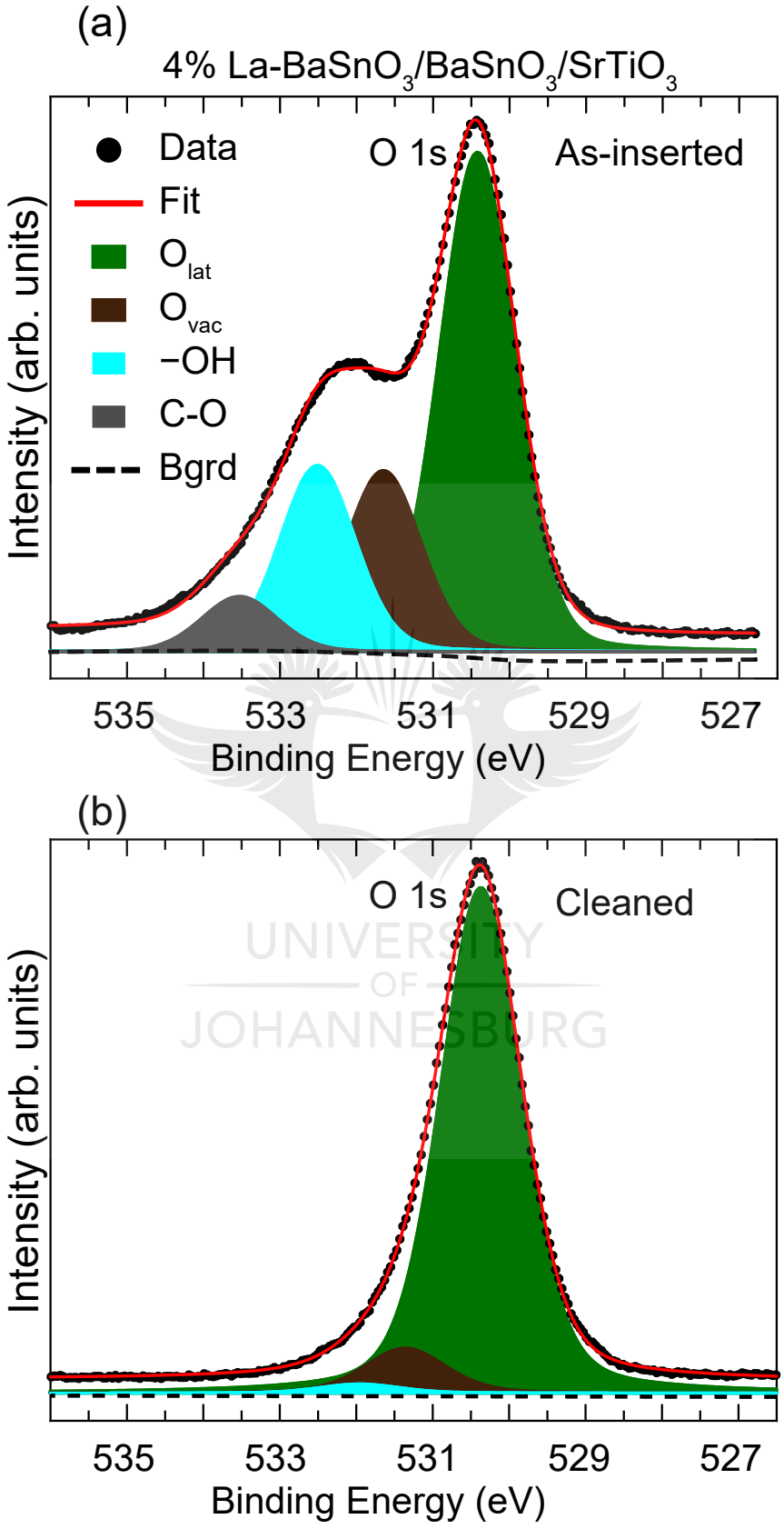

Figure C.6: XPS O 1s core regions for the (a) as-inserted and (b) cleaned 4% La-$BaSnO_3$ (100 nm)/ $BaSnO_3$ (25 nm)/$SrTiO_3$ sample. Four and three singlet Voigt components are used to fit the spectra of the as-inserted and cleaned surfaces, respectively.

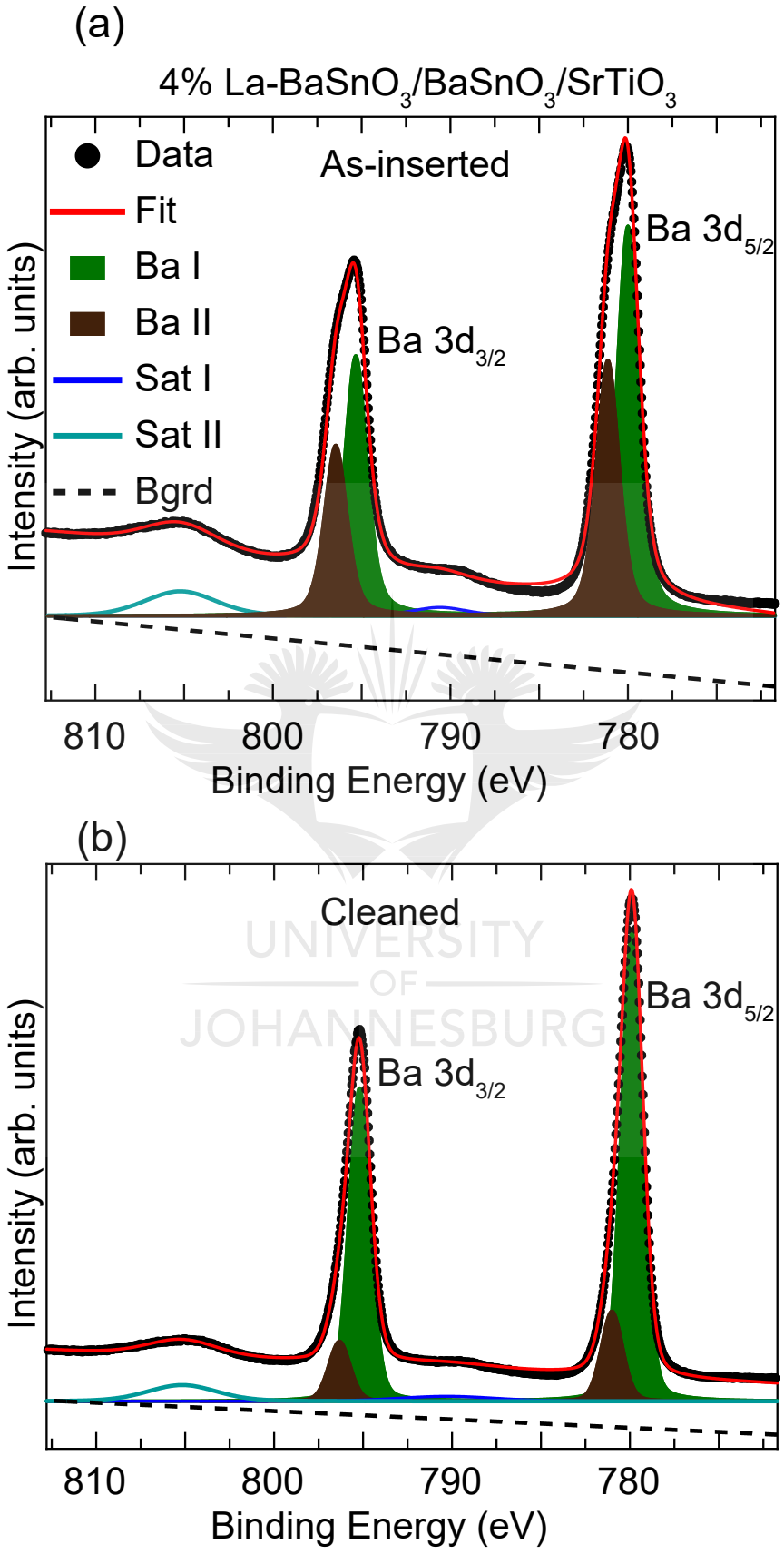

Figure C.7: XPS Ba 3d core regions for the (a) as-inserted and (b) cleaned 4% La-$BaSnO_3$ (100 nm)/ $BaSnO_3$ (25 nm)/$SrTiO_3$ sample. Two Voigt doublet components are used to fit the core spectra.

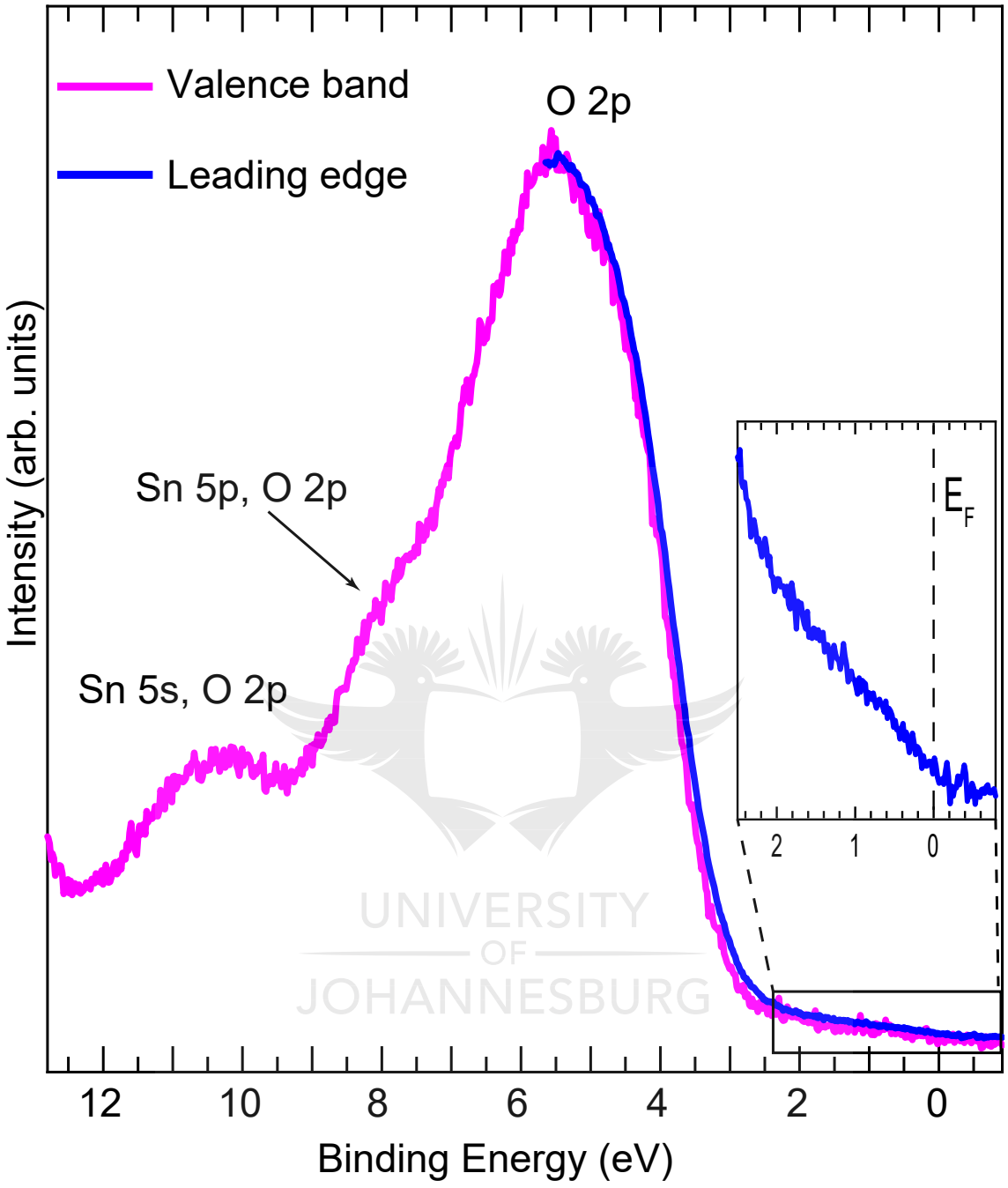

Figure C.8: XPS valence band region of the 4% La-$BaSnO_3$ (100 nm)/$BaSnO_3$ (25 nm)/$SrTiO_3$ sample. The leading edge (blue curve) was measured over a period of 20 hours. The magenta curve is normalized to the maximum intensity of the blue curve. The inset shows the enlargement of the area indicated by the black rectangle, for the blue curve only.

C.3 XPS Data of the La 3d Regions

In addition to the XPS data of the primary core levels presented in the main text such as Sn 3d, O 1s and Ba 3d, the core XPS spectra of La 3d are presented in Fig C.9. The green and blue curves represent the La 3d core electrons of the 2% La-$BaSnO_3$ (25 nm)/$TbScO_3$

and 6% La-$BaSnO_3$ (25 nm)/$SrTiO_3$ samples discussed in Sections 5.2.1 and 5.3 of the main text. The red and cyan curves are associated with the core levels presented in Appendixes C.1 and C.2, respectively for the 6% La-$BaSnO_3$ (25 nm)/$BaSnO_3$ (100 nm)/$TbScO_3$ and 4% La-$BaSnO_3$ (100 nm)/$BaSnO_3$ (25 nm)/$SrTiO_3$ samples. As can be seen, the La 3d signal is amplified as the concentration of the La content in the sample increases from 2% to 6%. It can also be observed that the line shape of the signal changes depending on whether a buffer layer is used or not. For instance, an additional feature is visible at the binding energy of ∼833 eV in the spectra of the unbuffered samples (blue and green curves). The origin of that feature is unknown. It should be noted that the intensities of all these spectra were different. For representation, the spectra were magnified by multiplying their intensities by factors of 2.5 (red curve), 5.6 (blue curve), 1.17 (green curve) and 7 (cyan curve).

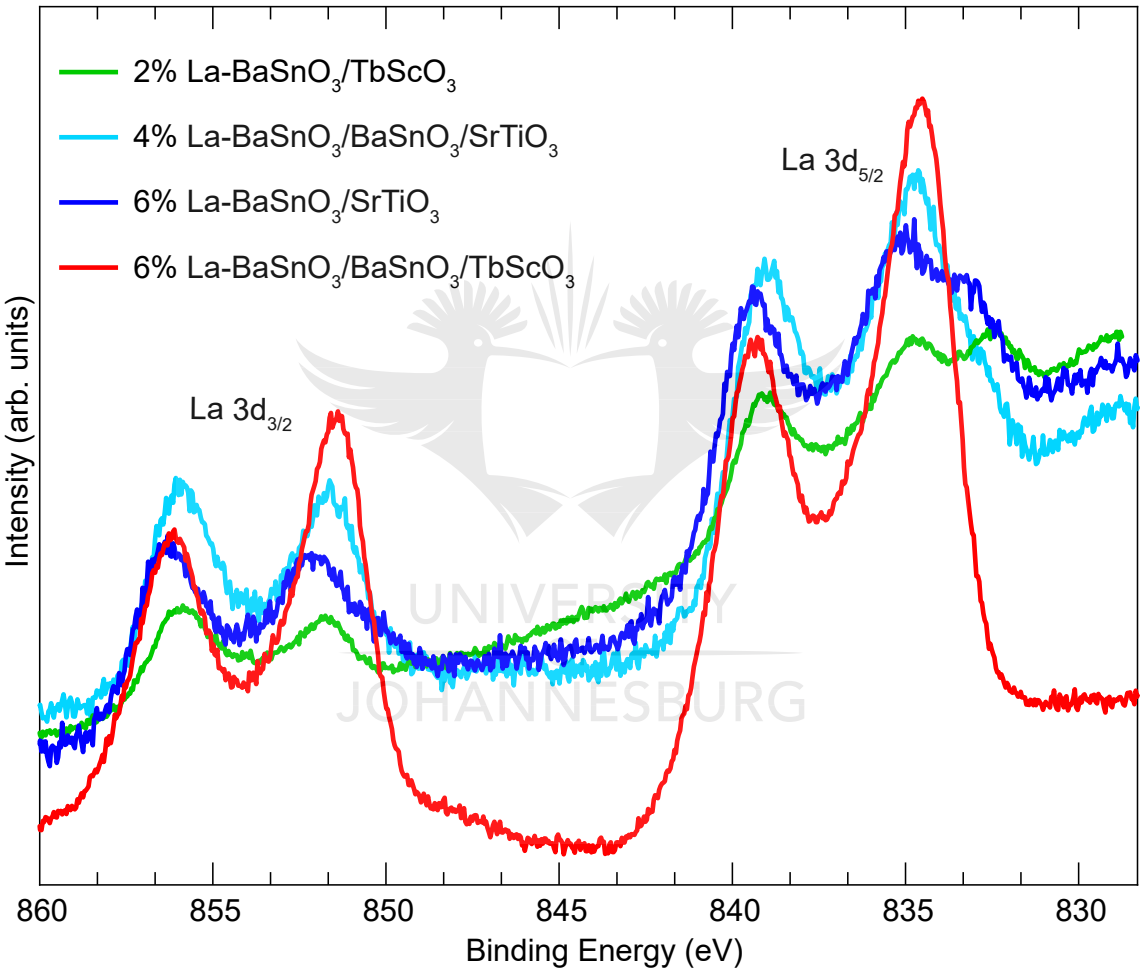

Figure C.9: XPS La 3d core regions for the 2% La-$BaSnO_3$ (25 nm)/$TbScO_3$ (green), 4% La-$BaSnO_3$ (100 nm)/$BaSnO_3$ (25 nm)/$SrTiO_3$ (cyan), 6% La-$BaSnO_3$ (25 nm)/$SrTiO_3$ (blue) and 6% La-$BaSnO_3$ (25 nm)/$BaSnO_3$ (100 nm)/$TbScO_3$ samples. These spectra are for samples cleaned in oxygen at different temperatures. For representation, offsets in intensity were applied as ×2.5 (red curve), ×5.6 (blue curve), ×1.17 (green curve) and ×7 (cyan curve).

C.4 XPS Data of a $SrZrO_3$ Buffered Sample

The fits of the Sn 3d (Fig. C.10), O 1s (Fig. C.11) and Ba 3d (Fig. C.12) core XPS spectra for as-inserted and cleaned surfaces of a 6% La-$BaSnO_3$ (25 nm)/$SrZrO_3$ (100 nm)/$TbScO_3$ sample are presented in this section. Tables C.7, C.8 and C.9 give the parameters used to perform the fits. The data were collected with an experimental resolution of 0.78 eV using the Al K_α source. The $SrZrO_3$ buffer layer was grown at 1400 °C, and had an electron mobility of 127 ± 4 cm^2 V^{-1} s^{-1} at a carrier density of $(4.66 \pm 0.06) \times 10^{20}$ cm^{-3}. This sample was annealed at 1186 °C in vacuum. The surface was believed to have been damaged during cleaning due to the high temperature annealing. The large shift of the peaks to higher binding energies, especially in the cleaned surface, could be associated with sample charging. The clamp that held the sample and ensured grounding may not have made good contact with the sample. Note that the O 1s spectrum of the cleaned surface (see Fig. C.11(b)) is completely dominated by one component (see Table C.8). The residual −OH component due to water that was reported in surfaces prepared at lower temperatures as discussed in the main text is completely removed from the surface.

Table C.7: Fitted parameters of Sn 3d regions for the as-inserted and cleaned sample shown in Fig. C.10. The peak position (P), the relative intensity (R) and the FWHM (F) are given.

	As-inserted			Cleaned		
Error	P (eV) (±0.05)	R (%) (±1)	F (eV) (±0.05)	P (eV) (±0.05)	R (%) (±1)	F (eV) (±0.05)
Screened	487.24	63	1.25	489.68	54	1.07
Unscreened	488.04	37	1.40	490.48	46	1.49

Table C.8: Fitted parameters of O 1s regions for as-inserted and cleaned surfaces shown in Fig. C.11. The peak position (P), the relative intensity (R) and the FWHM (F) are given.

	As-inserted			Cleaned		
Error	P (eV) (±0.05)	R (%) (±1)	F (eV) (±0.05)	P (eV) (±0.05)	R (%) (±1)	F (eV) (±0.05)
O_{lat}	530.89	48	1.23	533.42	99	1.61
O_{vac}	532.1	21	1.23	535.16	1	1.61
−OH	532.96	23	1.23	—	—	—
C-O	533.86	8	1.23	—	—	—

Table C.9: Fitted parameters of Ba 3d regions for as-inserted and cleaned surfaces presented in Fig. C.12. The peak position (P), the relative intensity (R) and the FWHM (F) are given.

	As-inserted			Cleaned		
Error	P (eV) (±0.05)	R (%) (±1)	F (eV) (±0.05)	P (eV) (±0.05)	R (%) (±1)	F (eV) (±0.05)
Ba I	780.46	65	1.57	783.33	85	1.59
Ba II	781.59	35	1.57	784.46	15	1.59

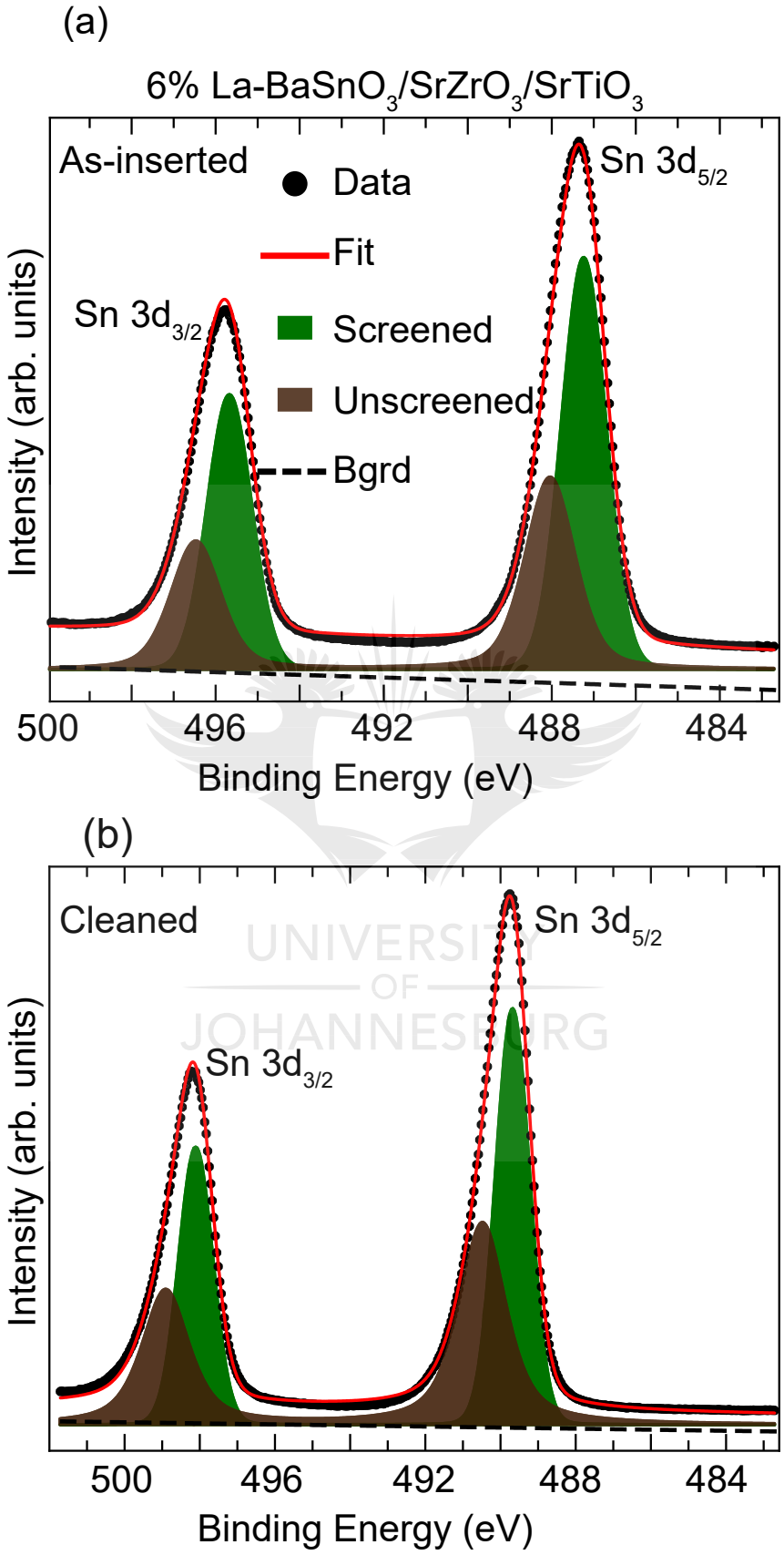

Figure C.10: XPS Sn 3d core spectra for the (a) as-inserted and (b) cleaned 6% La-$BaSnO_3$ (25 nm)/$SrZrO_3$ (100 nm)/$TbScO_3$ sample. The spectra are fitted to two doublet Voigt components.

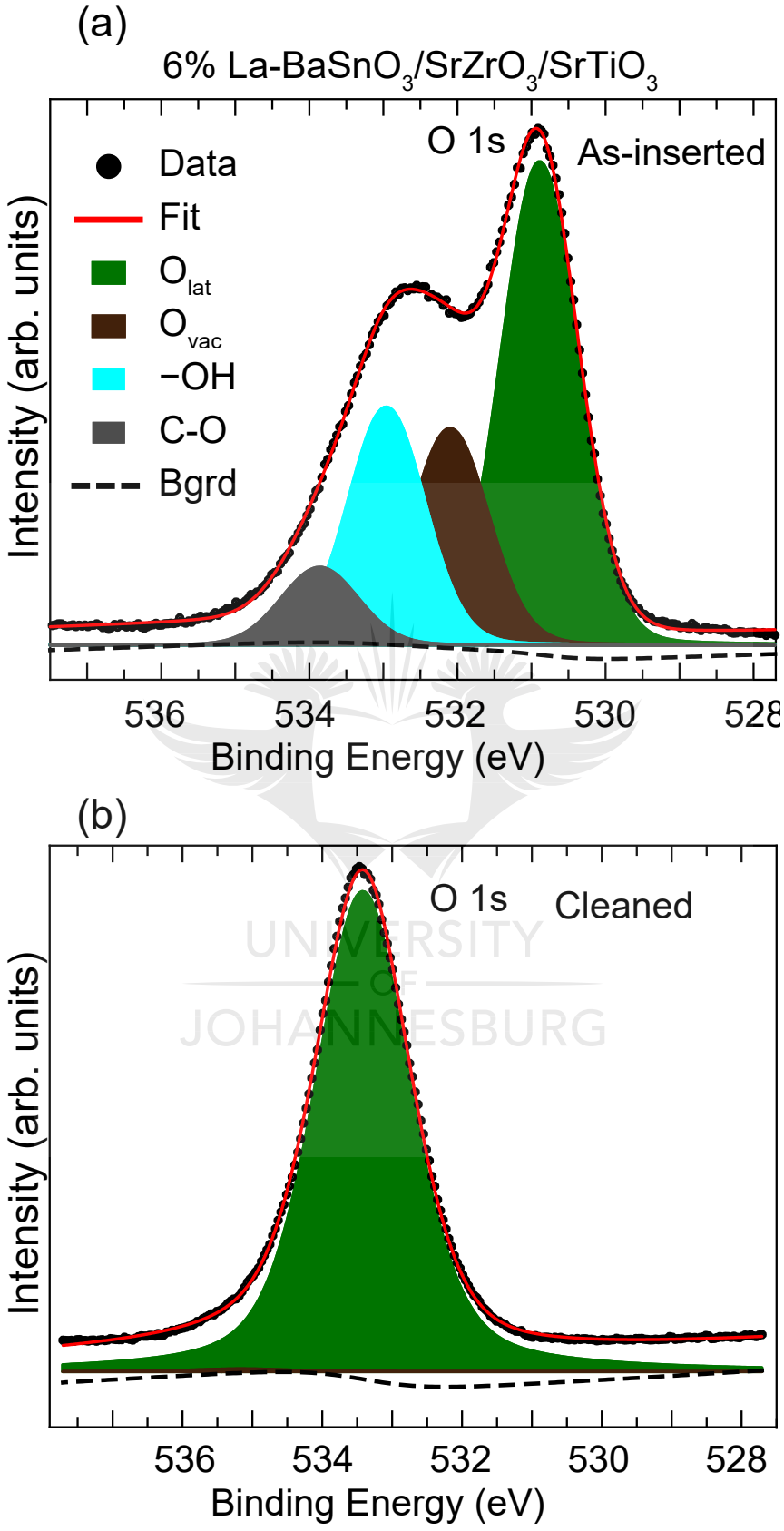

Figure C.11: XPS O 1s core spectra for the (a) as-inserted and (b) cleaned 6% La-$BaSnO_3$ (25 nm)/$SrZrO_3$ (100 nm)/$TbScO_3$ sample. Four and two singlet Voigt components are used to fit the spectra of the as-inserted and cleaned surfaces, respectively.

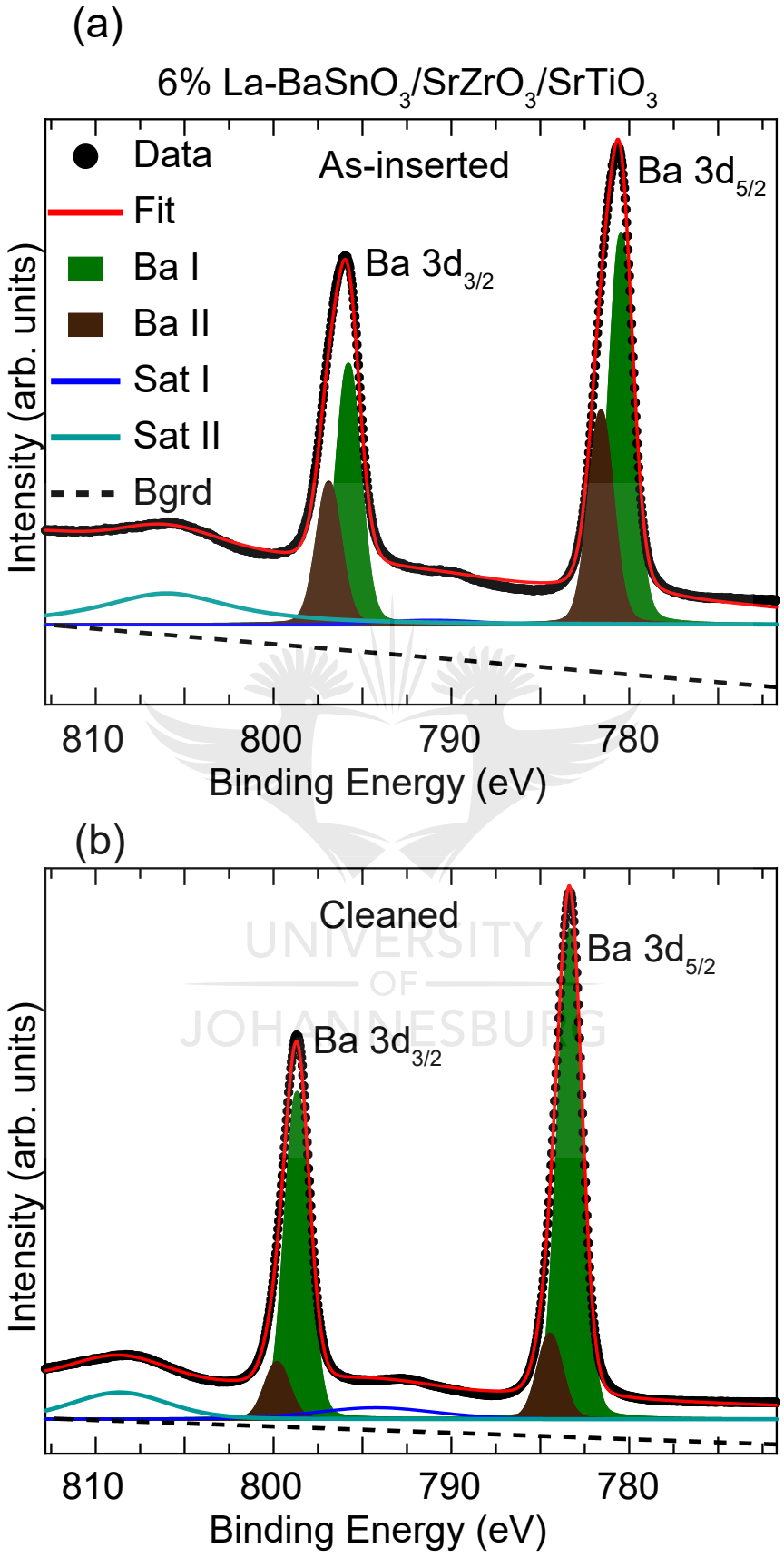

Figure C.12: XPS Ba 3d core spectra for the (a) as-inserted and (b) cleaned 6% La-$BaSnO_3$ (25 nm)/$SrZrO_3$ (100 nm)/$TbScO_3$ sample. The spectra are fitted to two doublet Voigt components.

C.5 Spectroscopic Data of a Sample Cleaned and Measured at the Max Planck Institute

In this section, the ARPES data for a 6% La-$BaSnO_3$ (25 nm)/$BaSnO_3$ (100 nm)/$TbScO_3$ sample measured at the Max Planck Institute for Solid State Research in Stuttgart, Germany are presented. The sample was grown in the PLD chamber and *ex situ* transferred into the ARPES chamber while limiting air contamination. Figure C.13 shows the LEED images of the surface at different stage of the preparation prior to ARPES experiments. These images were taken at different electron energies. Looking at the images, it seems as if the LEED of the surface after annealing in UHV at temperatures up to 200 °C gets worse compared with the LEED of the surface as inserted. However, the LEED improves again after annealing at 630 °C for 5 minutes in 1×10^{-6} mbar of O_2, indicating the cleanliness of the surface.

Figure C.14 depicts the comparison of the ultraviolet photoemission spectroscopy (UPS) data of the valence bands measured with He I on the surface annealed at 200 °C in UHV (magenta curve) and 630 °C in O_2 (green curve). It can be observed that the valence band spectra are shifted with respect to each other. This is probably due to electrical charging of the surface. Furthermore, the inset which represents the enlargement of the area close to E_F delimited by

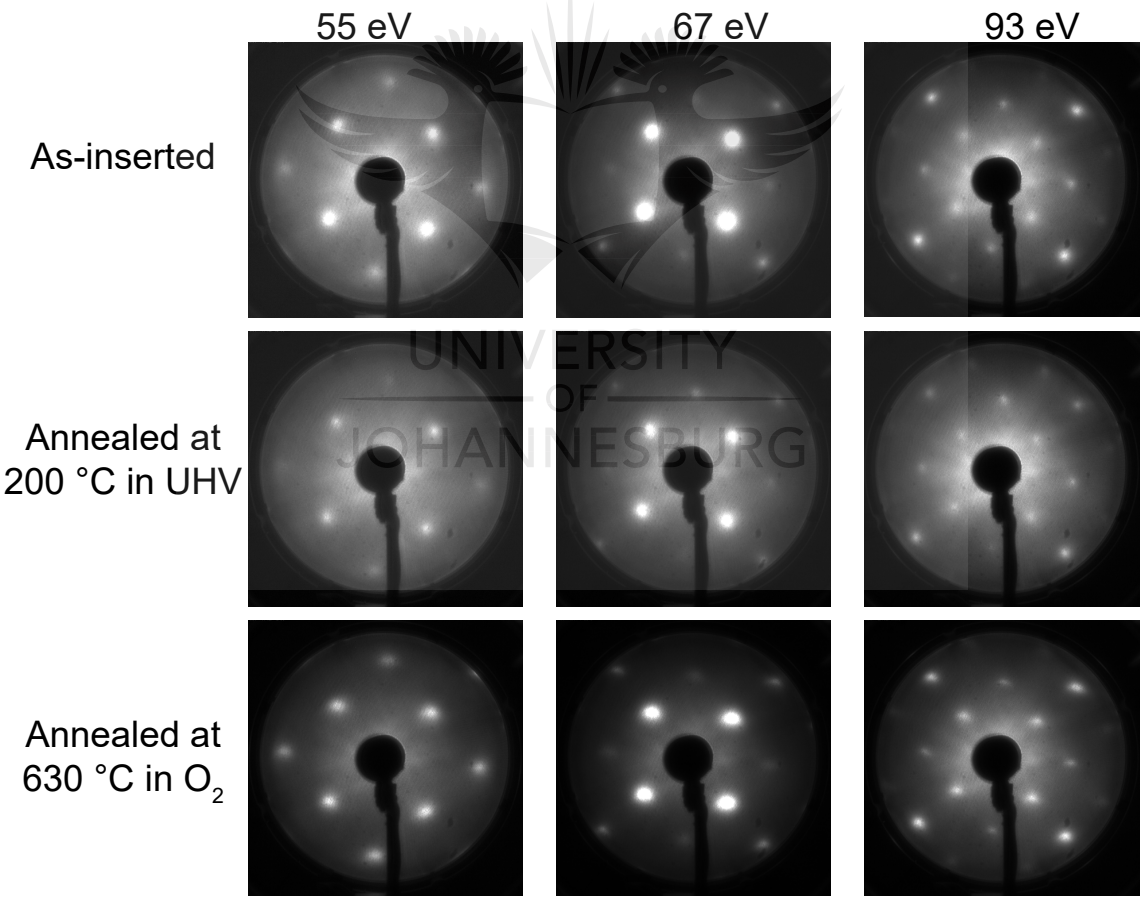

Figure C.13: LEED images from the surface of the 6% La-$BaSnO_3$ (25 nm)/$BaSnO_3$ (100 nm)/$TbScO_3$ sample prepared for ARPES measurements. The images are taken at various electron energies on the surface at different stages of cleaning.

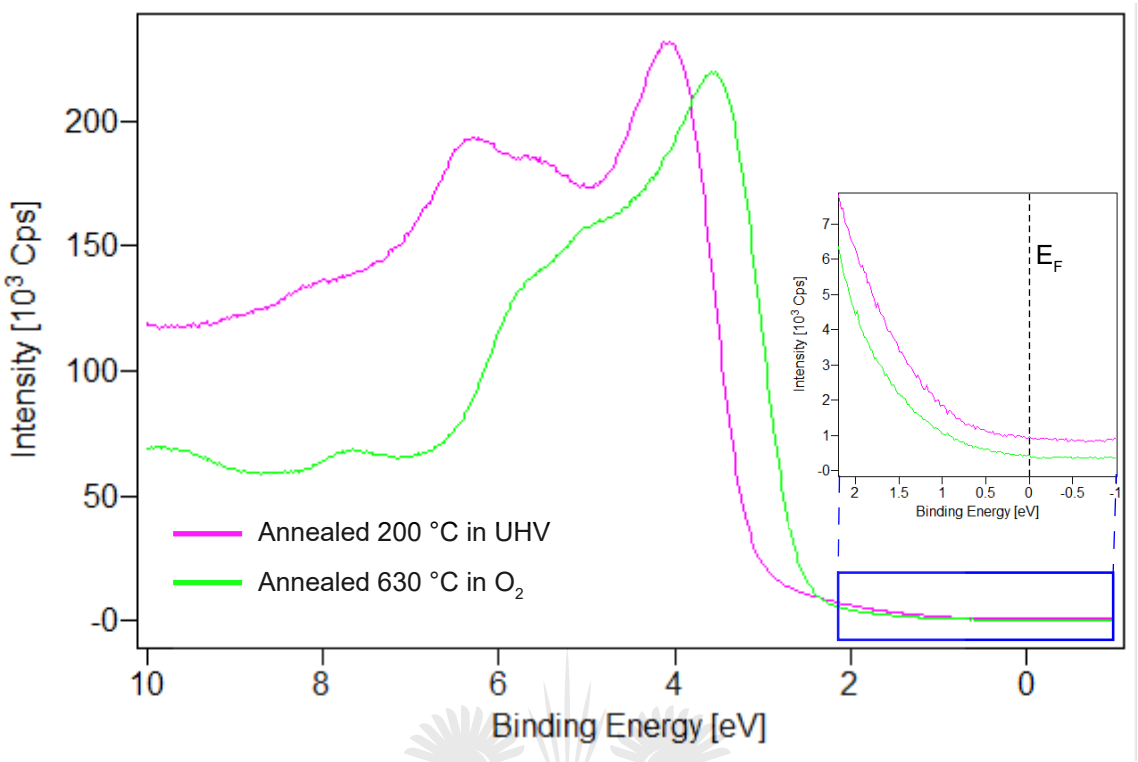

Figure C.14: UPS spectra of the valence bands of the surface of the 6% La-$BaSnO_3$ (25 nm)/$BaSnO_3$ (100 nm)/$TbScO_3$ sample annealed in vacuum (magenta curve) and in O_2 (green curve). The inset shows the enlargement of the region close to E_F indicated by the blue rectangle.

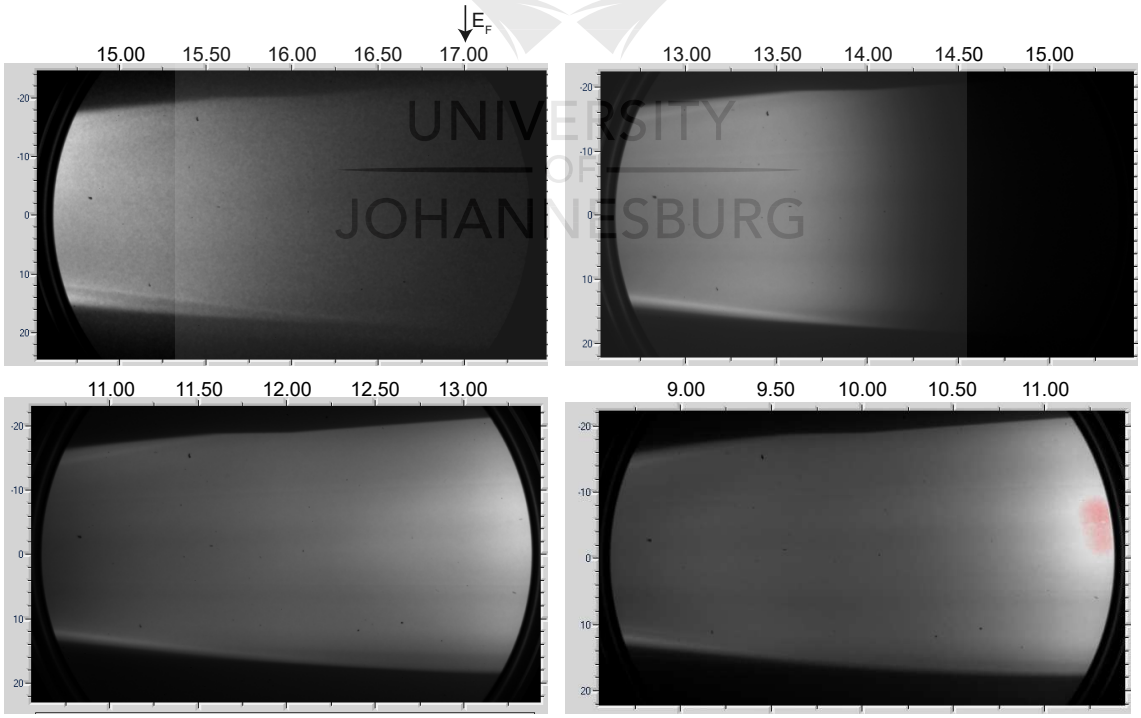

Figure C.15: 2D ARPES maps of the valence band in various kinetic energy ranges measured from the surface annealed at 630 °C in O_2. The bands are not visible.

the blue rectangle shows no conduction band state. The conduction band feature could not be detected in the surface prepared at 630 °C probably because this surface still contained a small amount of contamination, as evidenced by the XPS measurement of the C 1s region (not shown here). It is noteworthy that the surface was exposed to He I radiation for about 2 hours, and it seemed as if He I had no effect in creating or developing the states both in the band gap and at the CBM as reported in literature [6] and discussed in the main text in Section 5.3. In Ref. [6] however, the sample was exposed to radiation for a significantly longer time.

Figure C.15 presents the 2D ARPES maps of the valence band acquired with He I in various kinetic energy ranges on the surface prepared at 630 °C in O_2 for 5 minutes. Looking at the figure, neither the valence nor the conduction bands are visible. These bands could still not be resolved on surfaces annealed in O_2 for a longer period of time and also at slightly higher temperatures.

Bibliography

[1] H. Paik, Z. Chen, E. Lochocki, H. Ariel Seidner, A. Verma, N. Tanen, J. Park, M. Uchida, S. Shang, B. C. Zhou, M. Brützam, R. Uecker, Z. K. Liu, D. Jena, K. M. Shen, D. A. Muller, and D. G. Schlom, APL Mater. **5**, 116107 (2017).

[2] M. Stróżak, M. Jalochowski, and M. Subotowicz, Acta Phys. Pol. A **81**, 239 (1992).

[3] E. N. Kaufmann, *Characterization of Materials* (John Wiley & Sons, Inc., Hoboken, 2012).

[4] J. Choi, C. B. Eom, G. Rijnders, H. Rogalla, and D. H. A. Blank, Appl. Phys. Lett. **79**, 1447 (2001).

[5] A. Prakash, J. Dewey, H. Yun, J. S. Jeong, K. A. Mkhoyan, and B. Jalan, J. Vac. Sci. Technol. A **33**, 060608 (2015).

[6] E. B. Lochocki, H. Paik, M. Uchida, D. G. Schlom, and K. M. Shen, Appl. Phys. Lett. **112**, 181603 (2018).

Appendix List of Publications

Publications

1. Arnaud P. Nono Tchiomo, Wolfgang Braun, Bryan P. Doyle, Wilfried Sigle, Peter van Aken, Jochen Mannhart, and Prosper Ngabonziza, *High-temperature-grown buffer layer boosts electron mobility in epitaxial La-doped $BaSnO_3/SrZrO_3$ heterostructures*, APL Mater. **7**, 041119 (2019).
2. Arnaud P. Nono Tchiomo, Ganga Babu-Geetha, Emanuela Carleschi, Prosper Ngabonziza, and Bryan P. Doyle, *Surface characterization of clean $SrTiO_3(100)$ substrates by x-ray photoelectron spectroscopy*, Surf. Sci. Spectra, **25**, (2018).

Conferences Attendance

1. **Postgraduate Conference**, *University of Johannesburg, South Africa*, 16th October 2019. Oral presentation.
2. **International Workshop on Oxide Electronics**, *Les Diablerets, Switzerland*, 1st - 3rd October 2018. Poster presentation.
3. **Inter-Faculty Postgraduate Symposium**, *University of Johannesburg, South Africa*, 27th October 2017. Oral presentation.